Daniel Schwindt



Permafrost in ventilated talus slopes below the timberline

A multi-methodological study on the ground thermal regime and its impact on the temporal variability and spatial heterogeneity of permafrost at three sites in the Swiss Alps

Permafrost in ventilated talus slopes below the timberline

A multi-methodological study on the ground thermal regime and its impact on the temporal variability and spatial heterogeneity of permafrost at three sites in the Swiss Alps

Dissertation zur Erlangung des
naturwissenschaftlichen Doktorgrades
der Bayerischen Julius-Maximilians-Universität Würzburg

vorgelegt von
Daniel Schwindt

aus
Leverkusen

Würzburg, 2013

Eingereicht am: 19.03.2013

1. Gutachter: PD Dr. Christof Kneisel

2. Gutachter: Prof. Dr. Birgit Terhorst

der Dissertation

1. Prüfer: PD Dr. Christof Kneisel

2. Prüfer: Prof. Dr. Bernd Zimanowski

der mündlichen Prüfung

Tag der mündlichen Prüfung: 03.07.2013

"Each piece of the puzzle leaves an outline of the next"

Ben Weaver (2011), Grass Doe

Acknowledgements

"Each piece of the puzzle leaves an outline of the next". A great citation to paraphrase the evolution of this thesis. I will always be grateful to PD Dr. Christof Kneisel (University of Würzburg), who handed me the first piece of the puzzle by introducing me to the awesome permafrost site in the Val Bever, offered me the opportunity to write my PhD thesis in his working group, and gave me the freedom and time to collect and put together all the other pieces that build up this thesis.

I would like to thank Prof. Dr. Roland Baumhauer, who provided the possibility to write this thesis in a continuously pleasant working environment at his Institute of Geography and Geology at the University of Würzburg, for his steady support. I am especially grateful to Prof. Dr. Birgit Terhorst for her support during the final period of this thesis, for introducing me into the world of landslides and mass movements and for offering me perspectives and a wide field for future research projects.

This study wouldn't have been possible without the personal grant from the elite network of Bavaria (Bayerisches Eliteförderungsgesetz; BayEFG). Furthermore I would like to thank Reinhold Gröner, for the steady consulting and processing of numerous proposals and invoices.

A special thanks goes out to Tobias Rödder for creative and constructive discussions, for many hours of jogging during lunch breaks and for the always great time in the field, and especially the numerous races uphill with far too much weight in the backpacks! Furthermore, I would like to thank all the colleagues and friends at the University for creative discussions and distractions with a cup of coffee or with an excellent Franconian

beer. Thank you, Andy, Angela, Anja, Birgit, Chrischne, Christian, Daniel, Doro, Gernot, Jens, Julie, Jürgen, Kolli, Philipp, Sabine, Sebastian, Stefan, Tobias & Tobias!

For proof reading of this thesis I would like to thank Sabine Baumann, Jens Brauneck, Aline Finger, Christine Sandmeier, Anja Scholten and Tobias Ullmann. Thanks for your comments and especially your endurance!

For this study, more than 2700 times electrodes and almost 1300 times geophones had to be positioned for geophysical measurements. This wouldn't have been possible without the help of many hands. For support and assistance in the field I would like to thank Cornelius Buschbaum, Adrian Emmert, Aline Finger, Julie Kästl, Philipp Konrad, Birgit Mannig, Tobias Rödder, Nils Roth, Christine Sandmeier and Susanne Wagenbrenner. Thank you very much!

I would like to thank the municipalities of Bever, Brülisau and S-Chanf for permissions and their kind support.

Many thanks to my old friend Christian Marx, who spent quite some time with me in the locksmithery developing and constructing the electrode concept for the ERT-monitoring arrays. Thanks for your help and for all the hours of cycling!

Around 50.000 kilometres were covered to collect all the data that built up this thesis. A special thanks goes out to Neil Young, Tom Waits and Leonard Cohen, who accompanied me and kept me awake during endless hours on the road!

I am eternally grateful to Christine Sandmeier for her support and friendship, and especially during the last month of this thesis, for offering me a shoulder to lean on and for helping me back on my feet when I broke my ribs and had a herniated disk.

For their steady support I would like to thank my family and in especial my father, who helped me with his remarkable technical and scientifical knowledge. Thank you for your sympathetic ear, for endless creative discussions with a glass of always fantastic French wine.

Lastly, I would like to thank Aline who went with me through some harsh times during this thesis, for her support, patience and trust, and for the numerous hours she helped me in the field under often unpleasant weather conditions, sometimes even without grumbling. Thank you, for the great time!

Summary

In the central Alps permafrost can be expected above 2300 m a.s.l., at altitudes where mean annual air temperatures are below -1 °C. Isolated permafrost occurrences can be detected in north-exposed talus slopes, far below the timberline, where mean annual air temperatures are positive. Driving factors are assumed to be a low income of solar radiation, a thick organic layer with high insulation capacities as well as the thermally induced chimney effect.

Aim of this study is to achieve a deeper understanding of the factors determining the site-specific thermal regime, as well as the spatially limited and temporally highly variable permafrost occurrences in vegetated talus slopes.

Three supercooled talus slopes in the Swiss Alps were chosen for investigation. Substantially different characteristics were a central criterion in the selection of study sites. Located in the Upper Engadin, climatic conditions, altitude as well as dimensions of the talus slopes are comparable for the study sites Val Bever and Val Susauna; major differences are rooted in the nature of talus substrate and in humus- and vegetation distribution. Characteristics of the Brüeltobel site, located in the Appenzeller Alps, diverge with regard to climatic conditions, altitude and dimensions of the talus slope; humus- and vegetation compositions are comparable to the Val Susauna site.

Confirmation and characterisation of ground ice is accomplished by the application of electrical resistivity and seismic refraction tomography. The estimation of the spatial permafrost distribution is based on quasi-3D resistivity imaging. For the confirmation of permafrost and the analysis of its temporal variability electrical resistivity monitoring

arrays were constructed and installed at all study sites, to allow year-round measurements. In addition to resistivity monitoring, the – up to now – first seismic refraction tomography winter monitoring was conducted at the Val Susauna to analyse the permafrost evolution during the winter half-year. Investigations of the ground thermal regime were based on the analysis of temperature logger data. Besides recording air- and ground surface temperatures, focus was set on the temperature evolution in vents and in the organic layer. To analyse the relationship between permafrost distribution on the one hand and humus- and vegetation distribution on the other hand, an extensive mapping of humus characteristics and vegetation composition was conducted at Val Susauna.

The existence of permafrost could be proven at all study sites. Spatially, permafrost bodies show a narrow transition to neighbouring, unfrozen areas. As observed at Val Susauna, the permafrost distribution strongly correlates with areas with exceptionally thick organic layer, high percentages of mosses and lichens in the undergrowth and dwarf grown trees. The temporal variability of permafrost has proven to be exceptionally high, with the magnitude of seasonal variations distinctly exceeding intra-annual changes. Thereby, the winter season is characterised by a significant supercooling. During snowmelt a growth in volumetric ice content is induced by refreezing of percolating meltwater on the supercooled talus.

The results confirmed the fundamental influence of the chimney effect on the existence and temporal variability of permafrost in talus slopes. Divergences in the effectiveness of the thermal regime were detected between the study sites. These are based on differences in the nature of talus material, humus characteristics and vegetation composition.

During summer, the organic material is usually dry at the daytime, inducing a high insulation capability and a protection of the subsurface against high atmospheric temperatures. Bouldery talus slopes typically show an organic layer that is fragmented by large boulders, which induces a strongly reduced insulation capability and allows an efficient heat exchange by convective airflow and percolating precipitation water. In the winter half-year, the thermal conductivity of the organic layer increases massively under moist or frozen conditions, allowing an efficient, conductive cooling of the talus material. The convective cooling in bouldery talus slopes affects an earlier onset and a higher

magnitude of supercooling than under consistent humus conditions. Here, conductive heat flow is dominant and the cooling in autumn is buffered by a prolonged zero curtain. The snow cover has proven to be incapable of prohibiting an efficient supercooling of the talus slope in winter, almost independent from thickness.

Zusammenfassung

In den zentralen Alpen kann oberhalb einer Höhe von 2300 m ü NN, bei mittleren Jährlichen Lufttemperaturen von weniger als -1 °C mit Permafrost gerechnet werden. Isolierte Permafrostvorkommen können jedoch in nordexponierten Hangschutthalden bei positiven Jahresmitteltemperaturen bis weit unterhalb der Waldgrenze gefunden werden.

Ziel dieser Arbeit ist es ein tieferes Verständnis des Faktorenkomplexes zu erreichen, der das standortspezifische, kleinräumige thermale Regime bedingt und damit die räumlich begrenzten, zeitlich hochvariablen Permafrostvorkommen in Hangschutthalden unterhalb der Waldgrenze steuert und ermöglicht.

Drei unterkühlte Hangschutthalden in den Schweizer Alpen wurden zur Untersuchung ausgewählt. Bei der Auswahl wurde im Speziellen auf fundamentale Unterschiede der Standortfaktoren Wert gelegt. Im Unterengadin gelegen sind die klimatischen Bedingungen, Höhenlage sowie die Dimensionen der Hangschutthalden an den Standorten Val Bever und Val Susauna vergleichbar; Eigenschaften des Hangschuttes, Charakteristik der organischen Auflage sowie der Vegetation unterscheiden sich. Der in den Appenzeller Alpen gelegenen Standort Brüeltobel unterscheidet sich in Bezug auf die klimatischen Bedingungen, der Höhenlage und der Ausmaße der Hangschutthalde deutlich, zeigt jedoch eine zum Val Susauna ähnliche Humus- und Vegetationscharakteristik.

Der Nachweis und die Charakterisierung von Untergrundeis basiert auf der Kombination von elektrischer Widerstandstomographie und seismischer

Refraktionstomographie. Zur Detektion der räumlichen Verbreitung von Untergrundeis wurden diese Methoden durch quasi-3D Widerstandstomographie ergänzt. Zum Nachweis von Permafrost und zur Analyse seiner zeitlichen Variabilität wurden Monitoringauslagen konstruiert und an den Standorten fest installiert. Widerstandsmessungen wurden ganzjährig durchgeführt. In Ergänzung zu dem Widerstandsmonitoring wurde im Val Susauna erstmalig seismische Refraktionstomographie zum Monitoring der Permafrostentwicklung im Winter durchgeführt. Die Analyse des thermalen Regimes basiert auf der Analyse von Temperaturlogger Daten. Dabei wurden neben Luft- und Bodentemperaturen vor allem die Temperaturentwicklung in den Schloten sowie in der Humusauflage berücksichtigt. Zur Untersuchung des Zusammenhangs der Permafrostverbreitung mit der Humus- und Vegetationscharakteristik wurde im Val Susauna eine Kartierung der Humuseigenschaften sowie der Vegetationszusammensetzung durchgeführt.

An allen untersuchten Standorten konnte Permafrost nachgewiesen werden. Räumlich sind die Permafrostkörper sehr scharf von benachbarten Hangbereichen abgegrenzt. Am Standort Val Susauna konnte ein hoher räumlicher Zusammenhang zwischen der Permafrostverbreitung und Bereichen mit besonders mächtiger Humusauflage, einem hohen Anteil an Moosen und Flechten im Unterwuchs sowie einem ausgeprägtem Zwergwuchs nachgewiesen werden. Die zeitliche Variabilität des Permafrost hat sich an allen Standorten als außergewöhnlich hoch herausgestellt. Dabei übersteigt die Magnitude der saisonalen Variabilität die mehrjährigen Veränderungen deutlich. Das Winterhalbjahr zeigt sich durch eine effiziente Unterkühlung geprägt. Die Schneeschmelze im Frühling steht in Verbindung mit einem deutlichen Eiszuwachs, der durch ein wiedergefrieren des versickernden Schmelzwassers an dem unterkühlten Hangschutt verursacht wird.

Die Ergebnisse haben den fundamentalen Einfluss des Chimney Effekt auf die Existenz und zeitliche Variabilität von Permafrost in Hangschutthalden bestätigt. Unterschiede in der Wirkungsweise des thermalen Regimes konnten herausgestellt werden, die in erster Linie auf die unterschiedliche Ausprägung der Humusauflage, Charakteristik des Hangschutts, und die Vegetationszusammensetzung zurückzuführen sind.

Während des Sommers ermöglicht die sehr geringe thermische Leitfähigkeit der im oberflächennahen Bereich meist recht trockenen organischen Auflage eine ausgeprägte

Isolation des Untergrundes gegenüber hohen Außentemperaturen. Die in grobblockigen Hangschutthalden zu findende ungleichmäßige, von Blockmaterial fragmentierte organische Auflage zeigt eine deutlich geringere Isolationsfähigkeit und ermöglicht einen effektiven, Wärmeaustausch durch Konvektion und perkolierendes Niederschlagswasser. Im Winterhalbjahr steigt die thermische Leitfähigkeit des organischen Materials unter durchfeuchteten sowie gefrorenen Bedingungen massiv an und ermöglicht eine effiziente Auskühlung der Hangschutts. Die Unterkühlung in grobblockigen Hangschutthalden zeigt aufgrund des auch im Winter ausgeprägten konvektiven Wärmeflusses eine höhere Magnitude und ein früheres Einsetzen als bei homogenen Humusauflagen, wo konduktiver Wärmefluss dominiert und eine Auskühlung im Herbst durch eine ausgeprägte zero-curtain Periode gepuffert wird. Der Einfluss der Schneedecke auf das thermale Regime ist insgesamt gering; ihre Isolationsfähigkeit ist, annähernd unabhängig von der Schneemächtigkeit, stark reduziert.

Table of Contents

List of Tables

List of Figures

List of Equations

List of Abbreviations

a.s.l.	above sea level
BH	borehole
BTS	bottom temperature of the winter snow cover
BT	study site Brüeltobel
DDF	freezing degree-day
DDT	thawing degree-day
ERT	electrical resistivity tomography
ERTM	electrical resistivity tomography monitoring
FDR	frequency domain reflectometry
IQR	interquartile range
ISR	inverted specific resistivity
MAR	measured apparent resistivity
RSD	relative standard deviation
SRT	seismic refraction tomography
SRTM	seismic refraction tomography monitoring
TTOP	temperature at the top of permafrost
VB	study site Val Bever
VS	study site Val Susauna
ZC	zero-curtain
ZCP	zero-curtain period

PART I – INTRODUCTION

1 Introduction

1.1 Motivation

Permafrost is defined as ground that remains at or below 0 °C for at least two consecutive years (Everdingen, 1993). Thereby, the presence of ice in the subsurface does not constitute a precondition. The factors allowing for a genesis and the perennial existence of ground ice, or determine its degradation, can be very complex and often exceed climatic conditions as the controlling parameter. While the impact of climatic changes (Beniston, 2004; IPCC, 2007) induced substantial warming of permafrost temperatures in the northern hemisphere during the last 20-30 years (Brown & Romanovsky, 2008), recent formation of permafrost can be observed where the ground thermal regime experiences fundamental modifications; for example in boreal forest, under thickening moss (Davis, 2001), due to anthropogenically induced shading effects (Davis, 2001), or in recently deglaciated glacier forefields (Harris et al., 2009; Kneisel, 1998).

The world's largest permafrost occurrences exist in the northern hemisphere, where about one fifth of the ground is perennially frozen (see Davis, 2001; French, 2007). Permafrost areas are – according to French (2007) – subdivided into latitudinal or polar permafrost (i.e. arctic regions of North America and Asia), plateau or montane permafrost (i.e. Quinghai-Tibet Plateau) and, with the smallest share, alpine or mountain permafrost. While permafrost research at high latitudes has a long tradition (an outline of periglacial research is given by French (2007)), Haeberli et al. (2010) describe mountain permafrost as a "young research filed". The importance of permafrost research, particularly in the last decades, is exemplified by the high sensitivity of permafrost to climate change (Haeberli & Beniston, 1998; IPCC, 2007) and, especially in densely populated regions of the Alps, the high hazard potential that is associated with the degradation of permafrost (Haeberli, 1992; Harris, 2005; Harris et al., 2001; Harris & Vonder Mühll, 2003; Kääb et al., 2005; Kneisel et al., 2007; Marty et al., 2009). Mountain permafrost studies mainly focus on the discontinuous permafrost belt above the timberline, investigating rock glaciers (e.g. Barsch, 1973; Haeberli & Vonder Mühll, 1996; Hoelzle et al., 2002), glacier forefields (e.g.

Delaloye & Lambiel, 2008; Kneisel & Kääb, 2007) and rock-wall permafrost (e.g. Krautblatter & Moser, 2009). Since the mid-1990s, the development of regional (e.g. Lambiel & Reynard, 2001) and supra-regional (e.g. Boeckli et al., 2012; Keller, 1992) permafrost distribution maps reported an increased interest.

Generally, permafrost distribution is closely coupled with, and directly linked to climatic conditions. Whereas below MAAT of -1 °C permafrost is possible, significant amounts of permafrost can be expected at MAAT below -3 °C (Haeberli et al., 2010). This indicates a lower altitudinal permafrost limit of around 2300 m a.s.l. for the European Alps. Topographical (exposition) factors and ground surface conditions (nature of substrate; vegetation, snow cover) can though substantially modify general climatic conditions (Haeberli et al., 2010; Harris et al., 2009), leading to variations within mean annual ground surface temperatures of up to 15 °C within a distance of 1 km (Haeberli et al., 2010). According to the rules of thumb, developed by Haeberli (1975), permafrost can be expected under favourable conditions far below the timberline, where mean annual air temperatures are positive. Even though the number of below-timberline permafrost studies has recently increased, they are still easily outnumbered by research on high-mountain permafrost above the timberline.

Studies on below-timberline permafrost have so far tried to confirm and characterise permafrost in talus slopes below the timberline (Kneisel et al. (2000b), Kneisel & Hauck (2003), Hauck & Kneisel (2008b) as well as Delaloye (2004)). Furthermore, Schwindt (2007) and Kneisel & Schwindt (2008), investigated the areal distribution of permafrost by geophysical mapping and quasi-3D electrical resistivity tomography. Lately, electrical resistivity tomography has been applied to monitor temporal variability of permafrost in talus slopes below the timberline (Kneisel et al., accepted; Morard & Delaloye, 2010; Schwindt & Kneisel, 2010).

The existence of permafrost in low altitude talus slopes is usually ascribed to a specific thermal regime that allows for a supercooling of talus slopes, controlled by (I) a low income of solar radiation (northern exposure, shading effects), (II) duration and distribution of the insulating snow cover, (III) high insulation capability of the organic surface layer, and (IV) the thermally induced chimney effect as the decisive factor (Delaloye & Lambiel, 2005; Delaloye & Lambiel, 2007; Delaloye et al., 2003;

Gude et al., 2003; Haeberli, 1975; Morard, 2011; Morard et al., 2008; Sawada et al., 2003; Zacharda et al., 2007).

The central aim of this study is to achieve a deeper understanding of the factors determining the site-specific thermal regime, as well as the spatially limited and temporally highly variable permafrost occurrences in ventilated talus slopes below the timberline.

1.1.1 General aspects on the ground thermal regime of permafrost sites

Fundamentally, the ground thermal regime is directly coupled to the atmosphere and mainly influenced by conductive heat exchange with a vertical gradient (Williams & Smith, 1991). According to the second law of thermodynamics, the heat flow is in direction of colder temperatures. However, the interaction between atmosphere, ground surface and subsurface is distinctly more complex, as a variety of additional factors alternate, buffer or reinforce the heat exchange. Besides the general climatic conditions of a place (as discussed above), the ground thermal regime, and therefore, the permafrost distribution, is influenced by microclimatic conditions, that commonly override the influence of larger scale macroclimatic factors (Williams & Smith, 1991). Decisive factors for permafrost distribution are assumed to be a) local topography (income of solar radiation), b) surface and subsurface substrate, c) snow cover (thickness and duration) as well as vegetation cover, and d) distribution of organic material at the ground surface. Furthermore, water percolation (precipitation and meltwater) is an important factor for heat transport into the subsurface (Gruber & Haeberli, 2007; Krautblatter & Hauck, 2007; Williams & Smith, 1991). Thereby weighting the importance of permafrost influencing factors remains difficult and differs between polar/subpolar regions and mountain permafrost settings. The discontinuousness of mountain permafrost is mainly a result of strong topographic and microclimatic variability (Etzelmüller et al., 2001); vegetation cover and the accumulation of organic material are usually sparse. In this context, vegetated talus slopes containing permafrost may be regarded as the "missing link" between lowland and mountain permafrost. Lowland permafrost sites are distinctive in that the specific microclimate is fundamentally influenced by the activity of the so-called chimney effect (Harris &

PEDERSEN, 1998; WAKONIGG, 1996), a reversible air circulation that determines a rapid, convective heat transport and a supercooling of talus slopes.

The influence of snow cover on ground thermal regimes

The influence of the snow cover on ground thermal regimes can be ascribed to its very low thermal conductivity, ranging between 0.086 and 0.34 W/m K (FRENCH, 2007), as a function of its density (LUETSCHG & HAEBERLI, 2005), its high albedo and emissivity, as well as latent heat effects during snowmelt (HARRIS et al., 2007; ZHANG, 2005). Thereby, the snow cover affects the ground thermal regime depending on snow cover duration and snow thickness. A snow cover thickness of more than 60-80 cm is assumed to be an efficient insulator, which results in a decoupling of air- and ground-surface temperatures (HAEBERLI, 1973; KELLER & GUBLER, 1993; LUETSCHG et al., 2008), resulting in relatively higher mean annual ground surface temperatures compared to atmospheric temperatures (WILLIAMS & SMITH, 1991; ZHANG, 2005). As a consequence, a delayed onset of an insulating snow cover in autumn enables for a distinct cooling of the subsurface (LUETSCHG et al., 2008). This effect can be amplified under a shallow snow cover affecting an enhanced cooling as results of the high emissivity of the snow (autumn-snow-effect; cf. KELLER (1993) KELLER & TAMAS (2003)). Likewise, high insulation capability of the snow cover in spring/summer protects the subsurface from warm atmospheric temperatures. According to LUETSCHG et al. (2008), delays in early-winter snow insulation and snow disappearance in summer are equally important to ground thermal conditions. Snow-melt patterns and soil temperatures are furthermore strongly affected by the redistribution of snow by avalanches and snowdrift, with a positive effect on the preservation of permafrost (LUETSCHG et al., 2004). BERNHARD (1998) showed that for an active rock glacier snow funnels can develop as a result of vertical air movement, which reduces a thermal insulation effect of the snow cover and allows for a coupling of the active layer to the cold winter atmosphere.

Influence of organic surface layer and vegetation on ground thermal regimes

Likewise to snow cover, soil organic material acts as an effective insulator (WILLIAMS & SMITH, 1991). Studies analysing the influence of organic surface material and vegetation cover on the ground thermal regime mainly focus on lowland permafrost at high latitudes (e.g. MOSKALENKO, 2003; PAVLOV & MOSKALENKO, 2002). This is most

probably due to the fact that the distribution of alpine permafrost is mostly beyond the tree line and therefore not associated to organic material and vegetation cover.

Investigations in supercooled talus slopes are focused rather on the effect of low soil temperatures on vegetation, organic material and faunal properties (e.g. Alvarez-Uria & Körner, 2007; Cassagne et al., 2008; Hoch, 2008; Körner & Hoch, 2006; Körner & Paulsen, 2004; Molenda, 1996; Růžička & Hajer, 1996; Zacharda et al., 2005) than on the effect of vegetation and humus cover on the ground thermal regime.

Walker et al. (2003) show that the insulation provided by more dense plant canopies and thicker soil organic horizons could counter the trend of increased active layer thickness as a results of warmer air temperatures. Results from Yi et al. (2007) indicate, that a thin surface of organic cover can significantly buffer permafrost against severe degradation and will modulate the regional impact of climate warming on permafrost thaw. Sannel & Khury (2008) state, that despite of detected trends in climatic warming, permafrost conditions in peat plateaus have remained stable until present. However, the thermal conductivity of organic material varies with the seasons in dependence of moisture and temperature. Pavlov & Moskalenko (2002) relate the cooling effect of surface organic layers to soil temperatures in both, winter and summer. Thereby the thermal conductivity increases with increasing moisture and decreasing temperatures, from extremely low values under dry conditions (0.05 W/m K) to a high thermal conductivity under moist and frozen conditions of up to 2 W/m K (French, 2007). Consequently, the organic material shields the subsurface from warm atmospheric temperatures under dry conditions in summer, and allows for an effective cooling of the subsurface under moist and frozen conditions with decreasing atmospheric temperatures in autumn and winter (Kane et al., 2001; Williams & Smith, 1991). This affects that mean temperatures at the ground surface, which are generally much lower when covered with an organic layer, compared to adjacent areas with no organic material (Williams & Smith, 1991). The vegetation cover influences the ground thermal regime indirectly, by reducing the income of solar radiation, interception of precipitation, evapotranspiration and by modifying the snow cover distribution (Walker et al., 2003; Williams & Smith, 1991; Woo & Marsh, 2005).

Influence of substrate and thermal ventilation on ground thermal regimes

Recently, a number of studies focused on the influence of different substrate types (e.g. coarse blocks, fine-grained sediments or bedrock) on ground thermal regime, and showed that coarse blocky substrate can affect thermal conductivity, reduce warming effects of snow cover and provoke a negative thermal anomaly in blocky debris (e.g. GRUBER & HOELZLE, 2008; HERZ et al., 2003; JULIUSSEN & HUMLUM, 2008; RÖDDER & KNEISEL, 2012; SCHNEIDER et al., 2012). Following from these studies, small-scale thermal anomalies are frequently detected in talus slopes, above and below the timberline, and are often associated with sporadic permafrost occurrences.

HARRIS & PEDERSEN (1998) describe convective heat transport by the Balch effect, the chimney effect and, as an extension of the chimney effect, a continuous air exchange with the atmosphere as the most likely causes for negative thermal anomalies beneath coarse blocky materials. Analysing the non-conductive heat transfer within frozen soils, KANE et al. (2001) distinguish the convective heat transport into *free convection* and *forced convection*. Thereby, the chimney- and Balch effects correspond to the free convection, which occurs as a result of temperature-induced variations in air-density (Kane 2001); corresponding to the continuous air exchange with the atmosphere, the forced ventilation is driven by air pressure gradients. A cooling of blocky material due to the absorption of latent heat affected by evaporation/sublimation of water/ice, is assumed to be effective when the air is relatively dry, but is thought to play a minor role under humid conditions (HARRIS & PEDERSEN, 1998; WAKONIGG, 1996). However, significant cooling effects due to evaporation have been detected within near-surface soil and organic material (KANE et al., 2001).

The Balch effect is assumed to operate only when large, connecting spaces between blocks are present. The effect is based on the fact that cold air is denser than warm air and tends to displace the warmer air in the voids of blocky material (HARRIS & PEDERSEN, 1998).

The theory of the chimney effect has been developed as an explanation for seasonal behaviour of air circulation in ice caves (e.g. LUETSCHER (2004); see also FIGURE 1.1). WAKONIGG (1996) has adopted the theory to explain the supercooling of ventilated talus slopes, and gives a broad summary of the development of the theory during the 19th and 20th century. The chimney effect is based on a seasonally reversible air

circulation that is driven by the gradient between air temperatures (and correspondingly air densities) of the atmosphere and the interior of talus slopes. The activity of the chimney effect has been proven to be associated to supercooled subsurface conditions in various talus slopes, below (DELALOYE et al., 2003; GUDE et al., 2003; MORARD, 2011; WAKONIGG, 1996; ZACHARDA et al., 2007) and above the timberline (DELALOYE & LAMBIEL, 2005; HILBICH & DELALOYE, 2007; PHILLIPS et al., 2009).

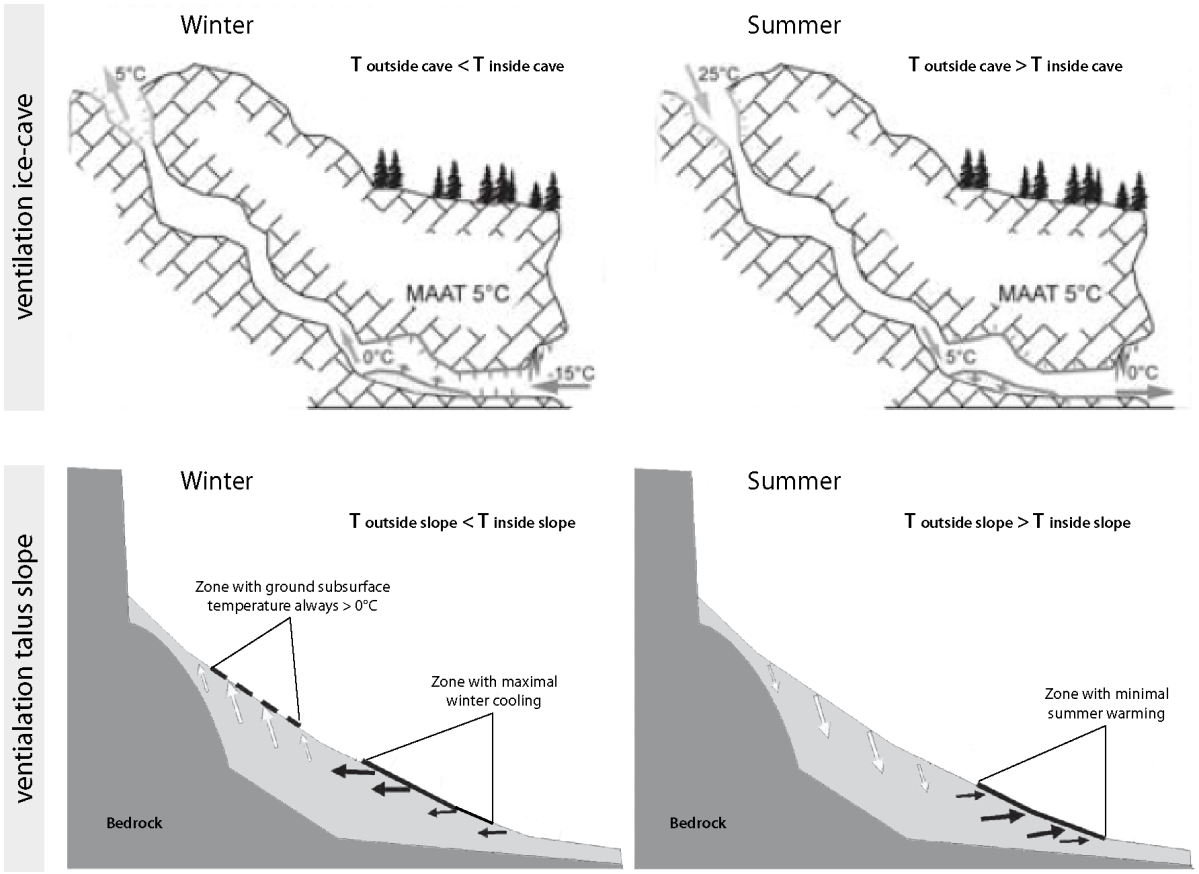

Figure 1.1: Schematic models of the seasonal behaviour of the chimney effect in an ice cave and in ventilated talus slopes (modified after LUETSCHER et al. (2004) (ice cave) and DELALOYE (2004)

In winter, the interior of the scree slope is warmer than the atmosphere, causing less dense air to rise and to flow out through vents and voids in the upper parts of the slope. Necessarily, at the same time, cold air enters through vents in the lower parts of the slope. The air is warmed on its way up through the slope, cooling down the interior of the talus slope by extracting energy in forms of sensible and latent heat (condensation) from the talus material and ground ice. The magnitude of cooling is assumed to be highest in the area of the lower entrances (WAKONIGG, 1996).

In spring, the percolating melt water refreezes on the supercooled talus material, in forms of icicles and coatings around the blocks. Due to the release of latent heat, the processes of ice-volume growth proceeds conform to a warming of the interior of the scree slope (WAKONIGG, 1996).

In summer, when the interior of the talus slope is colder than the atmosphere, the chimney effect works in the opposite direction with colder and denser air flowing out through vents in lower parts of the slope. Consequently, warm air enters through vents and voids in the upper parts of the slope, is cooled on its way down, and warming up the interior of the talus slope, especially due to the loss of latent heat during ice-melt (WAKONIGG, 1996). During the spring- and autumn periods, the chimney effect is characterised by regular reversions of the direction of ventilation (WAKONIGG, 1996).

1.1.2 Geophysics in the study of permafrost

In the last decades, geophysical methods have developed as a standard tool for permafrost related questions. Even though borehole data provide direct information on subsurface temperatures and therefore definite results on the presence or absence of permafrost, as well as on its temporal evolution, they are limited to punctual measurements and are cost-intensive. Here, the application of geophysical methods offer advantages, as measurements are minimal invasive and provide spatial information on the distribution of geophysical parameters in the subsurface.

For general information on geophysical methods, reference is made to REYNOLDS (2011), BURGER et al. (2006), TELFORD et al. (1990) and KNÖDEL et al. (2005). A review of the application of geophysical methods to permafrost related problems is given by SCOTT et al. (1990) and lately by KNEISEL & HAUCK (2008) and HAUCK & KNEISEL (2008a). According to these studies, electrical resistivity methods, refraction seismics, as well as ground penetrating radar (GPR) have developed as the standard methods in periglacial environments. Thereby, the combination of at least two different methods is widely recommended to overcome the limitations of applying one method alone, and to achieve more sophisticated information on geophysical subsurface parameters (IKEDA, 2006, 2008; KNEISEL & HAUCK, 2003; MAURER & HAUCK, 2007; VONDER MÜHLL et al., 2002). Limitations and potentials of geophysical methods are listed and discussed in

Hauck (2001), Vonder Mühll et al. (2001), Kneisel et al. (2008) and Hauck & Kneisel (2008a).

The application of geophysical methods for permafrost related problems in the Alps goes back to the early 1970s, when Barsch (1973) used refraction seismics for the detection of the top of the permafrost body in rock glaciers. Since then refraction seismics as well as electrical methods have been widely applied for the detection of permafrost on different landforms in the Alps, initially mostly as one dimensional vertical electrical and seismic soundings (Etzelmüller et al., 2003; Kneisel, 1998; Vonder Mühll, 1993). With the development of 2D-inversion schemes (Lanz et al., 1998; Loke & Barker, 1996b) in the last decade, geophysical mapping approaches increasingly gained importance (De Pascale et al., 2008; Kneisel et al., 2008; Kneisel & Schwindt, 2008; Rödder & Kneisel, 2011; Vonder Mühll et al., 2002), aiming at investigating the spatial heterogeneity of permafrost sites.

To detect spatial subsurface heterogeneity 3D electrical resistivity techniques have recently been introduced to mountain permafrost research as an advancement of geophysical mapping. First approaches of 3D resistivity imaging have been developed in the 1990s (Dahlin & Loke, 1997; Loke & Barker, 1996a), but have been seldom applied due to high computation intensity. With the reduction of computing duration quasi-3D imaging has been applied in various fields such as environmental (Bentley & Gharibi, 2004; Bichler et al., 2004; Chambers et al., 2007; Dahlin et al., 2002; Friedel et al., 2006) hydrological (Park, 1998) and soil science (Garré et al., 2011), as well as geotechnical engineering (Fischanger et al., 2007), investigation of contaminated and waste disposal sites (Rucker et al., 2009; Soupios et al., 2007) and archaeology (Morelli et al., 2004; Papadopoulos et al., 2007). First approaches to conduct quasi-3D imaging at the demanding terrain of mountain permafrost sites have been conducted by Schwindt (2007) and Schwindt & Kneisel (2009) at a vegetated talus slope and by Rödder & Kneisel (2011) in a glacier forefield.

In the context of climatic warming and an increased hazard potential associated with the degradation of permafrost (Gruber & Haeberli, 2007; Haeberli, 1992; Harris, 2005; Harris et al., 2001; Harris & Vonder Mühll, 2003; Kääb et al., 2005; Kneisel et al., 2007), monitoring of permafrost evolution significantly gained importance. Thereby, electrical resistivity tomography monitoring (ERTM) has developed as state

of the art, in monitoring the long-term, as well as seasonal permafrost evolution (HAUCK et al., 2005; HILBICH et al., 2009a; HILBICH et al., 2008; KNEISEL et al., 2008; KNEISEL et al., accepted; KRAUTBLATTER & VERLEYSDONK, 2008). Recently, the development of automated electrical monitoring systems enabled monitoring variations in electrical subsurface parameters at a high temporal resolution (HILBICH et al., 2011; KNEISEL et al., accepted), allowing for the deduction of short-term processes, for example the active layer evolution during snowmelt (RÖDDER & KNEISEL, 2012). Up to now, permafrost monitoring approaches are mostly based on electrical resistivity tomography alone, without additional information of a complementary method, resulting in a limited informative basis of monitoring results. HILBICH (2010) introduced a first approach of time-lapse refraction seismics to coarse blocky and ice-rich permafrost landforms.

Approaches to a quantitative interpretation of geophysical data measured at mountain sites with permafrost have been introduced recently. HAUCK et al. (2008; 2010) estimate the volumetric contend of rock, water, air and ice by electrical resistivity and seismic velocity of the subsurface. KRAUTBLATTER et al. (2010) achieved the quantitative interpretation of ERT by employing a smoothness-constrained inversion with an empirically measured normal reciprocal error model. HILBICH (2009a) analysed geophysical monitoring systems to assess and quantify ground ice evolution. The depth of investigation method (DOI; OLDENBURG & LI (1999)) has been applied by HILBICH (2009) for appraisal of electrical resistivity tomography measured at mountain permafrost sites with high contact resistances and strong resistivity contrasts in the subsurface. The application of back-and forth interpretation procedure (e.g. DEY & MORRISON, 1979; OLDENBURG et al., 1993) using synthetic data modelling, for appraisal of geophysical data has been applied to permafrost-related problems by FORTIER (2008) (see also HILBICH et al., 2009b; KNEISEL et al., 2008).

1.2 Objectives

Supercooled talus slopes can be expected worldwide at different altitudes; they are not restricted to high-mountain areas, but can also be found in low mountain ranges (vgl. CHAPTER 1.1.1). As a consequence of supercooling events in winter, it must be assumed that ground ice is formed during snowmelt in every ventilated talus slope. Whether ground ice occurrence outlasts the summer, remains a separate issue. Typically, permafrost sites in talus slopes below the timberline are sporadic and restricted to rather small areas at the foot of the slope. These sites are often related to dwarfed forests; yet in some cases the trees show a rather normal growth. Within the last years scientific research revealed basic information on factors controlling permafrost distribution in talus slopes below the timberline, with the chimney effect assumed to be of superior importance (vgl. CHAPTER 1.1.1). However, many issues remain unresolved.

Three supercooled talus slopes in the Swiss Alps were chosen for investigation. Thereby, emphasise was set on differences between the study sites with regard to fundamental parameters (altitude; nature of talus substrate, humus/vegetation composition), to achieve representative and assignable results. Two talus slopes were chosen, where the presence of permafrost/perennial ground ice has already been verified (Val Bever, Upper Engadin and Brüeltobel, Appenzeller Alps). The discovery of a third reference site (Val Susauna) has been a preliminary objective of the thesis; the achievement of this objective is anticipated at this point and will not further be discussed.

The central aim of the thesis is to *determine the temporal variability and spatial heterogeneity of permafrost in three supercooled talus slopes below the timberline and the relation of these factors to the site-specific ground thermal regime.*

To achieve this research goal the focus of investigations is set on the analysis of:

- *the permafrost distribution at the three study sites*
  Only rather small slope areas are assumed to be supercooled, with perennial ice or permafrost in the subsurface. The close proximity of frozen and unfrozen areas is usually attributed to heterogeneities in the ground thermal regime. For an analysis of relationships and an identification of controlling parameters, knowledge on spatial permafrost distribution is of importance. Spatial

distribution and characteristics of permafrost will be analysed by geophysical mapping and quasi-3D resistivity imaging.

- *the temporal variability of permafrost*

  Temporal permafrost variability in ventilated talus slopes is assumed to have a significant seasonal component; due to ventilation, variability is not restricted to annual variations in active layer thickness, as expected at most permafrost sites above the timberline and in the arctic lowlands, but might affect whole permafrost bodies. The analysis of temporal variations in the subsurface will be accomplished by geophysical monitoring.

- *the functional principle of the chimney effect in comparison to the seasonal permafrost evolution,*

  The chimney effect is regarded as the crucial factor for the existence of permafrost in talus slopes below the timberline. However, with regard to the distinctly divergent study site characteristics (especially substrate and climatic conditions) it is of interest if differences in the efficiency of the chimney effect are detectable and to what magnitude this affects the supercooling and warming of the talus slopes.

- *the interaction between organic surface layer and vegetation cover on permafrost distribution,*

  Numerous studies on arctic/lowland permafrost have attributed a substantial importance of the organic surface material and the vegetation cover on the ground thermal regime with variable impacts in the course of the year (vgl. CHAPTER 1.1.1). Studies on permafrost in vegetated talus slopes below the timberline mostly focus on the investigation of the chimney effect. The influence of humus/vegetation cover is often not taken into consideration, or is restricted to its insulation capability in summer. However, it appears reasonable to assume that seasonal variations in the thermal conductivity of the organic layer could decisively alter the ground thermal regime. Spatial differences in humus- and vegetation distribution might contribute to the sporadic appearance of permafrost in isolated slope areas, as well as the permafrost variability over time.

- *and the influence of the snow cover on the ground thermal regime.*

The snow cover is assumed to have fundamental influence on the ground thermal regime of permafrost sites above the timberline and arctic lowland permafrost; its influence at supercooled talus slopes is regarded to be of minor importance. However, the assignability of these assumptions will be analysed with regard to differences between the study sites as well as on the assumed small-scale heterogeneity of the thermal regime.

The attainment of objectives is fundamentally based on the application of geophysical methods. An additional aim of the thesis involves contributions to the application of geophysical methods to permafrost related problems. These include:

- *the development of a low-cost electrical resistivity monitoring array, which allows for robust year-round measurements,*
- *attempts to conduct seismic refraction tomography monitoring, to introduce advantages of the joint application of complementary methods to geophysical permafrost monitoring,*
- *an optimisation of the efficiency of quasi-3D resistivity imaging for the usually difficult terrain of mountain permafrost sites.*

1.3 Structure of this study

The thesis is subdivided into three central parts

Part I: After the general introduction and an overview on the scientific background, the objectives of this thesis are outlined in Chapter 1. Basic information on the methods applied in this study is given in Chapter 2. Thereby the focus is set on a general introduction and an explanation of the methods. Details on the specific application will be given in the context of the specific approaches. In Chapter 3 an overview on the study sites will be given, followed by an outline of the conducted field studies as well as the dates and periods of measurements.

Part II represents the central part of the thesis. The four chapters represent the central approaches addressing the objectives of the thesis. The chapters are each subdivided into a short introduction into the aims of the particular objective, an outline of the specific methodological approach, as well as the presentation and discussion of results and conclusions to be drawn. Chapter 5 deals with the optimisation of quasi-3D resistivity imaging, based on an extensive forward modelling approach, and a methodological analysis of results from quasi-3D imaging at the Val Susauna, as case study. A delineation of frozen ground distribution and characteristics is aim of Chapter 6. Emphasis is on quasi-3D resistivity imaging as well as on the joint application of electrical and seismic methods. Complementary geophysical methods were measured repeatedly in early- and late summer, to take into account the assumed high temporal frozen ground variability. Chapter 7 deals with monitoring the temporal frozen ground variability. Thereby, the investigations are mainly based on electrical resistivity tomography measured at an approximately monthly interval. For the analysis of geophysical results, synthetic data modelling has been conducted. Furthermore, temperature data are taken into account to achieve a more sophisticated interpretability of results. In addition, a first approach of seismic refraction tomography monitoring during winter is presented. Objective of chapter 8 is the analysis of the ground thermal regime, and a comparison between the three study sites. Results include an analysis of temperature logger data as well as repeated measurements of the bottom temperature of the snow cover in winter and a mapping of the humus/vegetation characteristics at the Val Susauna.

Part III: CHAPTER 9 will give a synthesis of the main findings of the thesis aiming at presenting a conceptualized model of the ground thermal regime and its influence on the permafrost distribution. An outlook on research issues that remain unanswered or emerged in the course of investigations will be given in CHAPTER 10.

During the course of investigations for this PhD project, it was possible to publish interim results in peer-reviewed journals in conference proceedings, or were presented at conferences in talks and posters. This especially concerns the approach of optimizing quasi-3D imaging for permafrost studies, as well as selected results from electrical resistivity tomography monitoring:

KNEISEL, C., RÖDDER, T., & SCHWINDT, D. (submitted) Frozen ground dynamics resolved by multi-year and year-around electrical resistivity monitoring at three alpine sites in the Swiss Alps. Near Surface Geophysics.

SCHWINDT, D. & KNEISEL, C. (2011) Optimisation of quasi-3D electrical resistivity imaging – application and inversion for investigating heterogeneous mountain permafrost. The Cryosphere Discussions, 5: 3383-3421.

KNEISEL, C., RÖDDER, T., ROTH, N. & SCHWINDT, D. (2011) Electrical resistivity monitoring for the detection of changes in mountain permafrost at different time scales. In: *Geoelectric Monitoring – Current Research and Perspectives for the Future*. International Workshop on Geoelectric Monitoring. Berichte der Geologischen Bundesanstalt, Nr. 93

SCHWINDT, D. & KNEISEL, C. (2010) Temporal permafrost variability at three subalpine talus slopes in the Swiss Alps, by geoelectrical monitoring and supplemental methods. Proceedings of the 3rd European Conference on Permafrost (EUCOP III), Svalbard, Norway. (extended abstract)

KNEISEL, C. BAST, A., RÖDDER, T., ROTH, N. & SCHWINDT, D. (2010) Ground Temperature Regime at three Permafrost Sites in the Swiss Alps – Analysis of perennial minilogger and borehole data. Proceedings of the 3rd European Conference on Permafrost (EUCOP III), Svalbard, Norway. (extended abstract)

2 Basic methods

Methods applied in this study aim at itemizing the cluster of factors facilitating the existence, as well as the inter- and intra-annual variability of permafrost or frozen ground in talus slopes below the timberline. Kneisel (1999) classified methods for permafrost prospection into direct, half-direct and indirect methods. As permafrost remains invisible in most cases, a direct investigation at natural or artificial outcrops states an exceptional case. The application of half-direct methods – first of all geophysics – allows a minimal-invasive detection and investigation of ground ice and permafrost, including areal (e.g. 3D or geophysical mapping) as well as temporal (geophysical monitoring) approaches. Indirect methods benefit from indicators that allow evaluating the probability of permafrost. Included are permafrost-related landforms (e.g. rock glaciers), the evaluation of temperature data at key positions (e.g. BTS, source temperatures) as well as GIS-based modelling of the potential permafrost distribution (e.g. Boeckli et al., 2012).

In this study a multi-method approach was performed for the characterisation of talus slopes with permafrost, combining geophysical methods (electrical resistivity tomography – ERT, seismic refraction tomography – SRT) with various approaches for the investigation of the ground thermal regime. These include BTS measurements, temperature logging at various slope positions, mapping of humus temperatures and humus moisture as well as GIS-based calculations of the solar radiation.

2.1 Geophysical methods

The application of geophysical methods enables the investigation of the two- and three-dimensional distribution of physical parameters in the shallow subsurface. Regarding permafrost related problems the application of geophysical methods is linked to changes of physical properties of earth-materials in the subsurface, which occur during the phase change from unfrozen to frozen state at temperatures slightly below 0 °C (Scott et al., 1990). Especially the joint application of different methods (Burger et al., 2006; Vonder Mühll et al., 2002) enables a more sophisticated interpretation of subsurface and permafrost characteristics, as the sensitivity of geophysical methods differs in regard to specific parameters, i.e. air and ice in the pore space (cf. Figure 2.1).

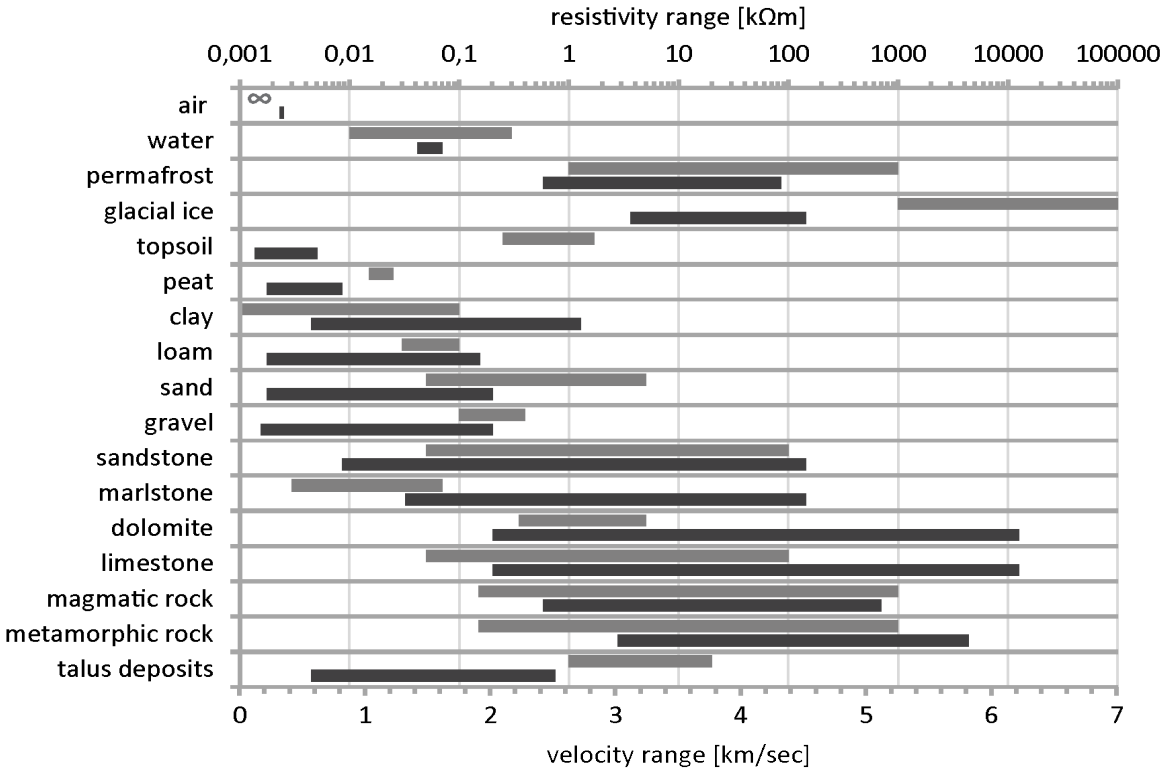

Figure 2.1: Electrical resistivities and seismic (p-wave) velocities of different earth materials (compiled after: Burger et al., 2006; Hauck & Kneisel, 2008a; Knödel et al., 2005; Reynolds, 2011; Telford et al., 1990)

To characterise permafrost in talus slopes below the timberline, the focus of this study was set on the investigation of electrical and seismic properties of the subsurface by applying electrical resistivity tomography and seismic refraction tomography in joint application. Measurements were conducted in 2D (single ERT and SRT measurements

for mapping and detecting frozen and unfrozen ground), in 3D (imaging of permafrost bodies by merging numerous 2D ERT arrays into one quasi-3D dataset) and in 4D (2D ERT and SRT monitoring with varying temporal resolution)

2.1.1 Electrical resistivity tomography (ERT)

The application of ERT is commonly based on a collinear four-electrode setup, galvanically coupled to the ground. A direct current is injected into the ground by two electrodes (C_1/C_2); two other electrodes (P1/P2) measure the resulting potential difference. By combining a number of 4-electrode setups along a transect or a three-dimensional grid, 1D, 2D and 3D subsurface resistivity images can be obtained. The resolution and penetration depth of each setup is driven by electrode spacing, number of electrodes and choice of measurement geometry, with Wenner, Wenner-Schlumberger and dipole-dipole being the most commonly used array types in permafrost studies (Kneisel et al., 2008).

The apparent subsurface resistivity (ρ_a) can be calculated according to Ohm's law from the injected current (I), the measured potential difference (ΔV) and the geometric factor K (describing the geometry of the applied electrode configuration) with:

$$\rho_a = K \frac{\Delta V}{I} \qquad \textit{Equation 2.1}$$

Hereby, the apparent resistivity (ρ_a) can not be regarded as a physical property of the subsurface but confers to the resistivity distribution of a homogeneous medium which is most unlikely for natural conditions (cf. Reynolds, 2011). The true specific resistivity (ρ_s) of subsurface materials (cf. Figure 2.1) is derived from the inversion of measured apparent resistivity data using commercial software (cf. Chapter 2.1.1.4).

The conductivity of most rock forming minerals is rather low (cf. Figure 2.1) with a negligible influence on the resistivity distribution in the subsurface (Knödel et al., 2005; Reynolds, 2011). Mainly the electrical conductivity in the subsurface is electrolytic, driven by ionic transport in conductive fluids distributed in the pore space or as a coating around grains and rocks. As a result, the electrical subsurface resistivity is highly sensitive to cooling and freezing as it affects the mobility of ions in the pore

water. Above the freezing point, sinking temperatures result in increasing resistivity values, as the mobility of ions in the increasingly viscose pore water is reduced. Below the freezing point the subsurface resistivity does not directly depend on temperature or ice content, but is driven by the content of water that remains unfrozen at subfreezing temperatures (Hauck, 2002). However, resistivity values markedly increase below 0 °C, with the degree and moment of change depending on moisture content, pore size, pore water chemistry, ground temperature and pressure of material (Scott et al., 1990).

2.1.1.1 Quasi-3D electrical resistivity tomography

Owing to the sensitivity of electrical resistivity measurements to frozen ground, quasi-3D ERT enables a detailed imaging of the subsurface heterogeneity – typical for alpine permafrost sites – and a differentiation between frozen and unfrozen areas. In contrast to common collinear ERT surveys measured along a straight line, two approaches are available to achieve a three dimensional image of the subsurface resistivity distribution. Hereby "real-3D" datasets can be achieved by building up an areal grid of electrodes and conducting measurements along the x- and y-direction, as well as diagonally. As this approach is uneconomic for most permafrost related problems (limited grid size, requirement of a high number of electrodes, logistical reasons), the quasi-3D ERT approach is preferable in many cases. To create a quasi-3D image of the subsurface a number of parallel or orthogonal measured 2D ERT surveys are collated into one dataset, which is then inverted, using a three dimensional inversion algorithm (cf. Chapter 2.1.1.4).

Assuming isotrope conditions, a resistivity measurement using a collinear 4-electrode setup is capable of providing – to a certain degree – 3D information of the subsurface, due to the fact that current flows away radially (Reynolds, 2011) and therefore penetrates areas in a circuit of the array. Hereby the sensitivity to both sides of a collinear 4-electrode Wenner array corresponds to the applied electrode spacing, meaning that the spacing between parallel ERT arrays should not be much larger than the smallest electrode spacing to achieve a complete 3D coverage (Loke, 2010).

Results and discussion of the approach to optimise the applicability, efficiency and interpretability of quasi-3D ERT to investigate the heterogeneous permafrost

distribution at mountain sites using a systematic forward modelling approach, are presented in CHAPTER 5.

2.1.1.2 Electrical resistivity tomography monitoring (ERTM)

Electrical resistivity monitoring at sites with permafrost aims to detect variations of frozen and unfrozen water content in the subsurface, as a result of seasonal, annual and long-term temperature variations. The precondition for monitoring time-dependent processes is a reliable reproducibility of measurements (KNEISEL et al., 2008).

Firstly, measurements are to remain constant throughout the monitoring period. This is achieved by using a fixed, buried setup (cable and electrodes) to obtain constant measurement conditions regarding electrode positions and spacing throughout the year. However, electrode coupling – e.g. loosening of electrodes due to freezing processes – as well as technical failures, e.g. damages of the cable due to snow pressure or rodents, must be considered as a potential source of errors. Details on the construction of the fixed monitoring arrays and the site-specific setups are given in CHAPTERS 7.1 & 7.2.2.

As mentioned above, the subsurface conductivity is determined by pore size, pressure, pore water chemistry, moisture content and ground temperature (SCOTT et al., 1990). Thus, secondly it is assumed, that temperature driven processes (i.e. frozen and unfrozen water content) are variable throughout the measurement period, while general subsurface conditions (pore size and volume, substrate/lithology) remain constant. Consequently, measured are only temporal variations of frozen and unfrozen water content, as well as effects of increasing or decreasing temperatures in the subsurface. In addition, the resistivity, especially near the surface is affected by short-term dry spells and precipitation events, as the availability of conductive fluids is reduced, or increased, respectively. This effect is strongest for surface substrates with low water storage capability like coarse, uncovered debris, but is minor for fine grained and/or vegetated surface material with a consistent organic layer.

2.1.1.3 Data acquisition

ERT data presented in this study are in general of two kinds. The approach of ERT-monitoring requires a fixed setup that is repeatedly measured. To achieve an areal characterisation of the study sites individual ERT arrays are measured in joint

application with SRT (cf. CHAPTER 6) or as an orthogonal grid for quasi-3D imaging (CHAPTERS 5 & 6.2.2). Except for this, the general data acquisition strategy is comparable for all measurements. Measurements were conducted using a 72-channel multi-electrode resistivity meter form IRIS instruments (Syscal Junior Switch).

In order to map permafrost occurrences using 2D and 3D ERT compromises have to be made regarding the choice of electrode spacing and array type. Besides information on permafrost characteristics, factors of interest are the areal distribution, active layer thickness and location of the permafrost base. While small spacings (< 2 m) have advantages in illustrating the active layer, spacings of ≥ 2 m are favourable for the detection of permafrost thickness and for mapping larger areas. Electrode spacings applied in this study are 1.8, 2 and 3 m (cf. CHAPTERS 6 & 7).

The number of electrodes used per array was determined to 36, based on the available cables and resistivity meter. For practical reasons and for comparability, 36 electrodes were also used for the self-constructed monitoring arrays. Electrode spacing was chosen based on site-specific conditions and problems. Test measurements were conducted at each site to select the optimal electrode spacing with regard to penetration depth, spatial- as well as near-surface resolution for each site. Information on set-ups is given in CHAPTERS 6 & 7.

The choice of array type at mountain permafrost sites is often a trade-off between resolution and robustness, as achieving an optimal electrode coupling can be challenging and the maximum current injected into the ground can be low (KNEISEL et al., 2008). Regarding error proneness the robust Wenner and Wenner-Schlumberger arrays provide more stable resistivity data (e.g. KRAUTBLATTER & VERLEYSDONK, 2008) and yield higher signal to noise ratios (e.g. HAUCK & VONDER MÜHLL, 2003b) compared to the dipole-dipole array. However, while Wenner and Wenner-Schlumberger arrays have advantages in delineating horizontal structures (permafrost base and table) the dipole-dipole array is more sensitive to horizontal changes in resistivity and therefore a good tool for mapping vertical structures (e.g. FORTIER et al., 2008; LOKE, 2010).

The Wenner array was used for all measurements. As a reasonable electrode coupling was achievable in most cases, the dipole-dipole array was measured in addition for repeated measurements (CHAPTER 6), for quasi-3D ERT (CHAPTERS 5 & 6) and for ERT-monitoring approaches (CHAPTER 7). The combination of these two array types

states an optimal complement of robustness, vertical resolution and depth penetration of the Wenner array to the superior spatial resolution of the dipole-dipole array. However, especially for monitoring measurements in winter with high contact resistances, the dipole-dipole array did not provide utilizable data for all measurements.

The relief of each survey line has been recorded as the estimated relative vertical distance between two neighbouring electrodes to enable an incorporation of relief data into the data inversion process (cf. CHAPTER 2.1.1.4).

2.1.1.4 Data processing and inversion

As shown above, measured apparent resistivity values do not coincide with the true specific resistivity distribution in the subsurface. To derive specific resistivities from measured data, an inversion process is applied that iteratively tries to minimise the misfit between resistivity data, calculated by forward modelling, and the measured data, until a predefined convergence criterion is obtained. Usually a homogenous half-space, calculated as the average of apparent resistivities, is used as a starting model. In this context, the choice of the correct iteration is of great importance for the interpretation of ERT-datasets, as a large number of iterations will tend to overfit data, such that artefacts will result from inversions of data errors. "A small RMS-error does not necessarily correspond to realistic model results" (HAUCK & VONDER MÜHLL, 2003b).

For all measured resistivity datasets the following steps were performed:

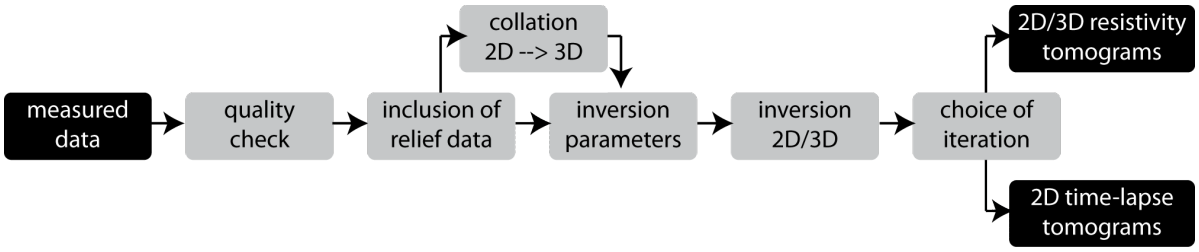

Figure 2.2: Flow chart data processing and inversion for ERT data

Quality-check of measured data was conducted within PROSYS II (IRIS Instruments). In this context data with implausible values (e.g. negative or zero) or data with a standard deviation > 3 after stacking were eliminated. In case of ERTM, single electrodes were occasionally damaged during the monitoring period and could not be fixed prior to the measurement. In these cases, all datum points that were measured

with the damaged electrode being involved were eliminated. The amount of deleted datum points was dependent on the used array types and time of measurement, with higher numbers of deleted points for the dipole-dipole array and for measurements during winter (cf. TABLE 4.1).

Relief data were recorded for all measurements, and included into the datasets before inversion, to prevent topographical effects in inversion results. A rugged topography influences the current flow, which is concentrated or focused in valleys or dispersed or diverged beneath a hill, with the result of distorted equipotential surfaces, which may mask or distort a real anomaly (TELFORD et al., 1990).

For quasi-3D imaging, the orthogonal measured 2D datasets were prepared as described above. 2D datasets were collated into one "quasi-3D" file using RES2DINV (GEOTOMO), to conduct a true three-dimensional inversion (RES3DINV, GEOTOMO) of two-dimensional data that allows resistivities to vary in all three dimensions. As relief data are only included along the 2D surveys RES2DINV interpolates the elevation data for quadrupoles located in-between survey lines. In case of rough topography, the interpolated elevation data often deviate from actual relief conditions and have to be checked and corrected manually before tomographic inversion.

The software packages RES2DINV and RES3DINV (both GEOTOMO) were used to perform a smoothness constrained tomographic inversion of 2D (LOKE & BARKER, 1995) and 3D datasets (LOKE, 2010). General setting for all inversions include the use of the robust inversion scheme (L_1-norm) to preclude smoothing of sharp resistivity boundaries (LOKE et al., 2003) that are assumed to occur especially at the boundary between active layer and permafrost body. An extended model with additional model blocks at the sides and beneath the original data array is used, to reduce side block effects and the susceptibility to artifacts at the edges (tomogram-sections that are not covered with datum points are shaded in the tomograms to prevent overinterpretation). Details on inversion parameters used for quasi-3D imaging are given in CHAPTER 5.

To achieve a more detailed analysis of time-dependent processes, time-lapse tomograms were created to illustrate alterations of subsurface resistivity characteristics between different measurements. The software package GEOPLOT was used to calculate the percental difference between the selected iterations of two measurements. As the inter-annual variations in subsurface resistivities in the investigated talus slopes

turned out to be markedly high (cf. CHAPTER 7.3.2), it has been refrained from using a single reference model for all following datasets. Instead, time-lapse tomograms were calculated for consecutive measurements.

2.1.1.5 Forward and inverse modelling

The forward and inverse problems in geophysics have been discussed by various authors (e.g. FORTIER et al., 2008; FRIEDEL, 2003; HILBICH et al., 2009b; OLDENBURG & LI, 1999; SCALES & SNIEDER, 2000), with the inverse problem trying to deduce specific earth properties from measurements and the forward problem trying to predict geophysical data from a model of the subsurface. While solutions of the inverse problem are non-unique, those of the forward problem are unique (with the existence of only one solution that is capable of representing the data). Consequently, forward modelling of synthetic data enables the evaluation of the aspired resolution of features of interest, the depth of investigation and the occurrence of inversion artefacts by investigating the response of the inversion process to a given structure (HILBICH et al., 2009b). The concept of a back-and-forth interpretation procedure is discussed amongst others by Fortier et al. (2008) for optimising the field procedure and for enhancing the interpretability of the inversion results of measured resistivity data. Forward modelling of synthetic resistivity data – representing a geocryological model based on prior information from field investigations and knowledge of site characteristics and landforms – can be used for choosing the ERT design (array type, array length, electrode spacing) and as a reference to the inversion results of observed resistivity data.

A forward and inverse modelling approach has been applied in this study to optimize quasi-3D imaging for permafrost related problems and to test the capability of various quasi-3D grid setups (cf. CHAPTER 5) as well as for the verification of ERT-monitoring data (cf. CHAPTERS 7.2.4 & 7.3.3). Details on the specific approach of synthetic data modelling are given in CHAPTERS 5.1 & 7.2.4.

2.1.2 Seismic refraction tomography (SRT)

Basis of all seismic methods is the detection of seismic subsurface properties by generating a seismic signal at a known time (e.g. sledgehammer or explosives) and

recording the traveltime of seismic waves towards the receiver (geophones). The resulting propagation velocity provides the potential to draw conclusion on specific subsurface materials. The propagation velocity of seismic waves depends on the elastic modulus and the density (ρ) of the specific subsurface material (SCHROTT & HOFFMANN, 2008) and is higher for P-waves (primary- or compressional waves) compared to the S-waves (secondary- or transverse waves):

$$V_P = \sqrt{(j/\rho)} \quad \text{and} \quad V_S = \sqrt{(\mu/\rho)} \qquad \textit{Equation 2.2}$$

with V_P and V_S as P- and S-wave velocities, respectively. The appropriate elastic moduli are given with j (elongational modulus) in case of P-waves and μ (shear modulus) in case of S-waves (REYNOLDS, 2011; SCHROTT & HOFFMANN, 2008).

In this context the application of SRT aims at detecting the material-specific propagation velocity (Figure 2.3) of compressional waves (P-waves) as well as the depth of interfaces between layers of different acoustic impedance (KNÖDEL et al., 2005). The calculation of traveltimes between seismic source and receiver is based on manually defining the first arrivals of P-waves at the receiver.

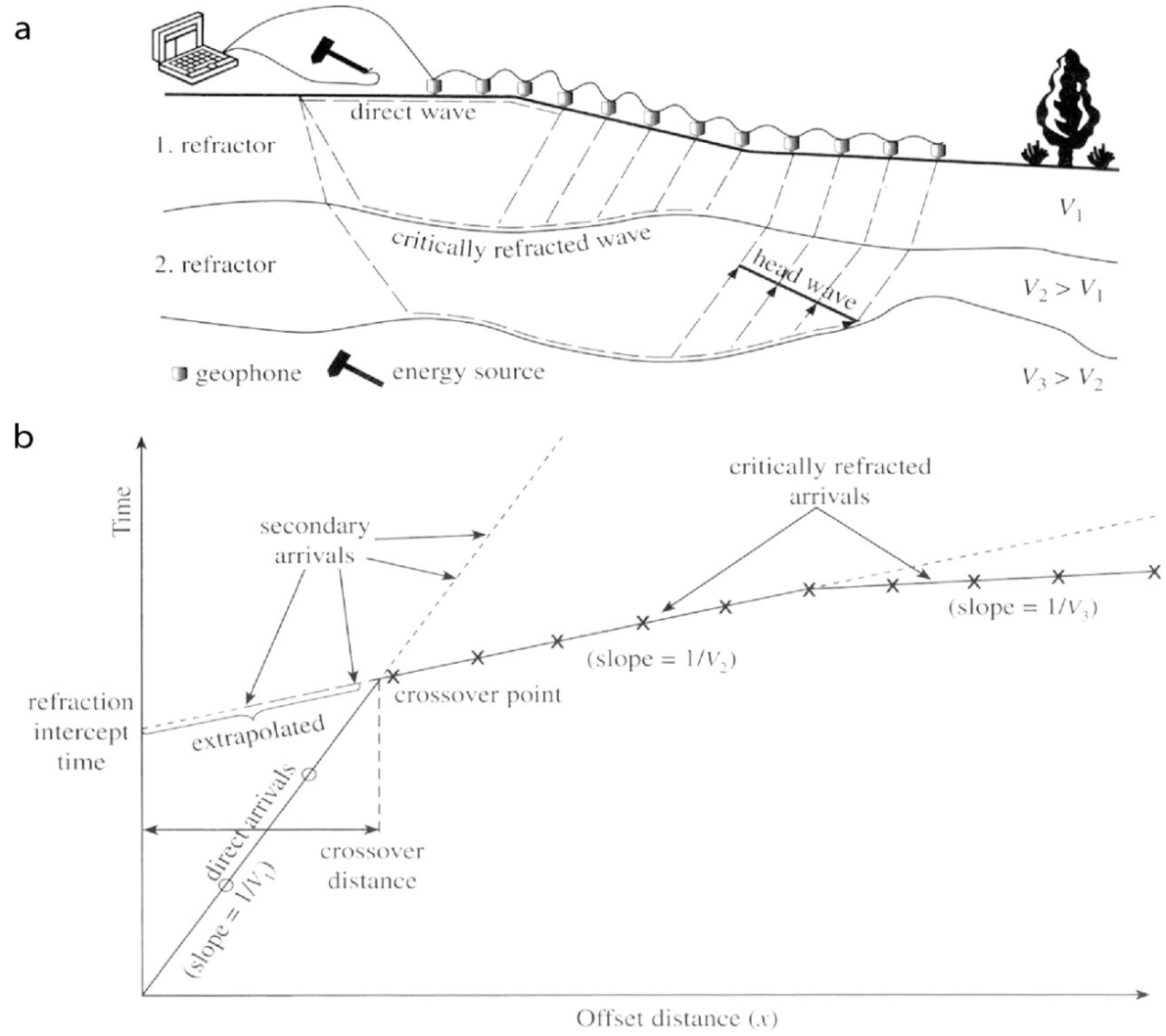

Figure 2.3: Setup and principle of refraction seismics. a) Design of a seismic survey and simplified raypath geometry in a subsurface with three layers. b) Time-distance plot of traveltimes of first arrivals, relating direct and critically refracted rays. (modified after Schrott & Hoffmann, *2008)*

The fundamentals of seismic refraction measurements are illustrated in Figure 2.3. Seismic waves induced by an external force on the halfspace propagate radially through the layered subsurface but also directly along the ground surface (direct wave). Depending on the angle of incidence, interfaces between layers of different acoustic impedance cause reflections and refraction of P-waves. Provided that the speed of propagation of the overlying material is smaller than that of the lower layer ($V_2 > V_1$), and that the angle of incidence reaches a particular value according to Snell's Law (critical angle), the wave gets refracted and travels along the upper boundary of the lower medium (Burger et al., 2006; Schrott & Hoffmann, 2008). The refracted wave, travelling with the velocity of the lower layer, generates waves (head waves) moving upward towards the surface. Direct and refracted waves are detected by geophones at

the surface and recorded by a seismograph, with the crossover distance (cf. FIGURE 2.3) being the offset where the refracted wave precedes the direct wave (SCHROTT & HOFFMANN, 2008). The offset of the crossover distance – as a result of the critical angle – is dependent on the thickness of the overlying layer as well as on the velocity gradient between V_1 and V_2 as illustrated in FIGURE 2.3.

The application of SRT to permafrost related problems is based on the strong contrast of physical properties between frozen and unfrozen material, up to an order of magnitude. As for different earth materials, seismic properties of frozen ground vary on a large range (FIGURE 6.1), reflecting the variable composition with mutable amounts of rock/debris, ice, unfrozen water and air. Thereby the seismic velocity of a mixture is driven by the acoustic properties and the amounts of its constituents. Timur (1968) used a three-phase time-average equation to estimate the compressional wave velocity for ice-liquid-rock matrix systems and showed, that the P-wave velocity in water-saturated rocks increases with decreasing temperatures, with the shape of velocity versus temperature curves being a function of lithology, pore structure and the nature of interstitial fluids. This is a result of an increase in density during the partial freezing of water with decreasing temperatures. Furthermore, as the density of rock exceeds the density of ice, the velocity of compressional waves is a decreasing function of the porosity and the degree of melting (ZIMMERMAN & KING, 1986). Lately, HAUCK et al. (2010) extended the equation of TIMUR (1968) that was based on the volumetric content (f) of the solid phases rock/soil (r) and ice (i) as well as the liquid phase (water, w) by adding a gaseous phase (air, a):

$$\frac{1}{\upsilon} = \frac{f_w}{\upsilon_w} + \frac{f_r}{\upsilon_r} + \frac{f_i}{\upsilon_i} + \frac{f_a}{\upsilon_a} \qquad \textit{Equation 2.3}$$

The equation by HAUCK et al. (2010) states that the reciprocal of the P-wave velocity (slowness) of a mixture equals the sum of the slownesses of the respective components, each weighted by its volumetric fraction. In contrast to the resistivity that increases continuously during cooling, the seismic velocity remains constant below the cryohydric temperature (TIMUR, 1968). At this point the mixture consists solely of rock/soil matrix, ice and air, with seismic waves propagating through solid material, while electrical conduction takes place in the – constantly decreasing – unfrozen portion of the pore water (KNEISEL et al., 2008).

The application of refraction seismics is especially well suited to differentiate between frozen and unfrozen areas and to detect active layer thickness. In contrast, the method is not capable of correctly detecting the permafrost base, as a major assumption in the application of SRT is the increase of seismic velocity with depth. This effect is due to the velocity inversion below frozen ground bodies, where the underlying layer with reduced acoustic impedance does not act as a refractor. A further limitation of SRT is the existence of blind layers and hidden layers (hidden zones) that are undetectable for SRT (Burger et al., 2006; Reynolds, 2011; Schrott & Hoffmann, 2008). In case of a blind layer – a velocity inversion of a layer (V_2) between two layers of higher acoustic impedance ($V_1 > V_2,\ V_1 < V_2,\ V_2 < V_3$) – the depth of the underlying layer will be overestimated. Hidden layers cause a refraction of seismic waves but head waves are not detected due to (i) a low contrast in acoustic impedance between layers, and/or (ii) the thickness of the layer is too small. Furthermore, a layer may remain undetected, if the geophone spacing is insufficient, meaning that the geophone spacing must be larger than the difference between two following crossover distances (Reynolds, 2011; Schrott & Hoffmann, 2008).

2.1.2.1 Seismic refraction tomography monitoring (SRTM)

As shown for ERT measurements, SRT is sensitive to variations of the unfrozen water content, as the P-wave velocity differs strongly between ice and water and therefore is capable of detecting temporal variations in frozen ground characteristics. In contrast to the large and still growing number of ERTM approaches, the use of seismic refraction for monitoring permafrost evolution is sparse. This is mainly attributable to the data acquisition and processing that is by far more work-intensive and time-consuming than it is for ERT measurements. Furthermore, the accessibility during winter with thick snow cover is much easier to achieve with an installed ERT array compared to SRT setups, as not only the cable connector has to be accessible, but also the shot points. Additionally the refraction seismic equipment with cables and geophones is costly and a low budget, self-made setup is not producible. The only approach applying time-lapse SRT for permafrost related problems has been presented by Hilbich (2010), who used fixed screws for attaching the geophones to ensure repeatable measurements with identical geophone locations.

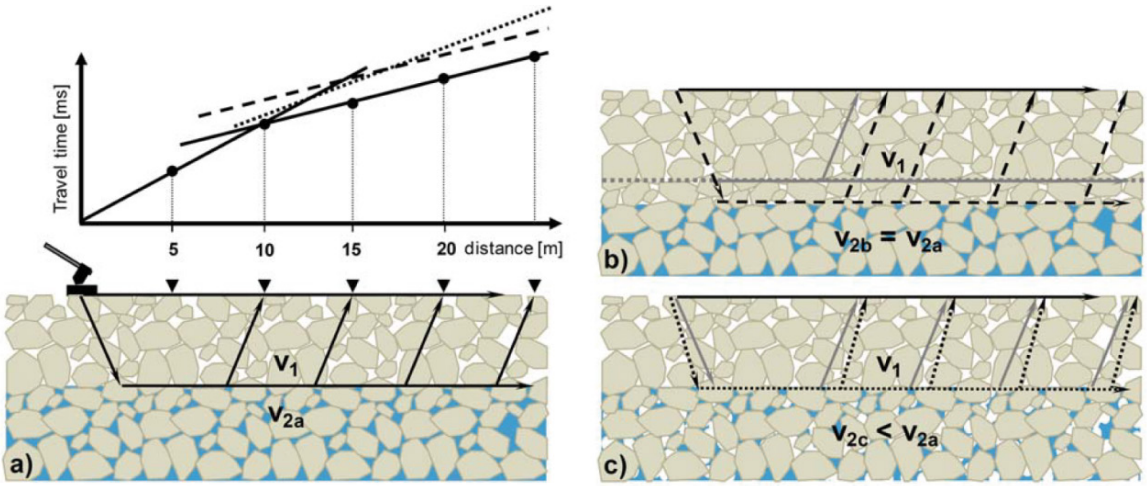

Figure 2.4: Idealised principle of time-lapse refraction seismics for permafrost-related problems. a) two-layer subsurface model with a coarse-blocky unfrozen overburden with air-filled voids and a saturated rock-ice-matrix underneath. The lower panels illustrate the change of travel times as a consequence of b) a vertical shift of the refractor (e.g. the seasonally varying interface between frozen and unfrozen conditions), and c) altered ice (and air) contents within the lower layer causing changes in seismic velocity. The corresponding travel time curves for all three scenarios are given to the upper left. (modified after Hilbich, 2010)

In contrast to the study by Hilbich (2010), who conducted measurements during the snow-free period, the application of SRTM in this study aimed at monitoring the permafrost evolution during winter, to enhance the interpretability of ERTM measurements. Besides this study, up to now, no approach is known, where time-lapse refraction seismic is used to monitor the permafrost evolution. Furthermore, to date, this represents the only study, where time-lapse SRTM is used to investigate the permafrost evolution below snow cover during winter.

Fundamentals for monitoring time-dependent processes as discussed for ERTM (Chapter 2.1.1.2) are conferrable to SRTM measurements. Comprised are (i) the reproducibility of measurements, (ii) a consistency of general subsurface conditions (pore size and volume, substrate/lithology) and (iii) the assumption, that only temperature driven processes are variable throughout the measurement period. To achieve reproducible measurements, cable and geophones were placed in early winter, before an unmitigated freezing of the humus cover. The consistent snow cover provided sufficient protection of cable and geophones against damage and rodents.

2.1.2.2 Data acquisition

The application of SRT in this study aims at complementing ERT results, to achieve an enhanced interpretability of subsurface characteristics, heterogeneity and temporal variability. 2D SRT measurements were conducted in joint application with ERT. As stated above, a SRT-monitoring approach has been conducted, to achieve a more detailed understanding of the complex processes that occur in the ventilated talus slopes during winter. The general data acquisition strategy is comparable for all measurements. Measurements were conducted using a 24-channel seismograph (Geode) from Geometrics, with variable, site- and problem specific geophone spacing.

For a given subsurface the resolution and penetration depth of a seismic survey is determined by the geophone spacing, offset distance and number of shot points, with penetration depth being about 1/3 – 1/5 of the offset distance (Schrott & Hoffmann, 2008). The number of shot points should be chosen according to the complexity of subsurface conditions. In case of a layered subsurface with planar layers a low number of shots can be sufficient, while dipping layers or strong inhomogeneities require for additional shot points with forward and reverse shots (Schrott & Hoffmann, 2008).

Dimensions of the seismic spreads used in this study were restricted to 24 geophones – based on the available cables and seismograph – with the geophone spacing adjusted to cover a comparable length as the corresponding ERT array. The number of shots locations was chosen specific to site conditions. Shots locations were usually situated between every second/every third geophone. As far as possible, remote sources – off- and end shots in front and behind the spread – were used. For measurements during the snow-free period, a sledgehammer (5 kg) was used for generating the seismic signal, hitting a steel strike plate with 10 stacks per shot point. For assurance of data quality, the trigger sensitivity was adjusted, so that only accurate shots were triggered. The snow cover during winter required for an adjustment of the data acquisition strategy for the monitoring approach. Cable and geophones were placed at the study site in early winter, before an unmitigated freezing of the humus cover. As removing the snow cover at the source points would alter the thermal conditions during the measurement period distinctly, a steel tube (1 m length, Ø 10 cm) stuck thorough the snow cover was used for striking. Shot locations were marked with wooden rods to ensure identical shot

positions throughout the monitoring period. Details on the specific setups are given in the CHAPTERS 6.1 & 7.2.3 (cf. TABLE 6.1, TABLE 6.4, TABLE 6.5 & TABLE 7.3).

As for ERT measurements, the relief of each survey line has been recorded as the estimated relative vertical distance between two neighbouring geophones to incorporation relief data into the inversion process (cf. CHAPTER 2.1.2.3).

2.1.2.3 Data processing and inversion

According to ERT measurements, the application of refraction seismics in this study aims at obtaining 2D tomograms of seismic properties in the shallow subsurface. However, processing of data is more demanding for seismic than for electrical data. For data processing and inversion the software package SeisImager/2D (GEOMETRICS) – subdivided into the modules PICKWIN and PLOTREFA – was used. FIGURE 2.5 shows the workflow for data processing and inversion of refraction seismic datasets.

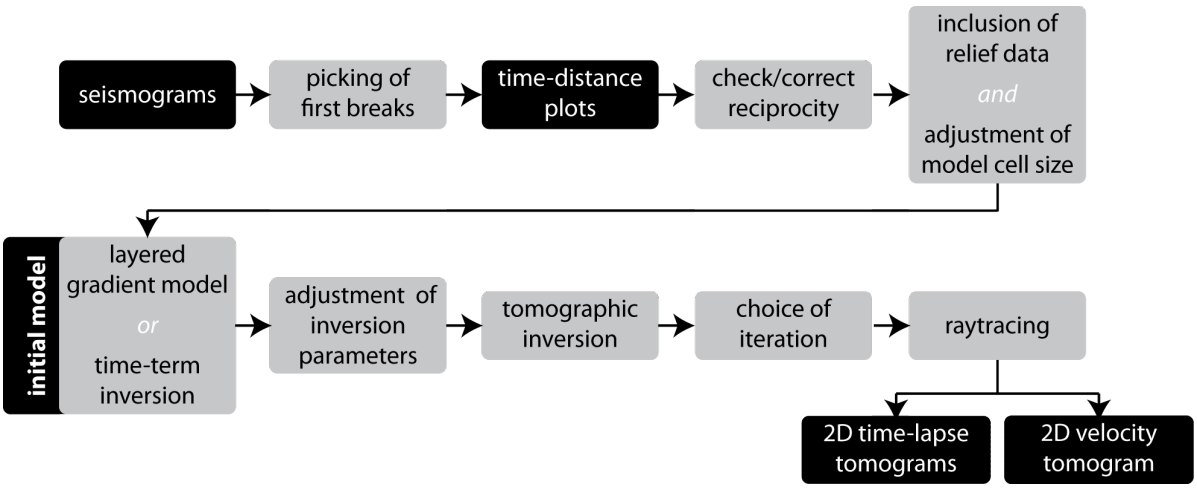

Figure 2.5: Flow chart data processing and inversion of SRT data, using SeisImager/2D

The module PICKWIN was used for picking first arrivals for all shots of each spread and for creating time-distance plots by combining the first arrivals of all shot points. This step also includes a quality check, as only clear first arrivals were picked. As the signal strength decreases with increasing offset distance (distance from shot point to geophone) first arrivals at the geophones furthest from the shot point were in some cases not clearly definable and therefore excluded.

Data processing in PLOTREFA included a check/correction of reciprocity, inclusion of relief data, the analysis of time-distance plots, definition of a starting model and the

tomographic inversion. PLOTREFA offers two ways for defining the starting model. The classic method is the development of a layered gradient model, where velocities increase with depth. Required are number and thickness of layers, as well as minimum and maximum velocity, while it is recommended that maximum velocities are preferably over- than underestimated to ensure sufficient initial ray coverage (HAUCK, 2001; LANZ et al., 1998). The second method offered is the time-term inversion. The time-term technique is a linear least squares approach, based on manually assigning layers as indicated by a change in slope of the time-distance plots (GEOMETRICS, 2009).

To consider topographical effects, relief data for each spread were recorded and included into the datasets prior to inversion. To define the horizontal model cell size in PLOTREFA – which was stated as not possible by SHEEHAN et al. (2005) – the elevation data file can be adjusted by setting the geophone spacing to the desired distance, as the horizontal cell size is equal to the geophone spacing in the elevation file. This additionally comprises the benefit, that – in case of a rugged topography – relief data are allowed to not only exceed the elevation data points for each geophone solely but may also include topographical information for the area in between geophones.

Tomographic inversion techniques are especially well suited for imaging subsurface distributions, which are expected to be more gradational than discrete, (GEOMETRICS, 2009) with strong horizontal velocity variations and in case of strong topography. The tomographic inversion tries to find the minimum traveltime between source and receiver for each source-receiver pair. Therefore the method starts with an initial model (generated from a layered model or by time-term inversion) and iteratively traces rays through the model, comparing the calculated traveltimes to the measured traveltimes, modifying the model, and repeating the process with the goal of minimizing the RMS error between observed and calculated traveltimes (GEOMETRICS, 2009; SHEEHAN et al., 2005). The inversion process is stopped when a predefined number of iterations is reached. The final model is chosen by analysing the evolution of the RMS error, with the correct iteration defined as the model where the RMS error deceeds a predefined value or an increase of the RMS error occurs. Raytraces of the final model constitute the raypaths through the subsurface between source and receiver with the minimum traveltime. Raytraces can be used for qualitatively determining areas of high/low reliability in the tomogram. A high ray-coverage constitutes reliable data, while the

interpretability of areas with a low density of rays, or with no ray-coverage, respectively, is limited.

To achieve a more detailed analysis of time-dependent processes, time-lapse tomograms were created to illustrate alterations of the acoustic characteristics between different measurements. The software package GEOPLOT (GEOMETRICS) was used to calculate differences in percentage between selected iterations of two measurements.

2.2 Methods for characterising the ground thermal regime

2.2.1 Bottom temperature of winter snow cover (BTS)

Since the development by HAEBERLI (1973), measurements of the bottom temperature of the winter snow cover (BTS) represents a widely applied method for the areal detection of permafrost (HOELZLE et al., 1993; ISAKSEN et al., 2002; ISHIKAWA, 2003; LAMBIEL & PIERACCI, 2008; SAWADA et al., 2003). The BTS method is based on the insulating properties of a sufficiently thick snow cover (> 80 cm), which causes a decoupling of the thermal regime at the soil/snow interface from short-term variations in the surface energy balance. Providing a consistent snow cover with a thickness of more than 80 cm, the BTS in high-winter (February/March) remains nearly constant, with temperature being controlled by heat transfer from the upper ground layers. BTS therefore constitutes an empirical indicator for the occurrence or absence of permafrost (FRENCH, 2007; WILLIAMS & SMITH, 1991).

BTS values are commonly classified into three categories with (i) *permafrost probable* (< -3 °C), (ii) permafrost possible (-2 °C to -3 °C) and (iii) *probably no permafrost* (> -2 °C). These categories are mainly based on BTS measurements above the timberline, where the requirements for a consistent snow cover can be met. Besides the thermal conditions of the subsurface, BTS values can be variable according to specific site conditions. LEWKOWICZ & EDNIE (2003) demonstrated a strong dependency of BTS values on snow cover characteristics. Remarkably low BTS values (< -10 °C) were detected at ventilated talus slopes (e.g. LAMBIEL & PIERACCI, 2008; SAWADA et al., 2003). BTS values exceeding temperatures anticipated for thermal subsurface characteristics can be ascribed to a supercooling, due to the activity of a chimney effect (cf. CHAPTER 1.1.1, see also WAKONIGG (1996), HARRIS & PEDERSEN (1998) & DELALOYE et al. (2003)). It could also be interpreted as a disturbance and, corresponding, a reduction of insulating properties of the snow cover, as a result of the occurrence of large boulders and/or trees/vegetation.

In this study, BTS measurements were applied to map the spatial permafrost distribution, and to identify the influence of annually variable snow- and climatic conditions on the ground thermal regime.

For measurements, a fibreglass rod with a thermistor at its front was plunged through the snow cover. The probe usually needs a few moments for adaption to temperatures at the soil/snow interface. Measurements are recorded as resistivity data using a multimeter and converted to temperature values (°C) afterwards. In addition to BTS the snow thickness, GPS positions as well as the elevation a.s.l. were recorded for each measurement point. The distance between neighbouring measurements was between 10 and 20 m, to enable for a plausible BTS-data interpolation.

Measured BTS values were standardised to a snow thickness of 1 m (KELLER, 1994). General classification of BTS values followed the values suggested by HAEBERLI (1973), but is extended for remarkably low temperatures, to achieve a more differentiated characterization of BTS values below -3 °C. Results from BTS mapping were interpolated using the geostatistical analyst within ArcGIS (ESRI). The IDW (inverse distance weighted) method was used for interpolation of BTS data (cf. CHAPTER 8.1.2).

2.2.2 Temperature data logging

For characterising the ground thermal regime at the investigated talus slopes a number of temperature data loggers were distributed in various positions of the study sites. Due to limited numbers, the distribution of data loggers was focused on measuring (i) the air- (AT) and (ii) ground surface temperature (GST), (iii) the temperature inside vents that could be associated to the activity of the chimney effect as well as (iv) the humus temperature in different depths. In the Val Bever, data from various additional temperature data loggers and a borehole were available. Information on logger types are given in TABLE 2.1; period and interval of measurements are presented in TABLE 4.2. Details on logger positions are given in CHAPTER 8.1.1 (see also maps in Figure 8.1 as well as TABLE 8.1 and TABLE 8.2).

For measuring the air- and ground surface temperature, various logger types were used, containing wireless mini data loggers and MLog (both Geoprecision) as well as UTL-1 data loggers (Universal Temperature Loggers). Loggers were attached to tree trunks or branches at 2 m height without being exposed to direct solar radiation for measuring the air temperature. As far as possible small trees, with a relatively small crown were chosen, to keep the influence of the thermal conditions to a minimum.

Loggers for measuring the ground surface temperature were placed in close distance to the AT-loggers, also trying to keep the exposition to solar radiation to a minimum.

Table 2.1: Details on temperature data loggers used in this study.

logger	fabricator	sensor	resolution [°C]	accuracy [°C]
MLog	Geoprecision	Dallas	0.065	± 0.25
wireless loggers	Geoprecision	PT1000	0.01	± 0.1
thermistor string	Geoprecision	Dallas	0.065	± 0.25
UTL-1	Universal Temperature Loggers	TMC-1T	0.1	± 0.27

Modified thermistor strings (Geoprecision) were used for monitoring humus temperatures in three depth-levels (cf. TABLE 2.1 & TABLE 4.2). Instead of sensors being placed along a single string, three strings with one sensor each were attached to the data logger. In the Val Bever, a borehole was drilled in September 2006 to a depth of 8 m (KNEISEL, 2010; KNEISEL & SCHWINDT, 2008). The borehole was instrumented with a thermistor string (Geoprecision) containing eight sensors (Dallas type; resolution: 0.065 °C; accuracy: ±0.25 °C) at various depths (0 m; 0.5 m; 1 m; 2 m; 3 m; 5 m; 7 m; 8 m).

To enable detection of expectedly rapid variations in the thermal regime, a short measurement interval of 20 minutes was chosen for all Geoprecision data loggers. The minimum interval for UTL-1 loggers was 40 minutes, due to the lower measurement capacity. Borehole temperatures were recorded at an hourly interval.

2.2.3 Humus, humus temperature and moisture mapping

The organic layer is assumed to distinctly influence the ground thermal regime, by (i) facilitating the chimney effect by "sealing" (WAKONIGG, 1996) the surface in the central parts of the talus slope and therefore focusing the circulation to the upper and lower vents, and (ii) by insulating the subsurface from warm outside air temperatures. The thermal conductivity of organic material is strongly dependent on the water content, with a low thermal conductivity for dry organic material (0.05 W/m K), increasing values for saturated material (0.5 W/m K) and a high thermal conductivity for saturated and frozen organic material (2.0 W/m K) (FRENCH, 2007; WILLIAMS & SMITH, 1991).

To measure humus temperature and water content, the WET-sensor with the HH2 moisture meter (Delta-T Devices) were used (cf. Figure 2.6). The WET-sensor measures temperatures with an accuracy of ± 1.5 °C. The soil moisture is measured with an accuracy of 3 %, using frequency domain reflectometry (FDR). For measurements, the steel rods of the WET sensor are plunged into the soil material. Measurements were conducted after the sensor has adapted to the specific humus temperatures, which usually took between one and two minutes. In consideration of small-scale inhomogeneities and disturbances due to dolomitic fragments within the humus material three measurements were conducted at each point of measurement and the results were averaged for each depth layer.

Figure 2.6: Humus moisture and temperature measurements using the WET sensor.

Additional parameters recorded for each profile involved a simple description of the humus forms and the identification of humus horizons (according to AG Boden, 2005; Arbeitskreis Standortskartierung, 2003; Green et al., 1993) as well as a rough estimation of the vegetation composition. GPS positions as well as the elevation a.s.l. were recorded at each survey point. Further details on the site-specific methodological approach are given in Chapter 8.1.3.

3 Study sites

Three vegetated talus slopes below the timberline were chosen in the Swiss Alps (FIGURE 3.1 and TABLE 3.1) for investigating the permafrost distribution, temporal frozen ground variability and for the characterisation of the site-specific ground thermal regime. Due to the variety of geomorphic and biogeomorphologic factors influencing the ground thermal regime, the chosen test sites constitute the potential to achieve an extensive interpretation of the cluster of factors that enables the existence of permafrost in low elevation talus slopes.

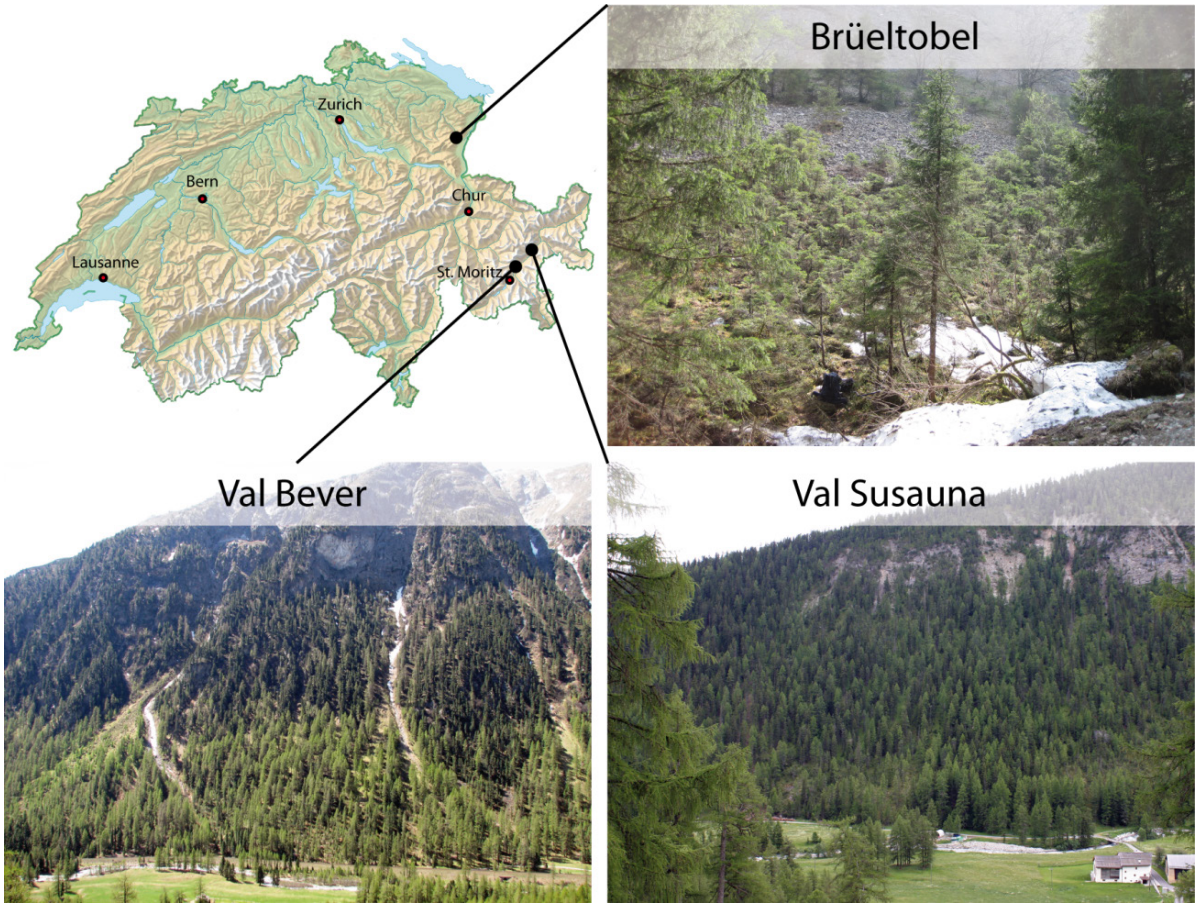

Figure 3.1: Study sites and location in Switzerland (map of Switzerland: geodata@swisstopo)

With the Val Bever and the Val Susauna two sites were chosen in the Upper Engadin that are comparable with view on the fundamental climatic conditions (MAAT and precipitation) and geomorphic setting (exposition, slope) (cf. TABLE 3.1) but differ with regard on the talus substrate. The Brüeltobel site, located in the Appenzeller Alps is

characterised by climatic conditions and a geomorphic setting (cf. TABLE 3.1) distinctly different to the Engadin sites but a talus substrate (limestone) that is comparable to the Val Susauna site (dolomite).

*Table 3.1: Specifications of study sites. (*Station Samedan Airport, **Station Brülisau; © MeteoSwiss)*

	Val Bever	Val Susauna	Brüeltobel
region	Upper Engadin	Upper Engadin	Appenzeller Alps
position	46°33'19" N 9°51'30" E	46°38'03" N 9°59'32" E	47°16'37" N 9°27'41" E
morphology	scree slope	scree slope	scree slope
elevation [m a.s.l.] (foot of slope/foot of rockwall)	1788 / 2100	1685 / 1880	1200 / 1240
exposition	N-NE	N-NE	N-NW
average slope	25°	25°	38°
substrate	granitic, bouldery	dolomitic talus	limestone talus
vegetation (trees)	*larix decidua, pinus cembra, picea abies*	*pinus cembra, pinus mugo, picea abies*	*picea abies, pinus mugo*
MAAT [°C] (2 m height)	2,3	2,2	5,5
MAGT [°C] (5 cm depth)	0,9	0,8	1,4
precipitation [mm]	664*	664*	1633**

The presence of permafrost at the test sites was not of major importance when the test sites were selected. In fact, first of all the existence of a thermal anomaly – a supercooling of the talus slope – was of interest. Solely for the Val Bever site, where borehole temperatures were below 0°C since autumn 2006, permafrost has been proven. At the Brüeltobel and the Val Susauna test sites, the azonal and small-scale delimited vegetation composition with dwarf grown trees and a consistent humus/lichen cover in conjunction with a thick humus layer point to an exceptional, supercooled microclimate. While a thermal anomaly and at least seasonal frozen ground condition in the talus slope of the Brüeltobel is known for a long time (BÄCHLER, 1930; FURRER, 1966), the Val Susauna site has been identified as a potential permafrost site below the timberline by the inspection of maps and subsequent site inspections in fall 2008.

3.1 Val Bever & Val Susauna - Study sites in the Upper Engadin

Located in the canton Grison (SE Switzerland) the Val Bever and the Val Susauna are both tributaries (orographically left) to the Upper Engadin Valley. The SW-NE-oriented valley of the Engadin owes its existence to the Engadin Line, a fault zone between the Bergell in the Southwest and Imst in the Northeast (LABHART, 2005). Due to morphological disparity, the Engadin is subdivided by the Punt'Ota (~1600 m a.s.l.) into the Upper Engadin with the Maloja mountain pass (1815 m a.s.l.) in the Southwest and the Lower Engadin with its lower end near Scoul (~1000 m a.s.l.) in the Northeast. While the Upper Engadin is wide, rich in lakes and first of all glacially shaped, the Lower Engadin valley is deeply carved by the activity of the Inn (HANTKE, 1991).

Built up by the geologic nappes of the Austroalpine, the Engadin exhibits a complex geology with a small scale variation of various rock types involving metamorphic rocks (e.g. gneiss, schist, mica schist), intrusive rocks (granite, diorite, gabbro) but also Mesozoic and Permian sedimentary rocks (GWINNER, 1971; HSÜ, 1995; LABHART, 2005; MÖBUS, 1997). Located in the Err-Bernina nappes complex of the Lower Austroalpine the Val Bever is, in the proximity of the study site, built up by granitic intrusive rocks. The Val Susauna is located in the western margins of the Silvretta nappe (Upper Austroalpine), where the Silvretta nappe overlies lenses of Triassic dolomites (Subsilvrettide lenses) and the Ela nappe, consisting of Upper Triassic and Jurassic sediments (TRÜMPY, 1980).

The climate in the Upper Engadin can be, due to the surrounding mountain range, characterised as continental, with a low mean annual air temperature, a high annual temperature amplitude, and moderate precipitation (cf. TABLE 3.1). HANTKE (1991) reckons the Engadin along with the remainder of the Inn-Valley, the Münstervalley and the Vintschgau, among the Central Alpine dry valleys. The climatic conditions in the Engadin (low precipitation rates, late onset of a consistent and often thin snow cover, low winter temperatures) alongside with widespread coarsely weathering substrate (low thermal conductivity due to high amount of air-filled voids) favour the distribution of permafrost, especially with regard on the high abundance of rock glaciers. In consideration of the -1°C isothermal line that is regarded as the lower limit for the potential existence of permafrost (HAEBERLI, 1990), discontinuous permafrost can be expected in the central Alps above 2400 m a.s.l. (LUGON & DELALOYE, 2001).

The timberline in the Central Alps with low precipitation and high amounts of incoming solar radiation is typically composed of pine (*Pinus cembra*) and larch (*Larix decidua*) trees (*Larici-Pinetum cembrae*) (Reisigl & Keller, 1989). The composition of the *Larici-Pinetum cembrae* can vary depending on substrate and exposition. Characteristic for north-exposed slopes is the *Larici-Pinetum cembrae rhododendretosum* (*Larix decidua* and *Pinus cembra* with *rhododendron ferrugineum* in the undergrowth), while reedgrass (*Calamagrostis vilosa*) is widespread in the undergrowth at south-exposed slopes (*Calamgrostio villosae-Pinetum cembrae*) (Reisigl & Keller, 1989). Dolomitic scree slopes are often characterised by shrubby or lying mountain pines (*Pinus mugo*), *L.-Pinetum cembrae mugetosum* (Reisigl & Keller, 1989). While the altitudinal limit of *Larix decidua* can be expected at around 2000 m a.s.l. the treeline (~2300 m a.s.l.) consists of *Pinus cembra* (Hiller & Müterthies, 2005). The timberline in the central Alps – predominantly conditioned by anthropogenic forest clearance – is currently located at an elevation between 2000 and 2200 m a.s.l. (Hiller & Müterthies, 2005).

3.1.1 Val Bever

The Val Bever is a tributary to the Upper Engadin valley. Originating at the Piz d'Err (3378 m a.s.l.) with the source of the Beverin river, the valley ends at the town of Bever (~1710 m a.s.l.) at the confluence of the Beverin and the Inn (~1700 m a.s.l.). The alignment of the Val Bever is differentiated into an upper part (origin - 2000 m a.s.l.), orientated from SW to NE and a lower part (2000 - 1710 m a.s.l.) oriented from W-NW to E-SE, determining an approximate orientation of the scree slopes to N-NE and S-SW, respectively.

The study site is located in a north-exposed valley section named "God Frasüroulas" (with "God" being Rhaeto-Romanic for forest) in the lower part of the Val Bever (cf. Figure 3.2). The elevation at the foot of the investigated talus slope is ~1780 m a.s.l., the foot of the adjacent rock-wall above – with the Cho d'Valletta (2496 m a.s.l.) as the summit – is located at ~2100 m a.s.l. (cf. Table 3.1). The rock-wall in the area of the study site is built up by bright granite, abound in orthoclase. The scree slope consists of mostly bouldery granitic talus material. Recent morphodynamic processes are

conspicuous, especially with regard on debris-flow channels and depositions (cf. FIGURE 3.2 b), rock falls and a high avalanche activity during winter.

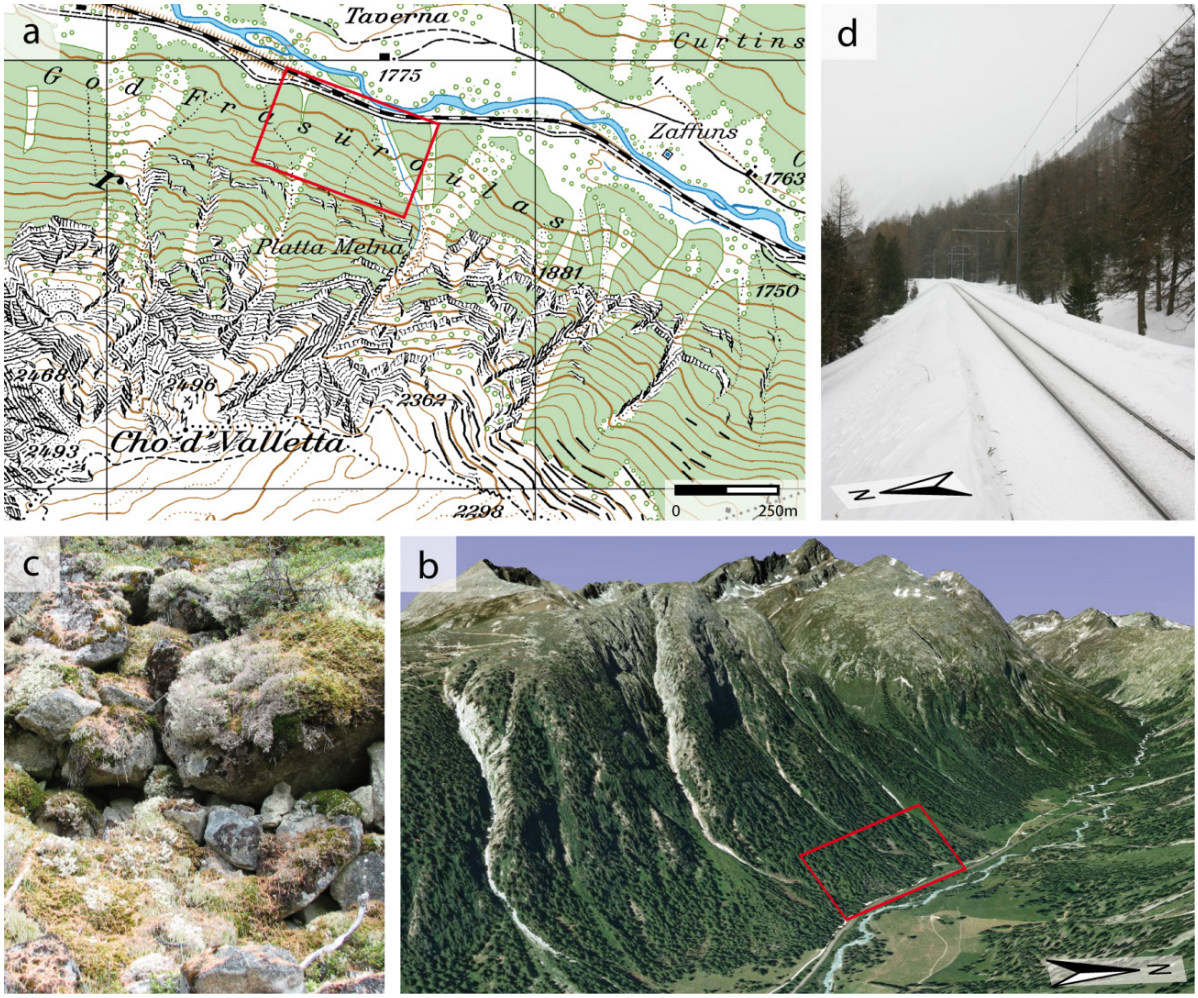

Figure 3.2: Details on the Val Bever site. a) Map excerpt of the Val Bever (© swisstopo) with delineated study site (red square). b) View into the Val Bever (© Google Earth) with delineated study site (red square). c) Picture of talus slope composition with granitic boulders and a fragmentary cover of mosses/lichen. d) Railroad embankment of the Albula line in the proximity of the study site.

While most parts of the valley floor in the section of the Val Bever study site is agricultural land (meadows, grazing management) both valley slopes are wooded (FIGURE 3.2). At the north-exposed study site the *Larici-Pinetum cembrae rhododendretosum* is widespread (cf. CHAPTER 3.1), with *Pinus cembra* and *Larix decidua* as the main tree species. The amount of larch trees decreases with elevation towards the rock wall. However, the vegetation composition and characteristics show a distinct variability along the valley alignment at the study site with regard on trees

(normal growth, dwarfing, forest aisles), and undergrowth (distribution of mosses/lichens, grasses and shrubs) (FIGURE 3.3).

The soil development at the study site is poor and is mostly confined to the accumulation of organic material due to low mineralisation rates, typical for cold alpine sites. In most cases, a thick humus layer (up to 30 cm thickness) superimposes bouldery granitic talus with no or low amounts of fine grained material (SCHWINDT, 2007). However, the humus/moss cover is fragmentary and variable in thickness as a result of the boulder talus material (cf. FIGURE 3.2 c and FIGURE 3.3 d).). In areas with fine-grained, siliceous material (e.g. fossil debris-flow deposits) micro-podsols can be found. The process of podsolization is regarded as the dominant soil-forming process at alpine sites below the timberline (HILLER, 2001; HOLTMEIER, 2000; MÜLLER, 1987), while soils usually remain shallow with an affection towards withering (MÜLLER, 1987).

The Val Bever permafrost site is target of research since the late 1990s. Investigations include repeatedly conducted BTS measurements (KNEISEL et al., 2000b; RIEDLINGER, 1999) and the joint application of various geophysical measurements including 1D and 2D resistivity measurements, 2D refraction seismics as well as measurements using the OhmMapper (HAUCK & KNEISEL, 2006; HAUCK & KNEISEL, 2008b; KNEISEL, 2003a, b; KNEISEL & HAUCK, 2003; KNEISEL & SCHWINDT, 2008; SCHWINDT, 2007). Further investigations included temperature measurements by numerous temperature data loggers since 1998 as well as borehole temperature data since 2006 (KNEISEL, 2007). The Val Bever permafrost site has also been focus of dendrochronological investigations (BAST et al., 2007). All investigations point to an occurrence of sporadic permafrost in the supercooled talus slope of the Val Bever, with a small scale heterogeneity with frozen and unfrozen areas in close vicinity (SCHWINDT, 2007). Applying a four-phase model, HAUCK & KNEISEL (2008b) assume ice contents between 15-25%, while borehole temperatures (September 2006, 8 m depth) of -0.22°C (KNEISEL, 2007) point to relatively warm permafrost temperatures.

Figure 3.3: Vegetation composition in the Val Bever. a) Normally grown trees (Larix decidua, Pinus cembra) in areas with no permafrost, grasses and shrubs in the undergrowth. b) Permafrost area with reduced tree size, crown density and tree density (Larix decidua, Pinus cembra). Undergrowth (details given in picture d) is characterised by a fragmentary cover of mosses and lichens and a high amount of litter (Larix decidua needles). c) Forest aisle as a result of recent morphodynamic processes (avalanche and rock fall activity). e) and f) prevalent shrubs in the Val Bever with e) Vaccinium vitis-ideae and f) Rhododendron ferrugineum.

3.1.2 Val Susauna

The Val Susauna is, just as the Val Bever, a tributary to the Valley of the Upper Engadin with its valley end located close to the transition between Upper- and Lower Engadin. The Val Susauna originates with the source of the Vallember at the Scalletta mountain pass (2606 m a.s.l.) and ends at the village of Chapella (1634 m a.s.l.) close to the confluence of the Vallember and the Inn (1610 m a.s.l.). The orientation of the Val Susauna is N-S in its upper part (Scalletta mountain pass to ~2200 m a.s.l) and, almost parallel to the Val Bever, W-NW to E-SE in the remaining course (1900-1634 m a.s.l.). The scree slopes in the lower parts of the Val Susauna are exposed towards N-NE and S-SW, respectively.

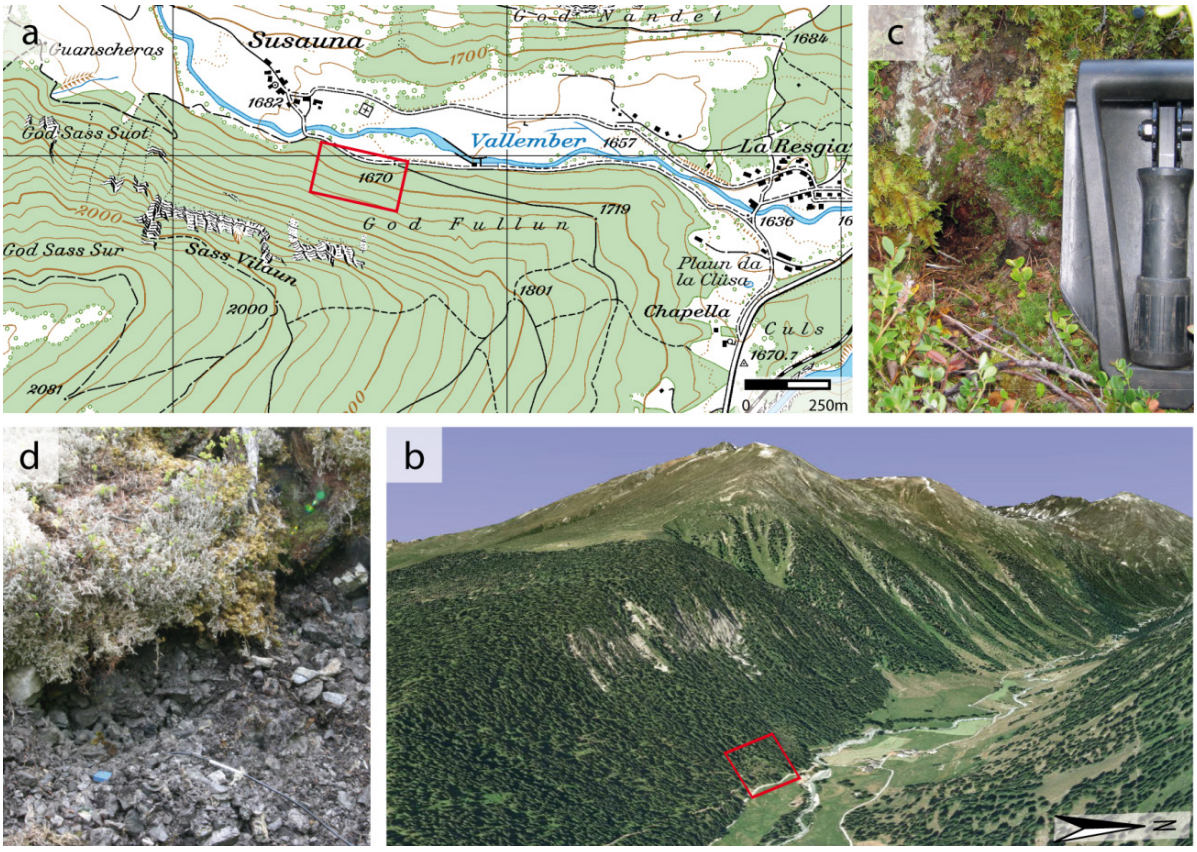

Figure 3.4: Details on the Val Susauna site. a) Map excerpt of the Val Susauna (© swisstopo) with delineated study site (red square). b) View into the Val Susauna (© Google Earth) with delineated study site (red square). c) Vent at the foot of the talus slope. d) Dolomitic talus superimposed by humus, mosses and lichens.

The study site in the Val Susauna is located in the north-exposed talus slope in the proximity of the village of Susauna (cf. FIGURE 3.4) in a valley section named "*God*

Fallun". While valley orientation and exposition of the study site in the Val Susauna are rather similar to the investigated valley section of the Val Bever, and the difference in altitude at the valley floor is only 120 m, the main regional distinction can be ascribed to geological conditions. While the granitic parent rock material in the Val Bever forms steep and rugged rock walls, the dolomitic mountain range (Subsilvrettide, cf. CHAPTER 3.1) of the Val Susauna appears rather gently contoured (FIGURE 3.4 b). As a consequence of the parental rock material the scree slope at the Val Susauna study site consists of predominantly plate-shaped dolomitic talus with a diameter of approximately 5-20 cm. The investigated talus slope ranges over a distance of ~250 m with an elevation of 1665 m a.s.l. at the foot of the slope and 1840 m a.s.l. at the foot of the adjacent rock-wall above (TABLE 3.1).

In its lower parts the Val Susauna is characterised by a wide valley floor with a gentle incline and is predominantly in agricultural use (meadows, grazing management). While both sides of the valley are wooded, patches of the south-exposed valley side, especially at the foot of the slope, are in agricultural use. The vegetation composition at the study site of the north-exposed talus slope exhibits a strong contrast between the supercooled, assumed permafrost section and the prevailing thermally undisturbed areas (FIGURE 3.5 a). *L.-Pinetum cembrae mugetosum* (cf. CHAPTER 3.1) with a consistent and thick cover of mosses and lichens, interspersed with various shrubs in the undergrowth can be encountered at the potential permafrost area. A distinct dwarfing, especially for *Pinus mugo* and *Picea abies*, can be observed. Larch trees are outnumbered. The vegetation composition in thermally undisturbed areas shows a thick forest with normally grown, tall trees (*Picea abies, Pinus cembra;* >10 m height) and shrubs and mosses forming a patchy undergrowth.

The soil development at the Val Susauna site is first of all confined to the accumulation of organic material. However, distinct variations are observable for thermally disturbed and undisturbed areas. A humus thickness between 30 and 70 cm (cf. Figure 8.5) superimposing the dolomitic talus (FIGURE 3.4 d) is characteristic for areas influenced by the potential permafrost occurrence. The humus layer in this area is consistent and area-wide superimposed by mosses and lichens. Thermally undisturbed areas are characterised by a more shallow humus cover of mostly less than 15 cm. High

amounts of difficulty decomposable needle material derived from the pine and spruce trees forms a pronounced layer of litter, patchily interspersed with shrubs and mosses.

In contrast to the Val Bever and the Brüeltobel, no preceding studies are known for the permafrost site in the Val Susauna.

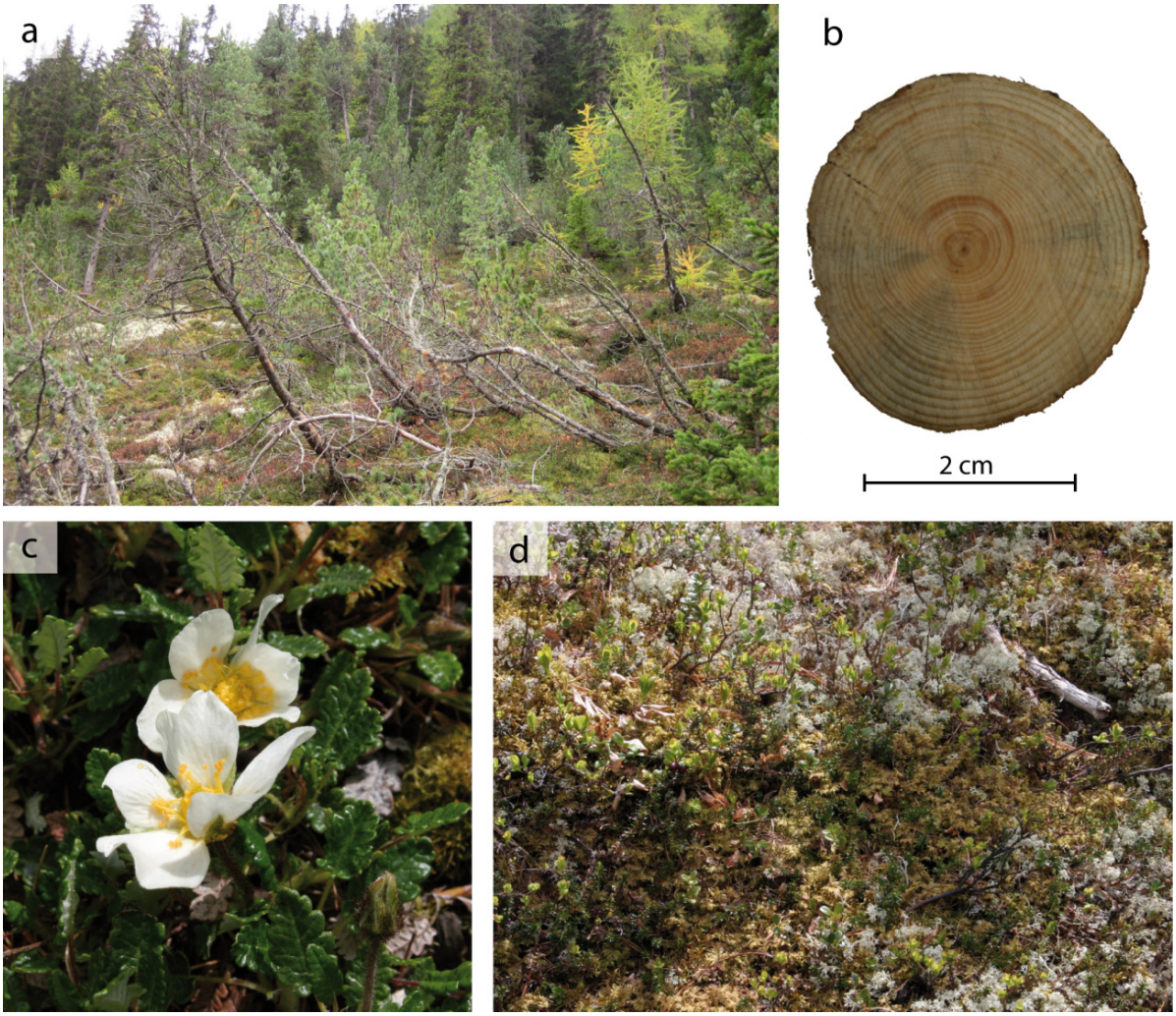

Figure 3.5: Vegetation composition at the Val Susauna site. a) Dwarfed and dieback trees (Pinus mugo, Picea abies) at the Val Susauna permafrost site. Trees in the background (Pinus cembra, Picea abies) in areas with no permafrost show normal growth. b) Slice of a dwarfed Pinus mugo tree with more than 35 year rings. c) Dryas octopetala. d) Characteristic undergrowth composition at the permafrost site with mosses, lichens (i.a. Cladonia rangiferina and shrubs (i.a. Vaccinium vitis-ideae, Vaccinium uliginosum, Empetrum nigrum)

3.2 Brüeltobel – Study site in the Appenzeller Alps

The Brüeltobel study site (47°16'37" N, 9°27'41" E) is located in in the Alpstein mountain range within the Appenzeller Alps (canton Appenzell Innerrhoden, NE Switzerland) near the village of Brülisau. The Alpstein is formed of the Helvetic Säntis nappe consisting predominantly of cretaceous limestone alternating with marl (Hsü, 1995; Möbus, 1997). A sequence of parallel folds with a strike angle from SW to NE is characteristic for the Alpstein mountain range (Heierli, 1984). The highest peak of the Alpstein is the Säntis with 2502 m a.s.l., the summit of the Hohe Kasten, superior to the Brüeltobel, reaches a height of 1794 m a.s.l.

The climate of the Alpstein region differs distinctly from conditions of the study sites in the Upper Engadin. Conditions are driven by the position of the Alpstein in the northern mountain range of the Alps, with precipitation values of up to 1600 mm per year (station Brülisau at the foot of the Alpstein) and more than 2600 mm for the summit of the Säntis (source: MeteoSwiss). The annual temperature amplitude is rather low, ranging between ~14 and -1°C (station Schwäbrig; source: MeteoSwiss). In consideration of the -1°C isothermal line that is regarded as the lower limit for the potential existence of permafrost (Haeberli 1990), widespread discontinuous permafrost occurrences in the Alpstein region are rather unlikely, regarding the fact, that the mean annual air temperature at the Säntis (2502 m a.s.l.) is -0.8°C (period 2006-2011; source: MeteoSwiss).

The Brüeltobel is a steep, V-shaped valley in the eastern part of the Alpstein mountain range. ("Tobel" is a term used in Switzerland and Austria for V-shaped valleys, characteristically with a gorge at the end of the valley) The origin of the Brüeltobel is located at the Plattenbödeli (1280 m a.s.l.; Alp Sigel-anticline) in the north-eastern margins of the Sämtiser syncline (Heierli, 1984) and declines on a distance of 2 km to the Pfannenstiel (945 m a.s.l.). The study site "Brüeltobel" is located at an elevation of ~1200 m a.s.l. (Table 3.1) in the N-NW exposed talus slope of the Brüeltobel. The morphology in the proximity of the study site is strongly influenced by the local small-scale geologic conditions (Figure 3.7). Located in the Alp Sigel-anticline, the scree slopes in the proximity of the study site consists of Schrattenkalk-talus (limestone) as derived from the vertical rock-wall above. The valley bottom of the Brüeltobel in this area is built up by eroded rock strata of the Alp Sigel-anticline

(FIGURE 3.7). A distinct steepening of the slope in the valley alignment proximately below the study site can be ascribed to a rock threshold (FIGURE 3.6b & c).

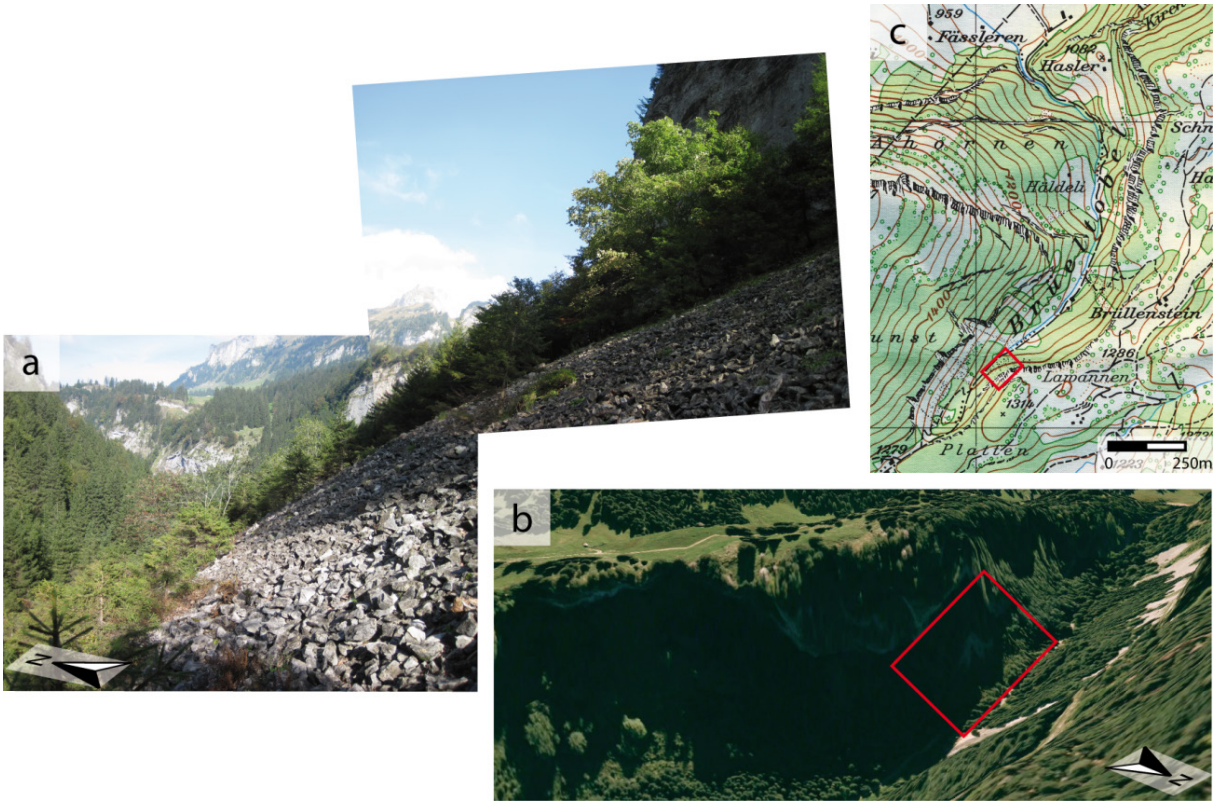

Figure 3.6: Details on the Brüeltobel site. a) Picture of uncovered limestone talus in the upper part of the investigated slope, with dwarfed spruce trees (Picea abies) downslope and normal grown trees, partly deciduous trees (Acer pseudoplatanus, Fagus silvatica, Fraxinus excelsion) upslope below the rockwall. b) View into the upper parts of the Brüeltobel (source: Google Earth) with the delineated study site (red square). c) Map of the Brüeltobel (© swisstopo) with delineated study site (red square).

Located in the transition area between montane and subalpine altitudinal belt, the vegetation composition of the Brüeltobel appears influenced by the complex geomorphological conditions. Up to an elevation of ~1400 m a.s.l. a montane *Abieti-Fagetum*, with *Fagus sylvatica* and *Picea abies* as the main tree species would be expected (REISIGL & KELLER, 1989). The potential natural vegetation of the subalpine altitudinal belt (1400-1600 m a.s.l.) is a conifer forest with spruce (*Picea abies*) as the dominant tree species (*Homogyne picetum*) (LANDOLT, 2003; REISIGL & KELLER, 1989). However, the steep area of the Brüeltobel, below the study site (945-1200 m a.s.l.) is vegetated with tall spruce trees. Above the study site, in the less steep area towards the Plattenbödeli (1280 m a.s.l.), deciduous woods (*Acer pseudoplatanus*, *Fagus sylvatica*) are widespread.

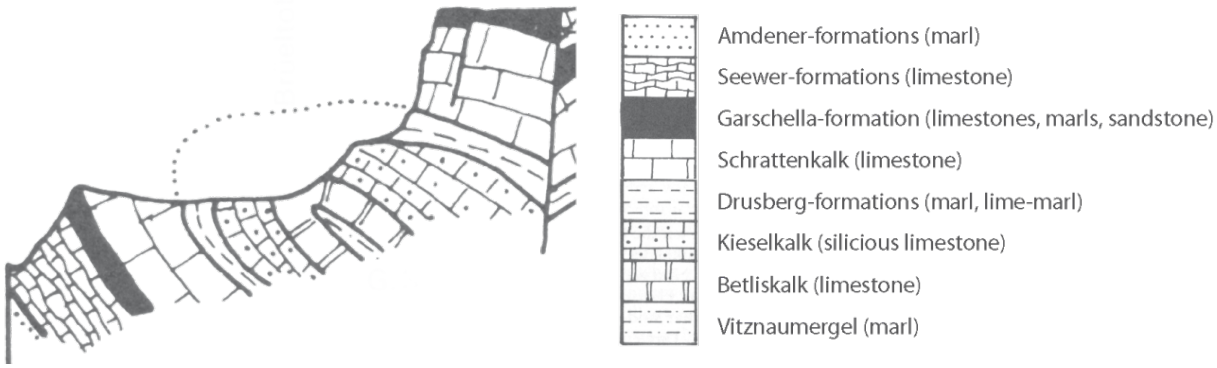

Figure 3.7: Geological cross-profile through the Brüeltobel (modified after HEIERLI, *1984)*

The supercooled talus slope of the Brüeltobel study site is located at the orographic right side of the valley (exposition NW). With an area of less than 100 x 70 m, the supercooled area is rather small. The talus slope consists of angular debris (<20 cm in diameter) derived from the steep, almost vertical rock wall (limestone/Schrattenkalk) above the scree slope. On the basis of the surface characteristics (vegetation, humus/soil, uncovered talus), the slope can be vertically subdivided into three markedly different areas (FIGURE 3.6 a). The lowermost slope range (1200-1220 m a.s.l.) is wooded with spruce trees (*Picea abies*) that show a distinct dwarf growth (Figure 3.8 a, b, c). With an estimated age of 60 to >100 years (WEGMANN, 1995) most of the trees are less than 1.5 m in height. The undergrowth is characterised by a consistent layer of mosses, superimposing a humus layer of up to 50 cm thickness. Dwarf-grown trees and the presence of *Dryas octopetala* (FIGURE 3.8 d) at its lower distribution boundary (1200-2700 m a.s.l. (LANDOLT, 2003)) point to a thermal anomaly and a supercooling of the talus slope. As a result of supercooled conditions, soil-forming processes in this area are mainly reduced to the accumulation of organic material that superimposes the limestone talus. The intermediate area of the slope (1220-1230 m a.s.l.) consists of uncovered limestone talus. The talus in this area is loosely bedded with resupply of talus by regular rock falls. The uppermost zone (1230-1240 m a.s.l.) with its upper margin adjacent to the rock-wall is vegetated with deciduous trees (*Acer pseudoplatanus, Fagus sylvatica, Fraxinus excelsior*) and a consistent grass cover (*Carex ferruginea*) in the undergrowth. In this area, a humic A-horizon is developed that is covered by a shallow organic layer. The activity of the soil-fauna in this area below the rock wall could be observed by means of the presence of earthworms.

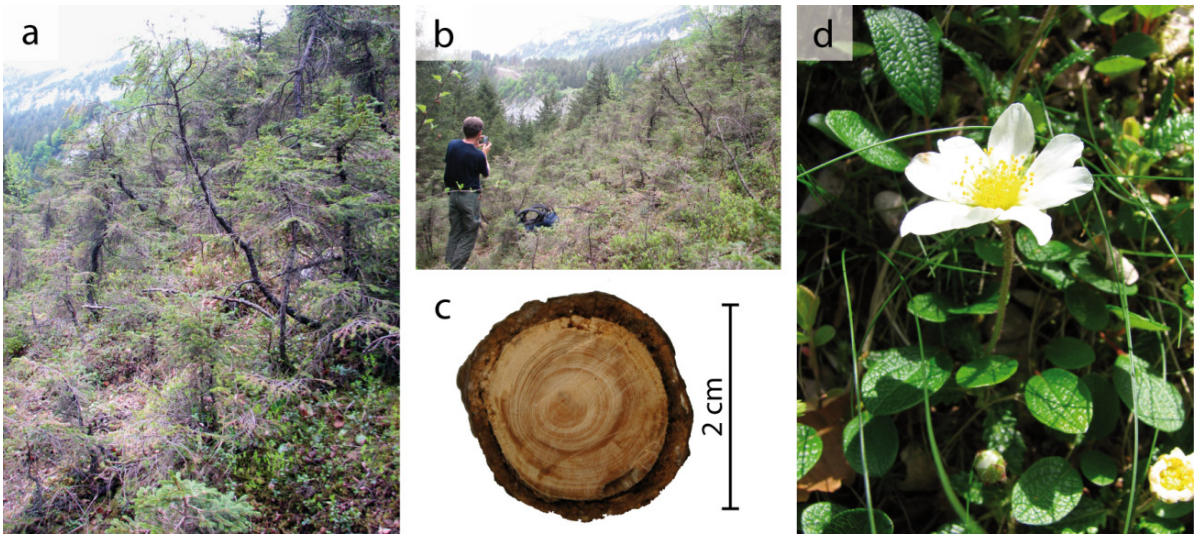

Figure 3.8: Vegetation composition at the Brüeltobel site. a) and b) Dwarfed spruce trees in the lower parts of the supercooled talus slope. c) Slice of a dwarfed spruce tree with approximately 60 year rings at a stem thickness of around 2 cm in diameter. d) Dryas octopetala.

Even though the Brüeltobel site with its exceptional thermal regime is known for a while (Bächler, 1930; Felber, 1884; Furrer, 1966) – especially due to the existence of the so called "*Hexenwäldli*" (*Witches Forest*) with dwarf grown spruce trees – recent research on the verification of the existence of permafrost in the Brüeltobel and the characterization of the ground thermal regime is sparse and restricted to unpublished theses. By the end of July 1915, Bächler (1930) detected ice in 1.5 m depth, and measured a temperature of -2.8°C. Wegmann (1995) applied geophysical methods (1D geoelectric, refraction seismics) as well as temperature measurements. A thermal anomaly has been detected by temperature measurements, but – measuring geophysics only once and with only 1D geoelectric available – no ground ice occurrence could be detected. Rist (2002) investigated the Brüeltobel – among 35 additional sites with a "*Hexenwäldli*" – using GIS-calculations for characterising the sites with regard on climatic factors, relief- and subsurface parameters. Investigations emphasized the importance of local, small-scale conditions with low income of solar radiation, low thermal insulation – which is in contrast to the assumption of most other authors investigating supercooled talus slopes (cf. Chapter 1.1.1) – and the activity of a convective flow inside the talus slope. Schudel (2002) predicts a disappearance of low-elevation supercooled talus slopes on the basis of dendroecological investigations at the Brüeltobel "*Hexenwäldli*", as growth, conform to climatic warming, could be detected for all spruce trees (dwarf grown as well as normally grown trees) in the Brüeltobel

4 Field studies

An overview on the field studies performed and methods applied in this study at each study site is given in TABLE 4.1. Details on temperature data loggers, logger positions and measurement periods are given in TABLE 4.2. Further details on methods are given in CHAPTER 2; detailed information on the application of methods with regard on the specific problem is given in the corresponding chapters within Part II.

*Table 4.1: Overview on performed field studies and methods. Study sites are given in abbreviations with VB - Val Bever, VS - Val Susauna and BT - Brüeltobel (*according to the number of utilizable datasets with Wenner/dipole-dipole, and solely Wenner datasets for the Brüeltobel study site).*

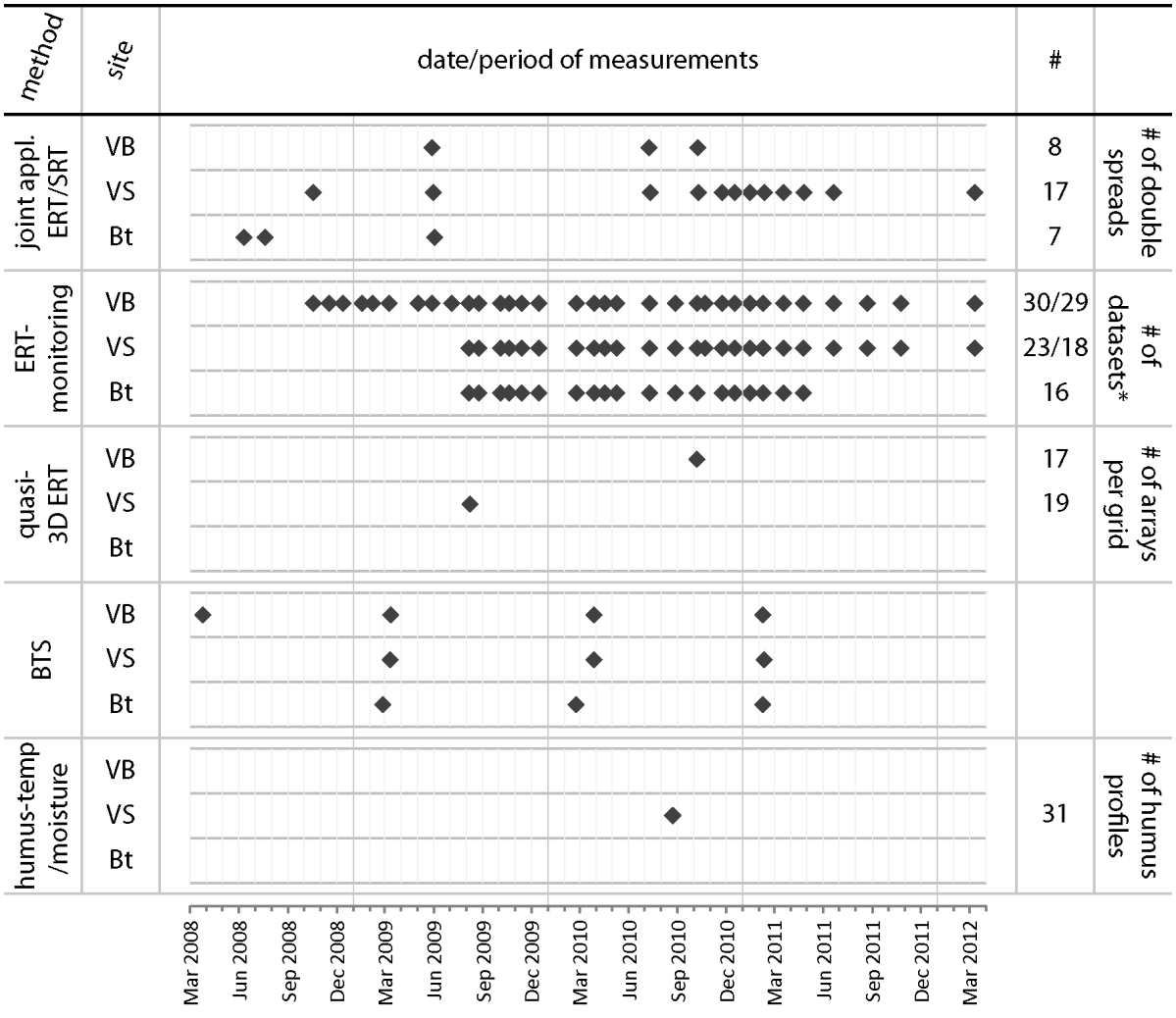

Geophysical measurements (TABLE 4.1) were applied for the detection of frozen ground and subsurface heterogeneities (joint application of ERT/SRT, quasi-3D ERT) as well as for the verification of permafrost and for characterising the temporal frozen ground

variability (ERT-monitoring, ERT/SRT-monitoring). Taking into account the high annual variability of subsurface characteristics, ERT-monitoring (CHAPTER 7) was applied monthly throughout the year. Data gaps are first of all ascribed to technical problems. Dates for measuring ERT/SRT in joint application (CHAPTER 6) were determined in spring/early summer (assumably highest amounts of ground ice) and in late summer/autumn, when frozen ground degradation is assumed to be highest, or frozen ground has disappeared. Quasi-3D ERT (CHAPTERS 5 & 6) was measured in late summer/autumn, when seasonal frozen ground is assumed degraded and only perennial ground ice/permafrost remains. The same is true for humus -temperature and -moisture measurements (CHAPTER 8.1.3). Measurements were conducted in late august, when temperatures are assumed to be highest. BTS measurements (CHAPTER 8.1.2) were conducted each winter at all study sites. The number of measurement positions at each site is highly variable as influenced by snow thickness and avalanche activity. With regard on the very sensitive ecosystem, geophysical and soil-scientifical investigations were reduced at the "*Hexenwäldli*" in the Brüeltobel.

Temperature data loggers were positioned at all study sites for characterising the ground thermal regime. Details on temperature data loggers, logger positions and measurement periods are given in TABLE 4.2 (see also CHAPTERS 2.2.2 & 8.1.1). The interval of temperature readings was set to 20 minutes for most data loggers but had to be adjusted towards measurements every 40 or 60 minutes, according to the abilities of the temperature loggers (UTL-1) (cf. TABLE 4.2). Data gaps are a result of technical failures. Some planned temperature measurements could not be realized due to technical failures and due to the disappearance of data loggers (rodents, avalanches).

Table 4.2: Details on temperature data loggers, period of measurements and logger positions. (Abbreviations: BH - borehole, AT - air temperature, GST - ground surface temperature, HT - humus temperature, VT - vent temperature. Additional specifications for Val Susauna and Brüeltobel: H - Hexenwäldli, U - position upslope, T - uncovered talus area, F - forest). For further information on logger positions, see Figure 8.1.

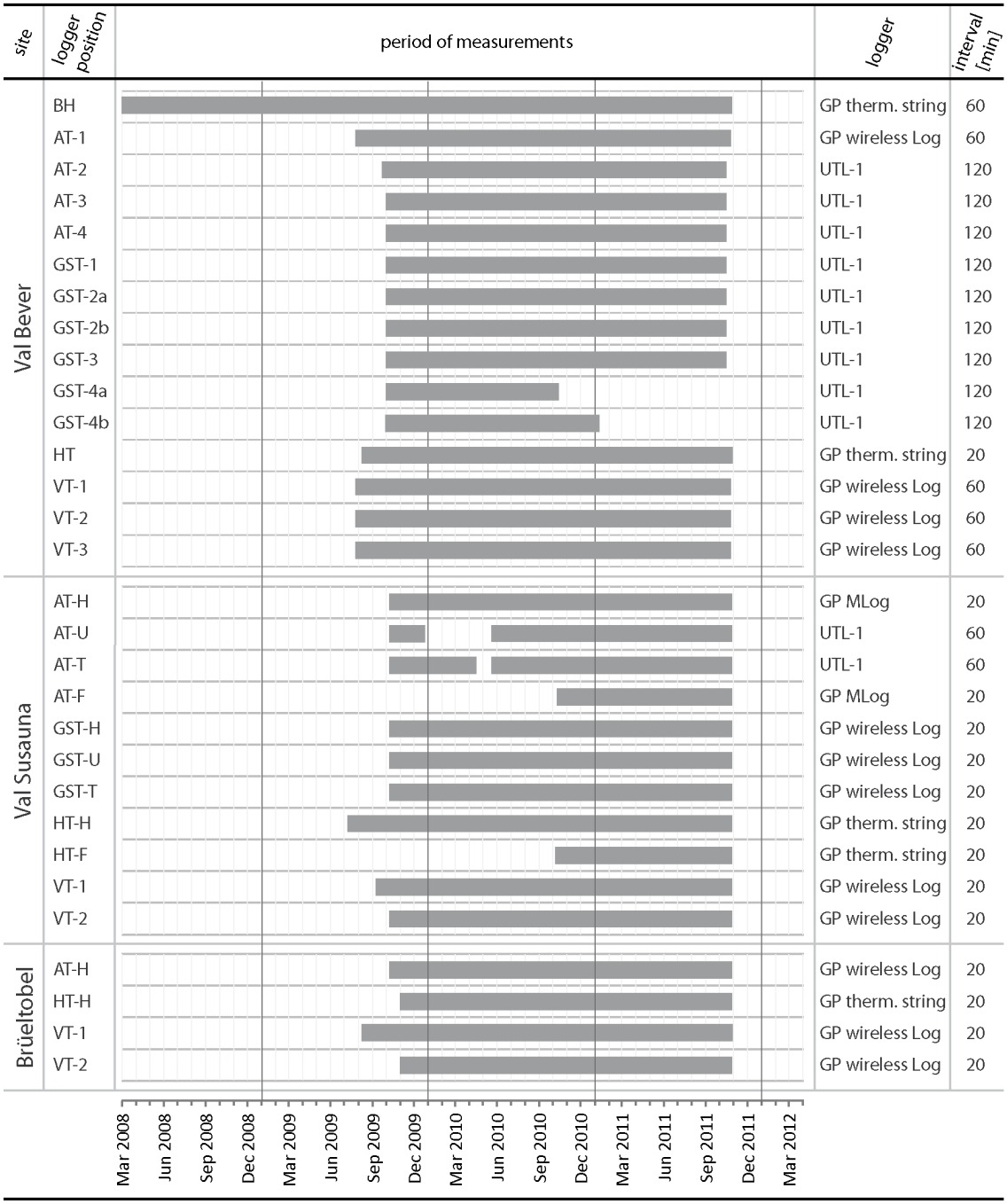

PART II – CASE STUDIES

5 Optimisation of quasi-3D electrical resistivity imaging for mountain permafrost studies

Distribution and characteristics of permafrost in both, mountainous and polar regions are a result of the site-specific ground thermal regime. In mountainous regions in particular, permafrost distribution is characterised by a small-scale heterogeneity induced by a variety of factors affecting microclimatic conditions, including solar radiation – as a result of topography and aspect – snow cover, surface and subsurface material, but also vegetation cover and soil/humus characteristics. Delineation of the three-dimensional distribution of mountain permafrost in the shallow subsurface greatly assists with understanding of geocryologic processes, and the ground thermal regime as well as geotechnical problems, especially in the context of claims of climatic change and subsequent frozen ground degradation.

Over recent decades geophysical methods and, in particular electrical resistivity tomography (ERT) have proven to be valuable tools for investigating permafrost related problems in mountainous and polar regions (Hauck & Vonder Mühll, 2003a; Kneisel et al., 2008). Even though techniques for three-dimensional electrical resistivity imaging were developed during the 1990s (Ellis & Oldenburg, 1994; Loke & Barker, 1996a; Park & Van, 1991; Sasaki, 1994) 2D ERT is still state of the art as a minimal invasive method in the study of permafrost. However, while 2D ERT has proven to be a valuable tool for detecting frozen ground and for monitoring its temporal variability (e.g. Hauck, 2002; Hilbich et al., 2009b; Kneisel, 2004; Kneisel et al., 2008; Krautblatter & Hauck, 2007; Krautblatter et al., 2010) there are drawbacks in detecting the spatial permafrost heterogeneity. Here 3D-techniques enable direct linking of surface conditions (debris size, solar radiation, vegetation, humus thickness) with subsurface- and ground ice characteristics. To date, studies applying 3D-ERT techniques for permafrost-related problems are sparse (Krautblatter, 2008; Rödder & Kneisel, 2011; Schwindt, 2007; Schwindt & Kneisel, 2009). In contrast, 3D techniques are generally more common in disciplines such as environmental (Bentley & Gharibi, 2004; Bichler et al., 2004; Chambers et al., 2007; Dahlin et al., 2002; Friedel et al., 2006) hydrological (Park, 1998) and soil science (Garré et al., 2011), as well as geotechnical engineering

(Fischanger et al., 2007), investigation of contaminated and waste disposal sites (Rucker et al., 2009; Soupios et al., 2007) and archaeology (Morelli et al., 2004; Papadopoulos et al., 2007).

"Real-3D" applications for studying permafrost-related problems are uneconomic in most cases. For mapping frozen ground in mountain environments, a grid size of at least 70 x 70m will be of interest in order to cover a sufficient area and to achieve an adequate depth penetration. Assuming a grid setup of 36 x 36 electrodes and a unit electrode spacing of 2 m, - an appropriate setup for permafrost-related studies – 1296 electrode positions would be necessary to build up a "real-3D" grid. With regard on logistics and time-efficiency constraints, this approach is not practicable in alpine environments. Here the application of the quasi-3D technique where a number of individually measured 2D ERT surveys are collated possesses distinct advantages (cf. Chapter 2.1.1.1).

The quasi-3D technique has been tested previously using forward modelling and presenting case studies for archaeological (cf. Papadopoulos et al., 2006) and environmental (cf. Gharibi & Bentley, 2005) problems. However, the assumptions for problems related to frozen ground differ greatly from those drawn in these studies regarding grid size, aimed resolution, resistivity contrasts in the subsurface as well as size and structure of the object of investigation. Most mountain sites with permafrost are more difficult to access and are characterised by a heavy terrain and complex topography, where the optimal installation of electrodes can be challenging. Aim of the study was to investigate the capabilities of various quasi-3D setups and to optimise quasi-3D imaging for permafrost related problems in numerical simulations. The purpose was to achieve best agreement between model resolution and efficiency of data acquisition through creating a series of synthetic quasi-3D images to test the effect of array type, electrode and line spacing as well as the relevance of perpendicular tie lines.

The main focus was on the efficacy of different grid setups for (i) correctly imaging the modelled high-resistivity structures and resistivity values (ii), respectively, but also for detecting (iii) active layer thickness and (iv) location of the permafrost base. The accurate reproduction of subsurface resistivity values and resistivity contrasts was analysed in terms of the interpretability of high-resistivity structures and the possibility of a quantitative interpretation approach (e.g. ice content, temperature). In addition, the effects of applying different inversion parameters to the synthetic models with

special focus on the convergence criterion on the inversion result were tested. To test the assumptions drawn from synthetic modelling a case study presenting results from quasi-3D measurements at the Val Susauna study site. The results of the case study presented in this chapter focus on the applicability and explanatory power of quasi-3D imaging supplemental to the approach of numerical modelling. A circumstantial analysis of results from quasi-3D imaging in the Val Susauna is given in CHAPTER 6.

5.1 Methodological approach

For optimising quasi-3D ERT to permafrost-related problems the approach of the back-and-forth interpretation procedure (for details on forward and inverse modelling see FORTIER et al. (2008) and CHAPTER 2.1.1.5) was adapted to quasi-3D resistivity imaging, to test the effect of different set ups of orthogonal 2D ERT surveys (array type, electrode spacing, line spacing, number of perpendicular tie lines) on the quality and interpretability of the resulting quasi-3D image and the ability to detect high-resistivity structures.

5.1.1 Synthetic 3D subsurface model and grid arrangement

A geocryologic subsurface model was generated (FIGURE 5.1), based on analysis of numerous ERT surveys measured at mountain sites with permafrost (KNEISEL, 2004; KNEISEL et al., 2000b; KNEISEL & SCHWINDT, 2008; SCHWINDT & KNEISEL, 2010). This model tries to reproduce the small-scale subsurface heterogeneity, with frozen and unfrozen material and varying ground ice characteristics (ice/liquid water content) of mountain permafrost sites. High-resistivity bodies (30 - 170 kΩm) are embedded in a matrix of 2kΩm, representing coarse grained talus material and 0.5 kΩm for the finer grained material at the foot of the slope. Modelled structures vary in dimension size, with an active layer thickness of 2 m, and a ground ice base between 5 and 10 m depth assumed for the geocryologic model. All modelled high-resistivity structures are located in the lower half of the grid, typical for permafrost settings in talus slopes below the timberline, where the permafrost bodies are usually located towards the foot of the slope.

In order to map frozen ground occurrences using 2D and 3D ERT compromises have to be made regarding the choice of electrode spacing and array type. Besides information on ice characteristics, factors of interest are the areal distribution, active layer thickness and location of the permafrost base. While small spacings (< 2 m) have advantages in illustrating the active layer, spacings of ≥ 2 m are favourable for detecting permafrost thickness and for mapping larger areas. The choice of array type at mountain permafrost sites is often a trade-off between resolution and robustness, as achieving an optimal

electrode coupling can be challenging. Regarding error proneness the robust Wenner and Wenner-Schlumberger arrays provide more stable resistivity data (e.g. KRAUTBLATTER & VERLEYSDONK, 2008) and yield higher signal to noise ratios (e.g. HAUCK & VONDER MÜHLL, 2003b) compared to the dipole-dipole array. However, while Wenner and Wenner-Schlumberger (hybrid between Wenner and Schlumberger) arrays have slight advantages in delineating horizontal structures (permafrost base and table) the dipole-dipole array is sensitive to both, horizontal and vertical changes in resistivity (e.g. FORTIER et al., 2008; KNÖDEL et al., 2005; LOKE & BARKER, 1995; MARESCOT et al., 2003).

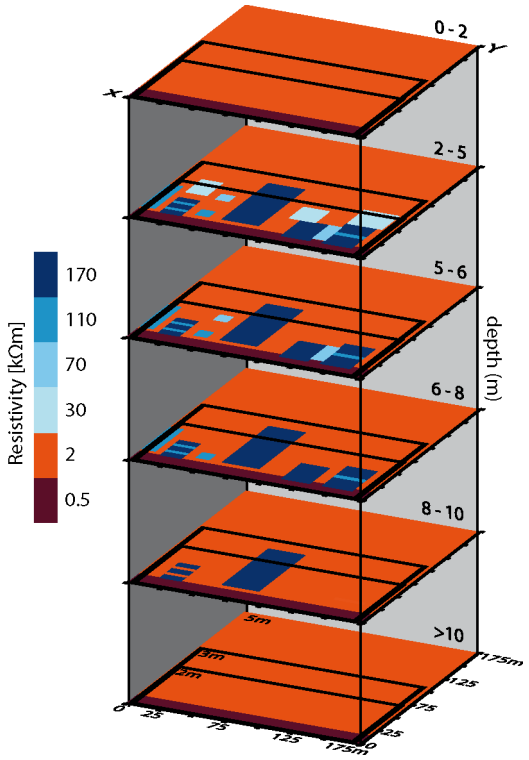

Figure 5.1: Geocryologic model of subsurface resistivity distribution for forward modelling. Dimension size is variable according to the applied electrode spacing (5m electrode spacing covers the whole model, grid size for 2m and 3m electrode spacing is given by the black squares). Grid size in y-direction for each different setup is based on the assumption of using 36 electrodes per array. Maximum grid size in x-direction is predefined by the geocryologic model.

The spatial extend of a quasi-3D measurement in the field is limited by electrode spacing and number of electrodes per 2D array, but can be extended using a roll-along technique (LOKE, 2010). For creating the initial models, 2D arrays with 36 electrodes and 2 m, 3 m and 5 m electrode spacing were used for the arrays in y-direction. The grid-size in x-direction was predefined by the size of the geocryologic model. Array length and

number of electrodes were adjusted for each of the applied electrode spacings to fit the grid size of the geocryologic model in x-direction. To achieve an even array length in relation to the number of electrodes grid size in x-direction slightly differs between 2 m, 3 m, and 5 m arrays. Dimension parameters of the different setups are given in TABLE 5.1 (see also geocryologic model in FIGURE 5.1).

Table 5.1: Dimension parameters of synthetic grid setups for double, triple and quadruple line spacing, 2, 3 and 5 m electrode spacing and the array types Wenner, Wenner-Schlumberger and dipole-dipole

		grid size (m)	# of Lines		# of electrodes	# of datum points		
			x	y		Wenner	Wenner-Schlumberger	dipole-dipole
double	2m	168 x 72	17	42	2124	24500	30320	37400
	3m	168 x 105	17	28	1620	14112	18672	24072
	5m	175 x 175	17	18	1260	6930	10080	14280
triple	2m	168 x 72	11	28	1404	16016	19856	24536
	3m	168 x 105	12	19	1116	9810	12960	16680
	5m	175 x 175	12	12	864	4752	6912	9792
quadruple	2m	168 x 72	9	21	1080	12726	15696	19296
	3m	168 x 105	9	15	864	7506	9936	12816
	5m	175 x 175	8	9	612	3366	4896	6936

5.1.2 Quasi-3D data processing and inversion

A total of 96 quasi-3D models were created using a number of synthetic 2D arrays testing the influence of electrode- (in-line) spacing (2 m, 3 m and 5 m), line-spacing between adjacent arrays (double, triple and quadruple electrode spacing), number and orientation of lines in y- and x-directions (cf. FIGURE 5.2) and choice of array type (Wenner, Wenner-Schlumberger, dipole-dipole) on the inversion results. To test the horizontal and vertical model resolution as well as the reproduction of default resistivity values (CHAPTERS 5.2.1, 5.2.2 & 5.2.3) setups with a full xy-grid were used, i.e. the distance between parallel lines in x- and y- direction being twice the applied electrode spacing. To increase the efficiency of quasi-3D measurements (CHAPTER 5.2.4) the number of 2D sections building up the model has been decreased by decreasing the number of perpendicular tie lines, the arrays in x-direction. Numbers of lines in x-direction were first reduced by half, implementing solely every second tie line into the

model (complete Y / half X grid). A second series of quasi-3D models was created using no tie lines at all (complete Y grid). The numbers of arrays in y-direction was kept constant according to the applied parallel line spacing. FIGURE 5.2 presents the series of synthetic quasi-3D models created for a unit electrode spacing of 3 m.

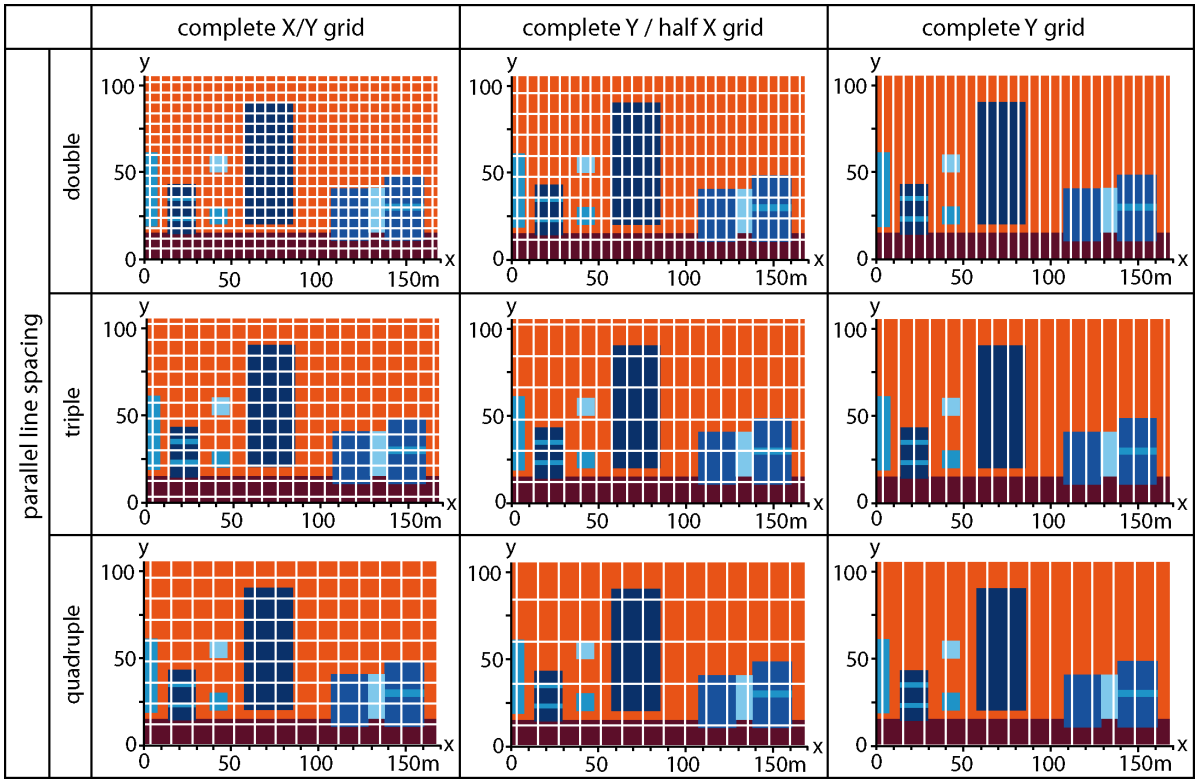

Figure 5.2: Modelled grid setups, exemplified using an electrode spacing of 3m. Parallel line spacing is based on the applied electrode spacing with double, triple and quadruple value. For testing the influence of minimising the number of arrays included in each model, distance between adjacent arrays is enlarged, using double, triple and quadruple electrode spacing. To test the importance of perpendicular tie lines, synthetic models were created with a complete x/y-grid, with a reduced number of lines in x-direction and without tie lines.

The software package RES2DMOD (LOKE, 2002) was used for specifying subsurface resistivity values for each 2D section according to the geocryologic model. Corresponding apparent resistivity pseudosections were calculated using the finite-difference method (DEY & MORRISON, 1979; LOKE, 1994) for the array types Wenner, Wenner-Schlumberger and dipole-dipole. A relatively low amount of random noise (3%) was added to each synthetic 2D array. Tests were conducted using different noise ensembles with 3, 5 and 8% of random noise for the different data sets.

Each of the 96 quasi-3D datasets was created by collating a number of synthetic 2D sections (TABLE 5.1) using RES2DINV (LOKE, 2010). Within RES3DINV (LOKE, 2010) the datasets were inverted using a true three dimensional inversion algorithm, that allows the model resistivity values to vary in all three dimensions. To preclude smoothing of sharp resistivity boundaries robust inversion (L1 norm) was applied (LOKE et al., 2003). The datasets were inverted using 5 iterations and only minor modifications on the standard inversion settings given by RES3DINV, with small damping factors (initial value for $\lambda = 0.1$) to obtain a high data consistency of the model. For achieving a reasonable computing time the Incomplete Gauss-Newton optimisation method (LOKE & DAHLIN, 2002) with high accuracy of 1% (referring to the convergence limit used in the incomplete Gauss-Newton method that calculates the approximate solution of the least-squares method) was applied. To provide better resolution, width and thickness of the model blocks of the top few layers were divided in half.

5.2 Results from synthetic modelling

5.2.1 Horizontal model resolution

To test the horizontal resolution of the different setups (FIGURE 5.3), the depth slices between 3 m and 5 m depth were compared for all configurations using a complete x/y grid (Wenner, Wenner-Schlumberger and dipole-dipole arrays with 2 m, 3 m, 5 m electrode spacing and double, triple and quadruple line spacing). At this depth level, all modelled resistivity structures of the geocryologic model were represented. With regard to array length and model cell size the quasi-3D images differ in size and depth of the slices for varying electrode spacing (3 – 4 m depth for 2 m and 3 m, 3.5 – 5 m for 5 m electrode spacing). While all quasi-3D models were inverted using 5 iterations, the third iteration was chosen as the best agreement to the geocryologic model.

All setups were able to detect the main high-resistivity structures, but there were strong differences in their ability to correctly reproduce size and default resistivity values of the structures as well as the resistivity contrasts to the matrix. As expected, the dipole-dipole array had a higher accuracy in horizontal resolution in all configurations compared to the Wenner and Wenner-Schlumberger arrays. Best agreement between inverted and geocryologic model was for the 2 m and 3 m dipole-dipole models, where even the use of quadruple line spacing provided better results than the setups using Wenner and Wenner-Schlumberger configurations. However, good results were achieved using Wenner and Wenner-Schlumberger arrays with an electrode spacing of 2 m (for all grid setups) and 3 m (double and triple line spacing) even though the contrast between high-resistivity features and the matrix was less sharp than for the dipole-dipole arrays. Nonetheless, differences between Wenner and Wenner-Schlumberger arrays were surprisingly marginal considering the considerably higher number of datum points for the Wenner-Schlumberger array (TABLE 5.1).

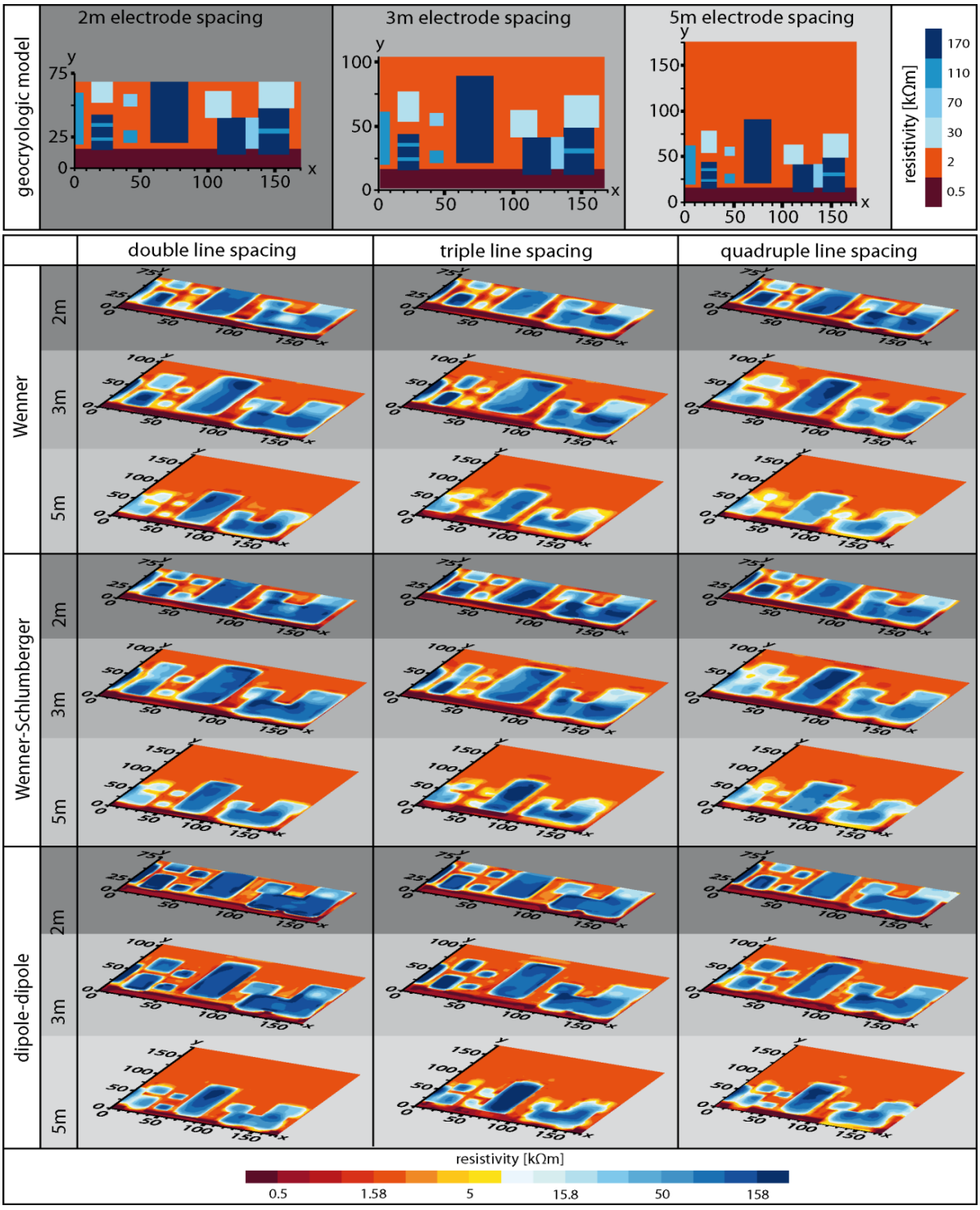

Figure 5.3: Lateral resolution of different setups in comparison to the geocryologic model. Presented are the depth slices between 3 and 4 m depths (grid setups using 2 and 3 m unit electrode spacing) and 3.5 - 5 m depths (5 m unit electrode spacing)

The main weakness for both arrays was in illustrating small resistive bodies in close distance in the left part of the quasi-3D images. While the 2 m as well as the 3 m arrays with double and triple line spacing were able to differentiate between the anomalies –

even though boundaries were blurry – the anomalies merged in the 3 m quadruple and the 5 m models. Large and isolated resistive bodies are well imaged for the 5 m-arrays but especially small structures in close distance tend to blur together (FIGURE 5.3; x-direction 0 m – 40 m). The two small anomalies between meters 40 and 50 in x-direction (10 x 10 m each) were clearly underestimated in size and resistivity value for the 5 m Wenner and Wenner-Schlumberger arrays. These effects were also visible, even though less pronounced, for the 5 m dipole-dipole arrays.

5.2.2 Vertical model resolution

Knowledge of the ability of different setups to resolve vertical structures is of great interest in permafrost studies to enhance the interpretability of geophysical data concerning the location of permafrost base and table. To test the vertical model resolution a set of depth slices along the XZ-plane was chosen exemplarily for the Wenner and dipole-dipole array comparing 2 and 3 m electrode spacing using triple line spacing and a complete x/y grid (XZ-Plane 1 and 2 in FIGURE 5.4). For a better quantification and comparability of vertical resistivity distribution virtual boreholes of subsurface resistivity values were created at three representative positions (VB1, 2 and 3 in FIGURE 5.4) for the Wenner and dipole-dipole array (2, 3 and 5 m electrode spacing, triple line spacing). Three representative locations were chosen for the virtual boreholes considering anomaly thickness (3, 4 and 8 m) and horizontal extent as well as default resistivity values (30 kΩm, 70 kΩm and 170 kΩm). Dimension sizes of the resistive blocks, as given by the geocryologic model, as well as the position of the virtual boreholes are marked in the XZ-slices. Due to limited space and no considerable advantages regarding data quality in comparison to the Wenner array, the Wenner-Schlumberger array was neglected for this section.

In terms of the ability to detect the top of resistive structures all the setups presented here produced good results. The top of the anomalies show a sharp transition to the conductive matrix above as given in the geocryologic model. The impact of resistivity gradients between anomaly and matrix on boundary conditions (cf. XZ-planes 1 & 2 and the virtual boreholes in FIGURE 5.4) was comparably low. In contrast, detection of

the base of resistive bodies was less consistent for the different setups and appears to be influenced by dimensions as well as resistivity values of the structures.

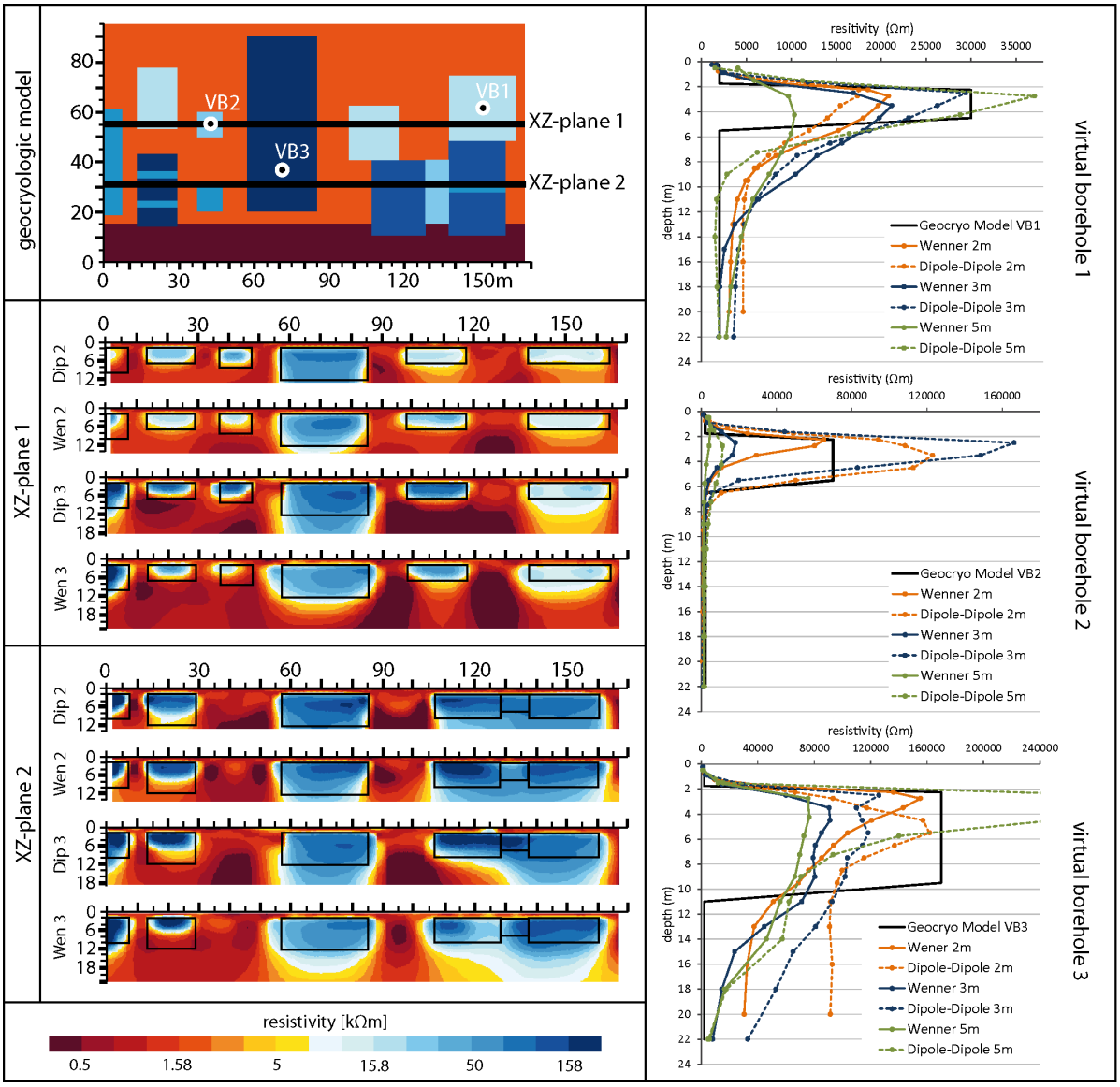

Figure 5.4: Vertical model resolution, i.e. detection of the top and base of resistive structures. 2D slices in xz-direction (location is marked in the geocryologic model on top of the figure) are compared for the array types Wenner and dipole-dipole (2m and 3m electrode spacing). Default dimension size of the resistive structures is given by the black rectangles. Three virtual boreholes (VB 1-3; marked by white dots) present the vertical resistivity distribution for all grid setups in comparison to default values of the geocryologic model (resistivity-scale is adjusted for each virtual borehole).

While all arrays produced good results in detecting the dimension size of shallow structures weaknesses are visible for resistive bodies with thicknesses of more than 6 m (base at 8 -10 m depth). Especially in the case of large structures (width > 20 m) the thickness is clearly overestimated (cf. VB3). The degree of overestimation is higher for

the dipole-dipole array and for small electrode spacings in comparison to the Wenner array and electrode spacings of ≥ 3 m. In case of the small structure (10 x 10 x 4 m, 70 kΩm) investigated in VB2 the dipole-dipole array provided better results than the Wenner array which underestimated structure size and resistivity for the arrays using 2 and 3 m electrode spacing. In comparison, the dipole-dipole arrays overestimated resistivity values by 50 kΩm (2 m electrode spacing) and 95 kΩm, respectively. Using 5 m electrode spacing the structure was clearly underestimated in size and resistivity (cf. VB2 and FIGURE 5.3).

The lowest resistivity (30 kΩm) was given in the geocryologic model for VB 1 (dimension size: 22 x 22 x 3 m). Reasonable results in relation to the structure's thickness were provided by the arrays using 2 and 3 m electrode spacings. Compared to the top of the anomaly the boundary at its base is less distinct with gradually sinking resistivities. Best results were provided by the Wenner and dipole-dipole arrays using 2m electrode spacing.

5.2.3 Reproduction of default resistivity values

The ability to reproduce default resistivity values appears to be a main weakness of all quasi-3D models calculated for this study. Comparing results presented in FIGURE 5.3 and figure 5.4 with special focus on the virtual boreholes in FIGURE 5.4 all quasi-3D setups show inconsistencies in correctly reproducing resistivity values of modelled anomalies. Except for areas below high resistivity anomalies, reasonable results were achieved regarding resistivity values of the matrix. For specific setups, no explicit tendencies in reproducing default resistivity values were evident. High-resistivity anomalies (170 kΩm, cf. VB3 in FIGURE 5.4) were underestimated by almost all arrays. Underestimation of calculated resistivity values ranged between ~50% (Wenner 3 and 5 m electrode spacing) and ~6% (Wenner and dipole-dipole, 2 m electrode spacing). In contrast, the dipole-dipole setup with 5 m electrode spacing overestimated the resistivity by ~200%. The same variability is visible for anomalies with specified low (30 kΩm) and intermediate (70 kΩm) resistivity values. Extremely divergent results were produced for the small structure represented in VB2 by the Wenner and dipole-dipole grids using 3 m electrode spacing. While values were underestimated for the Wenner setup by 74%, resistivity was overestimated by 137% for the dipole-dipole grid.

In general, resistivity values were underestimated by all of the arrays with a high variability in the degree of underestimation. Especially in the case of small resistive structures (VB2 in FIGURE 5.4) the degree of underestimation increased with the application of larger electrode and line spacing (cf. FIGURE 5.3). In contrast, the dipole-dipole setups tended to overestimate resistivities for structures with low and intermediate resistivity values, resulting in almost homogenous resistivity conditions for all modelled structures (FIGURE 5.3), complicating differentiation and interpretation of resistive anomalies.

5.2.4 Approach to increase the efficiency of quasi-3D data acquisition

Depending on grid size and site characteristics the application of quasi-3D measurements can be challenging and time consuming in mountain environments. To optimise the efficiency of measurements synthetic quasi-3D models were created with a stepwise decrease in the number of 2D arrays building up the model (cf. FIGURE 5.2) generated by enlarging the parallel line spacing (double, triple, quadruple electrode spacing) and by reducing the number of perpendicular tie lines in the x-direction (half grid; no lines in x-direction). Due to limited space and low variations between Wenner and Wenner-Schlumberger setups results are presented for the Wenner and dipole-dipole arrays only (FIGURE 5.5).

The results underline the importance of using perpendicular tie lines. Good results were generated by all array types by reducing the number of tie lines by half, using 2m and, in some cases, 3m electrode spacing. In comparison, the geocryologic model was not well reproduced in the synthetic models using only y-lines. Resistive structures were elongated in x-direction with almost seamless transitions between adjacent bodies. The application of 5 m electrode spacing only yielded acceptable results for the dipole-dipole array using double line spacing (cf. FIGURE 5.5). For all array types, the quality of results further debased, when the number of tie lines was reduced. Using larger line spacings boundaries of resistive bodies were blurred and not clearly definable and small structures are faded.

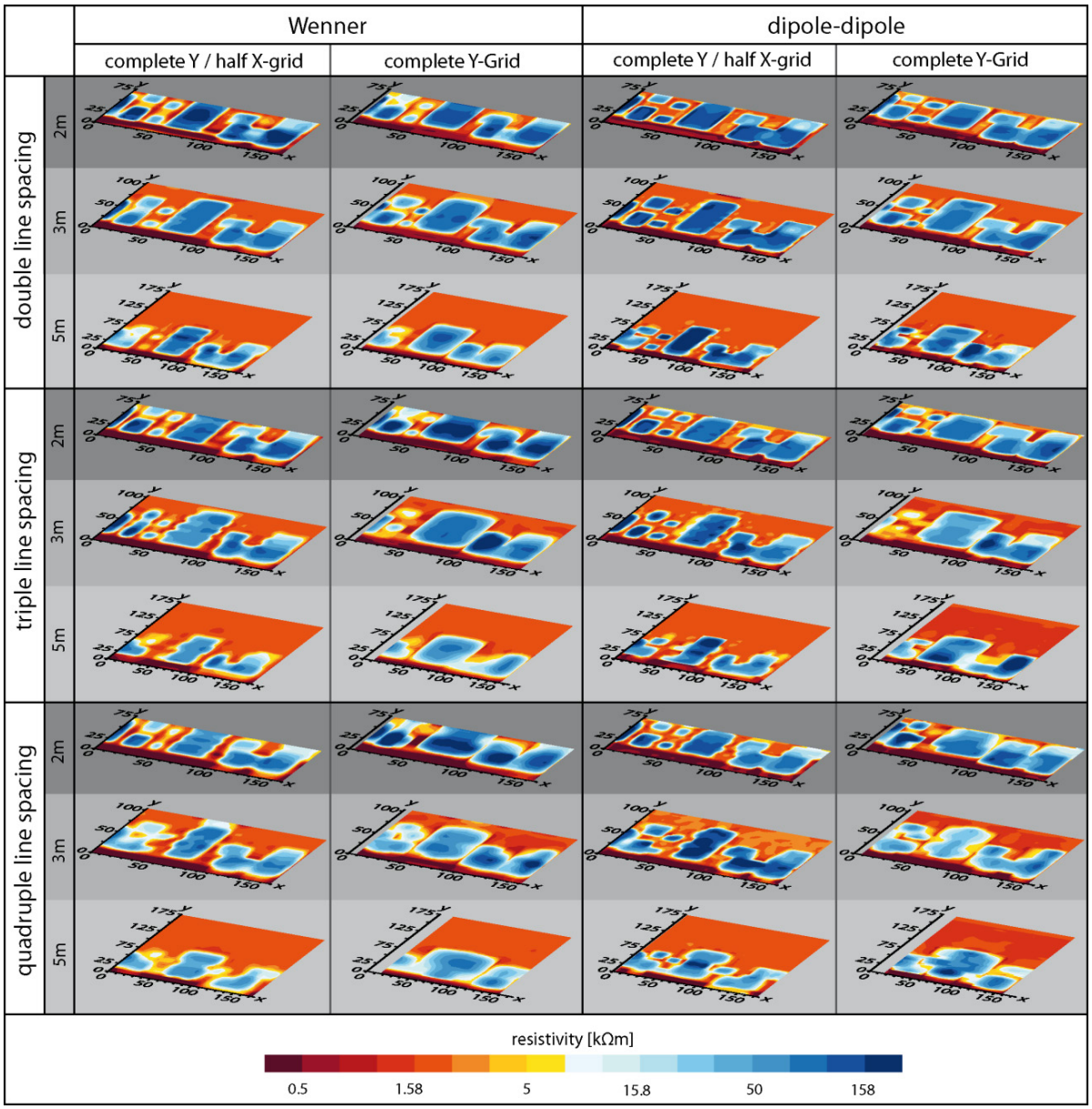

Figure 5.5: Effect of reduced number of 2D-arrays per quasi-3D grid on data quality and model resolution exemplarily for depth slices between 3m and 5m depth comparing Wenner and dipole-dipole array types.

Regarding the trade-off between data quality and efficiency of measurements, good results were achieved using triple line spacing. In the case of 2 m-arrays, the loss in quality of the quasi-3D image in comparison to the application of double line spacing and a full x/y-grid (FIGURE 5.3) was negligible. The 3 m grid was capable of correctly detecting most structures. Only in the case of the large resistive structure in the centre of the quasi-3D image boundaries were ragged for both Wenner and dipole-dipole array.

5.2.5 Convergence criterion

"Choice of the correct iteration is of great importance for the interpretation of ERT-datasets, as a large number of iterations will tend to overfit data, such that artefacts will result from inversions of the data errors. A small RMS-error does not necessarily correspond to realistic model results" (HAUCK & VONDER MÜHLL, 2003b). For the inversion of synthetic datasets in this study, the iteration process was terminated after 5 iterations. In the case of synthetic modelling the choice of iteration was based on the best agreement between the inverted and geocryologic model, an approach that is not applicable for measured data.

The effect of a prolonged iteration process is shown in FIGURE 5.6. Presented are all iterations for two depth levels compared to the geocryologic model. The aim was to quantify alterations in shallow depths with default homogenous, low resistive conditions ("active layer") and in high-resistivity bodies located in deeper layers during the iteration process. Resistivity values were extracted and averaged from two depth layers for three defined areas in the depth level between 4 and 5 m and their corresponding blocks in shallow depth (cf. Blocks 1-3 in FIGURE 5.6). One large high-resistive area (170 kΩm; Block 1), one small area with lower resistivity values (30 kΩm; Block 2) and Block 3, which represents matrix material with lowest values (2 kΩm), were chosen.

Best agreement between initial and inverted model was accomplished by the third iteration, even though the RMS-error still decreased by almost 4% towards the fifth iteration. While changes in the resistive structures of depth level 6 were marginal for the fourth and fifth iterations and lead to no improvement of the model, banding effects occurred in depth level 2. These artefacts clearly correspond to the resistive structures below. Averaged resistivity values of Block 1 (Level 2) increase drastically between the third and fifth iterations. This effect was visible but not as pronounced for Block 2. In contrast, both depth levels of Block 3 show a similar, constant trend with no artefacts accruing throughout the iteration process. Scattered structures occurring above high-resistivity structures during a prolonged iteration process can significantly influence the interpretation, especially in view of active layer thickness/permafrost table, but could also be interpreted as a result of bad electrode coupling.

The increase in resistivity values for Blocks 1 and 2 (Level 6) was highest between the first and third iterations. While values for Block 3 (Level 6) were close to the default

resistivity values (30 kΩm) for iteration 3 and 4 they decreased by almost 10kΩm towards the fifth iteration. In contrast, resistivity values increased slightly between the third and fifth iterations after an exponential increase between the first and third for Block 1 (Level 6) with maximum resistivity values far below default values. Results of HAUCK and VONDER MÜHLL (2003b), who showed that especially large resistivity contrast tends to be increased from one iteration to the next without a significant change of the RMS error cannot be confirmed for the quasi-3D case, at least not for the first 5 iterations.

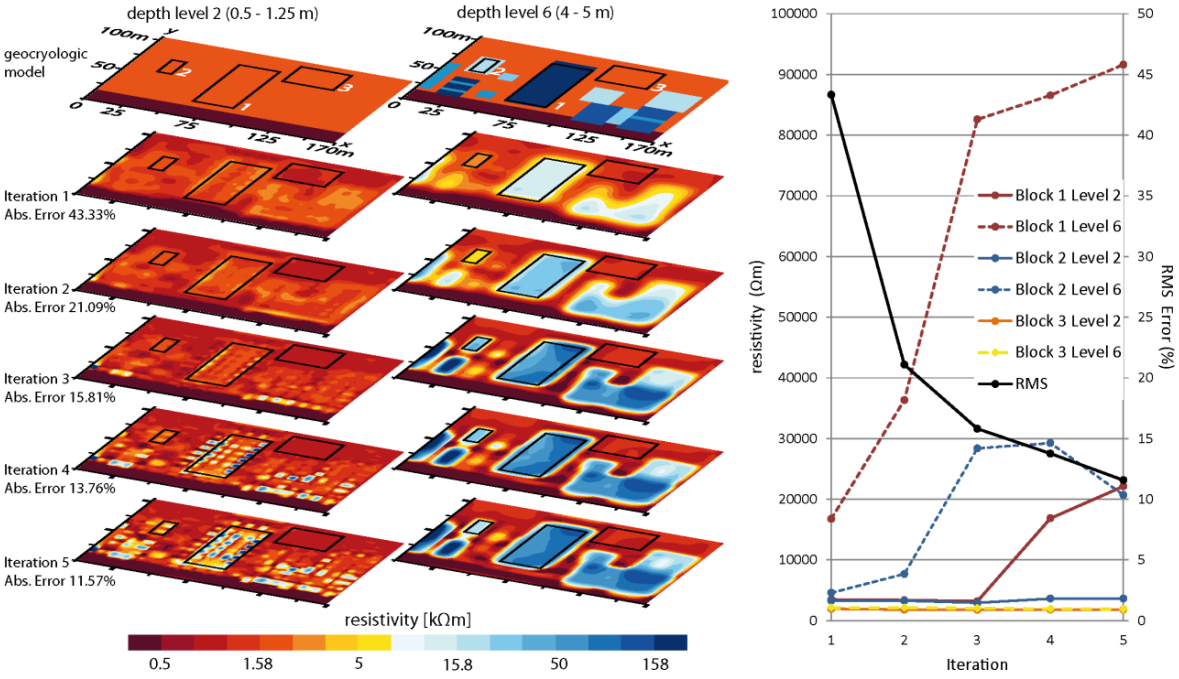

Figure 5.6: Response of iterative process on resistivity distribution and RMS error in two depth layers of an exemplarily chosen quasi-3D model (Wenner array, 3m electrode spacing, triple line spacing). Resistivities shown in the diagram represent averaged values for three blocks (locations are marked in the depth slices) of the depth layers 2 (0.5 m-1 m) and 6 (4 m-5 m) in comparison to the RMS error.

5.3 Case study – quasi-3D ERT Val Susauna

Presented are the results from quasi-3D imaging at the Val Susauna study site. Investigated was the lower part of the steep talus slope ranging between 1683 m and 1720 m a.s.l. where the dolomitic talus material is covered by a thick humus layer of up to 60 cm thickness. The study site in the Val Susauna constitutes a representative site for testing the application of quasi-3D imaging at a permafrost site. Excellent electrode coupling due to the conductive moss/humus layer provided high data quality, low noise ratios and therefore an optimal reliability and interpretability of measured data.

5.3.1 Methodological approach

In the summer of 2009 a quasi-3D grid was mapped out consisting of 12 2D arrays measured vertically to the scree slope (Y-direction) and 5 perpendicular arrays (x-direction) covering the central part of the study site. The grid was extended by another 7 profiles in y-direction in the summer of 2010 (cf. FIGURE 5.7). For data acquisition a Syscal Junior Switch resistivity meter (IRIS Instruments) was used, with 36 electrodes per array and an electrode spacing of 2 m resulting in an array length of 70 m. Triple electrode spacing (6 m line spacing) was used for parallel profiles in y-direction and 10 m line spacing for profiles in x-direction. Both, dipole-dipole and Wenner arrays were applied. Topographical information for each electrode position was gathered by recording the absolute elevation for each 2D array (details on general methodology are given in CHAPTER 2.1.1).

As described in CHAPTER 2.1.1.1, the 2D arrays were collated to a quasi-3D dataset and inverted using a true 3D inversion algorithm within RES2DINV/RES3DINV (LOKE, 2010). In contrast to the synthetic datasets, inversion parameters were adjusted for the data measured in the field. Banding effects were reduced by using a slightly higher initial damping factor ($\lambda = 0.15$) for the topmost layers and by applying a diagonal roughness filter (FARQUHARSON, 2008). The diagonal component reduced the tendency of the normal horizontal roughness filter to produce structures aligned along the x and y directions (LOKE, 2010). Width and thickness of the model blocks of the top few layers were divided in half to provide better resolution. The finite-element method (SILVESTER & FERRARI, 1996) was used, which is preferable for datasets containing topographical

information. As for the synthetic data, the Incomplete Gauss-Newton optimisation method with an accuracy of 1% was applied. To preclude smoothing of sharp resistivity boundaries robust inversion was applied.

Three quasi-3D models were inverted. Besides the Wenner and the dipole-dipole array, the third model was based on the inversion of a dataset created by merging the Wenner and dipole-dipole measurements into one file. This approach tries to combine advantages of both arrays, i.e. the lateral resolution of the dipole-dipole array with the low error-proneness and vertical resolution of the Wenner array.

5.3.2 Results of the case study

Presented are quasi-3D images of the Wenner and dipole-dipole array as well as the combined inversion of both datasets (FIGURE 5.7). Results of the different array types differ marginally with regard to a qualitative interpretation.

Compared to the dipole-dipole and the combined inversion of both datasets the Wenner setup produced a smoother subsurface model. Especially in shallow depth, slightly noisier data are produced by the dipole-dipole and combined Wenner/dipole arrangements. All setups showed a clearly definable high-resistivity anomaly in the centre of the models between 1.5 and 7 m depth that is divided into two main structures by an area with slightly lower resistivity values. A sharp transition to low resistive material towards the foot of the slope (0 - 10m in y-direction) but slowly decreasing resistivity values uphill are visible. The top of the structure is clearly differentiated from the low resistive material above. In comparison, the base of the structure is less clearly defined. Between 6 and 10 m depth, resistivity values slowly decrease. The resistive body is thicker for the dipole-dipole

A small structure is visible in the top three layers for all arrays (x-direction 30-40 m; y-direction 10-30 m), with slightly higher resistivity values. Unlike the largest parts of the investigated talus slope, this area was not covered by a conductive moss/humus layer. Due to air cavities, resistivity of the dolomitic material was much higher in comparison to the – up to 70 cm thick – humus/moss cover. Between 0-30 m (x-direction) an area with low resistivities was detected by all arrays, which corresponds to an area of finer grained material.

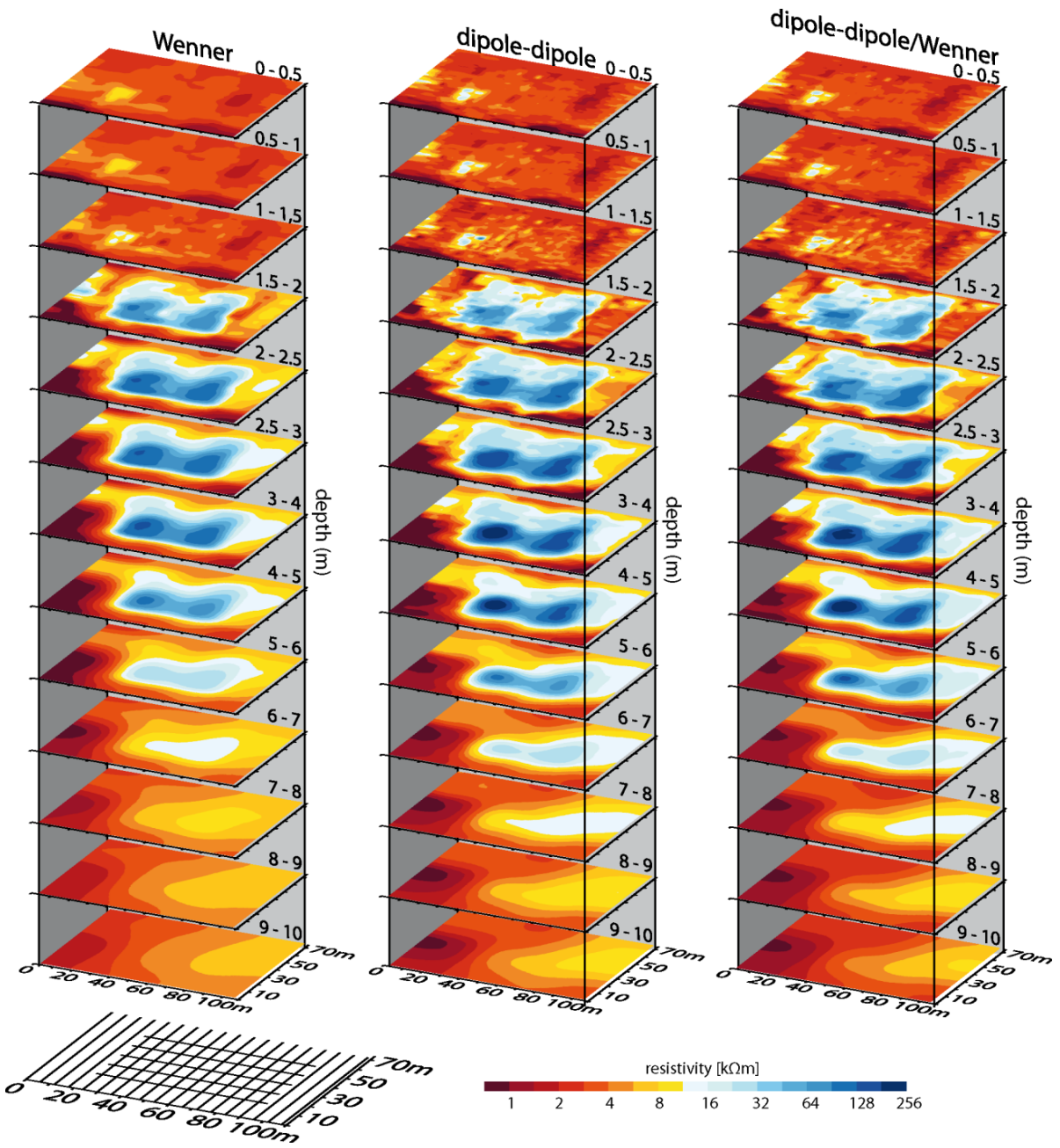

Figure 5.7: Depth slices of the quasi-3D image measured in the Val Susauna for the array types Wenner, dipole-dipole and an inversion of a collated dataset of both arrays as well as the line arrangement for the setups.

While all setups produced good results and coincided well regarding delimitation as well as the qualitative detection of surface and subsurface structures, a quantitative interpretation with regard to ice content and temperature, without the application of additional methods, is questionable. Resistivity values differed strongly between the Wenner and the dipole-dipole setups, with higher values for the latter. The combined inversion of the Wenner and dipole-dipole dataset produced even higher values. A virtual

borehole (FIGURE 5.8) was created to compare the data of the quasi-3D model with the measured 2D datasets at a crossing point.

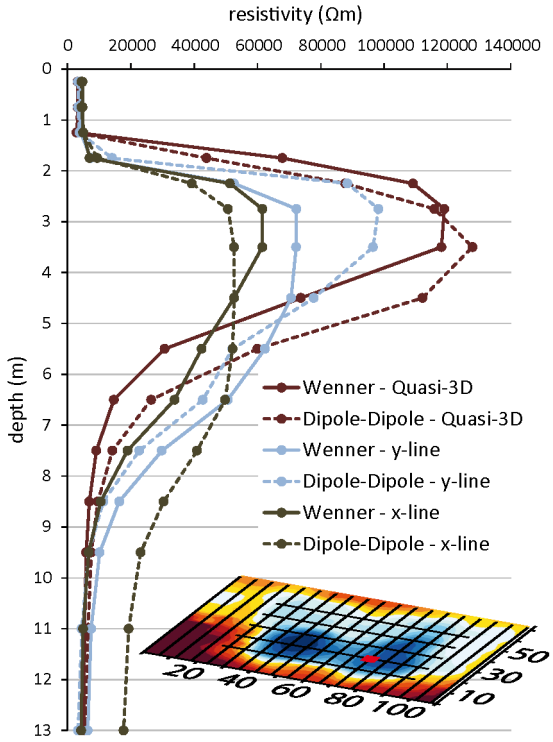

Figure 5.8: Virtual borehole of resistivity values at Val Susauna (location is given by the red dot in the grid setup, depth of the slice is 2.5 – 3 m of the combined dipole-dipole/Wenner quasi-3D image) comparing resistivity values of 2D-arrays measured in x- and y- direction with values of the quasi-3D image for the array types Wenner and dipole-dipole. Unit electrode spacing is 2 m.

Surprisingly, maximum resistivities of the quasi-3D models were markedly higher than values obtained from the inverted 2D arrays at the selected crossing point (cf. FIGURE 5.8). Significant differences were visible between the applied array types, but also between the longitudinal profile (measured in y direction vertical to the slope) and the perpendicular crossing profile. A comparison of the array types demonstrated that maximum values of the dipole-dipole array for the longitudinal profile were higher by 26 kΩm than results of the Wenner measurement. Results of the dipole-dipole array measured in cross direction were about 11 kΩm lower than data of the Wenner array for the same layout. Maximum resistivities were higher for the longitudinal profiles than for the cross profiles, with a larger gap between dipole-dipole measurements (48 kΩm) compared to the Wenner datasets (11 kΩm).

Besides maximum resistivity values the graphs show differences between 2D and 3D inversions in terms of location of the top and base as well as the internal characteristics of the high resistive structure. Despite of the top of the anomaly being slightly shallower the high resistive body is much more clearly delineated in the 3D inversion compared to the 2D data, which do not depict the base of the anomaly as sharply. With almost constant resistivity values the longitudinal Wenner array and the perpendicular dipole-dipole array point to homogenous ground ice conditions between a depth of ~2.5m and ~6.5m. In contrast, all other measurements show maximum resistivities at around 3m depth, decreasing strongly to values around 10 kΩm to 15 kΩm between 6 and 8 m depth. Location and characteristics of the base of the resistive anomaly are not clearly definable, as results are inconsistent for different inversions.

5.4 Discussion

Results provided by this study show that quasi-3D ERT is a valuable tool for ground ice related problems, with high potential for permafrost mapping. The resolution power of quasi-3D surveys is a function of array type electrode spacing and line spacing as well as the relative size, depth and location of the anomalous bodies with respect to the ERT lines (Gharibi & Bentley, 2005). In contrast to the established fields of application such as environmental (Bentley & Gharibi, 2004) or archaeological (Papadopoulos et al., 2007) studies quasi-3D imaging at mountain permafrost sites constitutes additional challenges due to the often demanding surface characteristics. A trade-off between resolution and efficiency of measurements is of fundamental interest for optimising the application in terms of time- and cost-efficiency.

Good results were provided by setups consisting of 2D arrays with 2 and 3 m electrode spacings. Even with a massive reduction in the number of arrays per grid, reasonable results were achieved regarding the horizontal and vertical model resolution. Best agreement for setups with enlarged line spacing was provided by using triple electrode spacing for adjacent profiles. A further enlargement to quadruple electrode spacing can only be recommended for setups using 2 m electrode spacing and, ideally choosing the dipole-dipole array. Further optimisation can be achieved by reducing the number of perpendicular tie lines. As shown in Figure 5.5 the reduction of tie lines by half provides results comparable to the full x/y-grid, with best results for 2m electrode spacing.

Nonetheless, site characteristics and objectives of the study are fundamental to the setup of quasi-3D grids. Grid setups using electrode spacings of less than 1 m are not suitable for most permafrost studies, due to the particularly small grid size and shallow depth of investigation, but might be favourable for detecting areal variations in active layer thickness. While the application of electrode spacings > 3 m have proven to be incapable of detecting small-scale changes in the subsurface (cf. Figure 5.4 & Figure 5.5), it might be useful for obtaining a rough overview of frozen ground distribution over a comparably large area and, in some cases, for achieving a higher sounding depth.

Using electrode spacings ≤ 1 m and single line spacing – meaning line spacing is equal to electrode spacing – Papadopoulos et al. (2006) stated that measurements in only one direction are adequate for producing a valid three-dimensional subsurface image. It

is questionable, if a quasi-3D image consisting of only parallel arrays (with line spacing larger than electrode spacing) is capable of reliably reproducing the three dimensional subsurface heterogeneity. As presented in FIGURE 5.5, the lack of perpendicular measurements results in contortions, as well as broadening of structures perpendicular to the line direction, and partially small structures are not detected. The application of perpendicular tie lines has two advantages. (1) To some degree, it is a matter of coincidence if a structure of interest is covered by a single 2D array or if it is situated between two adjacent lines. As it is not appropriate to base a measurement on coincidence, this factor can be reduced by minimising the line spacing or by perpendicular measurements that record subsurface conditions between adjacent lines. (2) Block size of the quasi-3D subsurface model depends on electrode spacing and parallel line spacing. Applying 2 m electrode spacing and 6 m line spacing, with no perpendicular tie lines, results in a model block size of 2 m x 6 m. By using tie lines, model block dimension in cross direction is not based on line spacing but on electrode spacing of perpendicular tie lines, resulting in a block size of 2 x 2 m. As a result, additional information on the subsurface is gained and resolution of the subsurface model is optimised.

The grid setup of the field example (FIGURE 5.7) constitutes a further trade-off for minimising the number of 2D arrays. This optimisation was based on knowledge of site characteristics and single 2D-measurements (ERT, SRT) applied in advance. Perpendicular profiles were arranged in the centre of the grid, where highest model resolution was of interest for a spatial characterisation of the subsurface resistivity distribution. Of less than 8 m the ground ice thickness at this site was quite low (cf. FIGURE 5.7). In this case, the applied electrode spacing of 2 m was capable of providing reliable results in detecting the base of the high resistive anomaly, as shown by forward modelling (FIGURE 5.4). Interpretation of the vertical extent of resistive structures posed a further challenge, as it is a function of the chosen array type, applied electrode spacing as well as the dimension size and resistivity contrast to the matrix. Results are more reliable for small structures and comparably low resistivity contrasts. Reliability on the thickness of structures decreased the closer the lower boundary of resistive structures was to the penetration depth of certain ERT setups (cf. FIGURE 5.4). Application of the depth of investigation (DOI) index method (BARKER, 1989; MARESCOT et al., 2003) on quasi-3D datasets would be a further step for verifying the quality of measurements and

for preventing misinterpretations of inversion results, as well as promoting reliability of resistivity values.

Another compromise for quasi-3D applications is the choice of array type – robustness against resolution power – an important question at sites with often demanding electrode coupling. Results presented in this study showed that – in consideration of the applied electrode spacing – all arrays compared (Wenner, Wenner-Schlumberger, dipole-dipole) were capable of detecting small scale resistivity variability in the subsurface (cf. FIGURE 5.3 & FIGURE 5.5) with mostly better results for the dipole-dipole array and negligible differences between Wenner and Wenner-Schlumberger arrays. In particular, the reproduction of boundary conditions was favourable for the dipole-dipole array. Even though the sharp contrasts given by the geocryologic model between high-resistive bodies and the low resistive matrix could be criticised as unlikely for natural permafrost conditions, results from synthetic modelling were confirmed by the field study in the Val Susauna (FIGURE 5.7). The transition zone between frozen ground and the matrix was less sharp for the Wenner than to the dipole-dipole array. In contrast, no significant differences were found in the ability of the applied setups to detect the top of the modelled structures (FIGURE 5.4 & Figure 5.7). A sharp transition from active layer to frozen ground was detected by all arrays, for both the synthetic model (FIGURE 5.4) and the site study (FIGURE 5.7). Results from synthetic modelling (FIGURE 5.4) showed a more distinct transition zone for the dipole-dipole array for setups with 2 and 3 m electrode spacing. This effect was controlled by the higher resistivity gradient for the inversion results of the dipole-dipole arrays between matrix and resistive bodies. Nonetheless, site characteristics should always be considered when selecting array type. Due to its higher error-proneness the dipole-dipole array is not always an adequate array type at sites with poor electrode coupling. Merging measurements using various array types with different preferences (robustness, vertical/horizontal resolution) into one dataset might pose an interesting possibility for some field sites, as presented for the case study above.

The reliability of resistivity values was detected as an element of uncertainty for quasi-3D imaging in this study. Comparison of default and inverted resistivity values showed distinct divergences. Results varied between underestimation and, in some cases, exponential overestimation of maximum values. These results confirmed the conclusion

of MARESCOT et al. (2003), based on DOI calculations for 2D arrays, that the values within the high-resistive zones cannot be determined accurately. DAY-LEWIS et al. (2005) stated that geotomography tends to overpredict the extent and underpredict the magnitude of geophysical targets; moreover, the spatial structure of tomograms may only weakly reflect the true spatial structure of the subsurface. For quantification of this "correlation loss" a number of approaches exist for image appraisal and data error estimation (e.g. ALUMBAUGH & NEWMAN, 2000; DAY-LEWIS et al., 2005; FRIEDEL, 2003; KRAUTBLATTER et al., 2010; OLDENBURG & LI, 1999). Relations between resistivity of 2D profiles in comparison to values of quasi-3D inversions were presented for the permafrost site in the Val Susauna (FIGURE 5.8). Results underlined the conclusion from synthetic modelling, that a quantitative interpretation of subsurface characteristics (ground ice conditions, ice content and temperature) from inversion results is not always appropriate. Differences arose not only between applied array types but also between measurements in the x- and y- directions (FIGURE 5.7). The effect of geometric layout of the survey lines influencing measurement results has been described by HAUCK and VONDER MÜHLL (2003b) for 2D-ERT measurements on an ice-cored moraine. These results were confirmed for the talus slope of the Val Susauna.

Besides grid setup, the correct alignment of inversion parameters is of fundamental importance for achieving interpretable quasi-3D images. Special focus in this study was placed on the convergence criterion, trying to extend the investigations of HAUCK and VONDER MÜHLL (2003b) for quasi-3D measurements. Results provided in FIGURE 5.6 underline the importance of choosing the correct iteration. While the increase of maximum resistivities under a prolonged inversion process was less pronounced for the quasi-3D case compared to results of HAUCK and VONDER MÜHLL (2003b) a distinct impact was proved for shallow layers. Inversion artefacts arose above high resistivity structures that could result in uncertainties and misinterpretations. The case study in the Val Susauna (FIGURE 5.7), proved to be an interesting example where the top three layers showed a small area with higher resistivities resulting from variations in surface substrate (dolomitic material in contrast to a consistent humus/moss cover). A prolonged inversion process would have resulted in banding effects – as shown for synthetic data in FIGURE 5.7 – above the high-resistive frozen ground. In return, small-scale surface variability could be superimposed by scattered artefacts in shallow depth layers. Likewise, banding effects above resistive bodies could result in misinterpretations

of active layer thickness. Scattered high-resistive structures in the shallow subsurface may also be interpreted as a result of bad electrode coupling and unfavourable contact resistances. Consequently, banding effects could lead to applying higher damping factors on the inversion algorithm, influencing resistivity values and resistivity contrasts between anomalies and background material (cf. HAUCK & VONDER MÜHLL, 2003b). The effect of applying different damping factors on a quasi-3D dataset from a permafrost site in the Murtèl glacier forefield was analysed by RÖDDER and KNEISEL (2011).

5.5 Conclusions

Delineation of the spatial ground ice distribution in mountain environments enables linkages between site specific surface and subsurface characteristics and enhances the explanatory power of geophysical studies regarding a variety of problems such as the thermal regime/energy balance as well as geotechnical problems such as alpine infrastructure as well as possible geohazards, especially in the context of anticipated global warming and subsequent permafrost degradation. Results from forward modelling and field measurements demonstrate the potential of quasi-3D resistivity imaging for permafrost studies in mountain environments. Based on synthetic modelling and site investigations the following conclusions on application, inversion and interpretation of quasi-3D resistivity imaging can be drawn:

- Quasi-3D grids should always consist of measurements in x- and y- direction to achieve reliable data and to detect small-scale heterogeneity in the subsurface. Using parallel lines only, the line spacing should not exceed the electrode spacing.
- The dipole-dipole setups provide best results regarding lateral resolution, permitting larger electrode and line spacings, but are more prone to errors. In contrast, the more robust Wenner/Wenner-Schlumberger arrays have a larger penetration depth and advantages in resolving the base of resistive structures. As for 2D-cases, array type should be chosen with view on surface characteristics. Combinations of different array types can provide superior results.
- Choice of electrode spacing poses a trade-off between horizontal resolution, detection of active layer thickness, and penetration depth, i.e. detection of the ground ice base. Best results are provided by grid setups using 2m and 3m spacings. Electrode spacings >3 m are not recommended due to distinct disadvantages regarding the horizontal resolution but might be necessary in some cases for exploring greater depth.
- The maximum line spacing that provides reliable results is a function of the electrode spacing. Quadruple line spacing provides good results using 2 m electrode spacing. Data quality diminishes as the electrode spacing enlarges. As a rule of thumb, the smaller the electrode spacing and the higher the number of perpendicular tie lines, the more the line spacing can be enlarged.

- In the case of trading efficiency of measurement against model resolution, the application of triple electrode spacing between adjacent profiles can be recommended for setups using electrode spacings of 3 m. In this case reducing the number of perpendicular tie lines by half, i.e. doubling the spacing of tie lines, provides reliable data.
- Choice of iteration should be based not only on the RMS error but also on the evolution of resistivity values, resistivity contrast and on the appearance of artefacts. A prolonged inversion process affects the resulting resistivity values and contrasts but also tends to produce noise and inversion artefacts in shallow layers especially above resistive structures. This may lead to reduced interpretability and misinterpretations of the quasi-3D data.
- Interpretability of the vertical extent of resistive structures is limited for all grid setups. The smaller the vertical extent of the ground ice body and the lower the resistivity gradient, the better the delineation of the ground ice base. Vertical extent is usually overestimated for large structures and high resistivity gradients.
- An absolute interpretation of resistivity values for deducing frozen ground properties (ice/liquid water content, temperature) using quasi-3D ERT-data is limited without extensive image appraisal and data error estimation. Measured and modelled resistivity values strongly depend on line orientation, electrode spacing and array type and are influenced by the site-specific geomorphological setting. Additional information on the subsurface (e.g. SRT, temperature logging) could enhance the interpretability of quasi-3D resistivity measurements.
- Use of the back-and-forth interpretation procedure is valuable for optimising the quasi-3D application for specific objectives and sites as well as for enhancing the interpretability of observed data.

Quasi-3D imaging has proven to be a valuable tool for detecting and investigating frozen ground in mountain environments. In particular, the possibility to delineate the often small-scale permafrost heterogeneity and spatial variability of active layer thickness is improved compared to single 2D measurements. This provides an enhanced potential to align permafrost distribution with site-specific surface properties and morphological settings.

6 Geophysical subsurface properties and frozen ground distribution

Geophysical subsurface properties at mountain permafrost sites are driven by the site-specific lithology, substrate, pore size and volume as well as the frozen and unfrozen water content. As a result, the site-specific geophysical parameters indicative for frozen ground conditions can vary on a wide range (FIGURE 6.1). While general subsurface conditions (substrate, pore size and pore volume) are assumed to remain constant over a certain period, the ground ice occurrences underlie seasonal as well as long term alterations with varying amounts of frozen and unfrozen water content. Therefore, non-recurrent geophysical measurements must be regarded as a snapshot of geophysical subsurface conditions. Deduction of geophysical boundary values representative for the site-specific frozen ground composition remains a difficult task and should be based on a multi-method approach (e.g. HAUCK & KNEISEL, 2008a; KNEISEL et al., 2008; VONDER MÜHLL et al., 2001) and, as far as possible on repeated measurements. Especially the joint application of ERT and SRT has developed as a standard method for the detection of ground ice and, in recent years, for the quantification of ground ice occurrences (HAUCK et al., 2008; HAUCK et al., 2010; HAUCK & KNEISEL, 2008b). IKEDA (2008) has demonstrated that the absence of permafrost from resistivity measurements alone is difficult to predict and recommends further improvements of studies based solely on DC resistivity methods.

Furthermore, the surface- and subsurface conditions at mountain permafrost sites, and, consequently the ground ice characteristics can show a distinct spatial heterogeneity, requiring a deduction of spatial frozen ground distribution. In this context approaches are at hand to determine the spatial frozen ground distribution by geophysical mapping and quasi-3D resistivity imaging (KNEISEL, 2006; KNEISEL et al., 2008; KNEISEL & SCHWINDT, 2008; RÖDDER & KNEISEL, 2011; SCHWINDT & KNEISEL, 2009, 2011). While geophysical mapping – preferably using a multi method approach – is useful to achieve a geophysical characterisation of a larger area, quasi-3D imaging allows a detailed investigation of the subsurface resistivity distribution of a delimited area.

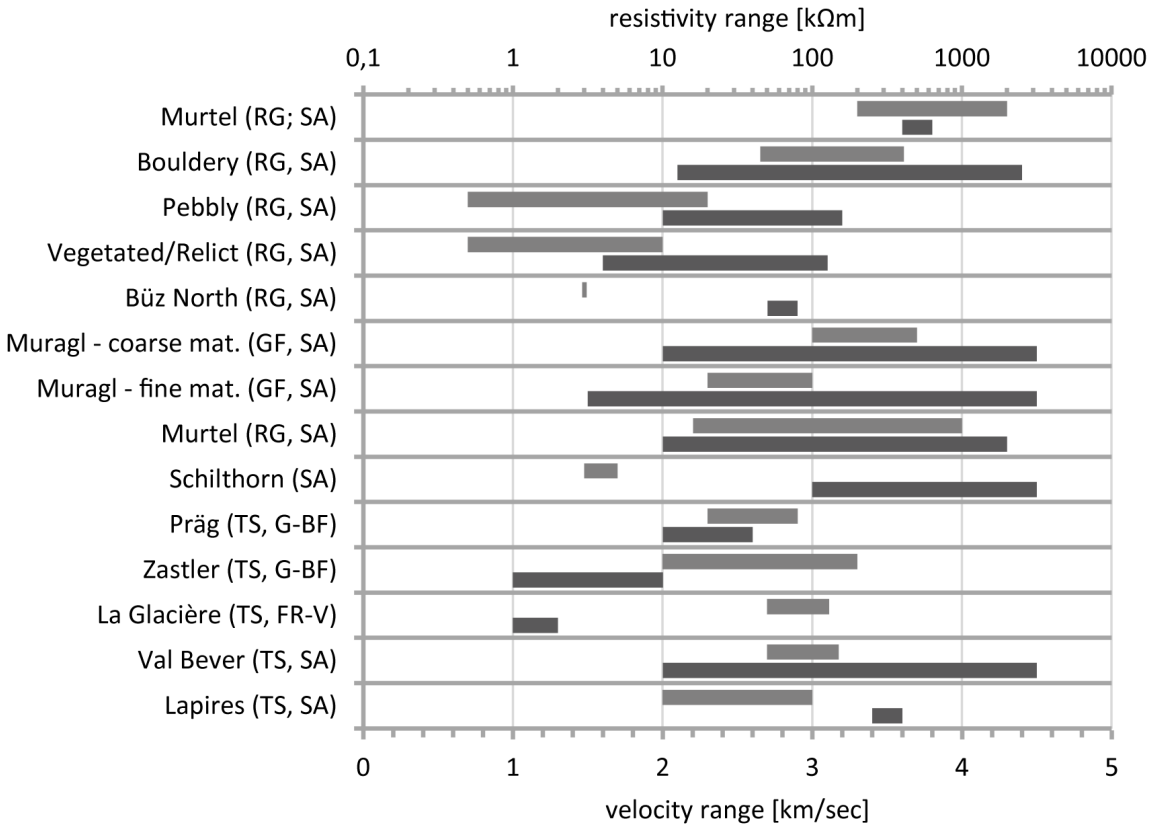

Figure 6.1: Compilation of electrical resistivity and seismic velocitiy values for miscellaneous mountain permafrost settings (compiled after: HAUCK & KNEISEL, 2008a; HILBICH, 2010; HILBICH et al., 2008; KÄSTL, 2012). Abbreviations: RG – rock glacier; GF – glacier forefield; TS – talus slope; SA – Swiss Alps; G-BF – Germany, Black Forest; FR-V – France, Vosges.

In this section a multi-method approach, including joint application of ERT and SRT at two dates of measurement, geophysical mapping as well as quasi-3D resistivity imaging, is used for:

- detecting frozen ground occurrences at the study sites,
- deducing site-specific boundary values of electrical resistivities and p-wave velocities for frozen and unfrozen ground,
- comparing the geophysical characteristics of the study sites with regard on preservation/grade of degradation of frozen ground between early and late summer,
- deducing the areal distribution of frozen ground using quasi-3D resistivity imaging and from geophysical mapping,
- achieving a first estimation of the connection between surface- and vegetation characteristics and frozen ground distribution.

6.1 Site-specific methodological approach

For the detection of frozen ground and a characterisation of geophysical subsurface properties, the methodological approach is based on joint application of ERT and SRT. Results from 2D measurements are expanded towards the third dimension by quasi-3D resistivity imaging and geophysical mapping. To consider the presumed high seasonal frozen ground variability, the geophysical characterisation using ERT and SRT is based on two dates of measurement; detecting the potentially highest ground-ice content in spring-early summer and the state of highest ground-ice degradation in late summer. Correspondingly, quasi-3D measurements were conducted in late summer, to detect the areal extent of the presumably perennial ground-ice distribution. Details on the site-specific setups are given below. Basic information on ERT and SRT (methodology, data acquisition and data processing) are given in CHAPTER 2.1; additional details on quasi-3D ERT can be found in CHAPTER 5.

6.1.1 Val Bever

Investigations in the Val Bever presented in this section include repeated joint application of ERT and SRT, quasi-3D resistivity imaging as well as borehole temperature measurements. Locations of the borehole and geophysical arrays are given in FIGURE 6.2.

Three representative sites were chosen in the Val Bever for a detailed characterisation of geophysical subsurface conditions using ERT and SRT in joint application at two dates of measurement (cf. FIGURE 6.2, TABLE 6.2). Site selection was based on previous measurements (KNEISEL & SCHWINDT, 2008; SCHWINDT, 2007), surface and vegetation characteristics (cf. CHAPTER 3) as well as on the location of a borehole equipped with temperature data loggers (KNEISEL, 2007). Subsurface conditions are considered to be approximately homogeneous throughout the study site, consisting of bouldery, granitic talus.

The general setups of ERT and SRT measurements are equal for all sites with regard on geophone and electrode spacing as well as array length; solely the number of shot locations is variable. Details on the setups are given in TABLE 6.1.

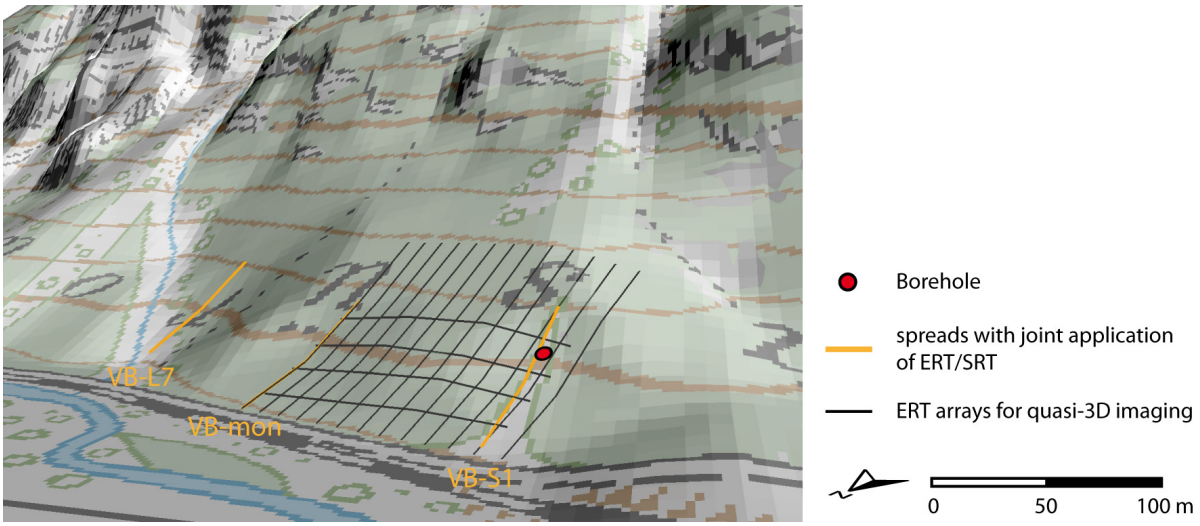

Figure 6.2: Val Bever study site with location of borehole and geophysical arrays (© swisstopo).

The joint spreads of VB-S1 are located in a forest aisle in the western part of the study site close to the borehole. The forest aisle is strongly affected by rockfalls and frequent avalanches in winter. While the eastern part of the aisle shows a thick humus layer superimposed by mosses and lichen, grasses, shrubs and a comparably shallow humus layer dominated the central and western part (FIGURE 3.3 c). It must be noted, that in contrast to the remaining sites, a precisely coinciding location for the subsequent measurements in spring and fall could not be accomplished. As the lower part of the study site is used for grazing during summer, the mark at the lower end of the array has been removed/destroyed. GPS position (precision ±5 m) and knowledge of the study site was used for orientating the arrays. However, the deviance between measurements in spring and fall is most likely less than 3 m vertically and less than 1 m horizontally, ensuring comparable measurements.

The location of VB-mon equals the location of the ERT-monitoring array in the Val Bever (cf. CHAPTER 7.2.2). The site is representative for a large area in the central parts of the study site with a thick cover of humus, superimposed by mosses and a high amount of lichens. The organic layer appears rather inconsistent and is disturbed by granitic boulders (FIGURE 3.2c & Figure 3.3b). Location and setups of measurements are equal for subsequent measurements.

VB-L7 is located in the western part of the study site and represents an exceptional site in the Val Bever. The lower part of the spread consists of mostly fine-grained material covered with shrubs and grasses and is characterised by a minor inclining slope.

The central and upper parts of the array are located in an area with steep slope, large granitic boulders, and a thick, consistent cover of organic material superimposed by mosses with trees showing a distinct dwarf growth.

Table 6.1: Details on joint ERT and SRT measurements at Val Bever with specification of site characteristics.

	Val Bever Mon		Val Bever L7		Val Bever S1	
altitude [m a.s.l.] (begin/end of spread)	1778 / 1810		1778 / 1808		1781 / 1806	
average slope	28°		25° (min 10°; max 30°)		21°	
substrate	granitic, bouldery talus		granitic, bouldery talus		granitic, bouldery talus	
site characteristics - stock of trees	*Larix decidua, Pinus cembra* (< 10 m), minor crown density		*Pinus cembra, Picea abies, larix decidua* (partly dwarfing)		clearing/forest aisle	
site characteristics - humus/undergrowth	gappy humus/moss cover, high amount of lichens		grasses (foot of slope); humus/moss cover (slope)		grasses and mosses, shallow humus cover	
	ERT	SRT	ERT	SRT	ERT	SRT
spread length [m]	70	69	70	69	70	69
electrode / geophone spacing [m]	2	3	2	3	2	3
# of electrodes / geophones	36	24	36	24	36	24
array type / # of shot points	Wenner, dipole-dipole	10 / 10	Wenner, dipole-dipole	10 / 13	Wenner, dipole-dipole	10 / 12
# of stacks		10		10		10
sample interval [ms]		0,125		0,125		0,125
record length [ms]		128		128		128
# of measurements	2	2	2	2	2	2
date of measurement	09.07.2010 / 09.10.2010		09.07.2010 / 09.10.2010		09.07.2010 / 09.10.2010	

A quasi-3D measurement has been conducted in the Val Bever covering the area between the monitoring location in the east and the forest aisle in the west of the grid (FIGURE 6.2). Information from joint application of ERT and SRT as well as borehole temperature data allows for a detailed interpretation of 3D resistivity data in this area. An electrode spacing of 3 m was chosen to cover a sufficiently large area. Based on the approach to increase the efficiency of quasi-3D measurements (cf. CHAPTER 5.2.4) the quasi-3D grid was created using triple parallel line spacing and a reduced number of perpendicular tie lines. Wenner and dipole-dipole configurations were measured to

achieve an optimal agreement between robustness and resolution (cf. CHAPTER 5.2). Details on the grid setup are given in FIGURE 6.2 and TABLE 6.2.

Table 6.2: Details on quasi-3D measurements at Val Bever.

	grid size [m]	electrode spacing [m]	line spacing [m]		# of arrays		electrode positions	# of datum points	
			x	y	x	y		Wenner	dipole-dipole
Val Bever	105x108	3	9	15	13	4	612	3350	6734

6.1.2 Val Susauna

The locations of geophysical arrays conducted at the Val Susauna study site are presented in FIGURE 6.3. Included are joint and repeated measurements of ERT and SRT as well as quasi-3D resistivity imaging. Details on setups and site characteristics are given in TABLE 6.4. As described (cf. CHAPTER 3.1.2), the study site is characterised by a sharp transition between distinctly differing vegetation compositions. The working hypothesis for the problem attended in this study presumes, that frozen ground is present in the dwarf-growth zone and absent in the neighbouring forest.

The geophysical mapping – conducted during spring – tries to identify the maximum frozen ground distribution and differences in geophysical characteristics between the dwarf-growth zone (arrays L1 and L2) and the normally grown forest (arrays L0). Array L3 is located at an exceptional site. A small, most probably anthropogenic cutting (~ 5 x 10 m) consisting of loose, uncovered talus is located at the foot of the slope (FIGURE 3.4d). Uphill, above the cutting, the slope constitutes the margins of the dwarf growth zone. The accessibility of the loose talus material in this area allows a direct comparison of electrical resistivities and seismic velocities with visible subsurface conditions.

Repeated measurements of ERT and SRT were conducted at two sites in the Val Susauna (FIGURE 6.3, TABLE 6.4). The ERT-monitoring location (cf. CHAPTER 7.2.2) in the central part of the dwarf-growth zone was determined as representative for a site with perennial frozen ground (VS-mon). VS-L5 is situated in the neighbouring forest, where frozen ground is anticipated to be absent. Details on site characteristics and setups of joint geophysical measurements are given in TABLE 6.4.

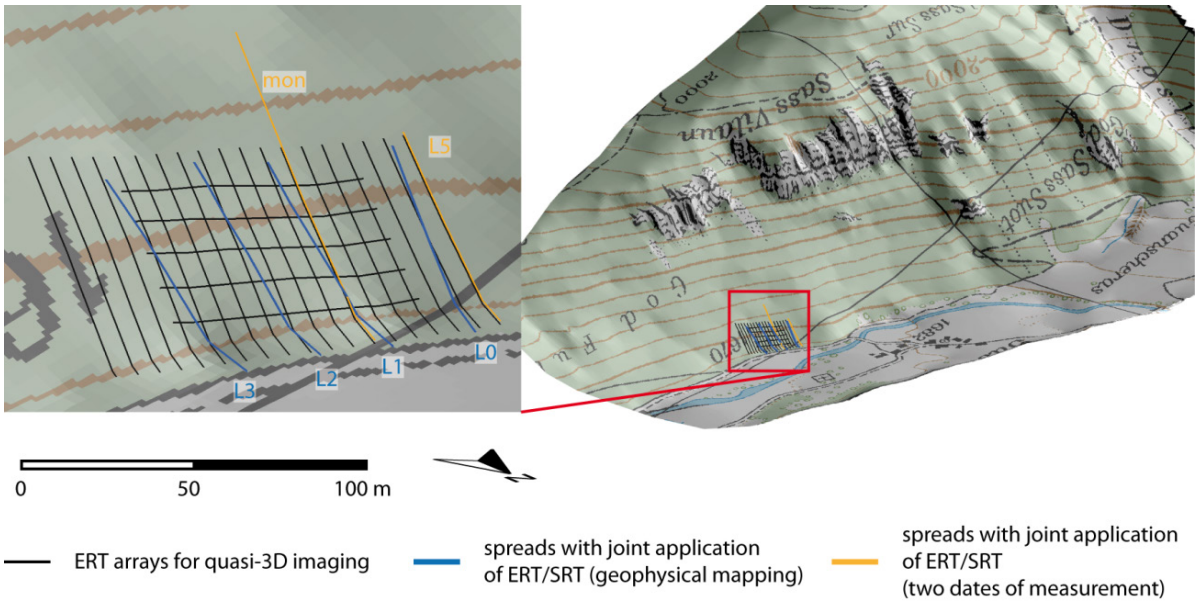

Figure 6.3: Val Susauna study site with location of geophysical arrays (© swisstopo).

A quasi-3D measurement was realized in the Val Susauna, which covers the complete dwarf-growth zone as well as neighbouring areas with normal tree growth in the western part of the slope. The setup of the quasi-3D grid is presented in detail in CHAPTER 5.3.1 (see also TABLE 6.3).

Table 6.3: Details on quasi-3D resistivity measurements at Val Susauna

	grid size [m]	electrode spacing [m]	line spacing [m]		# of arrays		electrode positions	# of datum points	
			x	y	x	y		Wenner	dipole-dipole
Val Susauna	69x108	2	6	10	19	5	864	4731	9555

Table 6.4: Details on joint ERT and SRT measurements at Val Susauna with specification of site characteristics.

	Val Susauna Mon		Val Susauna L5		Val Susauna L0		Val Susauna L1		Val Susauna L2		Val Susauna L3	
altitude [m a.s.l.] (begin/end of spread)	1663 / 1692		1663 / 1692		1663 / 1700		1663 / 1697		1663 / 1695		1663 / 1700	
average slope	23°		23°		27°		26°		25°		27	
substrate	dolomitic talus		dolomitic talus		dolomitic talus		dolomitic talus		dolomitic talus		dolomitic talus	
site characteristics - stock of trees	*Pinus mugo, Picea abies* (dwarf growth)		*Picea abies* (> 20 m)		*Picea abies* (> 20 m)		*Pinus mugo, Picea abies* (dwarf growth)		*Pinus mugo, Picea abies* (dwarf growth)		*Pinus mugo, Picea abies* (dwarf growth)	
site characteristics - humus/undergrowth	consistent thick humus/moss cover (>30 cm)		shallow humus cover mosses/shrubs in patches		shallow humus cover mosses/shrubs in patches		consistent thick humus/moss cover (>30 cm)		consistent thick humus/moss cover (>30 cm)		thick humus/moss cover uncovered talus at foot of slope	
	ERT	SRT	ERT	SRT	ERT	SRT	ERT	SRT	ERT	SRT	ERT	SRT
spread length [m]	105	69	70	69	70	69	70	69	70	69	70	69
electrode / geophone spacing [m]	3	3	2	3	2	3	2	3	2	3	2	3
# of electrodes / geophones	36	24	36	24	36	24	36	24	36	24	36	24
array type / # of shot points	Wenner, dipole-dipole	11 / 14	Wenner, dipole-dipole	10 / 13	Wenner	10 / 13	Wenner	11 / 14	Wenner	10 / 13	Wenner	10 / 13
# of stacks		10		10		10		10		10		10
sample interval [ms]		0,125		0,125		0,125		0,125		0,125		0,125
record length [ms]		128		128		128		128		128		128
# of measurements	2	2	2	2	1	1	1	1	1	1	1	1
date of measurement	12.07.2010 / 11.10.2010		12.07.2010 / 10.10.2010		31.05.2009		31.05.2009		31.05.2009		31.05.2009	

6.1.3 Brüeltobel

Due to complex site conditions at the steep slope of the Brüeltobel study site, with loose talus material and a high rock-fall activity measurements were reduced to a minimum. Furthermore, extensive measurements would have damaged the highly sensitive ecosystem in the steep slope.

Figure 6.4: Brüeltobel study site with location of joint ERT/SRT arrays (© swisstopo).

Joint ERT/SRT measurements could only be realized during spring 2009. The location of arrays is given in FIGURE 6.4; details on setups and site characteristics are presented in TABLE 6.5. Dimensions of geophysical arrays L1 had to be adjusted to fit the comparably short distance from the foot of the talus slope towards the foot of the rock-wall. The spacing of the 24 geophones was reduced to 2 m for SRT measurements. For ERT measurements 36 electrodes with unit electrode spacing of 2 m were used. However, only 34 electrodes were coupled to the ground to shorten the array length. All quadrupoles measured actuating the uncoupled electrodes were deleted prior to tomographic inversion. The disparity of contact resistances between vegetated areas (<5 kΩm) and uncovered talus (30-80 kΩm) is comparably high. Therefore, dipole-dipole measurements were not considered capable of providing reliable data. Thus, only Wenner arrays were measured.

Table 6.5: Details on joint ERT and SRT measurements at Brüeltobel with specification of site characteristics.

	Brüeltobel L1		Brüeltobel L2	
altitude [m a.s.l.] (begin/end of spread)	1200 / 1241 (1226 - SRT)		1184 / 1230	
average slope	34°		42°	
substrate	limestone talus		limestone talus	
site characteristics - stock of trees	*Picea abies* (dwarf growth)		*Picea abies* (dwarf growth)	
site characteristics - humus/undergrowth	consistent humus/moss cover (> 30 cm); *Dryas octopetala*		consistent humus/moss cover (> 30 cm); *Dryas octopetala*	
	ERT	SRT	ERT	SRT
spread length [m]	66	46	70	69
electrode / geophone spacing [m]	2	2	2	3
# of electrodes / geophones	34	24	36	24
array type / # of shot points	Wenner	9	Wenner	10
# of stacks		10		10
sample interval [ms]		0,125		0,125
record length [ms]		128		128
# of measurements	1	1	1	1
date of measurement	01.06.2009		01.06.2009	

6.2 Results

The results presented and interpreted in this chapter are divided into two main thematic sections. The first section aims at the confirmation of frozen ground and the determination of site-specific geophysical properties of frozen and unfrozen ground, based on 2D measurements of ERT and SRT. The second section is focused on the areal distribution of frozen ground based on geophysical mapping and quasi-3D resistivity imaging.

6.2.1 Confirmation of frozen ground and determination of site-specific geophysical properties of frozen and unfrozen subsurface material

In this section, results from the joint application of ERT and SRT are analysed to confirm the existence of frozen ground and to determine boundary values of electrical resistivity and seismic velocity for frozen and unfrozen ground. Repetitive measurements are analysed with regard to the variability of geophysical parameters between subsequent measurements. Electrical resistivity as well as p-wave velocity for frozen ground and the superimposing layer above frozen areas (in the following referred to as "active layer", even though the existence of permafrost could not yet be definitively confirmed for all sites) are evaluated for all sites to compare subsurface characteristics and their seasonal evolution for different settings.

6.2.1.1 Val Bever

Results from repeated ERT/SRT measurements of arrays S1, located in the forest aisle in the western part of the study site, are presented in FIGURE 6.5. Maximum resistivity (~300 kΩm) and velocity (~4.5 km/sec) values are generally rather high for all measurements and point to the occurrence of perennial frozen ground. Geophysical boundary values for frozen ground can be obtained from comparing borehole temperature data with the vertical course of resistivity and velocity values at the corresponding position (FIGURE 6.6). For the Val Bever resistivity values higher than 35 kΩm and velocities of more than 1800 m/sec are assumed representative for frozen ground.

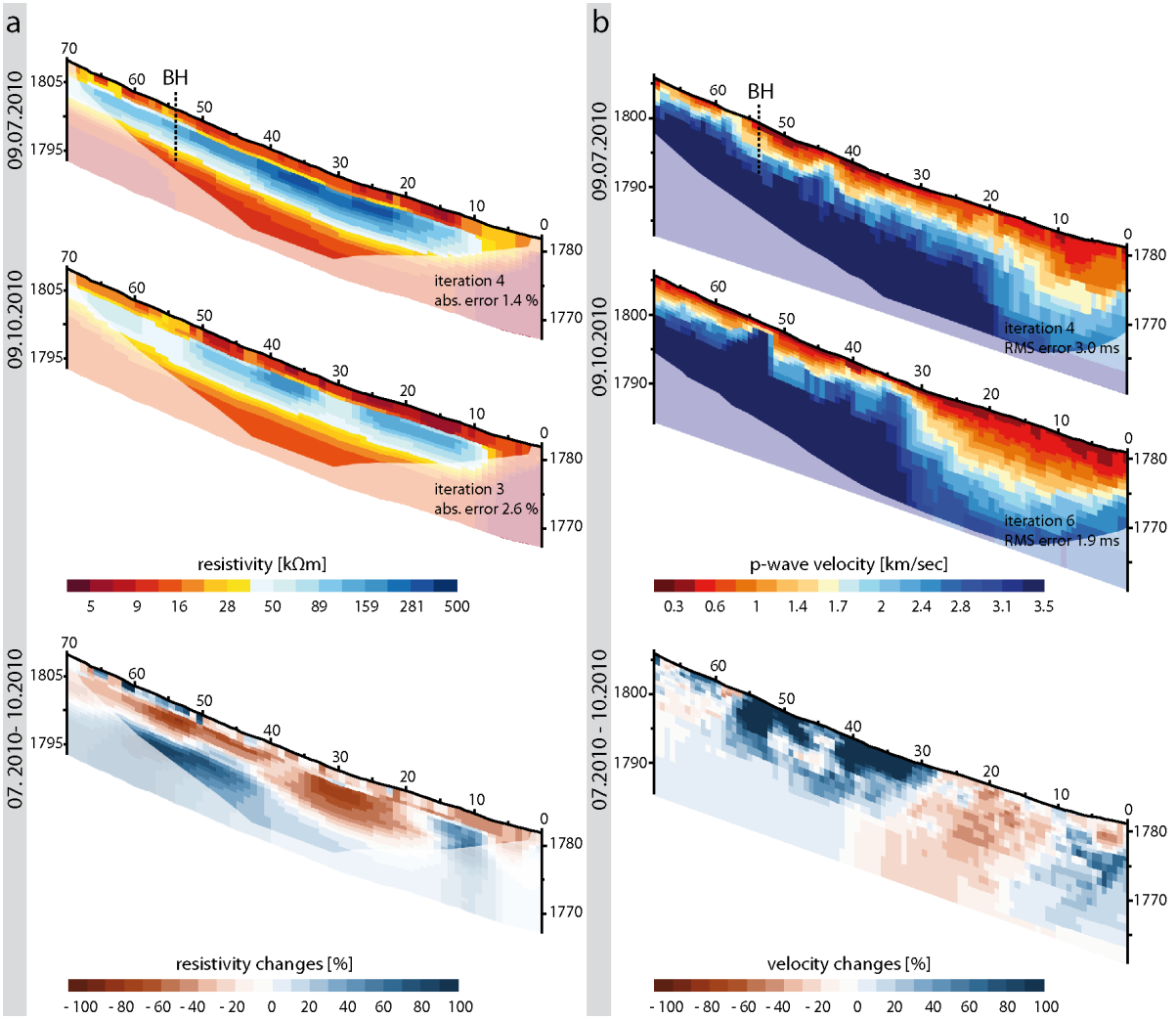

Figure 6.5: Tomograms from repeated geophysical measurements at Val Bever-S1, with (a) ERT-data and (b) SRT-data and corresponding time-lapse tomograms.

ERT tomograms (FIGURE 6.5) show a high resistive anomaly embedded into a matrix of relatively low resistivity (~10 kΩm). Beginning at meter 10 of the array, the anomaly pervades throughout the profile, with higher values located towards the foot of the slope. While the main shape of the frozen ground body does not alter during summer, resistivity values decrease conspicuously by up to 80%, while values of the matrix increase. The thickness of the frozen ground body estimated from ERT data is approximately 6-8 m. The active layer thickness, as derived from ERT data, appears to be rather constant (2-3 m) with little spatial and temporal variation in thickness. Resistivity values within the active layer vary in both directions between subsequent measurements.

While SRT data (FIGURE 6.5) generally coincide with ERT data regarding the verification of frozen ground, the evolution of subsurface properties appears partly contradictory. The frozen ground base is not detectable by SRT as no refraction occurs below the high-velocity anomaly (cf. CHAPTER 2.1.2). The horizontal extent of the anomaly detected by SRT varies distinctly between July and September. Beginning at horizontal distance of around 10-15 m (July), which is in agreement with ERT data, velocity values decrease by ~40% towards September in the lower parts of the slope, with the anomaly beginning at a horizontal distance of 30 m. Maximum velocity values remain constant between both measurements. In contrast to ERT, seismic data indicate a rather inhomogeneous active layer thickness, varying between 1 and 4 m.

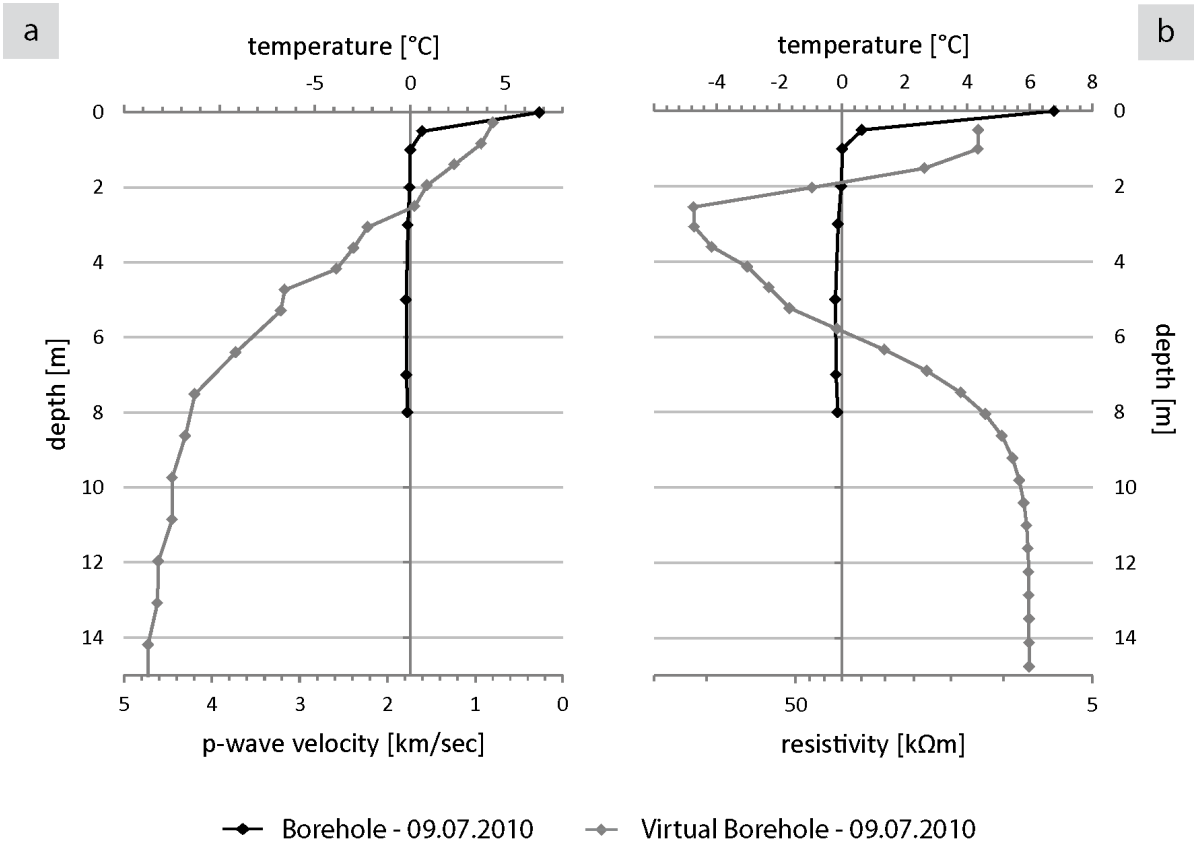

Figure 6.6: Borehole temperature date in comparison to p-wave velocity (a) and electrical resistivity values (b) recorded at Val Bever (VB-S1).

Borehole temperatures (FIGURE 6.6) measured in July 2010 show frozen conditions below a depth of 2 m. Minimum temperatures of only of -0.22 °C are measured in 5 m depth. The course of both, ERT and SRT data in the uppermost 2 m corresponds well with borehole temperatures, representing unfrozen conditions. Resistivity values show a

sharp increase between 1.5 and 2.5 m depth representing the transition zone from unfrozen to frozen, velocity values increase slightly towards 2.5 m depth and more rapidly below. Resistivity values point to a base of the frozen ground body between 6-8 m, and rather homogeneous matrix conditions below the frozen ground body. Borehole temperatures at 8 m depth still indicate frozen ground (-0.14 °C), however, a precise verification of the frozen ground base is not possible. Seismic velocities show a constant increase with depth towards a break point at 7.5 m depth. Below, the gradient of increase is reduced. This course reflects the explained drawback of SRT in detecting the thickness of structures (cf. CHAPTER 2.1.2).

Data from ERT measurements conducted at the ERT-monitoring site (FIGURE 6.7) resemble results presented for site S1, indicating comparable subsurface conditions. An elongated anomaly embedded in a low resistive matrix pervades throughout the resistivity tomograms at both dates of measurements, beginning at a horizontal distance of ~10 m. Maximum resistivity values of up to 600 kΩm exceed the values measured at site S1. The anomaly is between 6-8 m thick, with a maximum in the lower parts of the slope (horizontal distance 15-30 m). Active layer thickness obtained from ERT is between 2-3 m. The high resistivity values (40-80 kΩm) in the shallow subsurface measured in July can be interpreted as frozen or supercooled subsurface material. During summer resistivity values of the active layer and the high resistive anomaly decreases by up to 60%, while matrix values at depth below 6-8 m show a distinct increase by more than 60-80%.

The subsurface structures detected by SRT measurements differ noticeably from ERT data. Comparing the results from measurements in July, both methods coincide in the lower parts of the slope (10-30 m), where a delimited anomaly with high resistivity/velocity values of up to 600 kΩm and 4 km/sec is detected, indicating frozen ground conditions. While ERT data also indicate frozen ground between horizontal distances 30-70 m, SRT data show a gradual increase of velocities with depth in this area, with no indication for the presence of a refractor. For this area, frozen ground can not clearly be proven. The results from both methods correspond in terms of active layer thickness between horizontal distances 10-30 m indicating a depth of the frozen ground table at 2-3 m. Towards September, velocities of the frozen ground body at the

foot of the slope decrease by 40-80% to 1.8-2.5 km/sec, which is in accordance to decreasing resistivity values in this area.

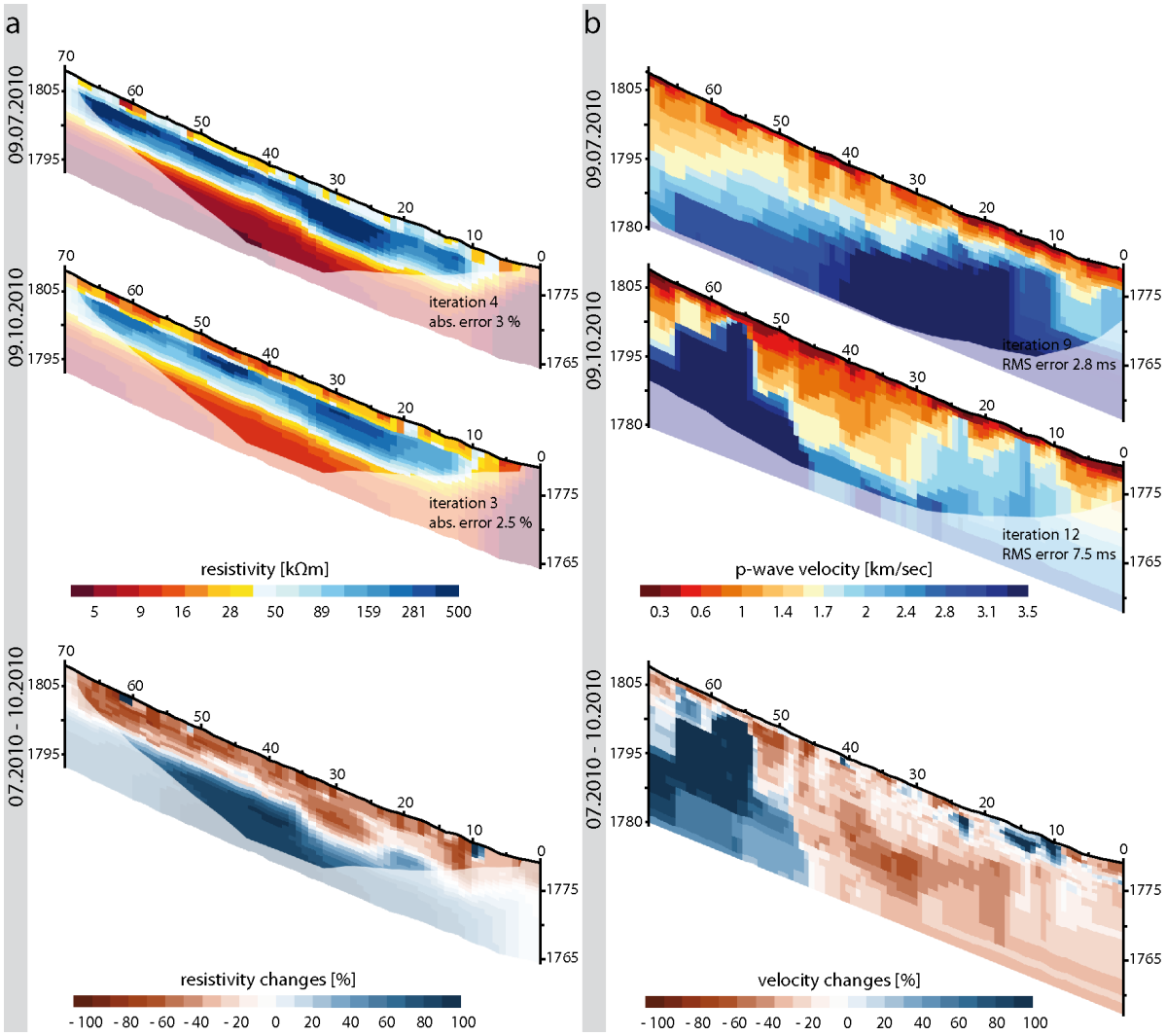

Figure 6.7: Tomograms from repeated geophysical measurements at Val Bever-mon, with (a) ERT-data and (b) SRT-data and corresponding time-lapse tomograms.

Corresponding to measurements from July, results of ERT and SRT from September do not coincide between horizontal distances 30-50 m. While resistivity values indicate the presence of frozen ground, velocities of less than 1.2 km/sec and the absence of a refractor contradict this interpretation. Between horizontal distances 50-65 m SRT data from October show a delimited high-velocity anomaly that is not present in the July-measurement. Velocities in this area are increased by up to 500%, while in general decreasing velocities (-30-40%) were detected by SRT. As ERT-data do not show any significant variation of subsurface parameters for this section of the array, the structure

shown in the seismic tomogram is not clearly interpretable. It is most likely, that the structure is reasoned by technical failures during the measurement (e.g. trigger problems due to fractures in the trigger cable).

The active layer thickness detected by SRT decreases during summer from ~2.5 m in July to ~1.5 m in October. Corresponding ERT-measurements indicate a rather constant active layer thickness of 2-3 m and a strong decrease of resistivity values between the two measurements. SRT time-lapse data show a strong increase of velocities in the shallow subsurface (+30 to +200%) at horizontal distances 8-18 m and 23-25 m. Resistivity and velocity values of the determined frozen ground body between 10 and 30 m decrease distinctly and point to a degradation of the ground ice body during summer.

The occurrence of perennially frozen ground has been proven for the site L7 in the Val Bever using ERT and SRT (FIGURE 6.8). However, the extent and evolution of subsurface geophysical properties causes problems in terms of the interpretation of results. Low resistivity values (<20 kΩm) and gradually increasing low velocities indicate unfrozen ground at the foot of the slope (0-12 m). The seasonal variation of geophysical properties is relatively low in this area (± 20-40 %). Upslope, a perennial frozen ground body with resistivities of 80-400 kΩm and velocities of 2-4 km/sec is detected.

ERT-data show – correspondingly to sites S1 and Mon – an elongated high resistive anomaly embedded in a matrix of lower resistivities. While the extend of the anomaly (top and base) remains rather constant, the resistivity values increase by up to 80% towards the measurement in October, while matrix values slightly decrease (-30%). This is in contradiction to the sites S1 and Mon, where the reversed can be observed. The base of frozen ground is located at a depth of approximately 10 m below surface. With 2-2.5 m active layer thickness derived from ERT-data is rather constant, with a general decrease of resistivity values.

The extent of the frozen ground body derived from SRT measurements differs distinctly from ERT results. A clearly delimited high velocity structure (1.9-3.8 km/sec) is observable between horizontal distances 12-35 m. Gradually increasing low velocities towards the uphill locations point to the absence of a refractor and consequently to the absence of frozen subsurface material. Velocity evolution of the frozen ground body is

divergent between the two subsequent measurements. While values below 7 m depth decrease by up to 40%, an increase by up to 20% can be observed between 3-7 m depth, with a generally strong spatial variability. Between horizontal distances 13 and 18 m velocities decrease from ~2 km/sec towards values below 1.3 km/sec, indicating a complete degradation of frozen ground in this area, while resistivity values of 60-90 kΩm in October are representative for frozen ground conditions.

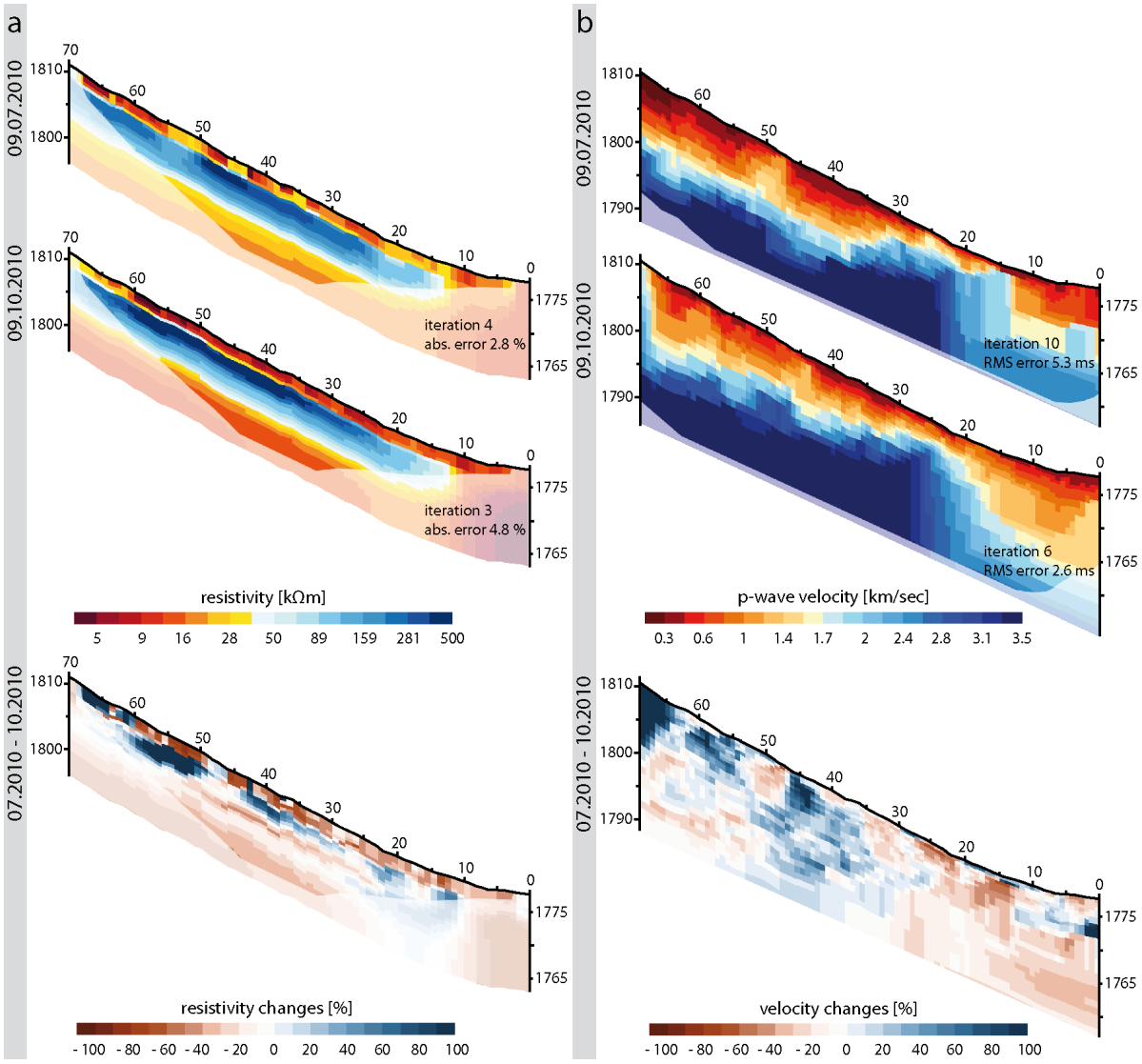

Figure 6.8: Tomograms from repeated geophysical measurements at Val Bever-L7, with (a) ERT-data and (b) SRT-data and corresponding time-lapse tomograms.

Active layer thickness derived from SRT-data is between 2-3.5 m with a strong spatial variability. Velocities decrease by 40-60% from July to October. The remaining areas of

the tomogram show a divergent evolution with increasing and decreasing velocity values (± 40%) in close proximity.

6.2.1.2 Val Susauna

Results from repeated ERT and SRT measurements in the Val Susauna are presented in FIGURE 6.10 and FIGURE 6.11. The delineation of geophysical boundary values for frozen and unfrozen ground conditions at the Val Susauna is based on the analysis of measurements conducted in July, as highest amounts of ground ice are assumed to be present. FIGURE 6.9 shows two virtual boreholes derived from measurements at the ERT-monitoring site and along array L5 (cf. FIGURE 6.3) in July 2010. Locations of the virtual boreholes are indicated in FIGURE 6.10 and FIGURE 6.11.

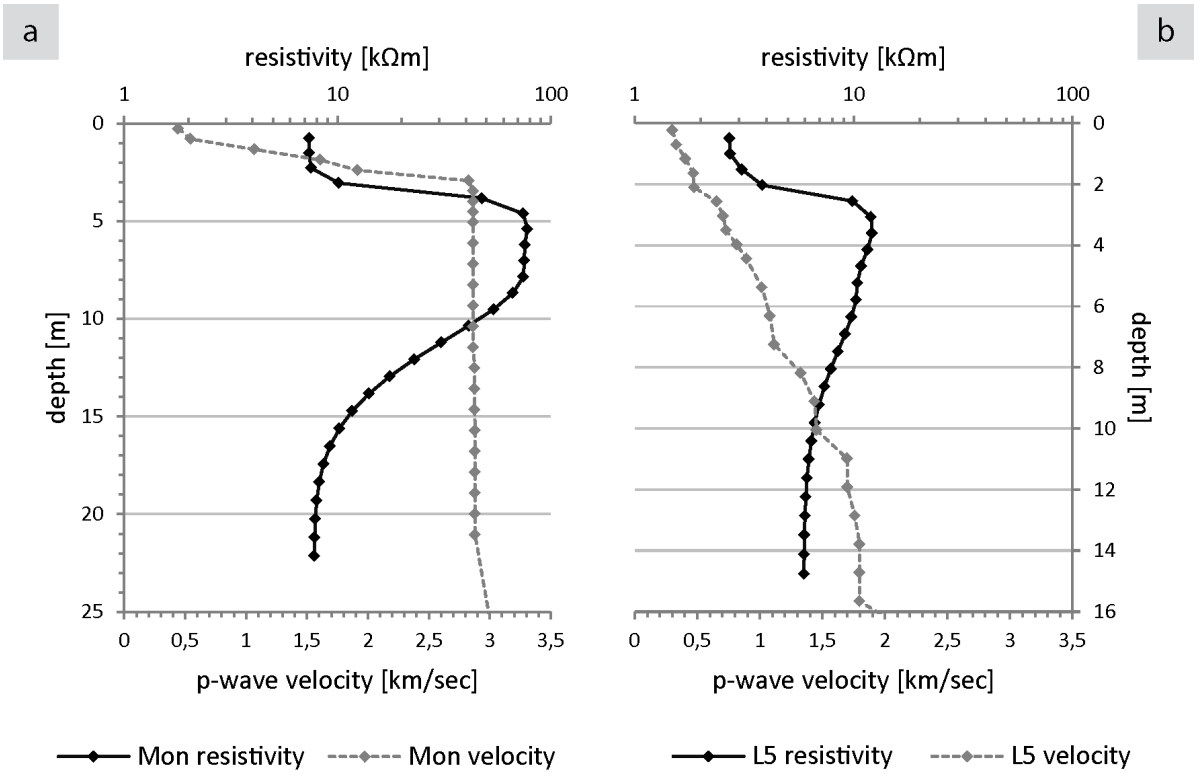

Figure 6.9: Virtual boreholes of electrical resistivity and p-wave velocity values measured at the Val Susauna monitoring site (a) and VS-L5 (b).

Virtual boreholes taken from the datasets at the monitoring site show a strong increase of values for electrical resistivity and seismic velocity data within the uppermost 2-3 meters. Seismic velocities reveal a sharp increase from 0.3 towards 2.7 km/sec at 2.5 m

depth. Below that point, velocities remain almost constant with increasing depth. Resistivity values of the uppermost 2.5 m are ~7.5 kΩm and increase towards a maximum value of 77 kΩm at 5 m depth. Below 9 m depth resistivities decrease, until they reach values between 8-9 kΩm at a depth of 16 m. Velocity data taken from array L5 show a slow, gradual increase of velocities from 0.3 km/sec towards 1.8 km/sec at 16 m depth. Minimum resistivity values of 3-4 kΩm within the uppermost 2 m are followed by an increase to a maximum value of 12 kΩm at 3.5 m depth. Below 3.5 m depth, resistivity values decrease slowly to ~6 kΩm at 15 m depth.

The presence of frozen ground at site L5 can be regarded as most unlikely. The lack of shifts in the course of the curve points to an absence of refractors within the uppermost 15 m depth. Even though a shift in the curve is observable at 2-3 m depth for ERT-data, maximum values are rather low (12 kΩm). Seismic velocities of more than 2 km/sec and high electrical resistivities of up to 77 kΩm are indicative for frozen ground towards the foot of the slope of the monitoring array. Seismic velocities of ~1.5 km/sec and an electrical resistivity of ~15 kΩm can be regarded as representative geophysical boundary values for frozen ground conditions in the dolomitic talus slope of the Val Susauna.

2D tomograms from repeated ERT and SRT measurements at the Val Susauna ERT-monitoring site (cf. CHAPTERS 7.2.2 & 7.3.2.2) are presented in FIGURE 6.10. ERT-data from July 2010 show an elongated anomaly extending from horizontal distance 8 m to 105 m, embedded into a low resistive matrix (<5 kΩm). Maximum resistivity values (77 kΩm) as well as the maximum thickness are observable in the lower parts of the slope (15-45 m). Upslope, resistivities are distinctly lower with values ranging between 13 and 22 kΩm. The table of the high resistive anomaly is located at a depth of 3 m, the base at 10-12 m depth.

The corresponding seismic tomogram shows a distinct high-velocity anomaly between horizontal distance 8 and 38 m. Seismic (up to 3.2 km/sec) and electric properties (up to 77 kΩm) indicate frozen ground in this area. Upslope, seismic velocities between 0.3 and maximum values of 0.9 km/sec are representative for unfrozen ground conditions. For this area, results from ERT and SRT are contradictory with regard to the frozen ground distribution. With a very high gradient of seismic velocities in the shallow subsurface (horizontal distance 8-25 m) from 0.3 to more than 3 km/sec on a vertical

distance of less than 2 m the active layer is very thin and varies between less than 1 (8-10 m; 15-20 m) and 2-3 m (20-35 m).

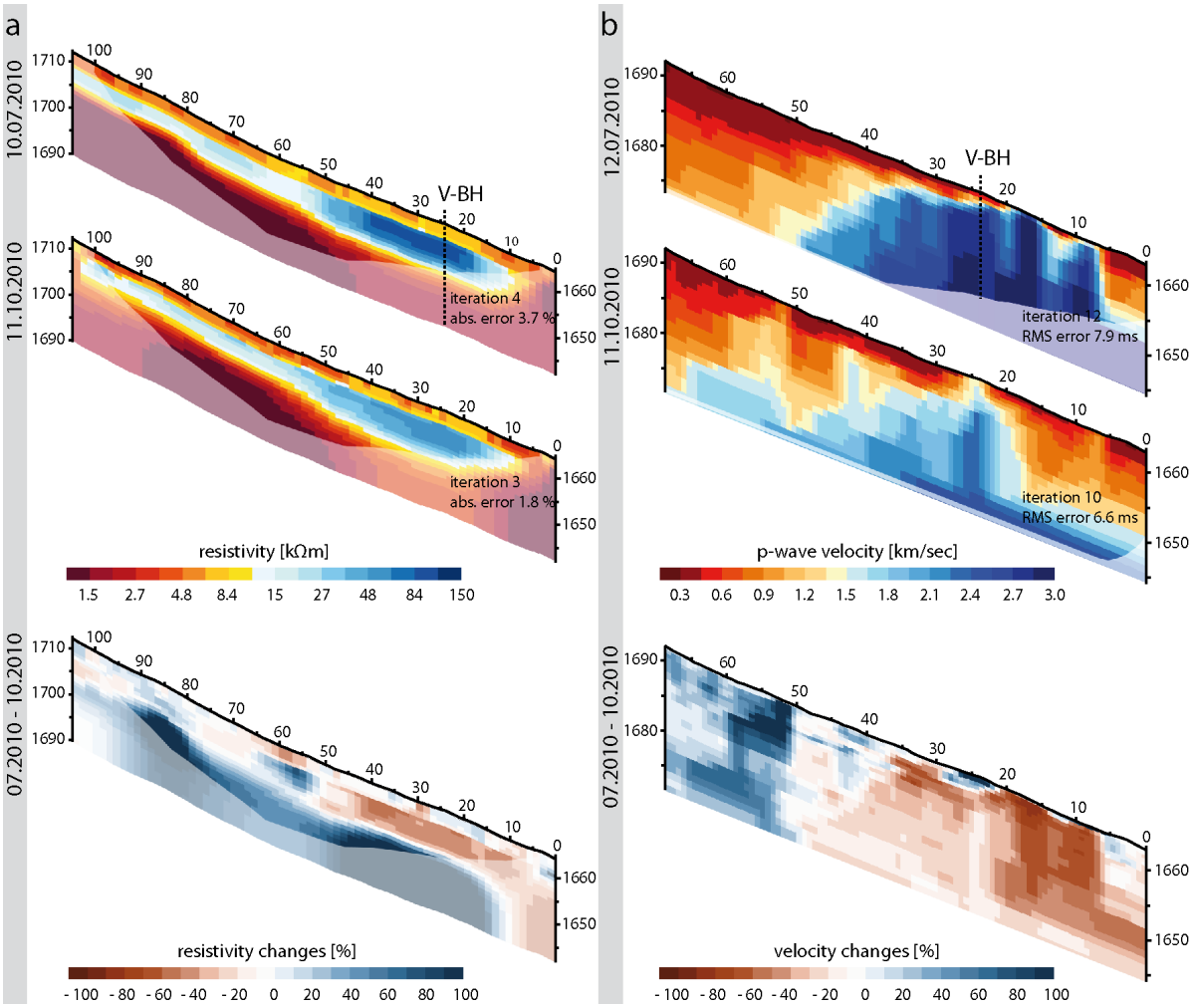

Figure 6.10: Tomograms from repeated geophysical measurements at Val Susauna-mon, with (a) ERT-data and (b) SRT-data and corresponding time-lapse tomograms.

Electrical resistivities and seismic velocities of the frozen ground body decrease noticeably during summer. However, values of 45-50 kΩm and 1.8-2.2 km/sec still indicate frozen ground conditions. Variation in subsurface resistivity conditions between July and October is highest for the frozen ground body (-30-45%) and the matrix below 6-8 m depth (+ 40-90%). Variations in the shallow subsurface and the active layer are low (± 0-20%). Only slight variations are observable for the resistive anomaly (horizontal distance 50-105 m, 3-8 m depth). In contrast to the verified frozen ground body, resistivities in this area do not show a consistent evolution. Areas with decreasing

and increasing resistivity values are observable in close proximity, while the degree of variability is comparably low (-10 to +40%).

Seismic velocities in the central parts of the frozen ground body (horizontal distances 20-35 m) decrease by 20-30%. The active layer thickness in this area is increased to 2-3 m. The most prominent changes can be observed between horizontal distances 8-18 m at the lower end of the frozen ground body. There, subsurface velocities decrease by up to 75%, from 3 to less than 1 km/sec. The evolution of subsurface velocities indicates a complete degradation of frozen ground in this area. At the upslope locations, (35-69 m) subsurface velocities distinctly increase during summer. However, values of less than 1.2 km/sec still indicate unfrozen conditions. The highest degree of change (+80-120%) is observable between horizontal distances 50-60 m accompanied by an increase of resistivity values of 30-80% in 3-8 m depth. While resistivity values (20-25 kΩm) imply frozen ground in this area, velocities of 0.9-1.2 km/sec point to unfrozen conditions.

Results from repeated ERT and SRT measurements of site L5 in the Val Susauna are presented in FIGURE 6.11. Both, ERT and SRT data from July 2010 indicate unfrozen ground conditions prevailing at site L5. Results presented in the virtual borehole (FIGURE 6.9) are conferrable to the remaining areas of the tomograms. ERT-data show certain areas (horizontal distances 15-70 m; 3-8 m depth) with electrical resistivities ranging around 10-16 kΩm. Corresponding areas in the seismic tomogram show velocities of 0.5-1 km/sec. Below a depth of 7-10 m, velocities of up to 1.9 km/sec are observable in some areas of the tomogram. While the increase of velocities with depth is slow and gradual towards the foot of the slope, a distinct increase of velocities (0.7 to 1.9 km/sec) – indicating the presence of a refractor – is observable at horizontal distances 45-50 m at a depth of 6.5 m. This structure is also recognizable – with lower values (~1.3 km/sec) – in the SRT tomogram from October. However, a corresponding structure cannot be identified in the resistivity tomogram, allowing for no definite interpretation.

The variability of geophysical properties between July and October is, compared to the monitoring site in the Val Susauna and to the sites in the Val Bever, rather low. The highest degree of change is detected in the low resistivity/low velocity area towards the foot of the slope (0-10 m), where fine grained material prevails. ERT and SRT data show slightly decreasing values for most parts of the tomograms. The area between

horizontal distances 45-50 m in the SRT tomogram again states an exceptional case. Velocities above the structure described above increase by 90-150% from 0.3/0.6 to 0.8/1.2 km/sec.

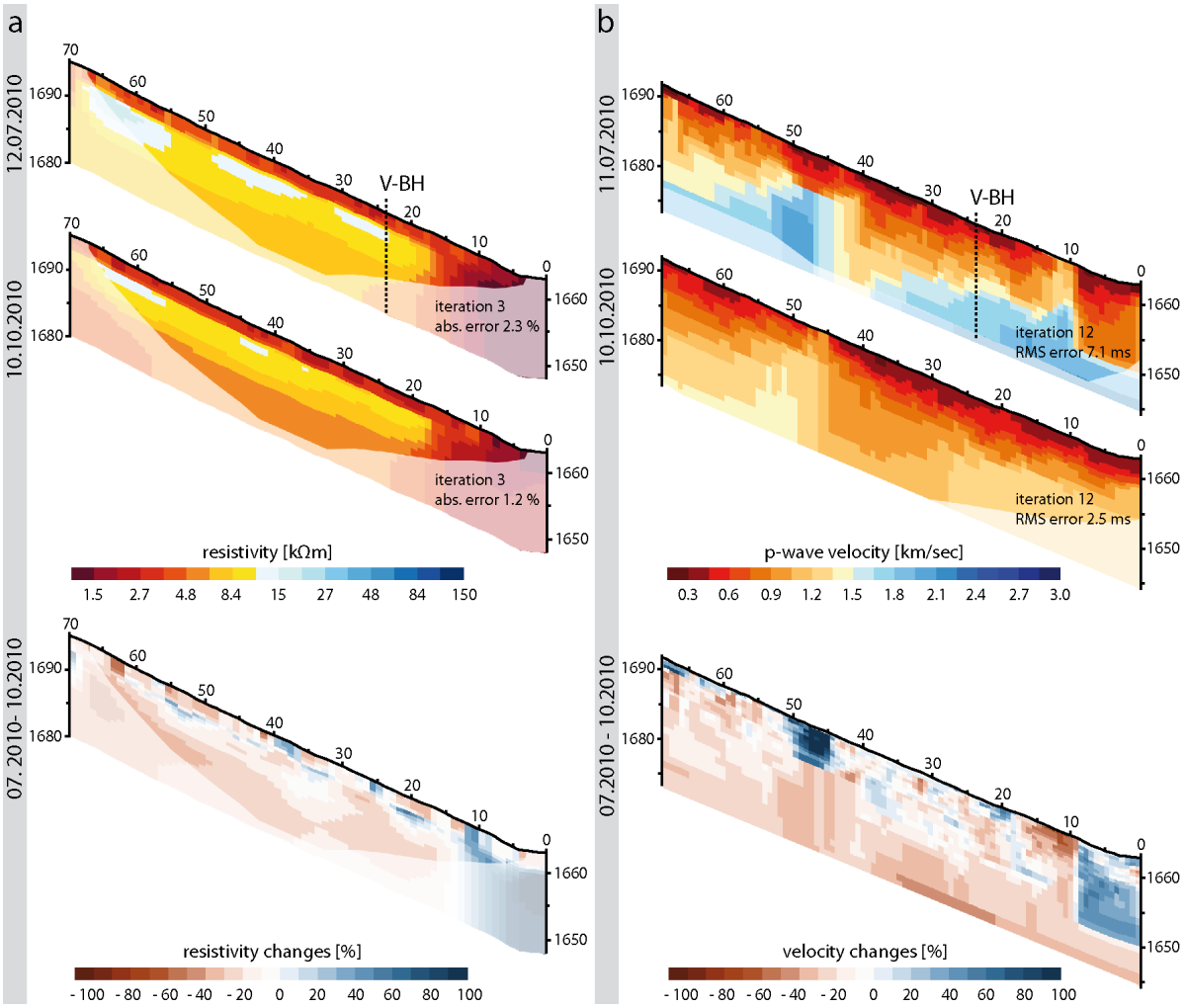

Figure 6.11: Tomograms from repeated geophysical measurements at Val Susauna-L5, with (a) ERT-data and (b) SRT-data and corresponding time-lapse tomograms.

Seasonal or perennial frozen ground occurrences must be regarded as most unlikely in the area of array L5, even though ERT-data indicate resistive anomalies ranging around the order of magnitude defined as boundary values for frozen ground conditions (~15 kΩm).

6.2.1.3 Brüeltobel

Results from joint application of ERT and SRT conducted in spring 2009 at two sites in the Brüeltobel are presented in FIGURE 6.12. Extracted data from all measurements

are presented as virtual boreholes in FIGURE 6.13. Geophysical boundary values representative for frozen and unfrozen ground conditions at the Brüeltobel are determined to be around 9 kΩm and 1.5 km/sec, respectively.

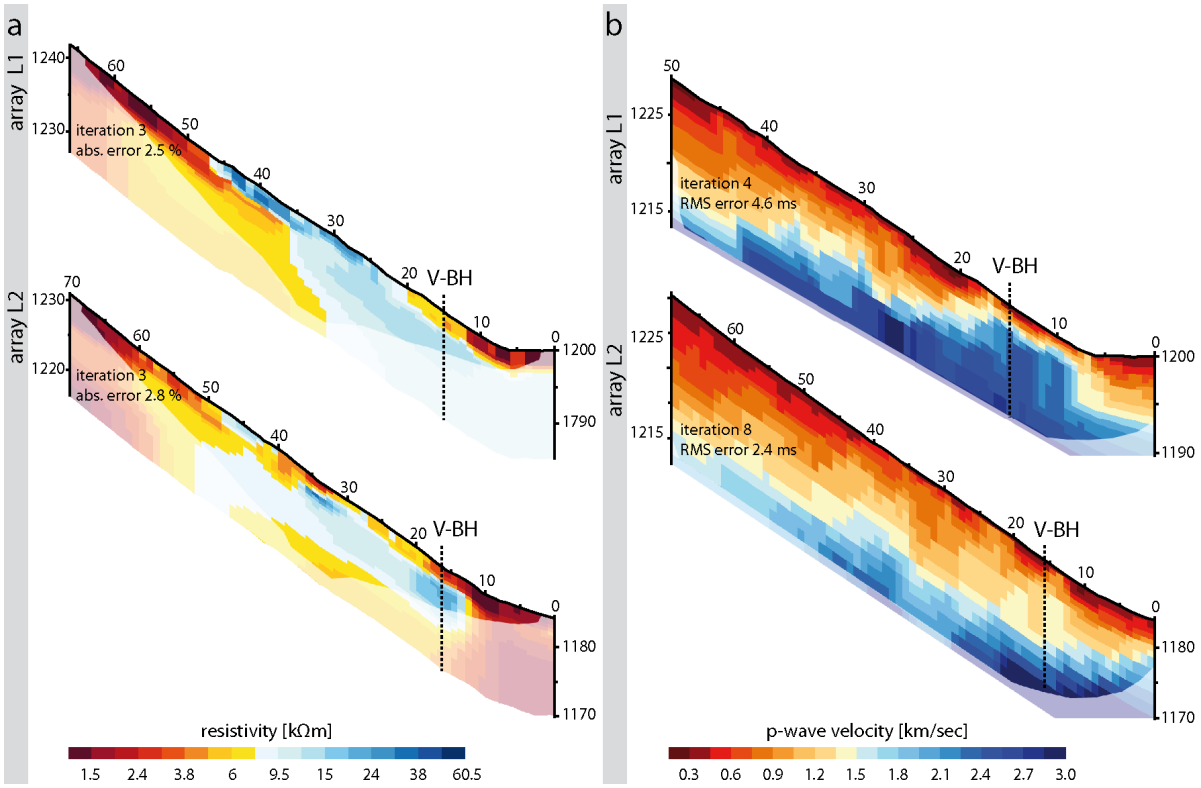

Figure 6.12: Tomograms from geophysical measurements at Brüeltobel L1 and L2, with (a) ERT-data and (b) SRT-data.

When comparing the ERT tomograms from arrays L1 and L2 a similar characteristic of the subsurface resistivity distribution is visible. Low resistivity zones (<4 kΩm) are detected at the foot of the slope and below the rock wall towards the top of the slope. The central parts of the tomograms can be differentiated into two sections (~26 m for L1; ~35 m for L2). The section towards the foot of the slope is characterised by a near-surface layer (0-2.5 m depth) with relatively low resistivities (1-8 kΩm) and a resistive anomaly (12-20 kΩm) in the subsurface. The opposite can be observed for the section towards the rock wall, with high resistivity values in the near-surface layer (up to 30 kΩm) and minor values (5-8 kΩm) in the subsurface. The resistivity distribution in the subsurface of the Brüeltobel study sites is in very good agreement with the site-specific surface and vegetation characteristics. A thick layer of conductive organic material, vegetated with dwarf-grown trees, superimposes the talus material in lower

sections of the slope. Upslope, the talus slope is unvegetated and high resistivities in the shallow subsurface reflect the resistive, loose limestone talus. Subsurface resistivity distribution shows high values below the vegetated slope section indicating frozen ground conditions in this area and unfrozen talus in the upper, unvegetated section. However, maximum resistivity values are, compared to the Val Susauna and Val Bever site, relatively low.

The corresponding SRT tomograms qualify for a more sophisticated interpretation of results. A delimited high velocity anomaly (1.5-2.5 km/sec) in the lower parts of the slope (7-17 m) of array L1 is in good agreement with the resistive anomaly detected by ERT and indicates frozen ground conditions in early June. As the contrast in electrical resistivity appears to be relatively low between frozen and unfrozen material, the thickness of the frozen ground body is hard to distinguish. An active layer thickness of 1.5-2.5 m can be derived from ERT and SRT data. Towards the upslope areas, ERT and SRT indicate unfrozen conditions. Results from ERT and SRT for array L2 do not coincide as well as shown for L1. Subsurface velocities indicate homogeneous subsurface characteristics with values increasing gradually with depth from 0.3 km/sec in the near subsurface towards 2-2.5 km/sec below 13-15 m depth. Corresponding to the resistivity maximum in the ERT tomogram between horizontal distances 10-20 m, a slight anomaly with velocities of 1.3-1.5 km/sec is indicated by SRT-data. Compared to velocities measured in L1 these values are relatively low. However, a definitive interpretation is hard to accomplish.

Virtual boreholes extracted from the ERT and SRT tomograms of array L2 in this area (FIGURE 6.13 b) illustrate the geophysical subsurface distribution in detail. Both, ERT and SRT of L2 show relatively low values from 0 to 2 m depth. Below, towards a depth of 3.5 m, resistivity values increase to 19 kΩm. Increasing values are also illustrated for seismic velocities in the depth section between 2 and 3.5 m. However, the gradient of increase and velocities of solely 1.4 km/sec are relatively low. In contrast, the virtual boreholes of array L1 (FIGURE 6.13 a) clearly indicate frozen ground conditions below 2.5-3 m depth. The active layer is characterised by relatively low values of 0.3-1.5 km/sec and 6-7 kΩm, respectively. In contrast to the velocity curve of L2, a sharp bend is observable in the course of the curve of L1, representing the location of a distinct refractor. The velocity-curve of L2 describes a smooth, S-shaped curve, with a

sharp bend at ~3 m depth, corresponding to the location of the top of the anomaly illustrated by ERT-data. The presence of frozen ground in this section of the slope can not definitively be precluded. Various effects – hidden or blind layers (cf. CHAPTER 2.1.2) as well as the effects of inappropriate geophone spacing – must be considered in the discussion of results.

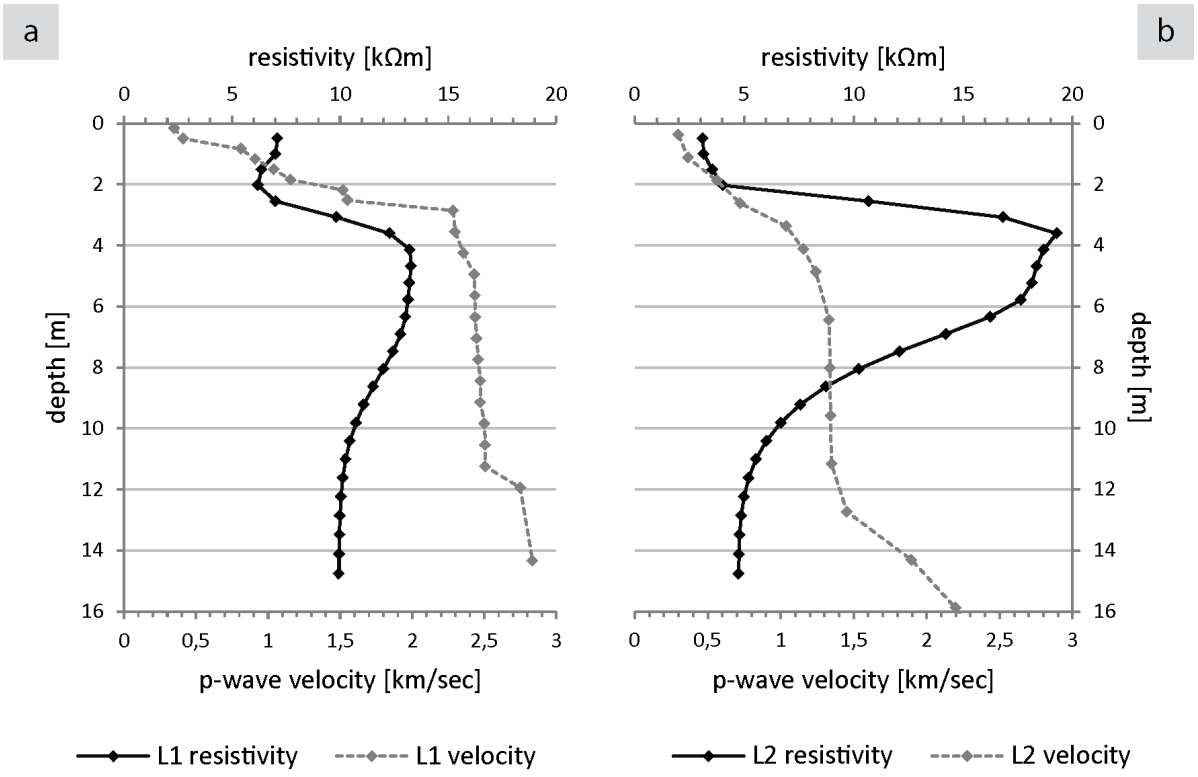

Figure 6.13: Virtual boreholes of electrical resistivity and p-wave velocity values measured at the Brüeltobel sites L1 (a) and L2 (b).

6.2.1.4 Comparison of geophysical subsurface properties in time and space

For a detailed interpretation and comparison of geophysical properties and their seasonal variability at the various study sites, electrical resistivity as well as seismic velocity values were extracted and analysed. Focus was set on areas defined as perennial frozen ground, the corresponding active layer (FIGURE 6.15) and on the comparison of overall values (FIGURE 6.14) for all sites of measurements.

Inverted specific resistivities (FIGURE 6.14) are in general distinctly higher at the granitic talus slope in the Val Bever compared to the Val Susauna (dolomitic) and Brüeltobel (limestone) study sites. This is a result of the diverse talus substrates and

the associated porosity. All sites, except for VB-S1, show decreasing values for maximum and median resistivities, and a decreasing interquartile range (IQR). It is notable that the median of resistivity values at the Val Bever sites are located in the lower half of the IQR, while values of the Val Susauna and Brüeltobel sites are located in the upper half. Measurements at the Val Susauna site show comparable median values for site L5 (6.75 kΩm/5 kΩm), where no ground ice was detected, and for the monitoring site (6 kΩm/5 kΩm), where perennial frozen ground is present. However, IQR and range of resistivity values are distinctly higher for VB-mon with perennially frozen ground. Values at the Brüeltobel site show a comparably high range of resistivity values compared to the IQR. This reflects the heterogeneous substrate and surface characteristics as well as the relatively low resistivity values of the frozen ground body determining a strong scattering of values. Low minimum values are driven by the high conductivity within the humus layer and areas at the foot and the top of the talus slope; high values by the loose talus material (cf. FIGURE 6.12). In contrast to the remaining sites, maximum values are not located within the frozen ground body, but near the surface in the unvegetated areas of the talus slope.

The analysis of inverted p-wave velocities (FIGURE 6.14) shows analogue conditions as ERT-data, with a decrease of median velocities and of the IQR. The evaluation of minimum and maximum velocities is less diagnostic than for ERT-data. Minimum velocities are driven by the direct waves (~0.3 km/sec), maximum velocities are influenced by parameters of the starting model and can be found in areas of the tomograms close to the maximum penetration depth, that are excluded from interpretation, as they are not covered by raytraces (cf. CHAPTER 2.1.2.3). The variability of median velocities and the IQR at the sites in the Val Bever are linked to the dimensions of the frozen ground bodies that are largest for VB-S1 and smallest for VB-L7. The most prominent variations appear at the Val Susauna sites. While median values of p-wave velocities show a slight decrease between July and October, maximum values and IQR decrease distinctly at both sites. While minimum velocities as well as the lower quartile remain almost constant, maximum values and the upper quartile show a distinct variability. Overall velocity values of VB-mon in October show a remarkable resemblance to July data from VB-L5, where frozen ground is assumed to be absent. The strong decrease of the IQR and maximum values for VS-L5 indicate supercooled subsurface material – with no clear indication of frozen ground – in July. Maximum

values in October decrease below the boundary values defined for frozen ground. However, the interpretability of overall-values is rather limited, as the spatial component – small frozen ground bodies, small-scale substrate heterogeneity – cannot be taken into account.

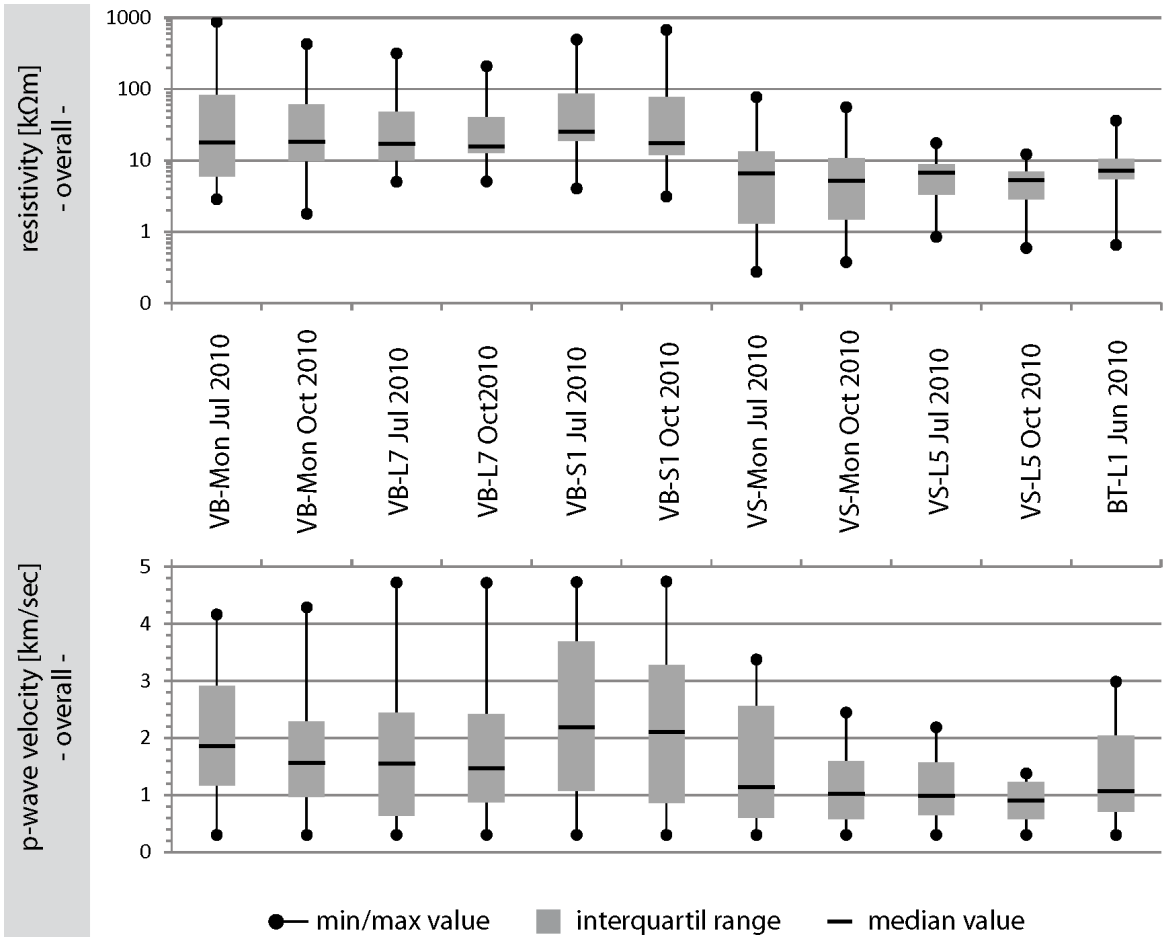

Figure 6.14: Boxplots of overall-values derived from ERT and SRT data for all study sites.

For a further analysis, focus was set on characteristic areas of the tomograms, i.e. frozen ground bodies and the corresponding active layer (FIGURE 6.15). Based on only two dates of measurements a precise assignment of areas to the active layer and frozen ground body is hard to accomplish. However, areas were defined as perennial frozen ground when both measurements detected values equal or higher than the site-specific boundary values for frozen ground. Data from above these perennial frozen ground bodies were defined as the corresponding active layer. Extracted data representative for frozen ground and the corresponding active layer are presented in FIGURE 6.16, comparing results from ERT and SRT. FIGURE 6.17 accentuates the characteristics of

geophysical properties within the active layer and the frozen ground body by relating median resistivity and velocity values for each site and each date of measurement.

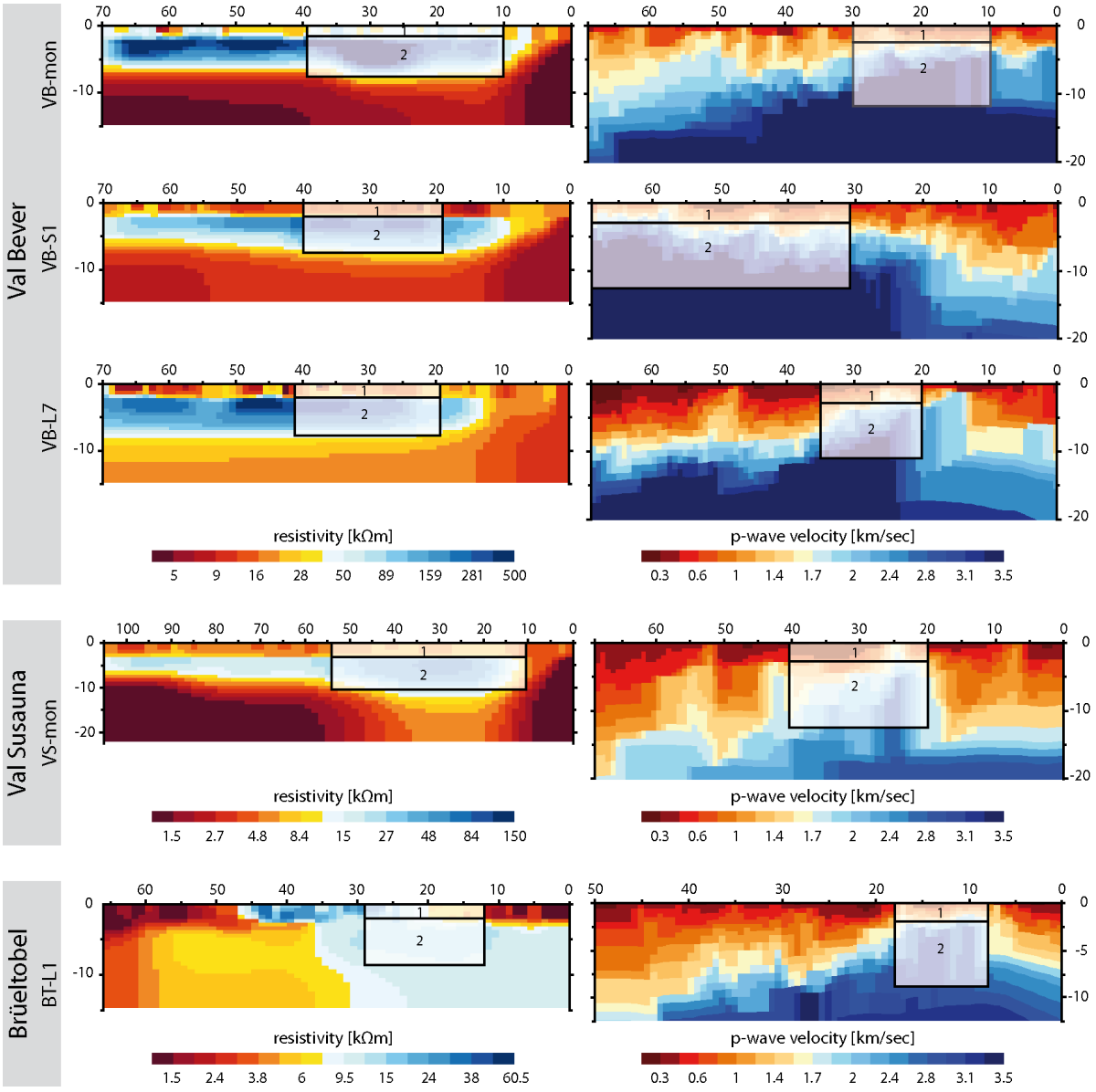

Figure 6.15: Positions for extraction of resistivity and velocity data for all sites, representing the active layer (1) and frozen ground (2).

The active layer is characterised by a strong heterogeneity of resistivity values within the different sites, along with a general trend to decreasing resistivity values towards the October measurement. Driven by the coarse, bouldery substrate, median and maximum resistivity values are higher at the Val Bever, although strong differences prevail among the three sites. This variability can be ascribed to the site specific surface characteristics (cf. TABLE 6.1) influenced by the presence and distribution of a

conductive humus and moss layer. Highest resistivity values and highest inter-annual variability (-50%) are detected for VB-mon, where humus and moss cover is fragmentary. VB-L7 shows a wide range of resistivity values (110 kΩm) in July, while the IQR (10 kΩm) is rather small, indicating only a few data points with above-average high/low values. This effect is most likely caused by partly frozen and drenched areas in juxtaposition. The same effect is assumed to cause the large resistivity range at the Brüeltobel at the beginning of June. Data from the Val Susauna show a very small scattering of resistivity values and a comparably slight inter-annual variation, most probably influenced by the consistent and conductive humus cover that determines sustained moist conditions in the near-surface. Within the active layer, SRT-data show minor variations of median velocity values ranging between 0.6 and 1 km/sec. Substrate-dependent variations in p-wave velocities in the shallow subsurface are rather small with 0.8-1 km/sec for the Val Bever, 0.6-0.75 km/sec for the Val Susauna and 1 km/sec for the Brüeltobel. Comparably high values at the Brüeltobel can be ascribed to partially frozen areas of the active layer at the beginning of June. Expectedly, minimum velocities are 0.3 km/sec, representing the velocity of the direct wave. The comparably high maximum velocities can be ascribed to the strong spatial and temporal heterogeneity of active layer thickness, respectively the depth of the frozen ground table. Regarding the inter-annual variability, all sites show decreasing median values (-10 to -20%) between July and October, except for VB-mon, where a slight increase of median values (+15%) and a strong increase of maximum values (+43%) can be observed.

The comparison of extracted data representing frozen ground conditions (FIGURE 6.16 & FIGURE 6.17) comprises a high complexity. A substrate-dependency is observable for both, ERT and SRT, with higher values (July measurement) for the granitic, bouldery talus compared to the dolomitic and limestone talus. While a general decrease of values between July and October was detected by ERT and SRT, the particular amplitude of decrease varies distinctly. The strongest decrease of resistivity values (-55%) has been detected for VB-S1. In the corresponding SRT dataset velocities decrease by only 2.2% from 3.16 to 3.09 km/sec. Resistivity values of the frozen ground body at VB-mon and VB-L7 decrease by ~30%; corresponding SRT-datasets show a decrease of 33% (2.85-1.9 km/sec) for VB-mon and of only 5% (2.5-2.4 km/sec) for VB-L7. At the Val Susauna monitoring site (VS-mon), electrical resistivity values and seismic velocities decrease by ~30%. While median resistivities of around 30 kΩm in October are still

indicative for frozen ground, seismic velocities decrease towards 1.6 km/sec, approaching boundary values defined for frozen ground. The contrary is observable for the Brüeltobel site. Low median resistivity values (12 kΩm) are accompanied by rather high p-wave velocity values (2.3 km/sec) in early June. The very small IQR indicates a minor scattering of resistivity values within the frozen ground body. The median of resistivities and velocities is located closer to the corresponding maximum than towards minimum values, pointing to a minor number of outliers with low values.

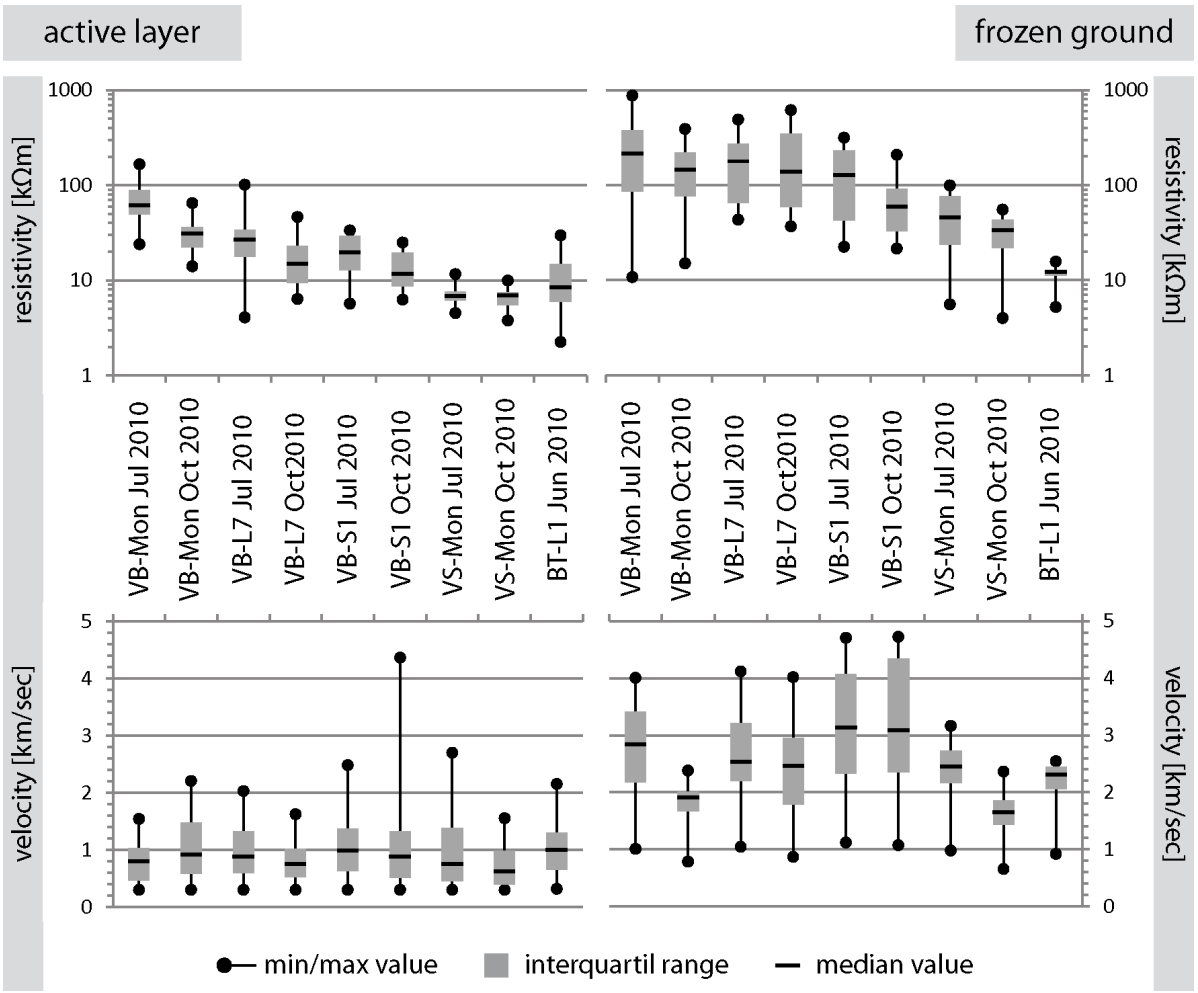

Figure 6.16: Boxplots of extracted resistivity and velocity data from all study sites, representative for the active layer (left) and frozen ground (right).

FIGURE 6.17 allows a direct comparison of the distribution and evolution of median resistivities and velocities within active layers and frozen ground bodies. Resistivity values within the active layer scatter on a large range (7-60 kΩm) compared to a rather small range for seismic velocities (0.6-1 km/sec). Values of the frozen ground bodies show a large scattering for both, ERT (12-204 kΩm) and SRT (1.6-3.1 km/sec).

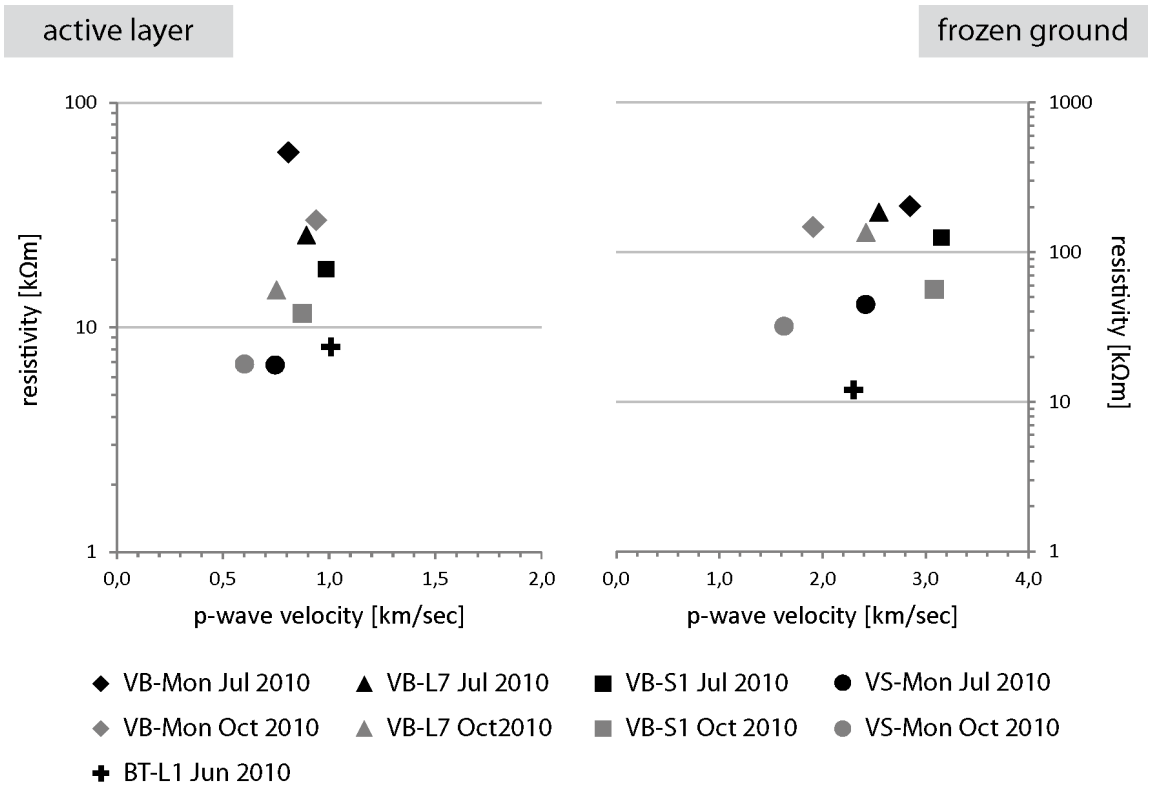

Figure 6.17: Relationships between electrical resistivity and P-wave velocity within the active layer and the frozen ground body. Extraction of data according to Figure 6.15.

6.2.2 Areal estimation of frozen ground distribution

Presented are results from geophysical mapping in the Val Susauna using ERT and SRT (FIGURE 6.19) as well as quasi-3D electrical resistivity images measured in the Val Bever and Val Susauna (FIGURE 6.18). The analysis of results – especially from quasi-3D ERT – is supported by information drawn from joint ERT/SRT measurements presented above. The quasi-3D image of the Val Susauna is presented in CHAPTER 5.3 focussing on the explanatory power and reliability of quasi-3D ERT. For location of the quasi-3D grids in relation to the remaining measurement presented in this chapter see FIGURE 6.2 & FIGURE 6.3.

Quasi-3D images (FIGURE 6.18) show high resistive anomalies below a depth of 1.5 m at both study sites. As presented above, the range of resistivity values representative for frozen and unfrozen subsurface conditions differs between the Val Susauna and Val Bever. Supported by results from joint ERT/SRT measurements, a continuous, large-area frozen ground occurrence is confirmed for both investigated talus slopes. Low resistivity values within the top three layers of both images indicate an active layer

thickness of 1.5 m, which is lower than the thickness indicated by 2D ERT (2-3 m) presented above (FIGURE 6.9 & FIGURE 6.13). The range of resistivity is rather homogeneous for most parts of the top three layers of both 3D images. At the Val Susauna site, a small area with higher values (8-15 kΩm) has been detected between 0 and 1.5 m depth (x-direction 20-30 m; y-direction 10-30 m). High values in the near-surface were likewise detected by array L3 (FIGURE 6.19) that is located in this section of the slope. An anomaly (20-60 kΩm) within the near-surface is also observable in the 3D image of the Val Bever, between x-distance 0-35 m and y-distance 0-50 m. Both anomalies can be ascribed to variations of surface characteristics. At the Val Susauna site a small area towards the foot of the slope consists of uncovered talus; the slope section in the Val Bever that corresponds to the near-surface resistivity anomaly is characterised by a fragmented humus and moss cover in contrast to the remaining parts of the slope, where a rather thick humus cover persists (Figure 3.2c).

The 3D images indicate vertical extents of the frozen ground bodies that range between 1.5 and 8 m for the Val Susauna and from 1.5 to 9 m for the Val Bever. Maximum resistivity values are located at a depth of 4-5 m (~300 kΩm) in the Val Susauna and between 3-4 m depth in the Val Bever (~400 kΩm). With regard to the areal extent of the frozen ground bodies and their spatial heterogeneity, the 3D images expose diversities between the study sites. The areal extent of the frozen ground body in the Val Susauna is strongly confined, with a high gradient of resistivity values towards both sites of the frozen ground body and towards the foot of the slope. Upslope (y-distance 40-70 m) an area with resistivity values around 15-20 kΩm follows the high resistive body. Corresponding to results from joint ERT/SRT measurements that are presented above (cf. FIGURE 6.10) it must be assumed, that no frozen ground is present in this area.

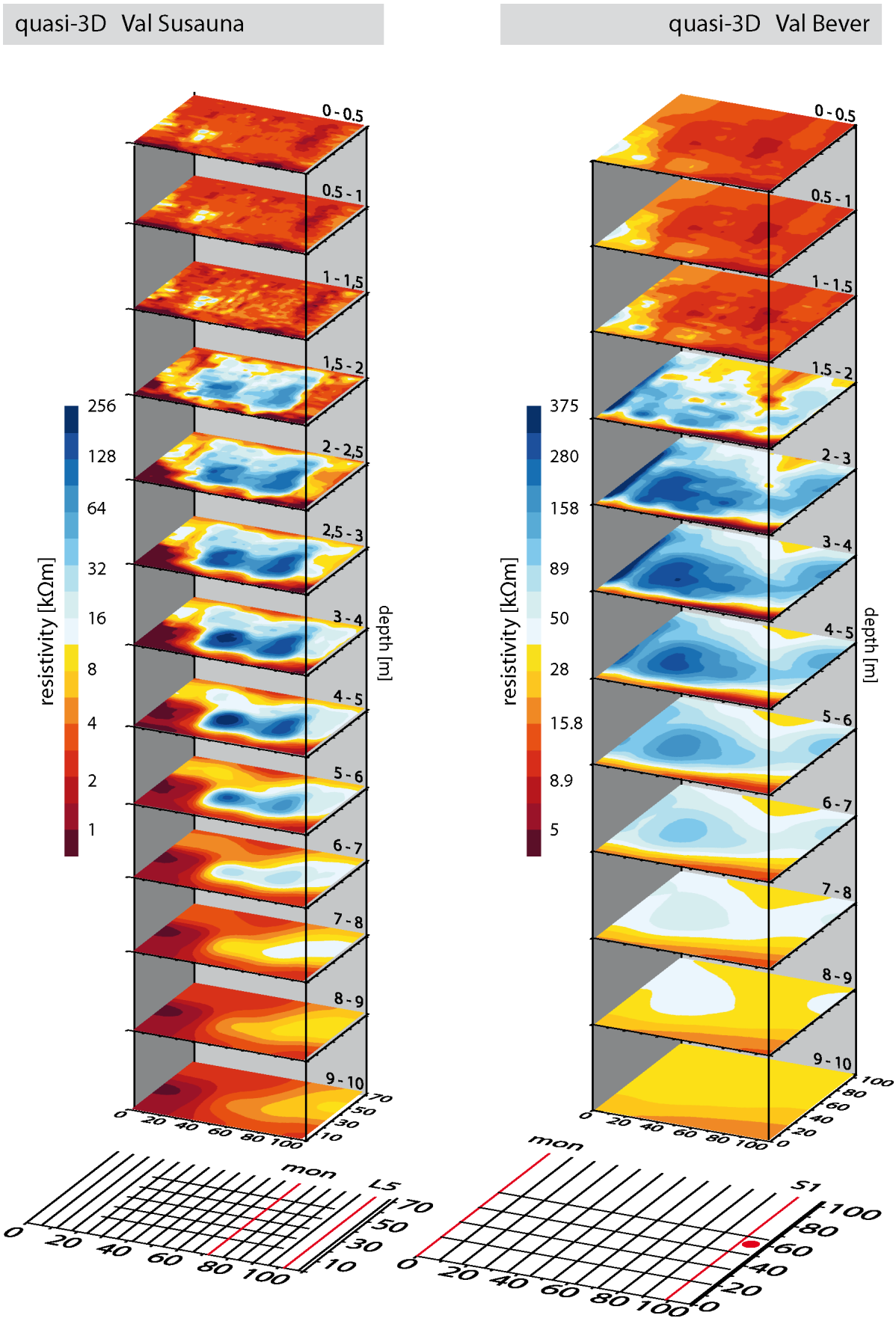

Figure 6.18: Quasi-3D resistivity images from Val Susauna and Val Bever with corresponding grid-setups.

In contrast, the 3D-image of the Val Bever indicates large-area frozen ground conditions for most parts of the investigated slope between 1.5 and 9 m depth. Unfrozen areas in this depth-section can only be found at the foot of the slope (y-distance 0-10 m). A distinct heterogeneity within the frozen ground bodies is detected at both studies. At the Val Susauna the frozen ground body is divided into two main high-resistive areas (>130 kΩm) by an area with resistivities of around 30-70 kΩm.

The 3D image of the Val Bever shows a differentiation of the frozen ground body into two main sections. The western part of the investigated site (x-distance 0-70 m) shows a large anomaly with maximum values orientated towards the foot of the slope (y-distance 20-40 m). A second structure is located in the western part of the grid (x-distance 80-100 m) towards the forest aisle (cf. FIGURE 6.5) with maximum values located in the upper parts of the investigated slope section (y-distance 50-90 m). This is in good agreement with measurements of VB-S1 and VB-mon presented above (FIGURE 6.5 & FIGURE 6.7).

The evident spatial heterogeneity detected by quasi-3D ERT at the Val Susauna is confirmed by geophysical mapping using ERT and SRT (FIGURE 6.19). Arrays L1, L2 and L3 are located in the dwarf-growth zone of the Val Susauna; L0 is located in the neighbouring forest (for location in relation to remaining measurements presented in this section see FIGURE 6.3. Data indicate a strong variability of geophysical subsurface conditions within a short distance. Arrays L1, L2 and L3 show delimited high resistivity/high velocity bodies located towards the foot of the slope. As presented for VS-mon (FIGURE 6.10) resistivity tomograms show a main high-resistive structure in the lower parts of the slope (horizontal distance 8-45 m) and a shallow, thin structure, that extents upslope. Corresponding to VS-mon, frozen ground can only be confirmed for the main structure in the lower parts of the slope with p-wave velocities of up to 4 km/sec. ERT and SRT data are in good agreement regarding the spatial heterogeneity of subsurface properties. Highest values are detected for array L2. Towards both sides values are highest for L2 (~200 kΩm; ~4 km/sec), in the central parts of the dwarf-growth zone, and decrease to both sides. The spatial extent of the frozen ground body increases towards array L1 – which is in good agreement with results from quasi-3D ERT (FIGURE 6.18) – and decreases towards array L3. The results are in accordance to

quasi-3D ERT (FIGURE 6.18) and array VS-L5 (FIGURE 6.11) as no frozen ground has been detected by array L0 in the neighbouring forest.

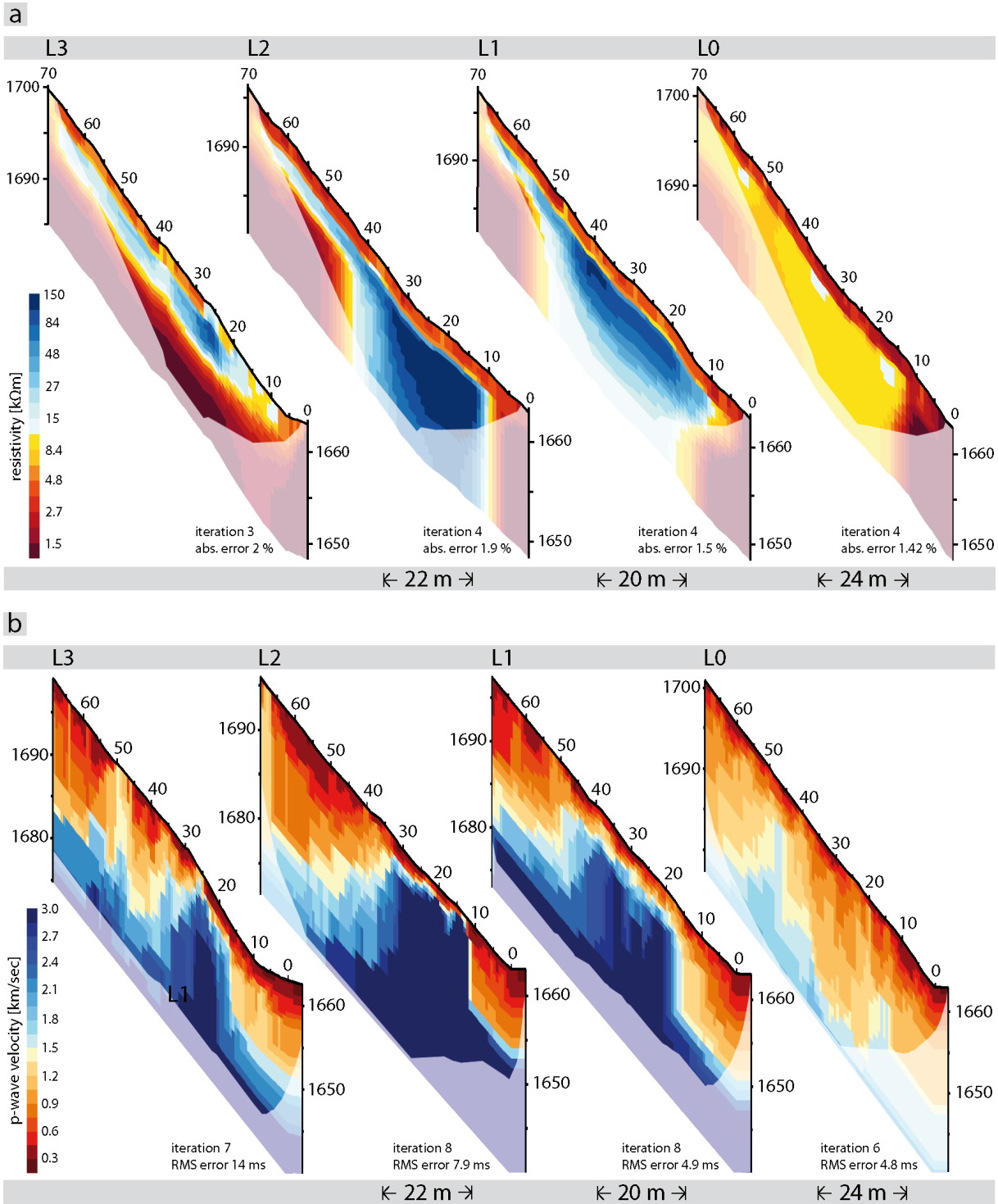

Figure 6.19: Tomograms from geophysical mapping at the Val Susauna, with (a) ERT data and (b) SRT data.

6.3 Discussion

In recent years the joint application of ERT and SRT has proven to be a reliable tool for the detection and characterisation of frozen ground (Ikeda, 2008; Kneisel et al., 2008; Vonder Mühll et al., 2001). Results presented in this study emphasize this fact and underline the statement by Ikeda (2008), who questions statements that are merely based on resistivity methods.

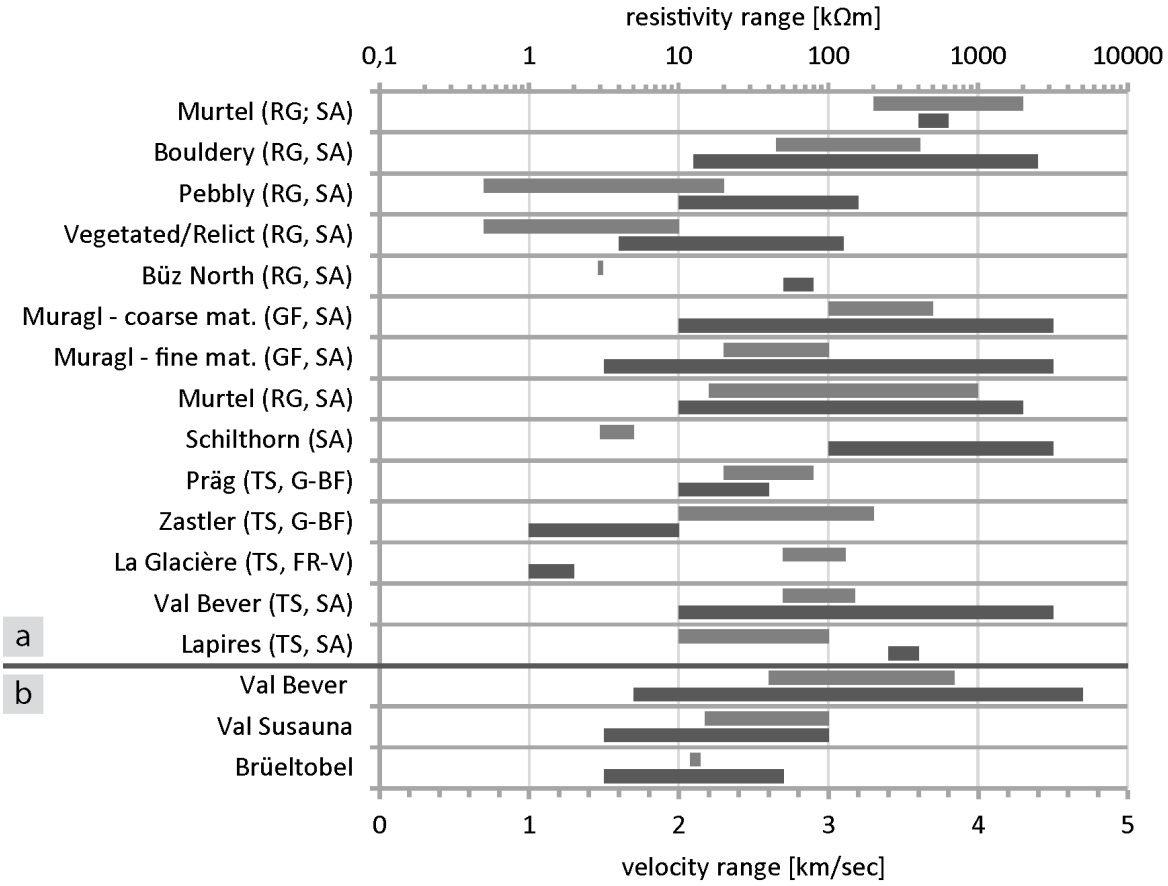

Figure 6.20: Electrical resistivity and seismic velocitiy values from the study sites Val Bever, Val Susauna and Brüeltobel in comparison to values from miscellaneous mountain permafrost settings (compiled after: Hauck & Kneisel, 2008a; Hilbich, 2010; Hilbich et al., 2008; Kästl, 2012). Abbreviations: RG – rock glacier; GF – glacier forefield; TS – talus slope; SA – Swiss Alps; G-BF – Germany, Black Forest; FR-V – France, Vosges.

Geophysical boundary values for frozen and unfrozen subsurface conditions were calibrated by comparison of ERT and SRT data and, at the Val Bever site, by comparing geophysical data with borehole temperatures. Direct comparison of vertical distribution of electrical resistivity and p-wave velocity values with borehole temperatures enables

for a sophisticated specification of boundary values. However, the direct comparison of the vertical course of ERT and SRT data has also proven to provide reliable data. KRAUTBLATTER et al. (2010) calibrated ERT with frozen rock temperatures by laboratory analysis to relate temperature and resistivity data. This approach is hard to perform for talus slopes, as it is probably impossible to do a laboratory analysis of a representative sample of talus material. Furthermore, it is most likely that the variable composition of the talus slopes with rock material, air filled voids, ice and unfrozen water is rather represented by a range of geophysical values. The four-phase model introduced by HAUCK et al. (2008; 2010) takes this variability into account by combining electrical resistivity and seismic velocity data to estimate volumetric content of rock, water, air and ice within the subsurface.

The range of resistivity and velocity values determined for frozen ground varies distinctly between the three investigated sites. However, boundary values and ranges of values are in accordance to the large ranges detected at other alpine sites with permafrost (FIGURE 6.20). Resistivity and velocity values are generally higher for sites with coarse-grained material compared to fine grained and pebbly material. This is in agreement with results presented in this study. Boundary values at all three sites within the granitic, bouldery talus slope of the Val Bever (35 kΩm; 1.8 km/sec) exceed values of the finer grained talus slopes of the Val Susauna (15 kΩm; 1.5 km/sec) and the Brüeltobel (9 kΩm; 1.5 km/sec). Applying the four-phase model to measurements in the forest aisle of the Val Bever (approximately same location as array VB-S1), HAUCK & KNEISEL (2008b) calculated ice contents of 15-25%. Based on an assumed porosity of 20% this value would indicate full ice saturation. High velocity (up to 4.5 km/sec) and resistivity values (300 kΩm) measured at site VB-S1 in July likewise indicate high ice-contents. However, varying maximum values and value ranges within the Val Bever shows that a prominent spatial heterogeneity and temporal variability persists. The deduction of a reliable, spatially alienable characterisation of subsurface properties should be based on more than one measurement at more than one site. For the scree slopes below the timberline Präg, Zastler and La Glacière (cf. FIGURE 6.20), HAUCK & KNEISEL (2008b) point to a possible existence of ground ice. The range of values for the three sites investigated by HAUCK & KNEISEL (2008b) deviate from results presented in this study. Consisting of bouldery talus, especially results for seismic velocities at Zastler and La Glacière are distinctly lower than for the Val Bever site and even below values

for the slopes of Val Susauna and Brüeltobel that consist of finer grained material. However, a direct comparison of geophysical parameters for frozen ground between different sites appears difficult with regard to spatial variability, even within one study site.

The comparison of ERT and SRT datasets depicts some discrepancies between results. Resistivity tomograms show elongated anomalies, pervading throughout most parts of the tomograms (Val Bever and Val Susauna), with maximum values and thicknesses towards the foot of the slope. SRT-data show delimited high-velocity bodies only in the lower parts of the slope and no indication of a refractor upslope. A definitive explanation of this effect is hard to accomplish. Especially within the Val Susauna site (FIGURE 6.10), resistivity values of the anomaly in the upper parts of the array are relatively low and close to the lower boundary values defined for frozen ground. Values between 10-25 kΩm could be ascribed to a high amount of air-filled voids in the upper parts of the slope. Unfrozen, loose talus would explain low velocities in this area. However, it is also possible, that frozen subsurface material exists, with minor thickness and/or low amounts of ice. In this case hidden layer effects (cf. Chapter 2.1.2, see also SCHROTT & HOFFMANN (2008) and REYNOLDS (2011) could appear. A related effect has been detected at the Brüeltobel site (FIGURE 6.12). Results of arrays L1 and L2 are opposed. Relatively low resistivity values (12-14 kΩm) stand in contrast to comparatively high velocity values (2-2.5 km/sec) in the lower parts of array L1. In the lower parts of array L2, high resistivity values of 12-20 kΩm were detected, while velocities in the corresponding section are below 1.4 km/sec (FIGURE 6.12 & 6.13). For array L2, no definite refractor has been detected. However, a potentially undetected frozen layer could be ascribed to an inappropriate geophone spacing (3 m). For array L1, the geophone spacing was 2 m and a clear refractor has been detected. The relatively low electrical resistivity and high velocity values detected for array L1 can be ascribed to the date of measurement early in the year, shortly after snowmelt. In early spring, the talus material is assumed to be supercooled as a result of the activity of the chimney effect. Refreezing of percolating melt water on the supercooled talus material causes a growth of the volumetric ice content. The release of latent heat during the freezing process increases the temperature of talus material and ground ice. Consequently, the volume as well as the temperatures of ground ice occurrences increases during snowmelt. Due to temperatures only slightly below the freezing point, unfrozen water content is

increased, likewise. The relatively low electrical resistivities are assumed to be driven by high contents of unfrozen water; high velocities reflect high ground ice volume. Unfortunately – in consideration of the sensitive eco-system – no further joint ERT/SRT measurements were conducted later in the year at this site. Further details on the temporal frozen ground variability will be given in CHAPTER 7.

The application of repeated ERT/SRT measurements turned out to state a distinct improvement in the characterisation of talus slopes with ground ice occurrences. In contrast to sites above the timberline, where the seasonal variability of permafrost is mainly restricted to variations in the active layer thickness, the temporal variability of talus slopes comprises the whole frozen ground body. During the last few years ERT-monitoring approaches were widely applied to permafrost related problems (HAUCK, 2002; HAUCK & VONDER MÜHLL, 2003c; HILBICH et al., 2011; HILBICH et al., 2008; KNEISEL et al., 2008; KNEISEL et al., accepted; KRAUTBLATTER & HAUCK, 2007; KRAUTBLATTER & VERLEYSDONK, 2008). However, time-lapse SRT was, up to now, only applied by HILBICH (2010).

Results of repeated measurements presented above show a distinct variability of subsurface parameters during summer with strong differences in the amplitude of variability. Furthermore, the trend of variability between measurements in July and October differs for ERT and SRT data among investigated sites. Generally it would be expected, that degradation of frozen ground within ventilated talus slopes is initialized by snowmelt in spring, with the refreezing of percolating water (see above). During summer, the fraction of ice is expected to decrease in the four-phase medium of the talus slope with the effect of decreasing electrical resistivity and p-wave velocity values. This is clearly observable for the site VS-mon at Val Susauna (Figure 6.10) and VB-mon at Val Bever (FIGURE 6.7), where decreasing values in lower parts of the slopes indicate strong frozen ground degradation. Aberrant results are detected for sites VB-S1 (FIGURE 6.5) and VB-L7 (FIGURE 6.8) at Val Bever. Frozen ground at VB-L7 is only detected by both methods in lower parts of the slope (horizontal distances 15-35 m). For upslope areas, both methods deliver opposing results (see discussion above for VS-mon). High resistivity values indicate frozen ground, while velocities are rather low, with no indication of a refractor. Towards the subsequent measurement, SRT-data show little variation with a trend to decreasing values for the area defined as frozen ground (Figure

6.8) and an increase of values for the unfrozen near-surface upslope areas. The resistivity tomogram shows a vertical differentiation of resistivity evolution within the anomaly. An increase is detected in shallow depth (2-4 m depth) and a decrease below. Results from VB-S1 show decreasing resistivity values for the whole frozen ground body, but a spatial differentiation of velocity data, with an increase of velocities upslope (27-60 m) and a decrease in the lower parts of the anomaly, indicating unfrozen conditions in October (horizontal distances 15-30 m).

Without direct measurements of borehole temperatures, a definitive interpretation of these results is hard to accomplish. However, the variable seasonal evolution within the Val Bever is assumed to be influenced by site-specific compositions of surface material (humus distribution, moss cover). The porosity of the subsurface is a variable, which cannot be determined with certainty and is assumed to be constant for the three sites within the Val Bever. Indications of frozen ground degradation are given by ERT and SRT for VB-mon, where the humus layer is fragmented and disturbed by granitic boulders. At this site interaction between humus/moss cover and frozen subsurface material are assumed to be lowest. VB-S1 and VB-L7 are characterised by a diverse vegetation composition with grasses and a shallow humus layer at the foot of the slope and mosses superimposing a thick humus layer upslope. The surface composition is reflected by resistivity values of the active layer (FIGURE 6.16) with higher values for VB-mon compared to VB-L7 and VB-S1. The strongest decrease of velocity values in VB-S1 is detected towards the foot of the slope, where the insulation capability of organic material (shallow humus cover, grasses) is lowest. However, this effect is not illustrated by ERT-data that show a homogeneous decrease of values. The increase of resistivity values in VB-L7 (FIGURE 6.8) is strongest where a thick humus/moss cover persists. In this area (horizontal distances 20-60 m) the conductivity of the active layer increases distinctly and with a higher amplitude compared to the remaining Val Bever sites. A definitive explanation of the processes inducing the evolution of geophysical parameters requires further investigations and cannot be presented at this point. However, it is assured, that the investigated frozen ground bodies of the Val Bever and Val Susauna persisted throughout the summer of 2010. With the last measurement conducted in October, it is furthermore highly unlikely, that further degradation occurred before winter 2010/2011.

Quasi-3D resistivity measurements were conducted at the Val Bever and the Val Susauna site to achieve a spatial detection and characterisation of frozen ground. Geophysical mapping using ERT and SRT in joint application has been conducted in the Val Susauna.

Areal frozen ground occurrences were detected by quasi-3D imaging at the Val Susauna and the Val Bever. However, as discussed above, there are some discrepancies between ERT and SRT data in the detection of frozen ground. ERT and SRT data coincide very well for areas in the lower parts of the slope, where ground ice is assumed to be thickest, but give opposing results for areas upslope. With regard to this, the areal extent of the frozen ground body in the Val Susauna (FIGURE 6.18) is assumed to be overestimated towards areas upslope. The sharp contrast in resistivity values towards both sides and at the foot of the slope indicates a sharp transition zone between frozen and unfrozen areas, which is in agreement with the vegetation composition. This is further supported by quasi-3D ERT results in the Val Susauna. Here, geophysical mapping using ERT and SRT underlines the presence and spatial heterogeneity of frozen ground in the dwarf growth zone, as well as the absence of frozen ground in the neighbouring forest. Quasi-3D imaging at the Val Bever site (FIGURE 6.18) likewise allows for a comparison of the subsurface resistivity distribution with surface characteristics. Low resistivities at lowest parts of the slope are correlated with fine-grained material. One main anomaly in the western part of the grid (x-distance 0-70 m; y-distance 10-60 m) is related to an area with the surface distribution of array VB-mon (cf. TABLE 6.1). A second, smaller anomaly in the eastern part (towards the forest aisle of array VB-S1) has its central parts shifted upslope, where a consistent humus cover prevails, while the lower parts are covered with grasses. In contrast to the Val Susauna, where the whole frozen ground body is imaged, the quasi-3D grid of the Val Bever only covers parts of the frozen ground occurrence. An extension of the grid towards both sides would be of interest.

The technical aspects of quasi-3D imaging have been discussed in detail in CHAPTER 5. Results have shown that some points have to be considered regarding the interpretability of active layer thickness, frozen ground thickness and maximum resistivity values. The comparison of datasets from 2D ERT, 2D SRT and quasi-3D ERT show rather variable results regarding active layer thickness. 2D ERT data indicate

thicknesses of 2-3 m with little variations between sites and measurements. The quasi-3D images also show rather homogeneous resistivity data for the top three layers. However, active layer thickness derived from quasi-3D is 1.5 m. Results from 2D SRT indicate a heterogeneous active layer thickness that generally increases during the summer, which states a plausible result. For an interpretation of quasi-3D images, it is advisable to consider an interpretation of 2D data and to apply complementary methods – for example SRT – at some grid locations to achieve a more sophisticated interpretability of results.

6.4 Conclusions

Results presented in this study emphasize the high explanatory power of the repeated joint application of ERT and SRT for permafrost studies. In talus slopes, where a high temporal variability of frozen ground conditions can be expected, repeated measurements enable for a more sophisticated characterization of the subsurface. At the same time, the areal approach, achieved by geophysical mapping and quasi-3D electrical resistivity imaging, allowed for a spatial characterisation of study sites with special regard to frozen ground distribution.

- Frozen ground has been detected at all three study sites using repeated ERT and SRT measurements. Data indicate that frozen ground persisted throughout summer, pointing to potential permafrost occurrences at the Val Bever and Val Susauna.
- Geophysical parameters strongly differ between study sites as a result of talus substrate, ice content and ice characteristics.
- Furthermore, geophysical subsurface parameters vary between surveys within each study site, indicating a distinct spatial heterogeneity of the frozen ground distribution
- Repeated measurements indicate a distinct temporal variability of frozen ground characteristics during summer. Thereby, a general decrease of electrical resistivity values and P-wave velocities point to strong frozen ground degradation during summer.
- The magnitude of variation of geophysical parameters during summer diverges between the survey locations, pointing to a complex evolution of subsurface characteristics. Thereby, variations of frozen ground characteristics (ice degradation, complete thawing, variations in unfrozen water content) effectuate electrical resistivity and P-wave velocity values at different magnitudes.
- The combination of geophysical mapping and quasi-3D ERT allowed for a superior determination of areal frozen ground distribution at the Val Bever and Val Susauna. Thereby, quasi-3D ERT allowed for an assignation of 2D information on subsurface characteristics, derived from joint ERT and SRT measurements, into the third dimension.

7 Geophysical monitoring of the seasonal and intra-annual frozen ground variability

The application of geophysical monitoring systems is based on the assumption, that fundamental subsurface parameters (e.g. lithology, porosity) remain constant over the period of measurements, while climate- and temperature-dependent parameters (e.g. ice and unfrozen water content) show a seasonal as well as a long-term variability. During the last years electrical resistivity tomography (ERTM) systems have developed as the state of the art in monitoring of permafrost evolution on different time-scales (Hauck, 2002; Hilbich et al., 2008; Kneisel et al., 2008; Kneisel et al., accepted; Schwindt & Kneisel, 2010). In contrast to permafrost sites above the timberline (e.g. rock glaciers, glacier forefields, rockwalls), where the permafrost variability is first of all restricted to variation in active layer thickness, repeated ERT and SRT measurements (Chapter 6) have shown a distinct seasonal variability throughout the frozen ground bodies in the investigated talus slopes below the timberline. Driven by the activity of the chimney effect (Chapter 1.1.1), the high seasonal variability of frozen ground can be ascribed to degradation processes during summer, supercooling of the talus material during winter and growth in volumetric ice-content during snowmelt in spring (Wakonigg, 1996).

In this section year-around ERTM is applied at the study sites Val Bever, Val Susauna and Brüeltobel to:

- verify the presence of permafrost within the investigated talus slopes,
- detect phases and magnitude of frozen ground degradation and aggradation,
- deduce potential disparities in the seasonal and long-term evolution of subsurface properties between the three study sites in consideration of talus material and surface composition.

Repeatability tests were conducted for appraising the accuracy and repeatability of ERT-measurements and the effect of variable contact resistances in summer and winter.

The interpretation of ERTM-data is supported by data from temperature measurements (air-, ground surface-, humus- and vent temperatures) and data on snow cover thickness to:

consider the influence of the seasonal and inter-annual climate and snow-cover variability, as well as the site-specific thermal regime on frozen ground evolution.

Drawbacks of applying only ERT measurements and benefits of the joint application of ERT/SRT have been discussed in detail in (CHAPTER 6). For supporting ERTM-data, a fixed SRT monitoring array was installed at the Val Susauna site to achieve a more sophisticated interpretability of the evolution of subsurface properties during winter and spring. To date this states the first study applying SRTM during the snow covered period in winter (cf. CHAPTER 2.1.2.1).

7.1 Technical setup of the fixed monitoring arrays

The fixed monitoring arrays installed at the study sites are based on a self-made cable construction and self-made stainless steel electrodes. To enable year-around measurements the fixed setup requires for an accessibility of the plug throughout the year, a robust construction to achieve reliable measurements, as well as the possibility for easily fixing damages. Details on the construction are given in FIGURE 7.1 and FIGURE 7.2.

The cable construction is based on five eight-core patch cables. Depending on the required electrode spacing, the patch-cables were slit (every 3 m for Val Bever and Val Susauna and every 1.8 m for Brüeltobel) and a single core was extracted as takeout, with a total of 36 take-outs per array. The slits were sealed using silicone and self-welding tape. For protection against rodents and other animals and snow pressure in winter, cables were placed within flexible empty conduits. The cable construction was buried, as far as possible. Each core of the cable-construction was soldered to a plug-in connector, which was fastened to a nearby tree, to allow a year-round accessibility.

The transitions between cable and electrode represent the location of highest interference liability. The construction aims to ensure constant contact resistances and to minimize the effect of corrosion. Soldering would be the best solution to avoid contact resistances between transitions. However, to enable for a practicable installation and reparability of the take-outs the extracted cores were crimped to ring tongue terminals. Electrodes (40 cm length) were countersinked (FIGURE 7.1 a), to achieve a planar surface and the best possible transition between electrode and ring tongue terminal (FIGURE 7.2 b). Stainless steel screws were used for bolting the ring tongue terminals to the electrodes (FIGURE 7.2). To ensure, that only resistivity variations in the subsurface are recorded, corrosion at the transitions between cable and electrode has to be prevented. Therefore, heat shrink tubes and water impermeable and electrically insulating self-welding tape was used to protect transitions against moisture and, in case of buried cable/electrodes, against the soil solution (FIGURE 7.2 c). Takeout cables were tried to be kept as short as possible, to minimize the damage-susceptibility.

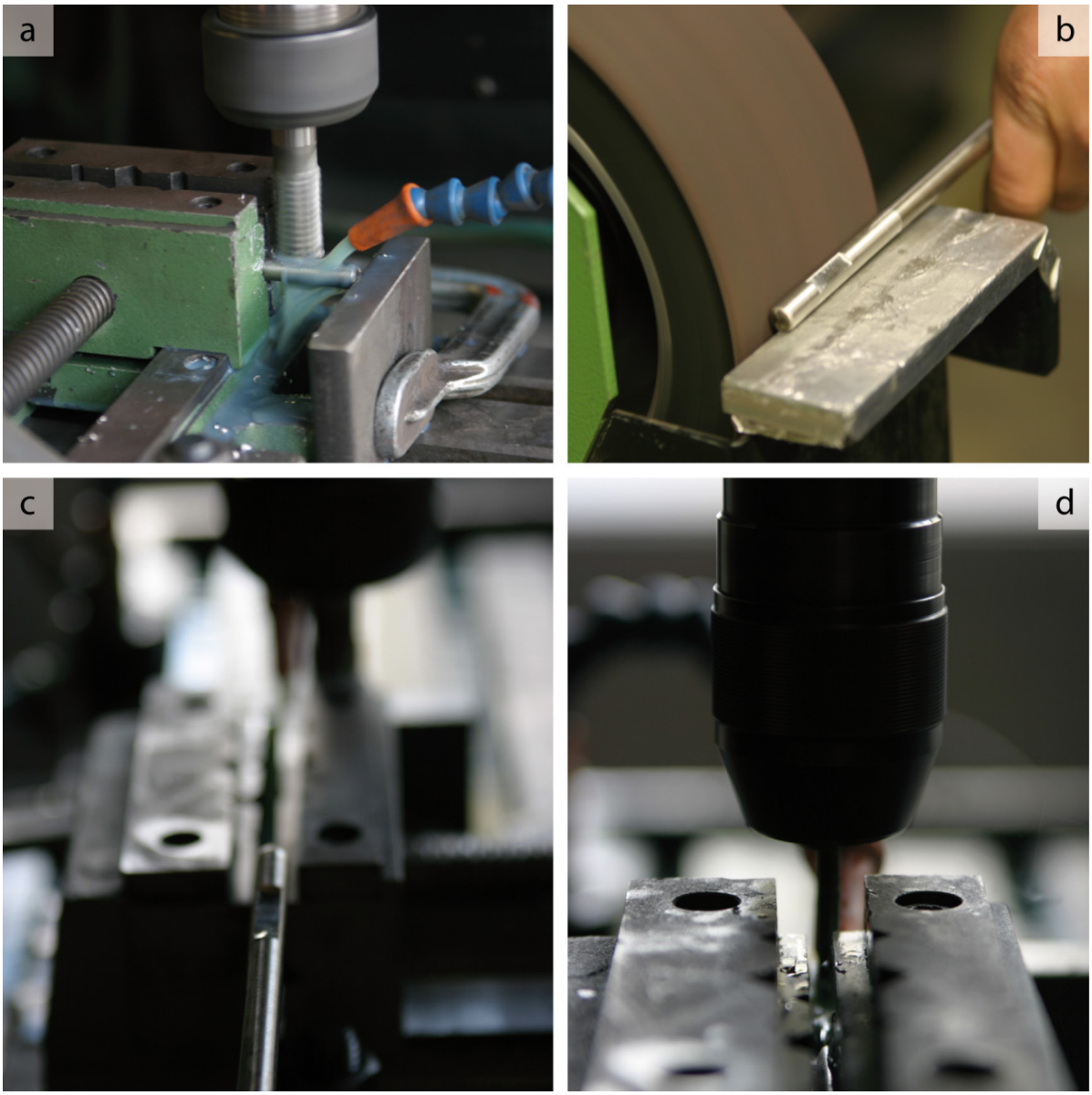

Figure 7.1: Preparation of stainless steel electrodes for ERT-monitoring, with (a) countersinking and (b) deburring of the electrode to achieve a planar surface; (c) and (d), drilling of the electrode for threading.

Figure 7.2: Installation of the fixed ERTM array, with connection and isolation of transitions between cable and electrode (a-c) and basic tools for the installation (d).

7.2 Methodological approach

The applied monitoring approach is based on repeated ERT measurements conducted at a monthly interval throughout the year. To support results from ERTM, and to achieve a more sophisticated interpretation of data, additional approaches were applied. Included are: (a) repeatability tests of ERT measurements, (b) synthetic data modelling for an appraisal of the reliability of ERTM-data, (c) the analysis of temperature- and snow-cover data and (d) a SRT-monitoring at the Val Susauna.

7.2.1 Repeatability tests

A fundamental precondition for monitoring time-dependent processes is the reliable reproducibility of measurements (cf. Chapter 2.1.1.2; Kneisel et al. (2008)). Near-surface conditions can vary distinctly during the seasons, with strong influence on the particular contact resistances. The humus cover at the study sites provides almost persistent moist conditions and therefore stable contact resistances during the snow-free period. This is in strong contrast to unvegetated sites, where contact resistances are strongly influenced by weather conditions (precipitation or dry spells). However, contact resistances within the humus cover distinctly increase during winter, when the moist organic material freezes. To evaluate the influence of altering contact resistances, repeatability tests were conducted at single dates in summer and winter at the Val Bever and Val Susauna study sites (see Table 7.1). For this purpose, the array types dipole-dipole and Wenner were measured rotationally three times in a row, beginning with the dipole-dipole array. Due to technical problems, only two complete datasets are available for analysis; datasets measured in winter at the Val Susauna and datasets from the summer-measurement in the Val Bever.

Krautblatter & Verleysdonk (2008) conducted repeatability tests between May and October at a permafrost-affected rock-wall using Wenner, Schlumberger, gradient and dipole-dipole arrays with 1.53, 4.6 and 10 m electrode spacing. Their results show more stable data for Wenner, Schlumberger and gradient arrays compared to dipole-dipole array and a strong link between raw data quality and RMS-errors to electrode spacing independent from the applied voltage. Peter-Borie et al. (2011) conducted repeatability tests and noise estimations with buried electrodes and cables for

monitoring water content in a rock mass to distinguish between variations in electrical resistivity due to noise and to changes in water content using the dipole-dipole array. Significantly, higher noise levels were detected for the first measurement of the day, compared to the following measurements. This effect is explained by an insufficient injected current, polarization of the system at the time of the first acquisition, or by damages of the buried cables.

Table 7.1: Details on dates, surrounding conditions and setups of repeatability test

site	date	humus temp [°C] 5/15/30 cm depth	mean contact resistance [kΩm]	# of measurements		resistivity meter configuration for injection
				dipole-dipole	Wenner	
Val Bever	08.02.2011	-8.27/-8.20/-8.21	430	2	2	V_{ab} = maximum
	22.08.2011	11.25/10.15/9.46	25	3	3	V_{ab} = maximum
Val Susauna	10.02.2011	-7.89/-7.43/-7.09	310	3	3	V_{ab} = maximum
	22.08.2011	7,62/3.45/2.78	8	1	1	V_{ab} = maximum

For an appraisal of the repeatability of ERT measurements, measured apparent resistivity values and inverted specific resistivity values are analysed. According to Hilbich et al. (2011; 2009b), the analysis of apparent resistivities can be more useful to monitor near-surface processes, as inverted specific resistivities might be affected by inversion artefacts, if large temporal changes occur.

7.2.2 ERT monitoring

Fixed ERT-monitoring arrays were installed in central areas at all three study sites. The selection of monitoring locations was based on the presence of perennial frozen ground – as detected by previous measurements (Kneisel & Schwindt, 2008; Schwindt, 2007 see also Chapter 6) and the site specific surface/vegetation composition (cf. Chapter 3 and Table 7.2). Location of monitoring arrays in relation to geophysical measurements presented in Chapter 6 is given in Figure 7.3. The monitoring arrays of the Val Susauna and Brüeltobel are located in the central parts of the dwarf-growth zone, where humus thickness is highest (Figure 3.5a and Figure 3.8). In contrast, the array in the Val Bever is located (equal to array VB-mon in Chapter 6) in an area where the organic layer appears rather inconsistent and is disturbed by granitic boulders

(FIGURE 3.2c and FIGURE 3.3b). An additional monitoring array was installed at the forest aisle in the western part of the Val Bever study site, comparable to site VB-S1 (CHAPTER 6, FIGURE 3.3c). However, due to technical problems no measurements could be conducted at this site.

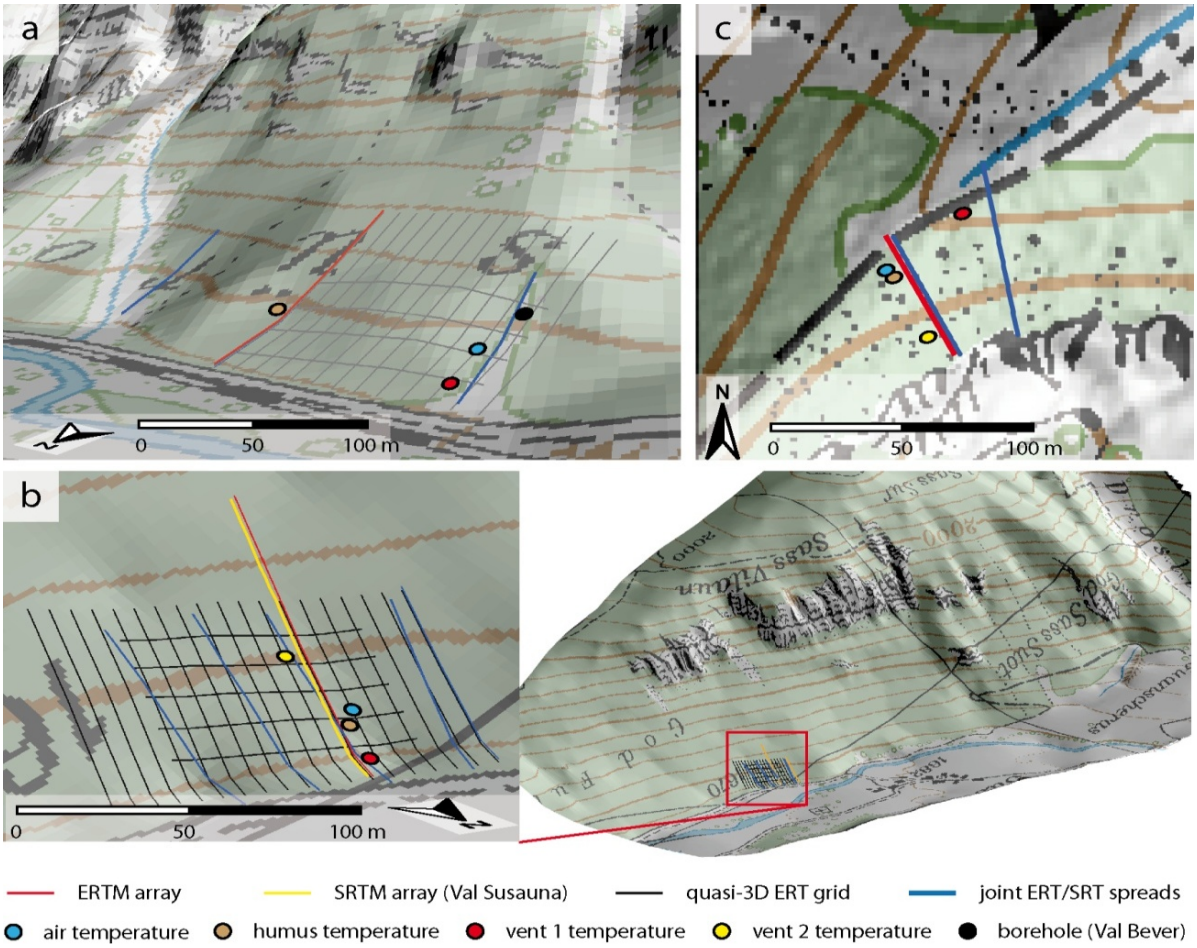

Figure 7.3: Study sites with location of monitoring arrays, borehole and temperature loggers; Val Bever (a), Val Susauna (b) and Brüeltobel (c) (© swisstopo). For orientation, geophysical arrays presented in CHAPTER 6 are indicated.

Details on the monitoring setups are given in TABLE 7.2. Setups are based on 36 electrodes with a unit electrode spacing of 3 m for the Val Bever and Val Susauna and 1.8 m for the Brüeltobel site. Array length at the Brüeltobel is limited by the comparable small size of the talus slope, with the array beginning at the foot of the slope and ending at the foot of the rock-wall (cf. FIGURE 7.3c). Monitoring arrays of the Val Bever and Val Susauna are located in the lower parts of the slope, the area, where supercooling is assumed to be strongest and where the main distribution area of frozen ground is

expected. Array length and electrode spacing in contrast to resolution and penetration depth has been discussed in CHAPTER 2.1.1.3.

Table 7.2: Specifics on ERTM setups, period of measurements and site-characteristics.

	Val Bever	Val Susauna	Brüeltobel
altitude [m a.s.l.] (begin/end of spread)	1778 / 1810	1663 / 1692	1200 / 1241
average slope	28°	23°	34°
substrate	granitic, bouldery talus	dolomitic talus	limestone talus
site characteristics - stock of trees	*Larix decidua, Pinus cembra* (< 10 m), minor crown density	*Pinus mugo, Picea abies* (dwarf growth)	*Picea abies* (dwarf growth)
site characteristics - humus/undergrowth	fragmented humus/moss cover, high amount of lichens	consistent thick humus/moss cover (>30 cm)	consistent humus/moss cover (> 30 cm); *Dryas octopetala*
# of electrodes	36	36	36
electrode spacing [m]	3	3	1,8
array length [m]	105	105	63
array types	Wenner, dipole-dipole	Wenner, dipole-dipole	Wenner, dipole-dipole
period of data acquisition	10.2008 - 03.2012	07.2009 - 03.2012	08.2009 - 04.2011
interval of measurements	year-around, monthly	year-around, monthly	year-around, monthly
# of measurements	32	25	16
# of utilizable measurements (Wenner/dipole-dipole)	30/29	23/18	16/0

As described in CHAPTER 7.2.2, cables and electrodes where buried to ensure constant electrode locations and protection against external impacts. In general, the electrode coupling did not pose a problem, due to the presence of a consistent and conductive humus/moss layer. Solely at Brüeltobel, a small area consisting of uncovered, loose talus (FIGURE 3.6a) posed demanding conditions. Especially in case of monitoring measurements that were conducted after periods with low precipitation in summer, contact resistances were relatively high (FIGURE 7.4). To enlarge the surface between electrode and talus material and to enhance electrode coupling, soaked sponges were used. During the measurement period of the fixed monitoring setup, water for soaking the sponges was only used under very dry conditions, with its amount kept to a minimum. The application of higher amounts of water would result in punctual

disturbances of subsurface conductivity around and below watered electrodes. Such an effect could not be kept constant throughout the measurement period and would affect the reproducibility of measurements. To provide consistent electrode coupling at monitoring sites electrodes were checked regularly, as various processes (freezing/thawing, movement of talus material, snow pressure) could loosen the electrodes.

Wenner and dipole-dipole arrays were measured for all sites, as an optimal complement of robustness, vertical resolution and depth penetration of the Wenner array to the superior spatial resolution of the dipole-dipole array. However, results presented in this chapter focus on Wenner measurements as dipole-dipole arrays did not provide utilizable data throughout the year.

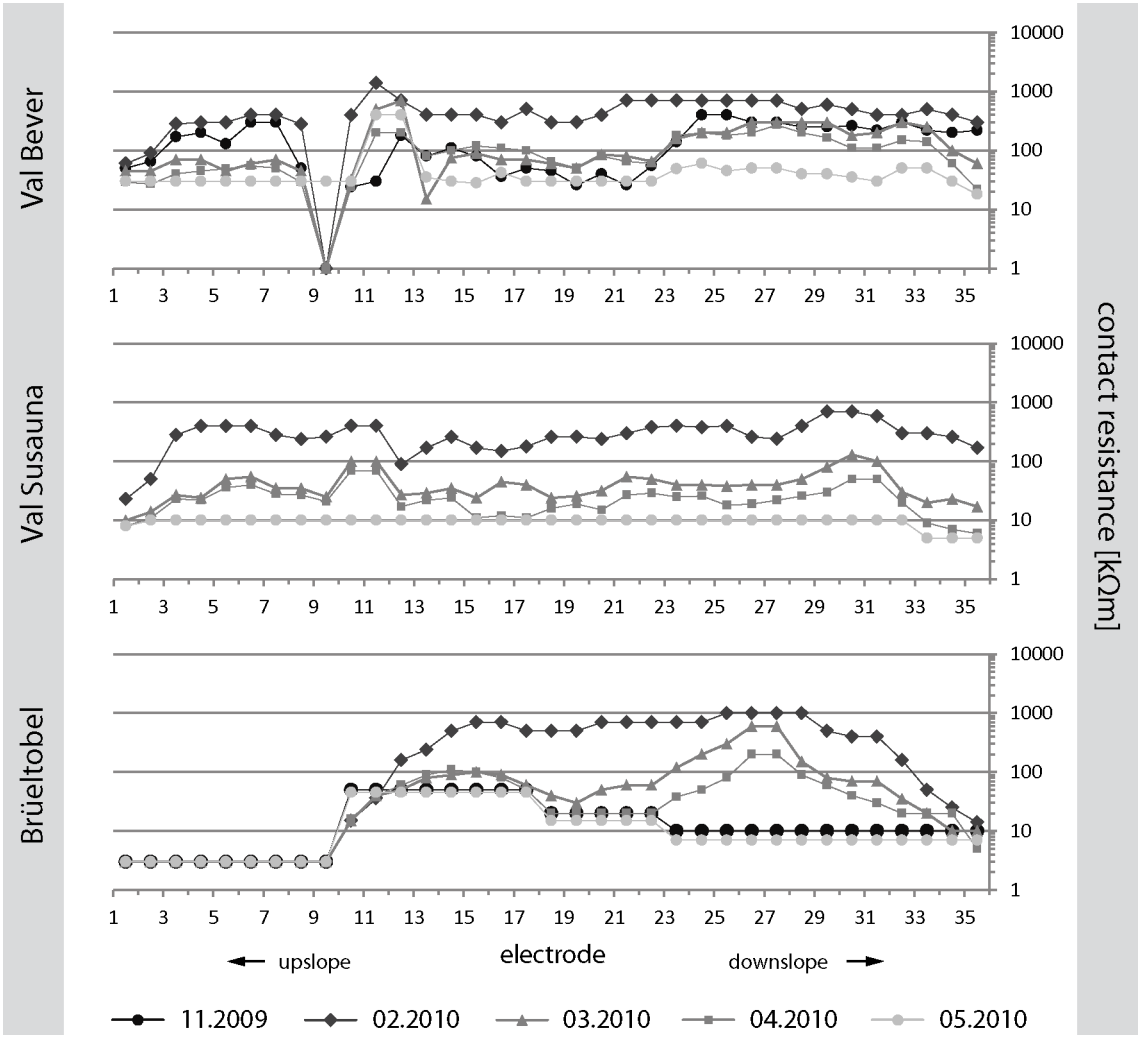

Figure 7.4: Evolution of contact resistances during winter. Due to a short-circuit between electrodes 9 and 10 at Val Bever, contact resistance had a value of zero kΩm; datum points recorded using theses electrodes were excluded.

In general, monitoring arrays were measured in a monthly interval throughout the year. Measurement intervals were adjusted in certain periods. Intervals were shortened in early winter, during the onset of a consistent snow cover and in spring during snowmelt. Data gaps occurred as a result of technical failures, and during high winter, when contact resistances are highest. Information on data processing, quality check and inversion are given in CHAPTER 2.1.1.4.

Time-lapse calculations were conducted using the program Geoplot included in the software package SeisImager/2D (GEOMETRICS). The percentage of change in subsurface resistivity distribution of inverted datasets was calculated. Time-lapse calculations were referenced for consecutive measurements, meaning that the reference model for time-lapse calculations is not retained throughout the monitoring period. This approach was chosen, as the amplitude of seasonal changes exceeds the long-term variations.

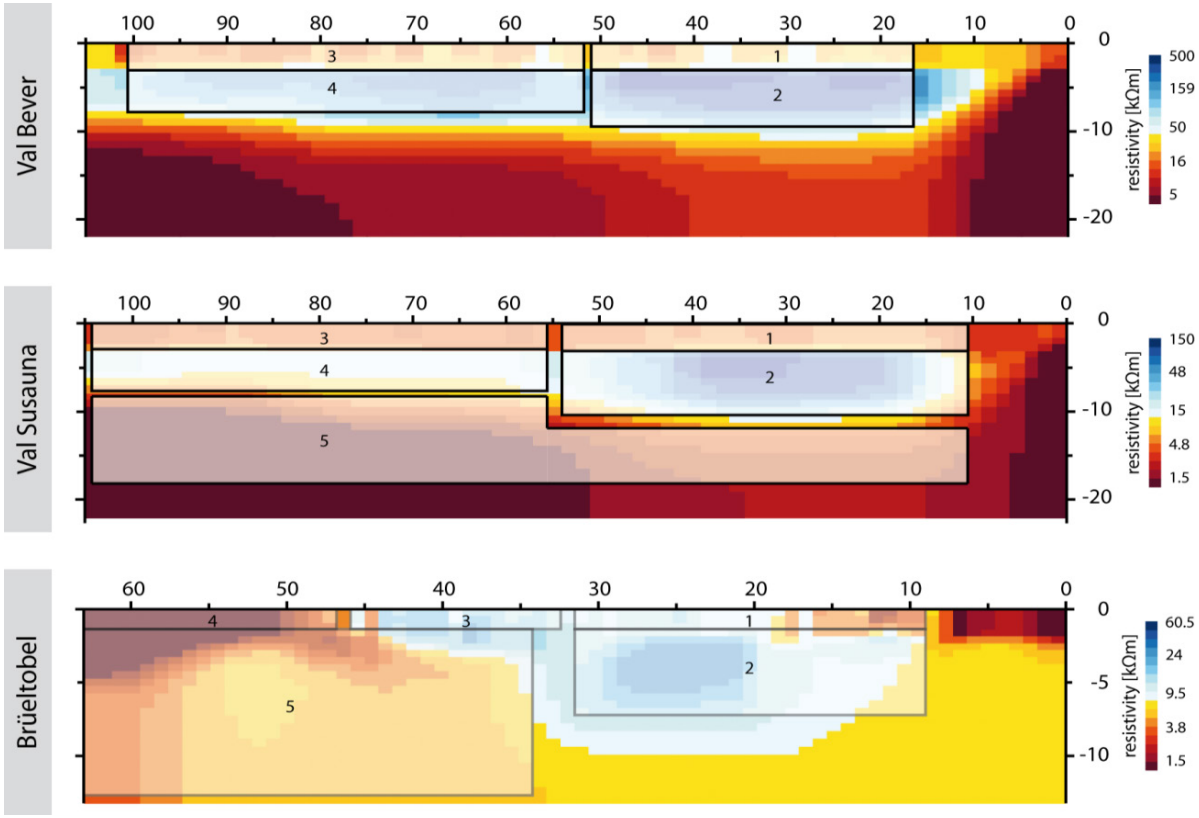

Figure 7.5: Positions for extraction of resistivity data for the monitoring sites. Description of positions for all sites: 1 – active layer; 2 – permafrost. Remaining positions: Val Bever: 3 – potential active layer, 4 – seasonal/perennial frozen ground; Val Susauna: 3 – near-surface layer, 4 – seasonal frozen ground, 5 – unfrozen talus; Brüeltobel: 3 – unvegetated talus material, 4 – fine grained, grass covered substrate, 5 unfrozen talus.

For a differentiated analysis of temporal subsurface resistivity evolution data were extracted from inverted datasets according to FIGURE 7.5. The assignment of tomogram sections as active layer and permafrost is based on the analysis of monitoring results. Sections were defined as permafrost, if monitoring measurements showed values equal or higher than the site-specific boundary values for frozen ground. The sections above the permafrost bodies were defined as the corresponding active layer.

The chosen contour scales for resistivity values and resistivity variations state a trade-off between a reasonable illustration and the coverage of the extremely large range of values, as well as the high temporal variability. Especially for measurements in winter, maximum values cannot always be clearly deduced from the tomograms. For such cases, absolute values will be given within the text. Furthermore, differing geophysical properties between the three study sites required a determination of site-specific contour scales.

7.2.3 Joint ERT/SRT monitoring

To achieve supplemental information on subsurface processes occurring between the onset of a consistent snow cover and snowmelt in spring, a fixed SRT-monitoring was installed parallel to the ERT-monitoring array at the Val Susauna in November 2010. Measurements were conducted in joint application with the ERT-monitoring in a monthly interval.

Based on 24 channels, the geophone spacing of the SRTM-array was set to 4.5 m, resulting in an array length of 103.5 m, to achieve a spread length comparable to the ERTM-array. Details on the SRTM-setup are given in TABLE 7.3. Information on data acquisition, data processing and inversion are given in CHAPTERS 2.1.2.2 and 2.1.2.3. Time-lapse calculations of SRTM-data were conducted in the same manner as presented for ERTM above, using the software Geoplot (Geometrics).

.

Table 7.3: Details on SRTM setup and period of data acquisition at the Val Susauna.

SRT-monitoring Val Susauna	
# of geophones	24
geophone spacing [m]	4.5
spread length [m]	103.5
# of shot points	16
# of stacks	10
sample interval [ms]	0.125
record length [ms]	128
period of data acquisition	24.11.2010 - 20.06.2011
interval of measurements	monthly
# of measurements	7

For a differentiated analysis of temporal evolution of the acoustic impedance in the subsurface and for comparison with ERTM data, p-wave velocity data were extracted from inverted datasets according to FIGURE 7.6. The assignment of tomogram sections as active layer and permafrost is based on the same approach as introduced for ERTM above.

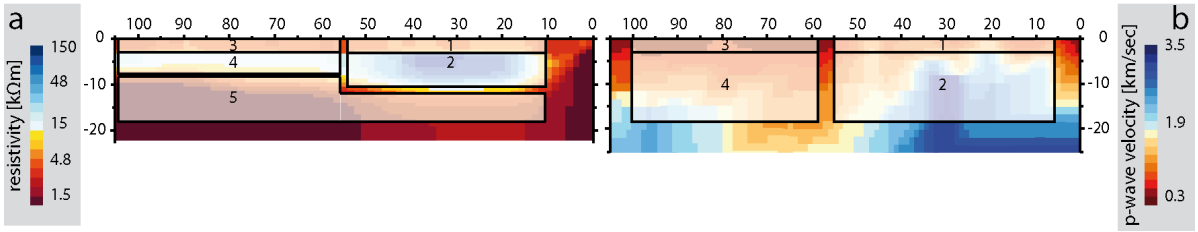

Figure 7.6: Positions for extraction of velocity data for the SRT-monitoring site at the Val Susauna (b). Position 1 – active layer, 2 – permafrost, 3 – near-surface layer, 4 – seasonal frozen ground. (a) – for comparison – positions for extraction of the corresponding ERT-monitoring datasets (description given in FIGURE 7.5).

7.2.4 Synthetic data modelling

Synthetic data modelling is used in this section to achieve a more sophisticated interpretation of ERTM-data, to deduce processes and to assess the effect of increasing contact resistances on measurements and data inversion. The aim of synthetic modelling

is to emulate the subsurface evolution during winter. Geocryologic models (FIGURE 7.27) are based on a unit electrode spacing of 3 m, using the Wenner array. To achieve best possible illustration, the geocryologic models are presented along with the inversion results in FIGURE 7.27. An explanation of the geocryologic models is given in the corresponding section CHAPTER 7.3.3.

The software package RES2DMOD (LOKE, 2002) was used to specify subsurface resistivity values for each 2D section according to the geocryologic model. Corresponding apparent resistivity pseudosections were calculated using the finite-difference method (DEY & MORRISON, 1979; LOKE, 1994) for the array types Wenner and dipole-dipole (only results for the Wenner array are presented). 5 % of random noise was added to each synthetic 2D array. Synthetic data were inverted as described in CHAPTER 2.1.1.4, using the software package RES2DINV (GEOTOMO). Details on synthetic data modelling, the back-and-forth interpretation procedure and on the forward and inverse problem are given in CHAPTER 2.1.1.5.

7.2.5 Supplemental parameters

To support results from geophysical monitoring and to achieve a better interpretation of results, supplemental data are used. For a profound understanding of processes and interpretation of monitoring results temperature data as well as data on the snow cover are taken into account. In addition to air temperatures, humus- and ground surface temperatures are considered, to detect the propagation of freezing and thawing within the active layer. Temperatures recorded inside the vents are taken into account to analyse the connection between the thermal circulation inside the talus slopes and the frozen ground evolution. Details on data logger positions within each study site are given in FIGURE 7.3, FIGURE 8.1, TABLE 8.1 & Table 8.2. Information on data loggers are given in CHAPTER 2.2.2; measurement periods and interval in TABLE 4.2.

It is assumed that the snow cover has a strong influence on the ground thermal regime and therefore on the distribution and evolution of permafrost (ISHIKAWA, 2003; KELLER & GUBLER, 1993; KELLER & TAMÁS, 2003; ZHANG, 2005). With regard to geophysical monitoring, the onset of a consistent snow cover and the period of snowmelt are of interest. As snow-cover data could not be recorded, data are derived from nearby climate stations. Data on snow thickness measured at the meteorological station Samedan

(1709 m a.s.l.) are used as reference for the Val Bever (~3 km linear distance from Samedan) and Val Susauna (~14 km linear distance from Samedan). For the Brüeltobel no utilizable data on snow cover are available. Meteorological stations in the proximity do not provide continuous snow-data during the monitoring period or lack of comparability (e.g. Säntis meteorological station, 2220 m a.s.l., ~9 km linear distance from Brüeltobel).

7.3 Results

Results presented in this chapter are divided into three sections. In the first section, results from repeatability test are presented. The second section includes results from ERT-monitoring and a comparison of the subsurface resistivity evolution for each site with data on temperatures and snow-cover distribution. For a more profound interpretation of ERTM data, results from synthetic data modelling are presented. The third section focusses on joint SRTM/ERTM during winter 2010/2011 at the Val Susauna site.

7.3.1 Repeatability tests

Results from repeatability tests are presented as 3D-scatterplots in FIGURE 7.7 and FIGURE 7.8; associated correlation coefficients are given in TABLE 7.4. Information on relative standard deviation (RSD) for repeated measurements is given in FIGURE 7.9.

Comparing apparent resistivities for summer measurements, Wenner and dipole-dipole show a high correlation (FIGURE 7.7a and TABLE 7.4) with values close to 1. Scattering of values is slightly higher for dipole-dipole data, which is best expressed in FIGURE 7.7b. The distribution of red dots (FIGURE 7.7b), representing the relation (m1/m2)/(m2/m3), shows a scattering towards values < 1, meaning that resistivity values of the first measurement are in general slightly smaller compared to the second and third measurement. This effect is more pronounced for the dipole-dipole compared to the Wenner array. Resistivity values recorded during winter are – as expected – distinctly higher than summer-data for both, Wenner and dipole-dipole datasets. Even though the scattering of values increases considerably, r-values (TABLE 7.4) are still high, ranging from 0.979 to 0.996 (Wenner) and from 0.979 to 0.999 (dipole-dipole). As shown for the summer-measurements, values of the first datasets are lower compared to the second and third measurements. Especially for the dipole-dipole arrays conducted in winter, outliers with comparably high values are detected.

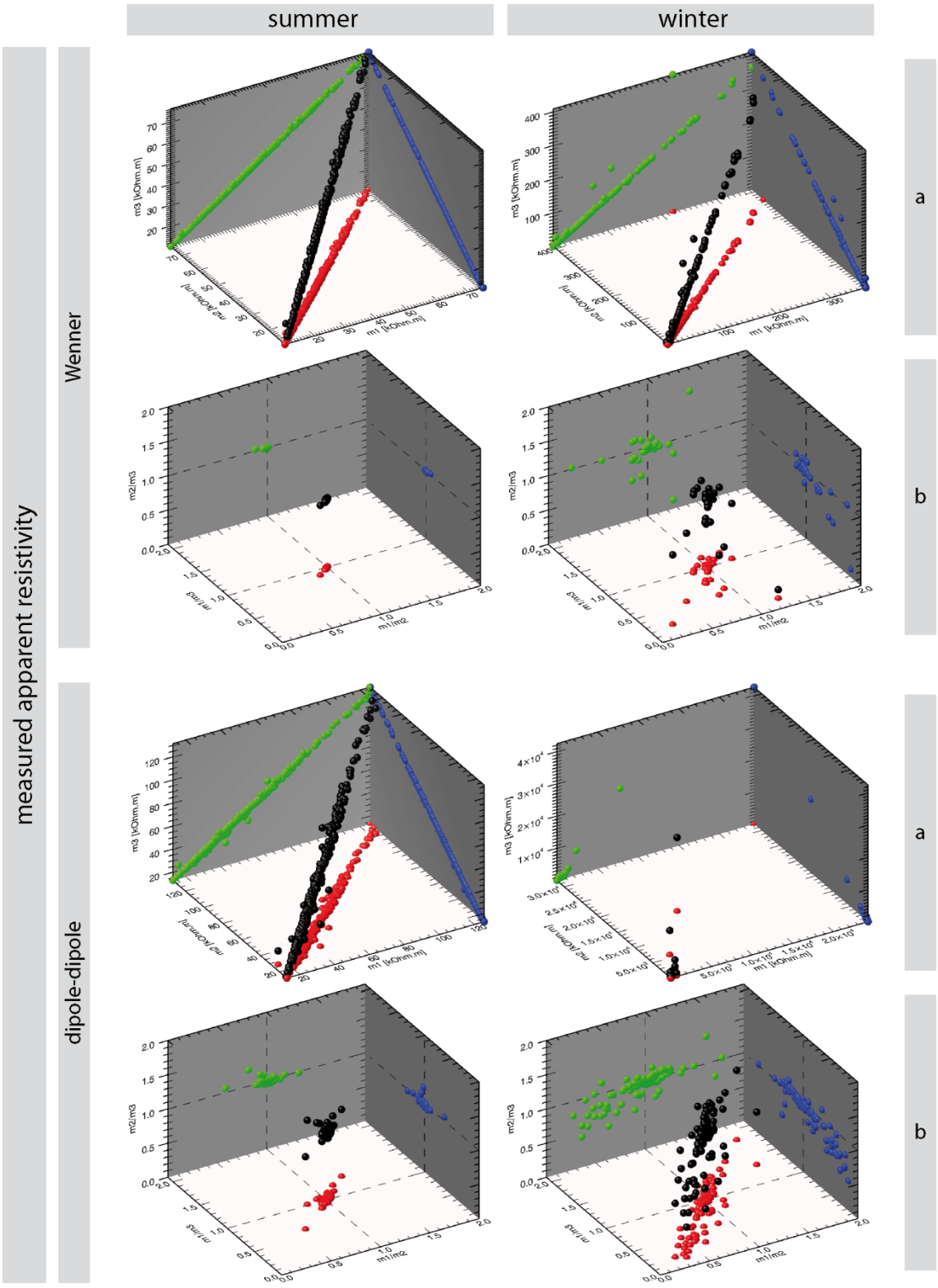

Figure 7.7: 3D-scatterplots of measured apparent resistivity values, comparing Wenner and dipole-dipole measurements conducted in summer and winter. With (a) relating resistivity values of repeated measurements for each datum point (red – m1/m2; green – m1/m3; blue – m2/m3, black – m1/m2/m3) and (b) comparing the relation of resistivity values (red – (m1/m2)/(m1/m3), green – (m1/m2)/(m2/m3); blue – (m1/m3)/(m2/m3). Note that the scale of absolute resistivity values (a) is different for Wenner and dipole-dipole measurements.

Focusing on the mean relative standard deviation (RSD) of measured apparent resistivity values (MAR) (FIGURE 7.9), the interquartile range for Wenner arrays differs only slightly between summer (0.74 %) and winter (0.61 %), while variations are higher for dipole-dipole arrays (summer – 1.05 %; winter – 3,51 %). However, the variance is distinctly higher for dipole-dipole in contrast to Wenner measurements and for measurements conducted in winter compared to summer-data. Maximum RSD-values for Wenner arrays increase from 5.6 % in summer to 92 % in winter; corresponding dipole-dipole arrays show values of 21.9 % in summer and 65 % in winter. However, for an estimation of the repeatability the interquartile range is a more valuable tool than the analysis of extreme values.

3D-scatterplots of inverted specific resistivity values show a similar distribution of resistivity values measured in summer (FIGURE 7.8 a) compared to MAR-data (FIGURE 7.7 a), with r-values ≥ 0.999 (TABLE 7.4). The comparison of the relation of resistivity values (FIGURE 7.7 b) shows in general a very high reproducibility of data, with values ranging close to 1. Green ((m1/m2)/(m2/m3)) and blue dots ((m1/m3)/(m2/m3)) are characterised by z-values close to 1, while x- and y- values, respectively, scatter slightly by $\pm$ 0.3. This means, that differences between m2 and m3 are in general smaller than differences between m1 and m2 and between m1 and m3. As shown for MAR-data, red dots ((m1/m2)/(m1/m3)) tend to show x/y values < 1, indicating in general smaller values for m1 compared to m2 and m3.

Compared to MAR-data the IQR of the mean relative standard deviation (FIGURE 7.9) of inverted specific resistivity values is slightly higher in summer (Wenner – 2.6 %; dipole-dipole – 2.35 %) and distinctly larger in winter (Wenner – 23.08 %; dipole-dipole – 23.27 %). Differences in the variances of values between MAR and ISR in winter and summer are in general marginal, only results for the dipole-dipole arrays measured in winter show markedly higher maximum values up to 132 %.

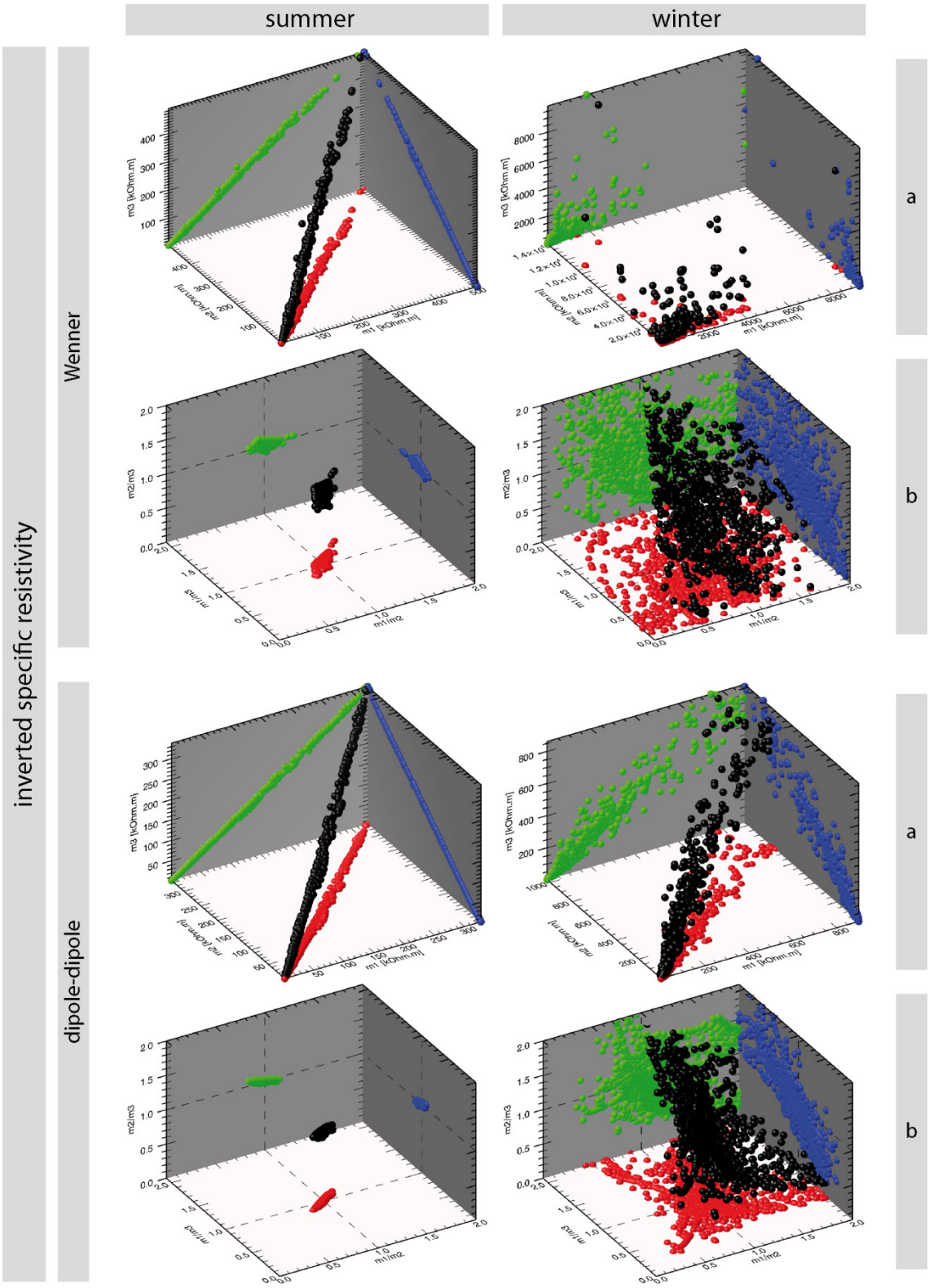

Figure 7.8: 3D-scatterplots of inverted specific resistivity values, comparing Wenner and dipole-dipole measurements conducted in summer and winter. With (a) relating resistivity values of repeated measurements for each datum point (red – m1/m2; green – m1/m3; blue – m2/m3, black – m1/m2/m3) and (b) comparing the relation of resistivity values (red – (m1/m2)/(m1/m3), green – (m1/m2)/(m2/m3); blue – (m1/m3)/(m2/m3). Note that the scale of absolute resistivity values (a) is different for Wenner and dipole-dipole measurements.

Table 7.4: Correlation coefficients for repeated measurements

		correlation coefficient (r)			
		Wenner		dipole-dipole	
		MAR	ISR	MAR	ISR
Summer	m1/m2	0,9996	0,9995	0,9976	0,9990
	m1/m3	0,9996	0,9997	0,9981	0,9989
	m2/m3	1,0000	0,9999	0,9996	0,9997
Winter	m1/m2	0,9838	0,9862	0,9856	0,3532
	m1/m3	0,9791	0,9704	0,9787	0,6702
	m2/m3	0,9957	0,9706	0,9991	0,7212

The most striking effect is the strong increase of the IQR and of mean values between apparent and inverted resistivity data in winter. This effect can be ascribed to inversion artefacts under strong resistivity contrast (Hilbich et al., 2011; Hilbich et al., 2009b). In winter, the median RSD of inverted specific resistivity values is around 17 % (Wenner) and 33 % (dipole-dipole), while corresponding MAR-values are distinctly smaller, with 0.41 % (Wenner) and 1.05 % (dipole-dipole).

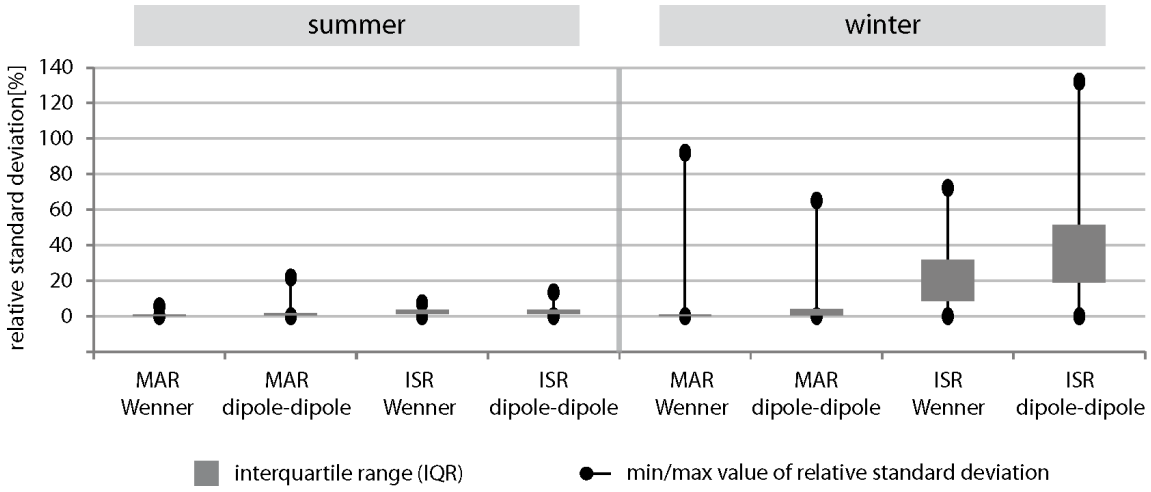

Figure 7.9: Boxplots of mean relative standard deviation (RSD) for repeated ERT measurements, comparing measured apparent resistivity (MAR) and inverted specific resistivity values (ISR) for Wenner and dipole-dipole arrays conducted in summer and winter.

7.3.2 ERT monitoring

7.3.2.1 Val Bever

Results from ERTM conducted between October 2008 and March 2012 at the Val Bever are presented in FIGURE 7.10, FIGURE 7.11, FIGURE 7.12, FIGURE 7.13 & FIGURE 7.14. FIGURE 7.15 shows the resistivity evolution of defined areas – according to FIGURE 7.5 – in comparison to humus-, air- and vent temperatures as well as data on snow cover distribution during the monitoring period.

The first monitoring tomogram from October 2008 (FIGURE 7.10) shows a subsurface resistivity distribution similar to results presented in CHAPTER 6.2.1, with an elongated high resistive anomaly of 6-8 m thickness embedded into a matrix with resistivity values < 10 kΩm. As shown in CHAPTER 6, at least the lower parts of the anomaly, where highest resistivity values are detected (horizontal distances 10-50 m), are confirmed as frozen ground. For a clarification of the terminology, this area can be ascribed as permafrost. To anticipate results presented in this chapter, ERTM-data indicate frozen subsurface conditions for the complete monitoring period (42 months). The presence of ground ice upslope could not be definitively confirmed by joint ERT/SRT measurements presented in CHAPTER 6; however, based on ERTM results permafrost must be expected within this slope-area.

FIGURE 7.10 covers the monitoring period between onset of a consistent snow-cover at the beginning of November and snowmelt in spring (cf. FIGURE 7.15), with patches of snow being still present in May 2009. Between measurements in October and November, the areal dimensions of the frozen ground body remain almost constant. An increase of resistivity values of 110-170 % within, and up to 130 % above the permafrost body (10-50 m) indicates an initiated supercooling of the frozen ground body and a freezing of the active layer. A further increase of resistivity values – by 400-1200 % – is observed for the permafrost body and the active layer towards December 2009. In general, the areal ratio of resistivity values representative for frozen ground conditions expands distinctly towards March. The evolution of the expansion of the high resistive body is rather complex. While the extent of the anomaly expands stepwise upslope, the central parts of the permafrost body show a decreased increase between December and January, followed by a decrease of up to 50 % between January and February and by

more than 80 % between February and March. Values in the surroundings of this area distinctly increase (300-800 %) during this period. Resistivity distribution in the shallow subsurface is less homogeneous for the measurement in March compared to previous datasets with decreased resistivity values.

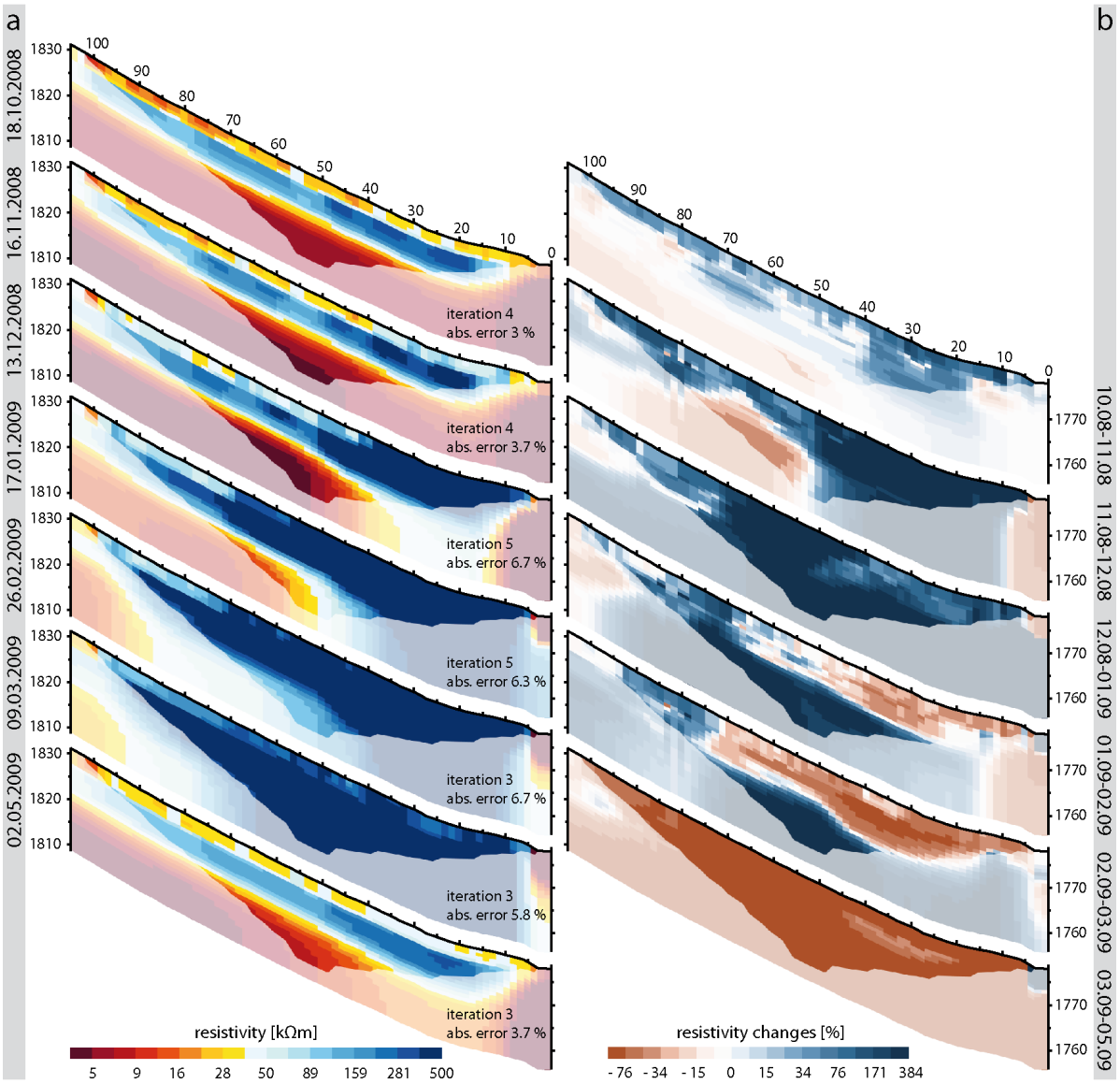

Figure 7.10: Val Bever ERT-monitoring – October 2008 - May 2009 (a) and time-lapse tomograms (b). Time-lapse tomograms are referenced for two consecutive measurements.

Between March and May (FIGURE 7.10) resistivity values drop by 30-50 % in the central parts of the permafrost body (20-45 m) and by up to 98 % for the remains of the tomogram. Resistivity values of the permafrost body in May (between 230 and 290 kΩm) partly fall below values measured in October 2008 (between 250 and 320 kΩm). Values

around 45 kΩm are indicative for partly frozen conditions within the active layer, especially between horizontal distances 10-40 m.

Variations of subsurface resistivity values during summer 2009 (FIGURE 7.11) are comparatively low. During May values of the elongated high resistive body show an increase in the upper parts of the slope (75-95 m) by 70-120 %; evolution of resistivity values downslope is variable, ranging between -10 and +40 %.

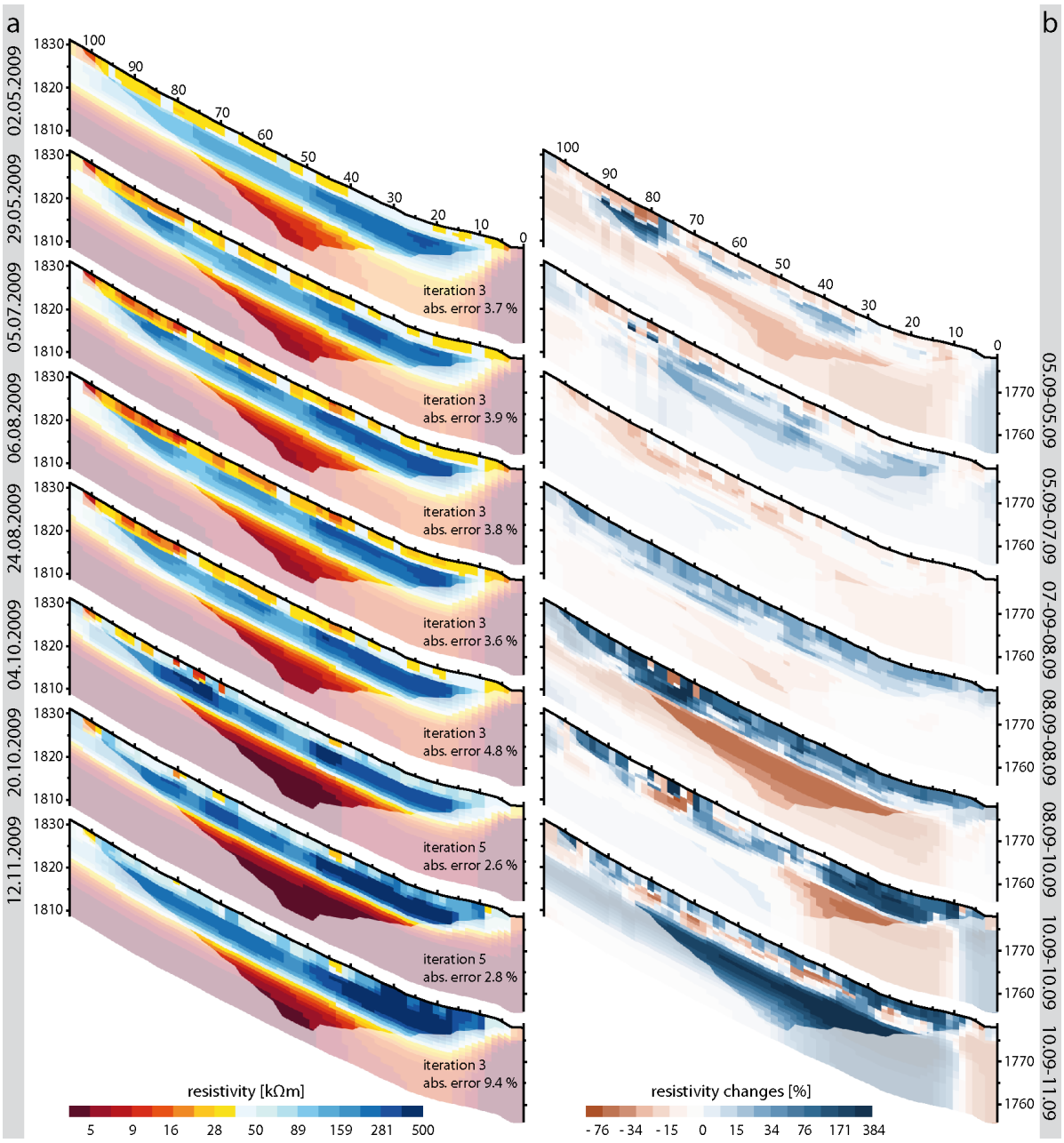

Figure 7.11: Val Bever ERT-monitoring – May 2009 - December 2009 (a) and time-lapse tomograms (b). Time-lapse tomograms are referenced for two consecutive measurements.

Between the end auf August and late October, the evolution of subsurface resistivity distribution is antipodal for the near-surface area (0-7 m depth) and the deeper subsurface (below 7 m depth). Thus, the boundary between these two areas proceeds through the lower parts of the permafrost body (2-10 m depth). During this period, the near-surface layer is characterised by a strong increase of resistivity values – throughout the array – by 30-120 % between consecutive measurements. The area below 7 m depth shows a homogeneous decrease of values during August (5-15 %) and between August and early October (30-60 %). Towards the end of October the area with decreasing values (40-60 %) is concentrated below the permafrost body (horizontal distances 10-50 m). Upslope only slight variations occur. Between measurements in October and November the upper sections of the permafrost body (3-5 m depth) show a slight decrease of values, while areas below and above are characterised by an increase of resistivity values (FIGURE 7.11b). In general, the resistivity values inside the permafrost body are rather stable, ranging from 300 to 400 kΩm indicating a low variability during summer. By the end of October 2009, resistivities of the frozen ground body increase to values between 600-900 kΩm, which is distinctly higher than values measured in the previous year (18.10.2008, 260-320 kΩm). Likewise the November-measurements of 2009 (300-1200 kΩm) show higher values for the permafrost body compared to 2008 (300-500 kΩm). Comparing the winter- (FIGURE 7.10) and summer-period (FIGURE 7.11), the resistivity evolution in winter appears to be initiated from the frozen ground body in the lower parts of the array, and stepwise expands upslope. In contrast, the evolution during summer appears more homogeneous with a relatively low horizontal- but a strong vertical differentiation.

FIGURE 7.12 shows the monitoring period between November 2009 and October 2010. Due to technical difficulties, no data are available for summer 2010. During winter 2009/2010 the evolution of the resistivity distribution proceeds in the same manner as described for winter 2008/2009 (FIGURE 7.10). The permafrost body and the superimposing active layer (horizontal distances 10-50 m) is the nucleus, where the increase of resistivity values is initiated between October and December. The temporal resolution and date of measurements differ for the first quarter of 2009 (FIGURE 7.10) and 2010 (FIGURE 7.12).

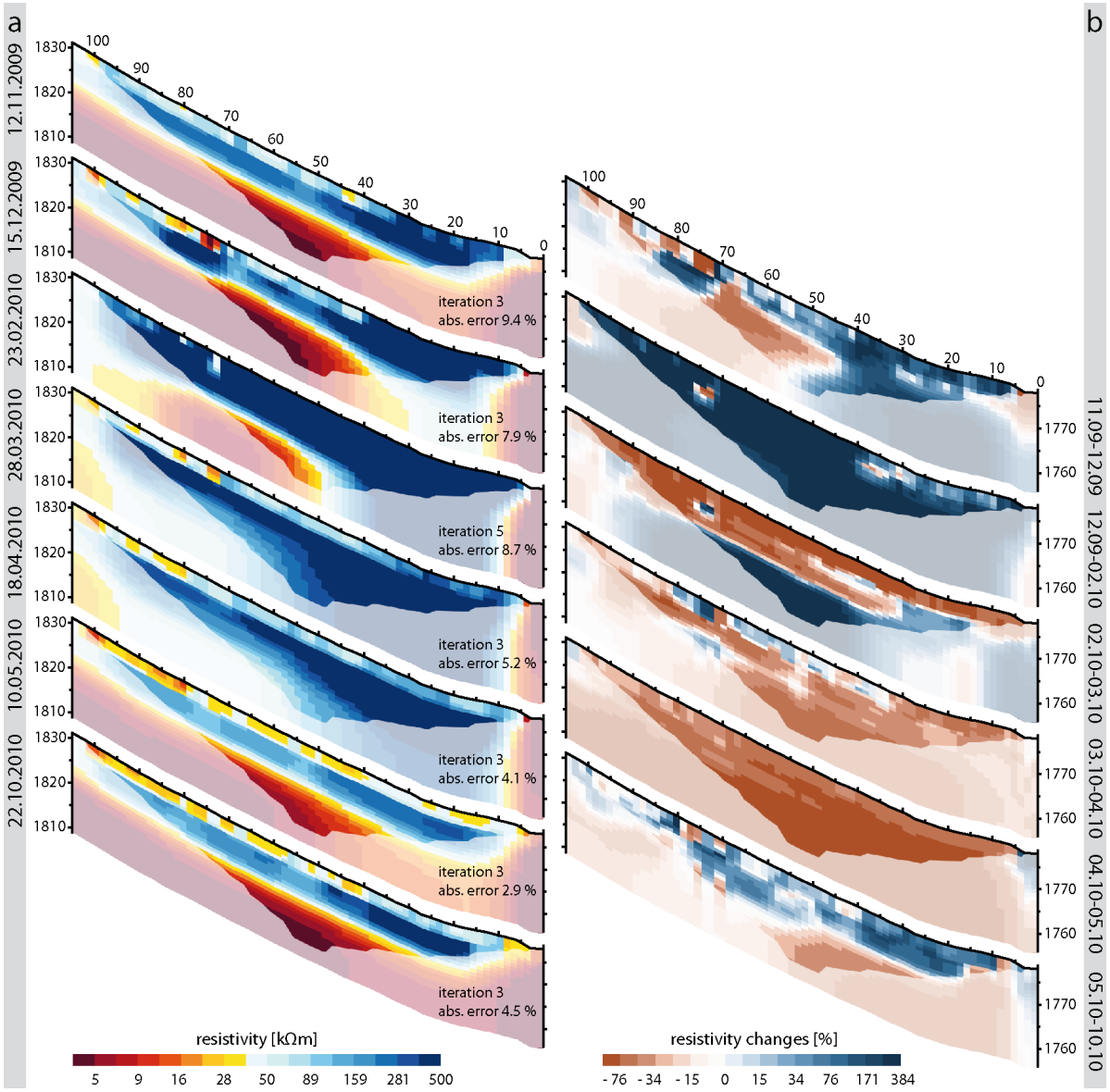

Figure 7.12: Val Bever ERT-monitoring – December 2009 - October 2010 (a) and time-lapse tomograms (b). Time-lapse tomograms are referenced for two consecutive measurements.

In 2009, maximum extent and maximum values of the frozen ground body were achieved by March 9th, followed by a decrease until May, with no measurements in between. Data from 2010 indicate a constant shrinking of the high resistive – presumably frozen – area during March and April. In May, the subsurface resistivity distribution corresponds to the typical "summer-conditions", where the high resistive structures of the permafrost bodies are embedded in a matrix of low resistivity values.

Focusing on the active layer evolution (0-3 m depth) between February and March 2010 (FIGURE 7.12) a massive decrease of resistivity values by 90-100 % is detected, indicative for snowmelt and associated alterations within the active layer. The remains

of the tomograms show a divergent evolution, with increasing values within the permafrost body (horizontal distances 10-30 m) and below a depth of 10 m, as well as decreasing values in the upper parts of the high resistive anomaly (horizontal distances 30-90 m, 3-10 m depth).

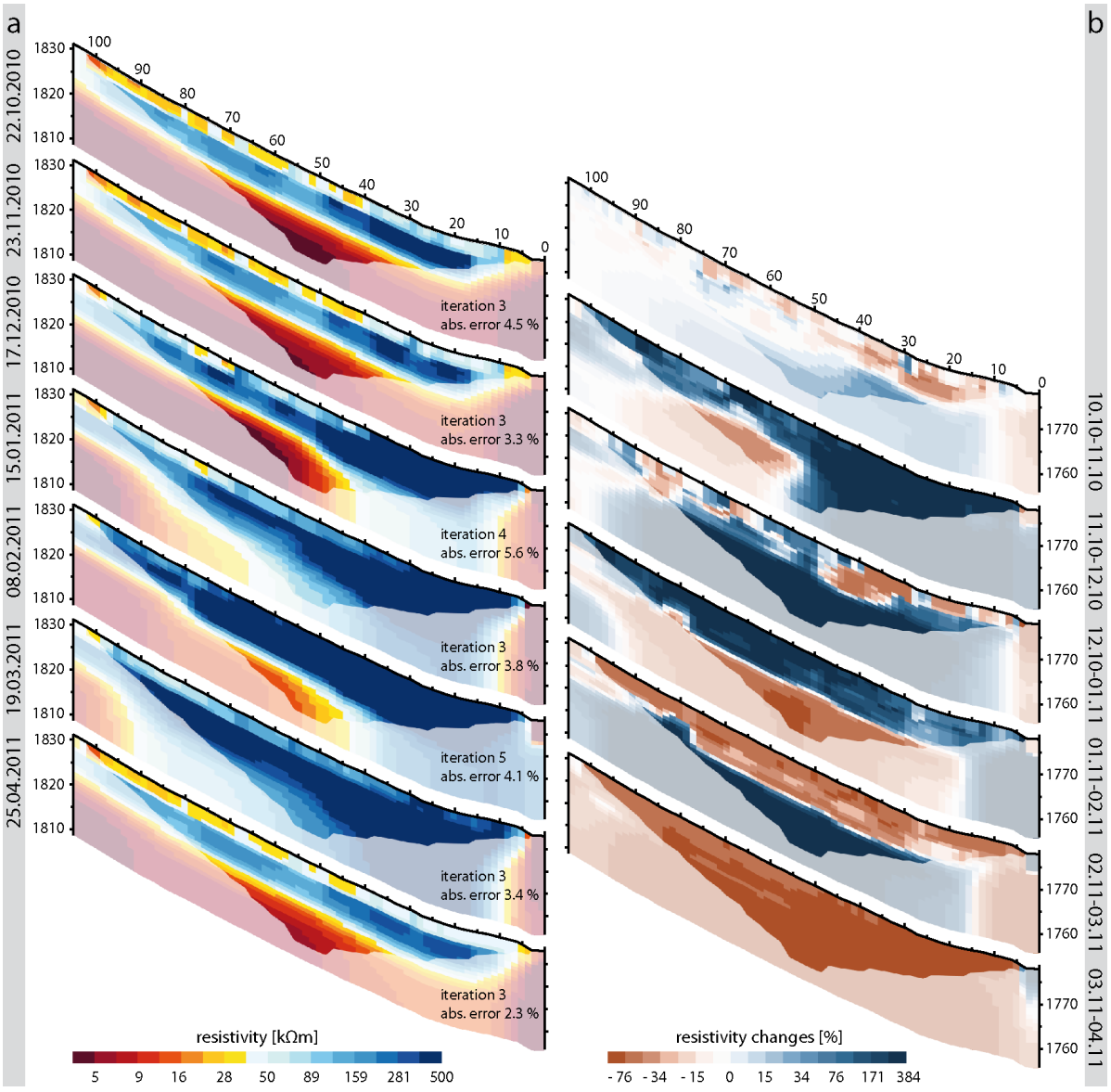

Figure 7.13: Val Bever ERT-monitoring – October 2010 - April 2011 (a) and time-lapse tomograms (b). Time-lapse tomograms referenced for two consecutive measurements.

A similar evolution has been detected during winter 2010/2011 (FIGURE 7.13). However, resistivity distribution differs strongly between April 2010 (FIGURE 7.12) and 2011 (FIGURE 7.13) with distinctly lower resistivity values and a smaller areal extent of the frozen ground body in April 2011. In correspondence to the previous years, results from

the following summer period (FIGURE 7.14) indicate only minor subsurface variability. Resistivity values in the active layer point to partly frozen conditions by the end of April and a complete thawing of the active layer (0-3 m depth) towards June. Increasing resistivity values within the active layer and the permafrost body (horizontal distances 10-50 m) indicate a freezing of the active layer and an initiated supercooling by the end of October 2011. The dataset from March 2012 shows a resistivity distribution comparable to the previous years, representing the highest level of supercooling inside the talus slope. Between October 2011 and March 2012 resistivity values increase by 1000-12000 %.

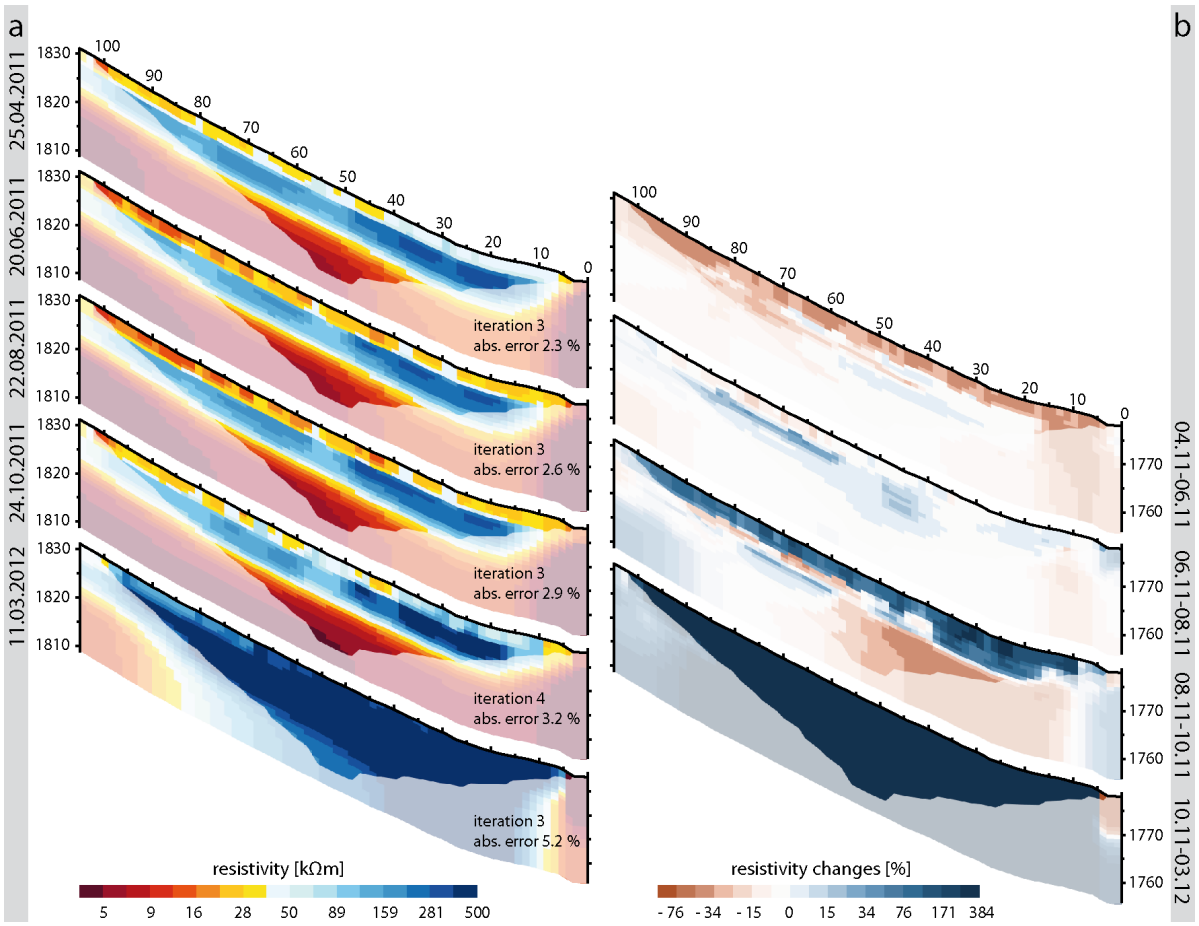

Figure 7.14: Val Bever ERT-monitoring – April 2011 - March 2012 (a) and time-lapse tomograms (b). Time-lapse tomograms are referenced for two consecutive measurements.

Figurative spoken, the high resistive anomaly pulsates during the winter half year, with initiation of expansion between October and November, maximum extent around the end of February and early March, followed by a decrease until the end of April/May. Resistivity distribution inside the permafrost body is relatively stable between May and

early October for all investigated years. Highest variability during summer is detected for the near-surface layer.

FIGURE 7.15 shows extracted resistivity values (cf. FIGURE 7.5) of the ERT-monitoring in the Val Bever in comparison to data on temperatures and snow cover distribution. The snow cover distribution (FIGURE 7.15 a) shows a high variability during the monitoring period, with above-average snow thickness in winter 2008/2009 and in 2011/2012, unexceptional values in 2009/2010 and a markedly low snow thickness in 2010/2011. While summer air temperatures show only slight inter-annual variability – with mean air temperatures ranging between 8.5 and 9 °C – winter temperatures vary, more pronounced, with regard to the temperature mean and the temperature profile. 2008/2009 states the coldest winter (-5 °C mean air temperature) of the monitoring period. Winter 2009/2010 is characterised by early cold spells during October and mean air temperatures of -3.8 °C. With mean air temperatures of -3 °C, winter 2010/2011 represents the warmest winter of the monitoring period and is characterised by several days with temperatures above 0 °C during high winter. Coldest temperatures (-23 °C) were recorded in winter 2011/2012. However, mean winter temperatures were around -3.8 °C, as temperatures distinctly increase by the end of February 2012.

Vent-temperatures in winter (FIGURE 7.5 a; logger locations given in Figure 8.1) mirror the influence of outside air-temperatures with an inflow of cold air into the talus slope. Summer-temperatures are rather constant, reflecting the outflow of cold air through vents at the foot of the slope. Mean vent-temperatures (MVT) are negative in summer 2009 (-0.44 °C) and 2010 (-0.58 °C), but positive in summer 2011 (0.13 °C). The temperature profile shows an increase of temperatures during July 2011. In winter, MVTs are distinctly lower than outside air temperatures throughout the period of measurements, by 0.17 °C in 2008/09 (MVT -5.17 °C), 2.3 °C in 2009/10 (MVT -6.1 °C) and by 1.4 °C in winter 2010/11 (MVT -4.1 °C).

Humus temperatures (FIGURE 7.5 b) are characterised by a long zero-curtain period of around two month in autumn (mid-October to mid-December) and spring (March/April until May/June). Cooling of the organic layer towards 0 °C in early winter occurs very rapidly and simultaneously for all depth levels. Solely ground surface temperatures show values above 0 °C. Warming of the humus layer in spring propagates from the surface downwards. Humus temperatures in summer show little variations with

depth and a strong coupling to air temperatures for all depth layers, indicating a relatively low insulation capability of the organic layer. Likewise, mean temperatures within the three depth layers diverge only marginally during the monitoring period (1.7 °C in 5 cm, 1.2 °C in 15 cm and 1 °C in 30 cm depth).

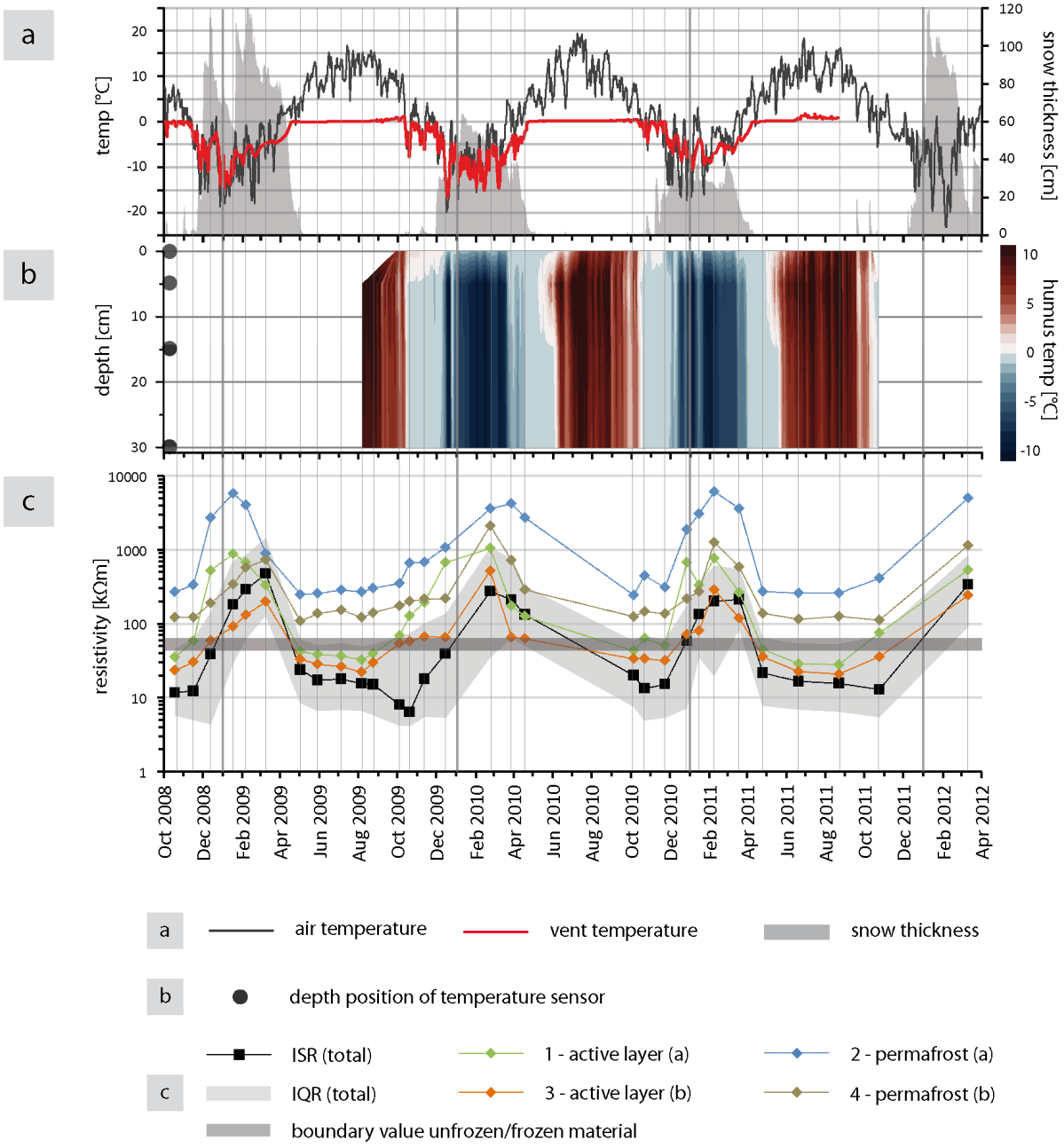

Figure 7.15: Val Bever – median of extracted resistivity data (c) in comparison to humus temperatures (b) and data on snow-thickness, air- and vent temperatures (a) for the monitoring period.

Resistivity curves of extracted data (FIGURE 7.5) show a pronounced annual cycle for all four extracted sections. A strong increase of resistivity values is registered for all

positions, as well as for overall values in early winter, followed by a rapid decrease by the end of high winter. Resistivity evolution during summer is in general characterised by a low intra- and inter-annual variability.

Permafrost can be assumed for sections 2 and 4 (cf. FIGURE 7.5), as resistivity values are distinctly higher than the boundary values characteristic for frozen ground (CHAPTER 6) throughout the monitoring period (42 month). Both sections defined as active layers show resistivity values representative for frozen conditions from mid-October to April/May (> 50 kΩm) and unfrozen conditions (< 45 kΩm) in summer.

Resistivity curves in winter 2008/2009 show an almost parallel curse for sections 1 and 2 (permafrost and active layer in the lower parts of the investigated slope area). After a massive increase – by a factor of 20 – the peak of the resistivity curve is achieved by mid-January followed by a constant decrease. Initial conditions, as detected in October 2008 are achieved in sections 1 and 2 by the beginning of May. A parallel course of curves is also detected for sections 3 and 4 (permafrost and active layer in the upper parts of the investigated slope area). However, a decelerated increase can be observed, with highest resistivity values detected in March 2009, at a date when the curves of section 1 and 2 are already on the downgrade. The magnitude of increase is distinctly higher for sections 1 and 2 (factor 20-25) compared to sections 3 and 4 (factor 5-8). Towards the following measurement, (02.05.2009) resistivity values decrease to pre-winter conditions.

Resistivity values in winter 2009/2010 show a different progression compared to the previous winter, with a more gradual increase. For all sections, a slight increase of values is detected between August and October – prior to the first cold-snap. Between the first – comparatively early – cold-spell by the beginning of October and mid-December resistivity values of the permafrost body (a) and the active layer (a) (cf. FIGURE 7.15) in the lower parts of the slope show a constant increase. Curves of sections 3 and 4 are almost constant showing no increase. The early – but leisurely – increase of values for sections 1 and 2 is in line with the early drop of air- and vent temperatures by the beginning of October and the onset of the zero-curtain phase within the humus layer. In contrast, to winter 2008/2009, sections 1, 3 and 4 reach their peak simultaneously (23.02.2009) while values of the main permafrost body increase until the end of March 2010. Due to technical difficulties, the phase of snowmelt and the correlated decrease of

resistivity values are not resolved for spring 2010. However, it should be noted that maximum resistivity values of sections 3 and 4 are higher in winter 2009/2010 compared to the previous year, while values of the permafrost body (section 2) are lower. Differences in resistivity values of the active layer in section 1 are negligible.

In October 2010 resistivity curves show an initial increase of values that can be correlated with a short cold-snap. Increase is strongest for the permafrost body and the active layer at the lower parts of the investigated slope section, minor for section 4 and negligible for section 3. Towards the end of November values decrease again, in correspondence to a period with air temperatures above 0 °C. In February, all curves reach their peak simultaneously with a course of the curves comparable to winter 2008/2009. Sections 3 and 4 show a slightly decelerated increase in comparison to sections 1 and 2. A drop of values is observable for section 1 in mid-January, while the remaining sections appear unaffected. The date of the drop concurs with a phase, where air temperatures are above the freezing point. Humus temperatures indicate frozen conditions for this period but an increase of temperatures from -9.9 °C (06.01.2011) to -3.6 °C at the date of the monitoring measurement (15.01.2011). All sections show a rapid decrease of resistivity values towards the end of April 2011, followed by a constant course of curves during the subsequent summer.

Last measurement of the monitoring period has been conducted in March 2012, with no resistivity data recorded during the preceding freezing/supercooling period. Resistivity values of the four sections in March 2012 – representing maximum winter values – show little deviance to measurements of previous years.

7.3.2.2 Val Susauna

FIGURE 7.16 - FIGURE 7.18 show results from ERTM conducted between August 2009 and March 2012 at the Val Susauna. The resistivity evolution of defined sections – extracted according to FIGURE 7.5 – in comparison to humus temperatures as well as data on snow-thickness, air- and vent temperatures during the monitoring period is presented in FIGURE 7.19.

The first tomogram from ERTM at the Val Susauna was measured in August 2008 (FIGURE 7.16 a). The general subsurface distribution is assimilable to results presented in CHAPTER 6 (cf. FIGURE 6.10) with an elongated high resistive anomaly of 4-8 m

thickness embedded into a matrix with resistivity values < 5 kΩm. Table of the resistive anomaly is located at a depth of 2-3 m. The presence of perennial frozen ground has been detected in the lower parts of the slope (horizontal distances 10-45 m) by repeated ERT and SRT measurements (cf. CHAPTER 6.2.1.2). For a clarification of the terminology, this area will be ascribed as permafrost. To anticipate results presented in this chapter, ERTM-data indicate frozen subsurface conditions for the complete monitoring period. The presence of ground ice upslope (45-105 m) could not be definitively confirmed by joint ERT/SRT measurements, even though resistivity values of around 14-20 kΩm point to frozen ground in this section. A seasonal frozen-ground occurrence is assumed for this area (cf. CHAPTER 6).

The tomograms and corresponding time-lapse data from summer 2009 (FIGURE 7.16) indicate a low variability of the subsurface resistivity distribution between August and November 2009. While the general shape of the high-resistive anomaly remains unaltered throughout this period, a slight but constant decrease of resistivity values within the permafrost body is detected. Magnitude of decrease is ranging around 1-5 % with highest rates between August and October (10-20 %). A constant increase during summer 2009 is detected for the seasonally frozen area between horizontal distances 45-105 m (3-6 m depth). Variability within the uppermost 3 m of the tomograms is rather low, showing a constant increase of resistivity values (5-90 % between consecutive measurements), followed by a decrease between the end of October and mid-November by 3-15 %.

As quality of the dataset measured in December 2009 is insufficient, the data-gap towards the measurement in late February 2010 is rather large. Between November 2009 and February 2010 resistivity values increase by 300-12000 % within the uppermost 8-10 m, throughout the tomogram. Matrix values below 10 m depth (horizontal distances 25-85 m) likewise increase, but at a much smaller magnitude of change (10-200 %). Resistivity values of below 8 kΩm remain indicative for unfrozen ground conditions. By the end of March 2010, resistivity values within the near-surface show a massive decrease by 80-95 %, while large parts of the subsurface are characterised by increasing resistivity values. Towards mid-April resistivity values decrease by 25-80 % for most parts of the tomogram. Resistivity values of up to 25 kΩm indicate widespread frozen conditions within the uppermost 2-3 m of the investigated slope section. An interpretation of the

high-resistive area below 8 m depth (horizontal distances 0-25 m) in February 2010, and of the corresponding time-lapse tomograms, is hard to accomplish. Amount of datum points in this area is limited and an artefact of the inversion in this section cannot be definitely precluded. Therefore, this section will be excluded from interpretation.

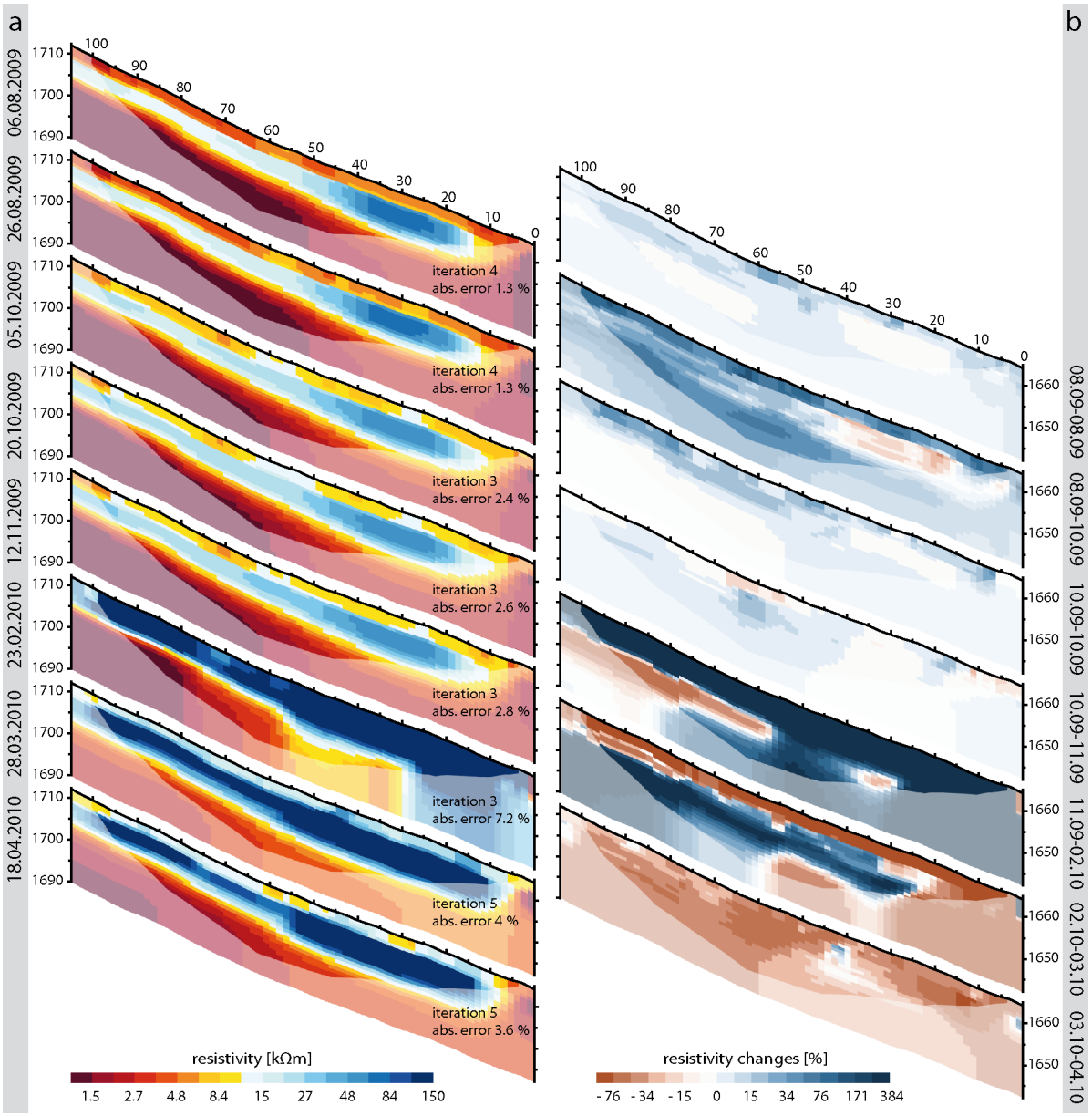

Figure 7.16: Val Susauna ERT-monitoring – August 2009 - April 2010 (a) and time-lapse tomograms (b). Time-lapse tomograms are referenced for two consecutive measurements.

The monitoring period between snowmelt in April and the onset of a consistent snow-cover in December 2010 is presented in FIGURE 7.17. Towards May 2010 the trend of decreasing resistivity values continues, except for the area beneath the permafrost body (horizontal distances 10-45 m) where values increase distinctly. Resistivity distribution

in May 2010 points to unfrozen conditions within the active layer and in parts of the section between horizontal distances 50-105 m (3-6 m depth).

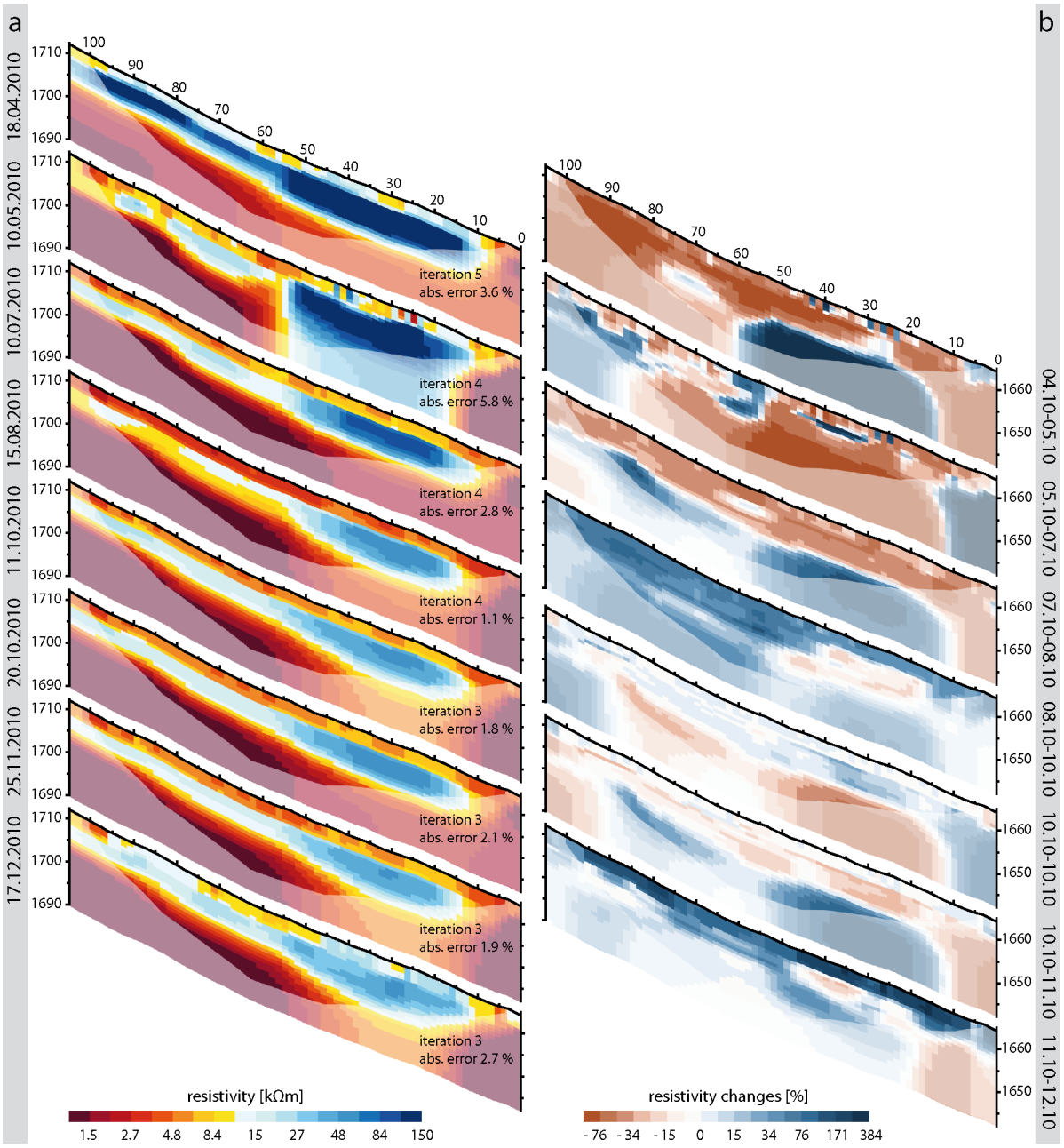

Figure 7.17: Val Susauna ERT-monitoring – April 2010 – December 2010 (a) and time-lapse tomograms (b). Time-lapse tomograms are referenced for two consecutive measurements.

Temporal subsurface variability is higher for summer 2010 compared to 2009. Between May and end of August resistivity values within the permafrost body decrease with a decreasing magnitude. Values slightly increase during October, followed by a period of decrease that lasts – for at least the central parts of the frozen-ground body – until mid-

December. Evolution of the near-surface layer is characterised by a general decrease of resistivity values between April and mid-August and a slight increase towards November. By December 2010 resistivity values indicate frozen conditions within large areas of the near-surface layer. It should be noted, that time-lapse calculation of August-October 2010 (FIGURE 7.17b) and August-October 2009 (FIGURE 7.16b) show markedly similar results. Both datasets show decreasing values for the permafrost body (5-20 %), while the remains of the time-lapse tomograms indicate an increase of values between the consecutive measurements by 30-80 %.

FIGURE 7.18 presents the ERT-monitoring period between December 2010 and March 2012. During winter, a strong increase of resistivity values is detected within the near-surface layer and the frozen-ground bodies, followed by a constant decrease, beginning in March. As shown for the Val Bever site, areas towards the foot of the slope (active layer and permafrost body) increase earlier and at a higher magnitude, compared to tomogram sections upslope. Maximum extent of the supercooled area is reached by February. Towards March, the evolution is differentiated, with an increase of values in the supercooled subsurface areas (3-8 m depth) and a decrease of values within the near-surface layer (0-3 m depth), most probably ascribed to snowmelt. Towards the end of October 2011, a trend to lower resistivity values is observable for the permafrost body, decreasing from ~200 kΩm in April to ~45 kΩm in October.

Towards the last measurement – conducted in March 2012 – resistivity values massively increase by 400-1000 %, with similar values and distribution in comparison to results of the previous years. Analysing the spatial distribution of the high resistive anomaly in high-winter of the monitoring period, it is striking, that results from February and March 2010 (FIGURE 7.16) show one elongated high resistive body, while results from 2011 and 2012 indicate a differentiation into two anomalies. Thereby a small section (horizontal distances 55-65 m) with resistivity values of 30-70 kΩm is located between the permafrost body (200-3000 kΩm) and the seasonally frozen area (horizontal distances 65-95 m; 150-700kΩm).

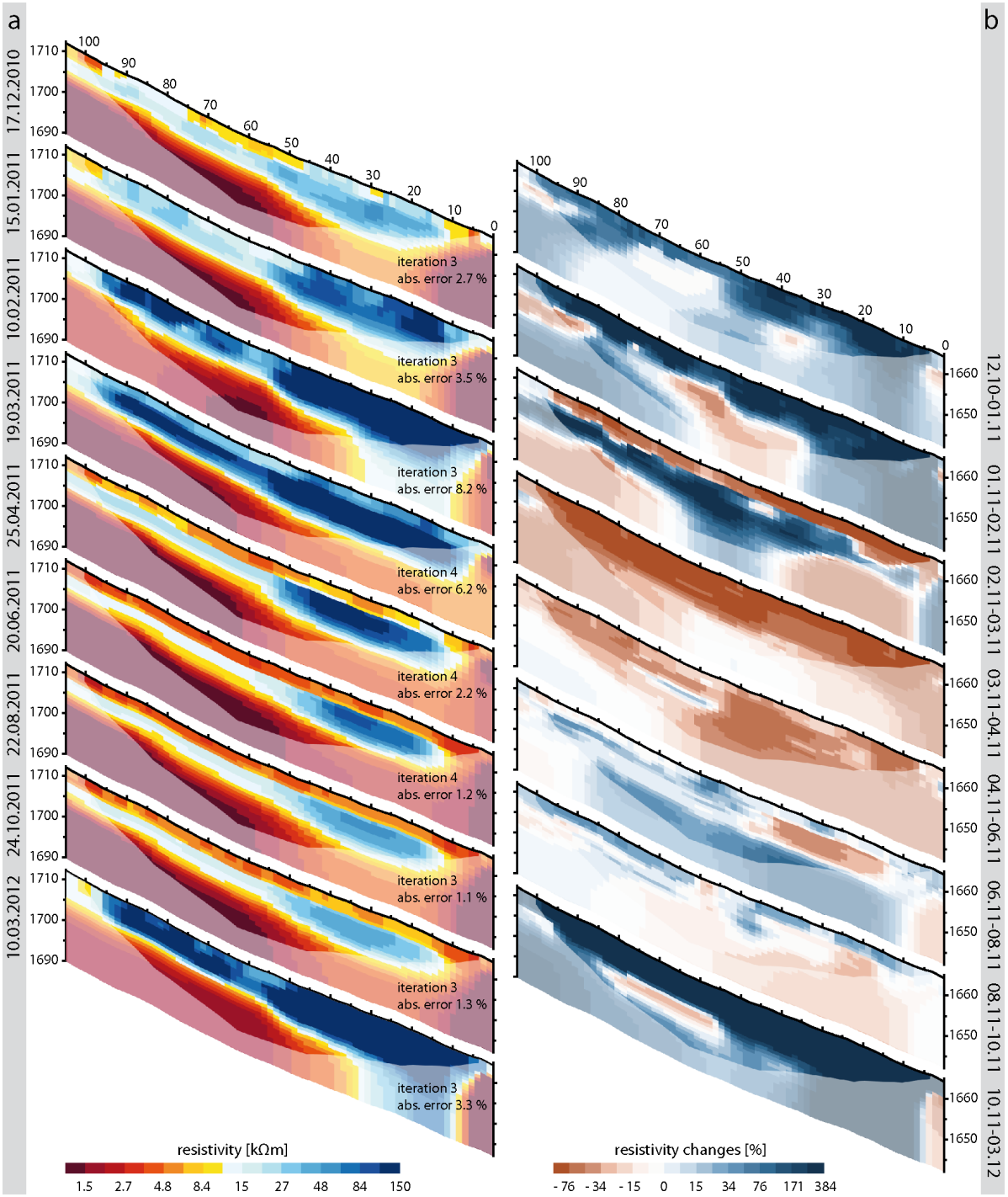

Figure 7.18: ERT-monitoring Val Susauna – December 2010 – March 2012 (a) and corresponding time-lapse tomograms (b). Time-lapse tomograms are referenced for two consecutive measurements.

Extracted resistivity values (cf. FIGURE 7.5) of the ERT-monitoring in the Val Susauna in comparison to temperature and snow cover distribution are presented in FIGURE 7.19. Data on snow cover thickness, derived from the meteorological station Samedan (FIGURE 7.19a) are equal to data presented in FIGURE 7.15.

Temperature evolution during the monitoring period is similar to data measured in the Val Bever. Mean summer air temperatures show only slight variability between 2010 (8.8 °C) and 2011 (9 °C). Variability of winter temperatures is more pronounced with regard to temperature profile and mean values. Lowest mean air temperatures are recorded in winter 2009/2010 (-5.3 °C), while minimum temperatures were lowest in winter 2011/2012 (-23 °C; mean air temperature -3.8 °C). Winter 2010/2011 represents the warmest winter of the measurement period (mean air temperature -3.2 °C) and is characterised by several days with temperatures above 0 °C during high-winter.

Vent temperatures are presented for vent 1, close to the foot of the slope and vent 2, located upslope (horizontal distance ~70 m of the monitoring array). During winter, vent temperatures are strongly related to air-temperatures but appear decoupled from air temperatures in summer. While the curves of the vent-temperatures show an almost parallel course, mean temperatures are in general lower for vent 1 compared to vent 2. In winter 2009/2010 MVT (-6.1 °C for vent 1; -3.7 °C for vent 2) are distinctly colder compared to 2010/2011 (-3.24 °C for vent 1; -1.62 °C for vent 2). Between mid-April and June/July temperatures of both vents show a continuous course with temperatures around 0 °C, followed by an increase to maximum values of 3-6 °C. Date of increase is earlier for vent 1; the magnitude of increase is higher for vent 2.

Snow-cover conditions in the upper Engadin during the monitoring period have been discussed above (Chapter 7.3.2.1), with a remarkable low snow thickness in winter 2010/2011, high snow thickness in winter 2011/2012 and unexceptional conditions in winter 2009/2010.

The time-depth plot of humus temperatures of the Val Susauna (Figure 7.19b) diverge strongly from data recorded at Val Bever. During summer, a strong gradient of temperatures is detected between the different depth levels, while data from high-winter show constant temperatures with depth. Onset of the zero-curtain period in autumn/early winter occurs very rapidly and lasts for around two month. The zero-curtain period in late winter/spring shows a strong vertical differentiation with a simultaneous onset but a distinctly diverse duration. While positive temperatures in 5 cm depth are recorded by the end of snowmelt in late April, the humus in 30 cm depth remains frozen until the end of June. During summer humus temperatures below a depth of 15 cm appear almost decoupled from daily variations in air temperatures with

maximum temperatures in 30 cm depth of only 4.3 °C in 2010 and 3.3 °C in 2011. A detailed analysis of temperature data will be given in CHAPTER 8, focusing on the ground-thermal regime of the study sites

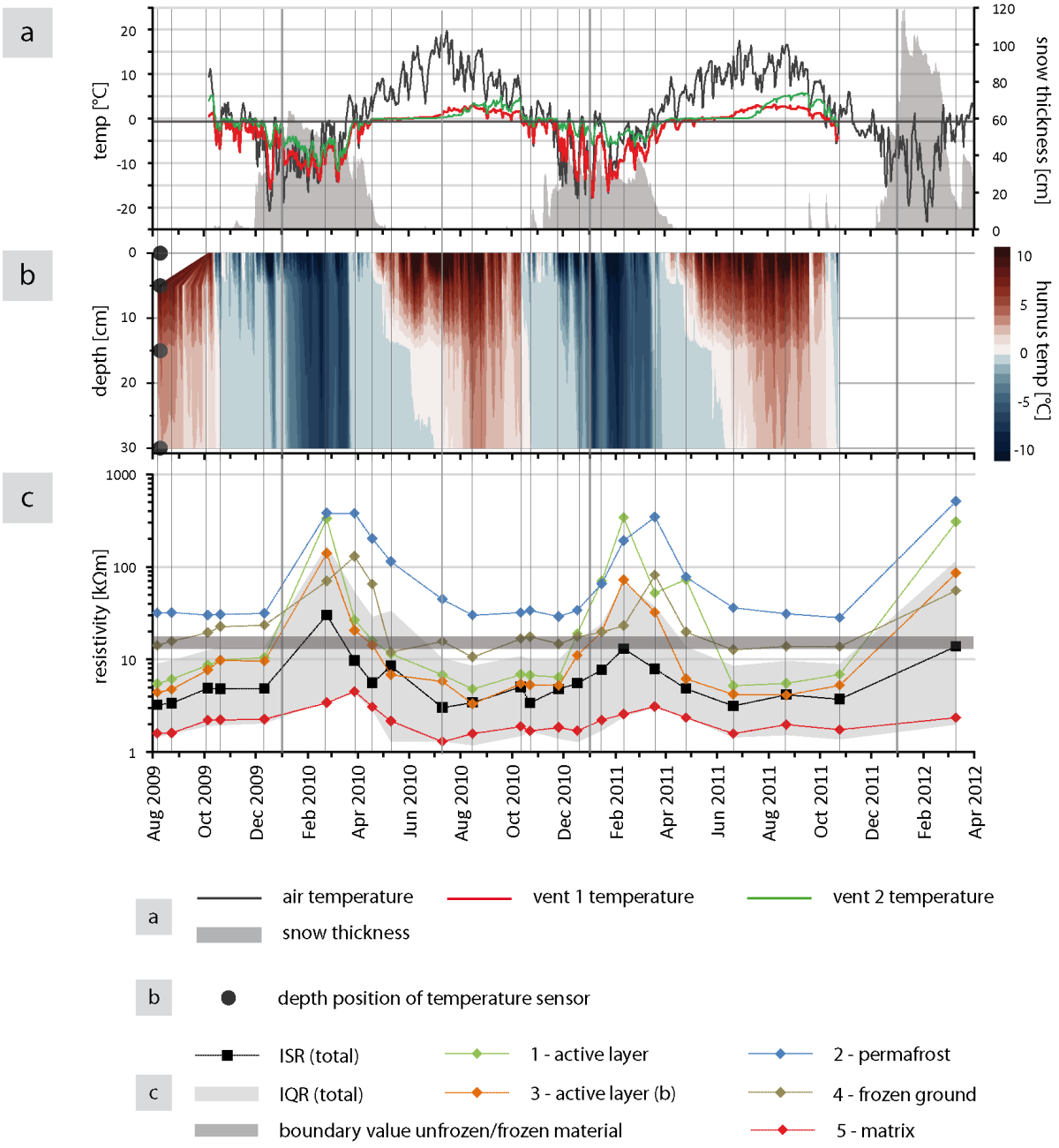

Figure 7.19: Val Susauna – median of extracted resistivity data (c) in comparison to humus temperatures (b) and data on snow-thickness, air- and vent temperatures (a) for the monitoring period.

A pronounced annual cycle is observable for all resistivity curves of extracted data (FIGURE 7.19). Increased resistivity values are recorded for all sections in winter, while summer values in general show a relatively low intra- and inter-annual variability. With resistivity values higher than 30 kΩm throughout the monitoring period, permafrost can be assumed for section 2 (boundary values for frozen ground conditions are according to results presented in CHAPTER 6 are around 15 kΩm).

Extracted resistivity data indicate unfrozen conditions in summer the summer half-year (April to late November) and frozen conditions during high-winter for sections 1 (active layer) and 3 (near-surface layer). Values of section 5 – defined as the matrix – are indicative for unfrozen conditions throughout the monitoring period with a low variability of values. While values of section 4 (frozen ground) are definitely indicative for frozen ground during winter, the course of resistivity values is ambiguous and hard to interpret during summer, ranging around the boundary values defined for frozen ground.

Between August 11th and December 2009, resistivity values of the permafrost body are almost constant (30.5-31.5 kΩm). Resistivity values of sections 1, 3, 4 and 5 as well as overall values increase towards October and remain constant throughout the zero-curtain period (30 cm depth, 22.10.2009-15.12.2009). Towards the end of February, sections 1-4 show a massive increase. Date of the following measurement (28.10.2010) coincides with the onset of the zero-curtain period in spring (27.03.2010). Active- and near-surface layer values strongly decrease towards this date, while values of the permafrost body remain constant. Sections 4 and 5 reach their peak. Resistivity values of section 4 rapidly decrease between mid-April and early May, and range around 10-17 kΩm during summer. The curves of sections 1-3 show a steady decrease with minimum values detected at August 15th 2010, at a date when humus temperatures are close to maximum (3.6 °C in 30 cm depth). The measurement in July coincides with the onset of positive temperatures in the humus layer (0.2 °C in 30 cm depth by July 10th) and the increase of temperatures within the two vents.

Similar to the previous year a slight increase of resistivity values is detected between August and October 2010 for sections 1-4. During the zero-curtain period (in 30 cm depth from 27.10.2010 to 15.12.2010) resistivity curves gently decline for all sections, followed by a massive increase of resistivity values during the period of supercooling.

For sections 1 (active layer) and 3 (near-surface layer) maximum values are observed during mid-February 2011, while curves of sections 2 and 4 reach their peak with a delay in late March. Resistivity curves of all sections show a steep decline towards the measurement in June 2011, followed by a complanate course towards late October. While values of the permafrost body slightly decrease during summer, values of the active layer as well as of the near-surface layer show a slight increase. The curve of section 4 indicates almost constant values. The last measurement of the monitoring period has been conducted in March 2012, with no additional measurements during the zero-curtain period. Resistivity distribution is comparable to results from measurements in high-winter of the previous years. Values of the permafrost body and active layer are quite similar (340-500 kΩm), even though the dates of the peaks are diverse. Likewise maximum values of the seasonal frozen ground body and the superimposing near-surface layer are corresponding (130-140 kΩm in winter 2009/2010; 70-80 kΩm in winter 2010/2011; 55-80 kΩm in winter 2011/2012). It is likely that values will increase until the end of March, comparable to the observations made in the previous year.

7.3.2.3 Brüeltobel

Results from ERTM conducted between August 2009 and April 2011 at the Brüeltobel are presented in FIGURE 7.20, FIGURE 7.21 and FIGURE 7.22. The resistivity evolution of defined tomogram sections – according to FIGURE 7.5 – in comparison to humus temperatures and data of air- and vent temperatures during the monitoring period are presented in FIGURE 7.23.

According to the general setting of the study site (CHAPTER 3.2) and the results from geophysical measurements (CHAPTER 6), the talus slope can be subdivided into five sections (see FIGURE 7.5). The central part of the study site is divided into an area characterised by a thick humus/moss cover (horizontal distances 8-32 m; section 1 – active layer) and uncovered, loose talus material between horizontal distances 32-47 m (section 3). Fine-grained material with resistivity values lower than 3 kΩm is located at the top of the slope, below the rock-wall and at the foot of the slope (horizontal distances 0-8 m and 48-63 m; section 4). The subsurface is characterised by two delimited areas defined as the permafrost body (horizontal distances 8-32, 2-8 m depth; section 2) and unfrozen matrix material (horizontal distances 35-63 m, below 2 m depth; section 5).

The composition of the talus slope is mirrored by the resistivity distribution and evolution during the monitoring period. Resistivity values of the matrix (section 5) and the near-surface areas at the top and the foot of the slope (section 4) show a comparably low variability. Resistivities remain below boundary values characteristic for frozen ground throughout the monitoring period (section 4: <1.5 kΩm; section 5: <6 kΩm). Variability of resistivity values of the uncovered talus (section 3), the active layer (section 1) and the permafrost body (section 2) is explicitly higher.

FIGURE 7.20 illustrates the subsurface resistivity distribution and evolution between early August 2009 and high-winter (February 22nd) 2010. Temporal variability of resistivity values within the permafrost body between August and mid-December is relatively low. In general, an increase of resistivity values within the permafrost body between August 4th (maximum value 18 kΩm) and November 13th 2009 (maximum value: 26 kΩm) has been detected, followed by a decrease of around 20-40 % towards December 15th.

The active layer (horizontal distances 8-32 m) shows only slight variations of resistivity values between August 4th and the end of September. Resistivity values remain below 6 kΩm, where the humus layer is thickest (horizontal distances 8-18 m), and below 10-12 kΩm (horizontal distances 18-32 m), where the humus layer is more fragmentary and higher amounts of loose talus can be found. Resistivity values of the uncovered talus (horizontal distances 32-47 m) are comparably high (high amounts of air-filled cavities and absence of fine-grained material) throughout the monitoring period and show a strong variability during summer, which is in contrast to the active layer. Resistivity values increase by 80 % to more than 300 % from 9-14 kΩm (August 4th 2009) to between 20 and 45 kΩm (August 24th 2009) and to 30-55 kΩm by September 29th 2009.

Similar to summer conditions, resistivity evolution of the active layer and the uncovered talus differs strongly during autumn/early winter. Between September and October 20th resistivity values within the active layer increase by up to 300 % from between 5 and 20 kΩm in September to between 10 and 60 kΩm in October. Values within the uncovered talus decrease during this period by 10-40 %. Between October 20th and November 13th, resistivity values within the active layer and the uncovered talus decrease strongly. The magnitude of decrease is distinctly higher for the active layer

(60-80 %) compared to the uncovered talus section (30-50 %). Resistivity values of 20-350 kΩm are indicative for a consistently frozen active layer by December 15th.

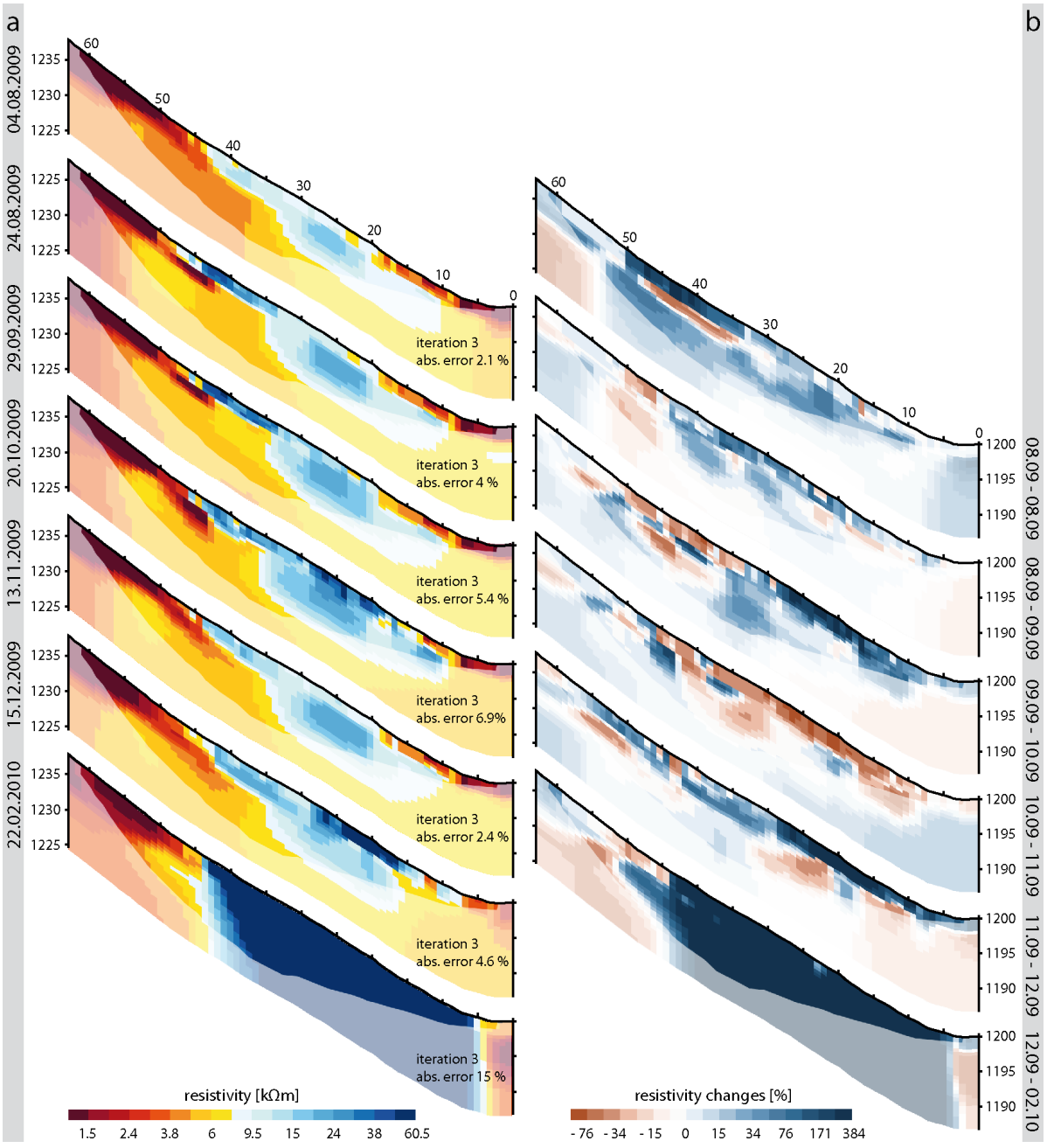

Figure 7.20: ERT-monitoring Brüeltobel – August 2009 – February 2010 (a) and corresponding time-lapse tomograms (b). Time-lapse tomograms are referenced for two consecutive measurements.

The uncovered talus section shows only little variations compared to the previous month, with resistivity values below 25 kΩm. Towards February 22nd 2010, resistivity values between horizontal distances 5-38 m increase almost exponentially by up to 50000 %. The limited contour scale implicates almost homogeneous subsurface

conditions, which is not the case. In fact, the differentiation of the subsurface retains during the period of supercooling in high winter. Resistivity values within the active layer (800-10000 kΩm) exceed values measured in the near-surface area with uncovered talus (100-3000 kΩm). Highest values of between 1000-7000 kΩm are detected within the permafrost body in areas towards the foot of the slope (horizontal distances 15-20 m, 3-8 m depth).

ERTM-data illustrated in FIGURE 7.21 represent the period between February and July 2010, characterised by snowmelt and increasing air temperatures, as well as the resistivity tomograms measured in October and November 2010. Due to technical difficulties, no data were recorded during August and September 2010.

The period between February and July 2010 (FIGURE 7.21) is characterised by a strong decrease of resistivity values. As shown for the Val Bever and Val Susauna sites, the supercooled area – characterised by above-average resistivity values – contracts distinctly towards a core that represents the permafrost body (horizontal distances 8-25 m; 2-8 m depth). Minimum values within the permafrost body (12-13 kΩm) were observed by July 7th 2010. The divergent evolution of resistivity characteristics in the active layer and the slope section with uncovered talus becomes obvious in the period from February to July: Between February 22nd and March 27th, resistivity values in both slope sections decrease by 90-98 %. Therefore, resistivities within the section of uncovered talus have achieved values characteristic for summer conditions (12-20 kΩm), while values within the active layer are distinctly higher (30-60 kΩm) and therefor indicative for frozen conditions. Towards July, values within the active layer consistently decrease by 30-50 % between consecutive measurements, indicating a thawing of the active layer. Variability within the uncovered talus is low, with a trend to higher resistivity values towards May, followed by a slight decrease between May and July.

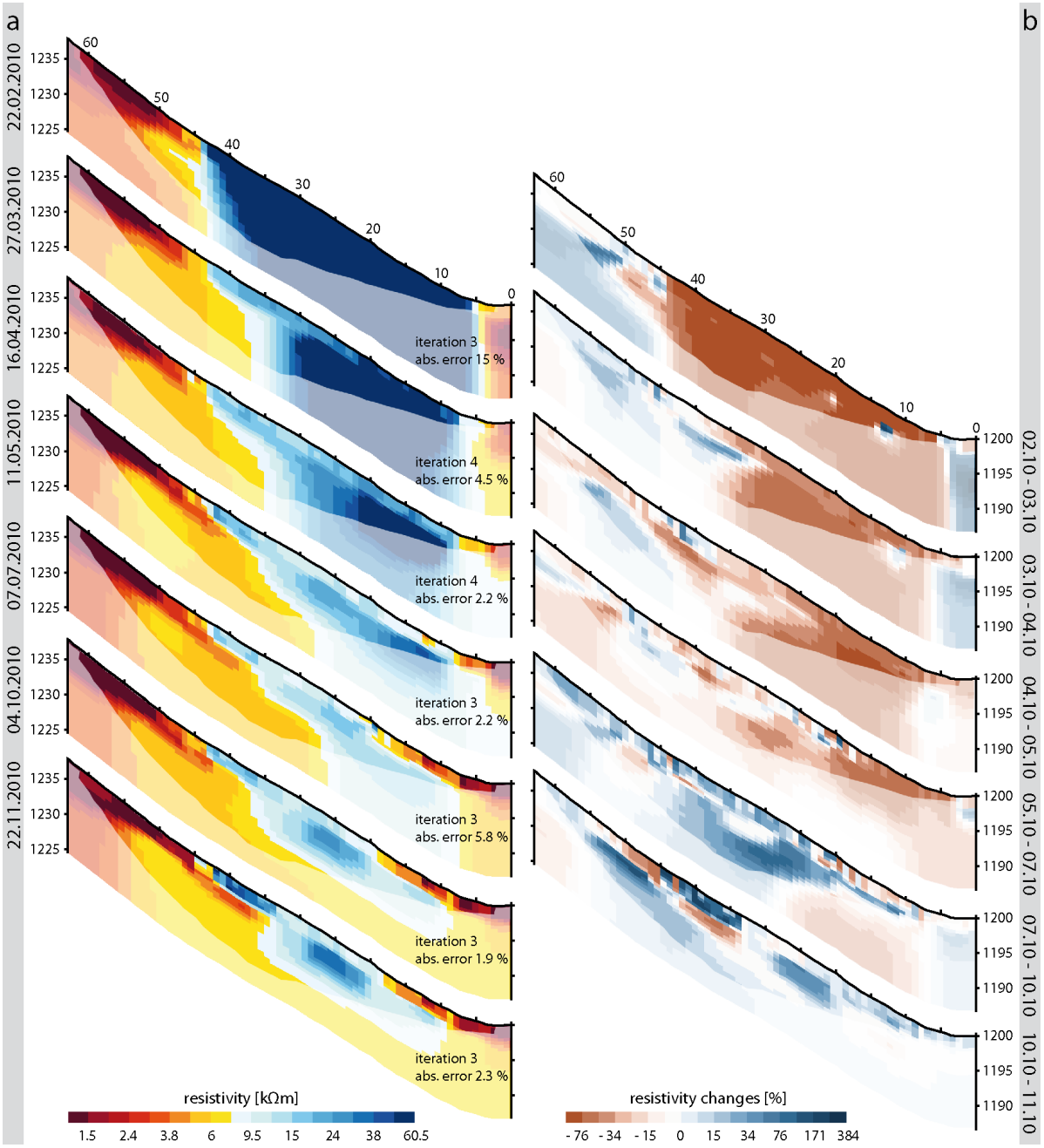

Figure 7.21: ERT-monitoring Brüeltobel – February 2010 – November 2010 (a) and corresponding time-lapse tomograms (b). Time-lapse tomograms are referenced for two consecutive measurements.

Regrettably, no data are available between July and October 4th 2010. Alterations in the near-surface are negligible between these two measurements. Most remarkable is the evolution of the resistivity distribution within the permafrost body. The "core" of the permafrost body, characterised by the area with highest resistivity values, has switched its position between May and October. Location of the permafrost core in spring (30-38 kΩm) is between horizontal distances 10-18 m (2-8 m depth). By July 7th, resistivity values within the permafrost section have reached their minimum (12-13 kΩm) with no

distinct core observable. In October, the section with highest resistivity values within the permafrost body (16-26 kΩm) is located between horizontal distances 22-30 m (2-6 m depth). Towards November 22nd, resistivity values within this permafrost-core increase by 30-40 % to values of 30-36 kΩm. As observed in the previous year, resistivity variations within the matrix, within the near surface layer at the foot of the slope and below the rock-wall are negligible.

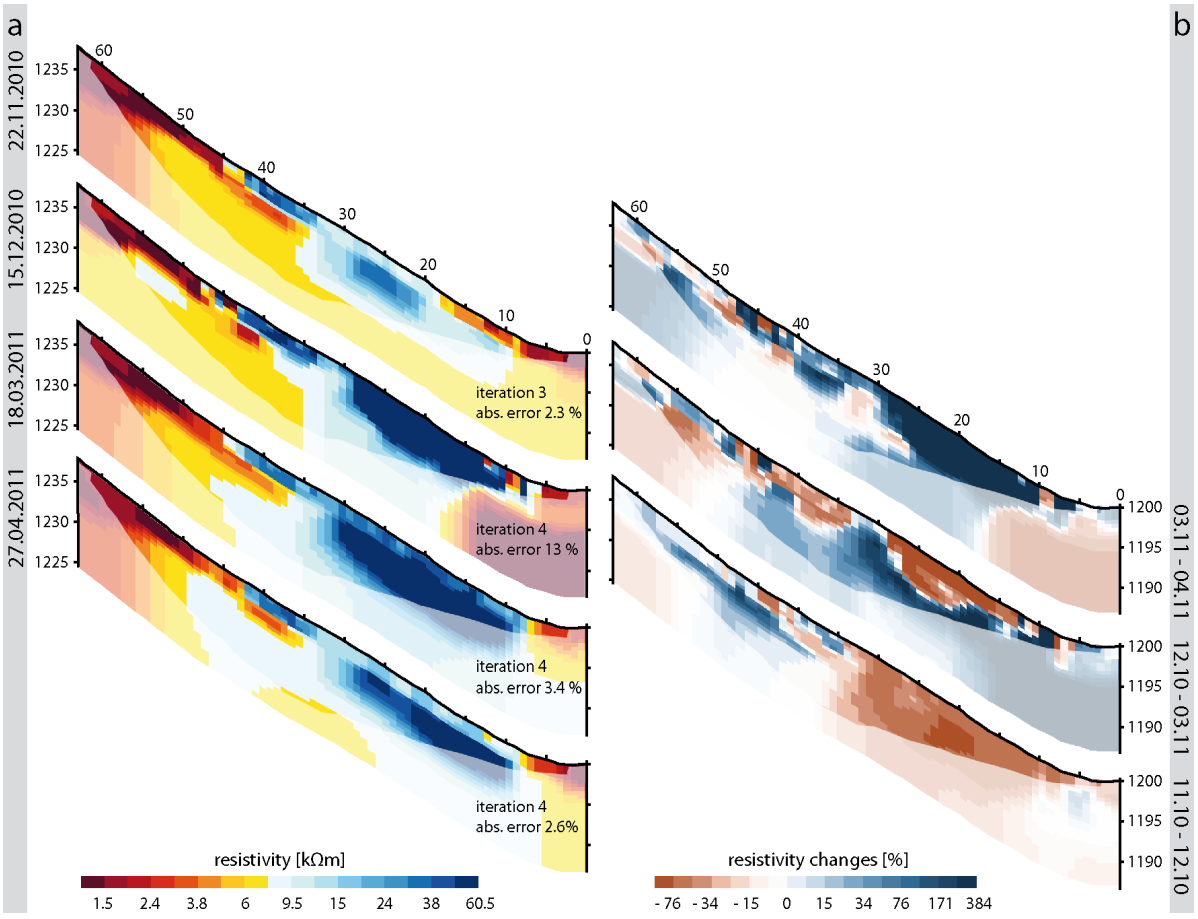

Figure 7.22: ERT-monitoring Brüeltobel – November 2010 – April 2011 (a) and corresponding time-lapse tomograms (b). Time-lapse tomograms are referenced for two consecutive measurements.

The temporal resolution of monitoring measurements during winter 2010/2011 (FIGURE 7.22) is limited, due to technical difficulties and insufficient data quality. However, data show results comparable to the previous year. By December 15th 2010, resistivity values within the active layer and the permafrost body are distinctly higher (100-600 kΩm) than values recorded in December 2009 (active layer: 30-300 kΩm; permafrost body 12-20 kΩm). This indicates an earlier onset of supercooling in 2010 compared to the previous year. No dataset is available for high-winter around February 2011, where

highest resistivity values are expected. By March 18th, a decline of values is detected within the near-surface of the active layer and the uncovered talus. As shown for the previous year, values within the section with uncovered talus remain almost constant towards the last measurement by April 27th; values within the active layer decrease consistently. Resistivity values of 10-16 kΩm are at least indicative for partly frozen active layer by April 27th 2011. Likewise, the area defined as permafrost shows a trend similar to the previous year, contracting towards a core (60-130 kΩm) between horizontal distances 10-20 m (2-8 m depth).

FIGURE 7.23 presents extracted resistivity data of the ERT-monitoring at the Brüeltobel in comparison to air-, vent- and humus temperatures. Data on snow cover distribution and evolution are not available. Various technical failures have affected the length of monitoring period at the Brüeltobel as well as the temporal resolution of monitoring measurements.

Mean air temperatures (FIGURE 7.23 a) during the winter half-years of the monitoring period at the Brüeltobel are relatively warm (-1.1 °C in 2009/2010; -0.47 °C in 2010/2011). The course of temperatures is characterised by several days with air temperatures warmer than 0 °C. Mean air temperatures in summer 2010 are 8.5 °C and therefore even slightly colder than temperatures measured at the Val Susauna (8.8 °C) and the Val Bever (8.7 °C).

Vent temperatures (FIGURE 7.23a) are presented for vent 1, close to the foot of the slope, and vent 2, located upslope (cf. FIGURE 7.3c), at the transition between the sections with uncovered talus and fine grained surface material (horizontal distance ~50 m of the monitoring array). During winter, temperatures of vent 1 are strongly linked to air temperatures (MVT -3.09 °C), while the course of the temperature curve during summer shows only little variability, with a maximum of 4.6 °C and a mean temperatures of 1.07 °C. Course of the temperature curve of vent 2 is vice versa, with a strong coupling to air temperatures in summer (MVT in summer: 9.7 °C) and ranges around 0 °C during winter (MVT in winter 2009/2010: 2.4 °C; winter 2010/2011: 3.35 °C).

The time-depth plot of humus temperatures at the Brüeltobel (FIGURE 7.23b; see also FIGURE 7.3c for location of the logger) shows a strong gradient of temperatures between the different depth levels, while data from high-winter show little variability of

temperatures with depth. Course of temperatures in autumn is characterised by a rapid cooling throughout the humus layer. Humus temperatures range around 0 °C from October 15th to January 8th. Coldest temperatures observed at the end of March were ranging around - 8 °C, followed by a rapid onset of the zero curtain. Propagation of warm temperatures within the humus layer shows a strong vertical differentiation. Constant positive temperatures in 5 cm depth were recorded by May 2nd, in 21 cm depth by May 30th and in 36 cm depth by June 13th. Humus temperatures in Winter 2010/2011 are characterised by a very long zero-curtain period (October 22nd – January 23rd), that is interrupted by short periods with temperatures slightly above the freezing point (November 2010) and short cold snaps between December and January. Temperatures distinctly below the freezing point are recorded between January 24th and March 13th, with minimum temperatures ranging around -4 °C. The zero-curtain period in spring 2011 is not completely covered by temperature records shown in FIGURE 7.23b.

As shown for Val Bever and Val Susauna sites, a pronounced annual cycle is visible for the curves of resistivity data extracted from sections defined as active layer (section 1), permafrost (section 2) and uncovered talus (section 3) (FIGURE 7.23c). Variability of resistivity values during the monitoring period for sections 4 (fine-grained surface material below the rock-wall) and 5 (matrix material) is negligible.

Median resistivities in the near-surface below the rock-wall (section 4) are relatively low (1.1-1.4 kΩm) and indicate unfrozen conditions throughout the monitoring period. Resistivity values of section 5 (matrix) can be regarded as characteristic for unfrozen talus material in the Brüeltobel, ranging between 4.5 and 6.3 kΩm.

Between August 4th and the last measurement within the zero-curtain period of autumn 2009 (December 15th) evolution of resistivity values extracted from sections 1, 2 and 3 is diverse. Median values within the uncovered talus increase strongly from 11 kΩm (August 4th) to 33 kΩm (September 29th), followed by a decrease with the onset of the zero-curtain period. The course of the curve of section 1 shows little variations between August and September (8-9.5 kΩm). The distinct peak to 23.5 kΩm by October 10th can be correlated to a cold-snap, causing a freezing at least in parts of the humus layer (FIGURE 7.23a and b). The decrease of resistivity values towards the subsequent measurement equals the previous increase in magnitude.

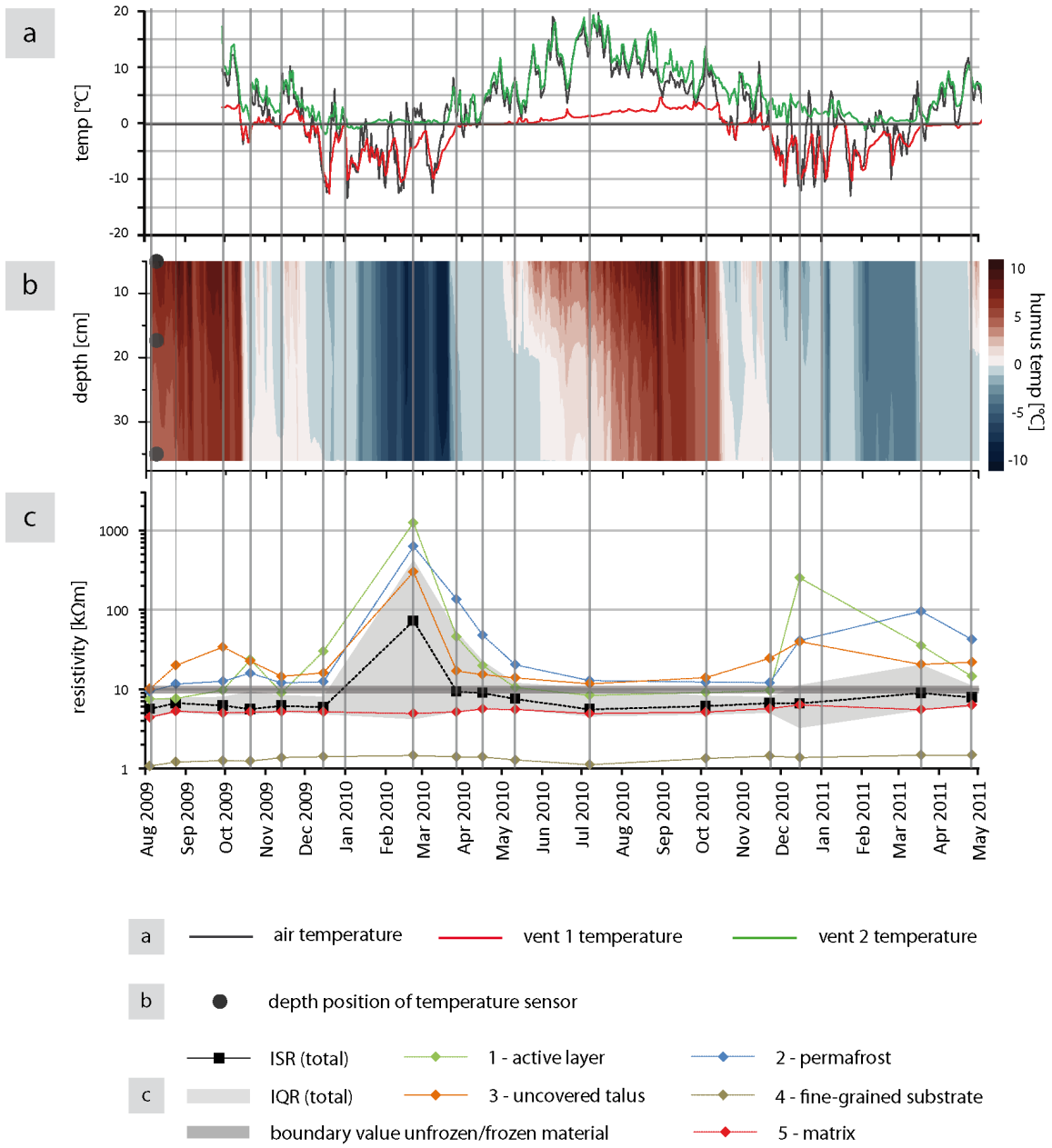

Figure 7.23: Brüeltobel – median of extracted resistivity data (c) in comparison to humus temperatures (b) and data on air- and vent temperatures (a) for the monitoring period. Location of the sections for extraction is given in FIGURE 7.5.

Within the permafrost body (section 2), median resistivity values slightly increase between August 4th (10.5 kΩm) and October 10th (15.9 kΩm), followed by a decrease to 12.5 kΩm by December 15th. A distinct cold-snap has been recorded around the date of the measurement in December (12.12.-20.12.2009), with observed minimum temperatures of -12 °C. While resistivity values within the active layer show a distinct increase from 10.5 to 30 kΩm, values within the permafrost body and the uncovered talus remain almost unaltered.

Maximum values for winter 2009/2010 are recorded by February 22nd 2010; no measurements could be conducted between December and February. Median resistivity values within the active layer (1247 kΩm) exceed values of the permafrost body (629 kΩm) and the uncovered talus (299 kΩm).

By March 27th, the resistivity curve of section 3 (uncovered talus) drops distinctly to 17 kΩm – equalling resistivity values prior to supercooling. During the zero-curtain period in 2010 (March 19th-May 30th), values within the active layer and the permafrost body show a gradual decrease towards May 11th. Between July and November 22nd variability of resistivity values is low for sections 1 and 2. A strong ascent of the resistivity curve of section 3 is observable between October 4th and November 22nd 2010, which cannot be correlated to any of the temperature events.

Data coverage in winter 2010/2011 is relatively low, with no data from high-winter available. However, the strong increase of resistivity values of sections 1 and 2 by December 15th can be correlated to a short cold-snap prior to the date of the measurement. Magnitude of increase is distinctly higher for the active layer (from 9 to 253 kΩm) compared to the permafrost body (from 12 to 40 kΩm). Data measured in March and April must be regarded as declining resistivity values, as maximum values could not be recorded in winter 2010/2011. However, comparing results from March and April of 2011 and 2012 for sections 1 and 2, resistivities do not differ significantly, even though temperatures were distinctly warmer in winter 2010/2011. By March 27th 2010, resistivities of section 1 (46 kΩm) and 2 (135 kΩm) are slightly higher, compared to March 18th 2011 (section 1: 35 kΩm; section 2: 96 kΩm). For April, the gap in resistivity values between the two years is reduced. Resistivities within the active layer are 19.8 kΩm by April 16th 2010 and 15 kΩm by April 26th 2011; median values in the permafrost body of 48 kΩm in 2010 oppose 42 kΩm in 2011.

7.3.3 SRT monitoring Val Susauna

Results from SRTM conducted between November 2010 and June 2011 at the Val Susauna are presented in Figure 7.24, Figure 7.25 & Figure 7.26. Corresponding results from ERTM, temperature- and snow-cover data of the monitoring period are illustrated for better visualisation and comparison of data.

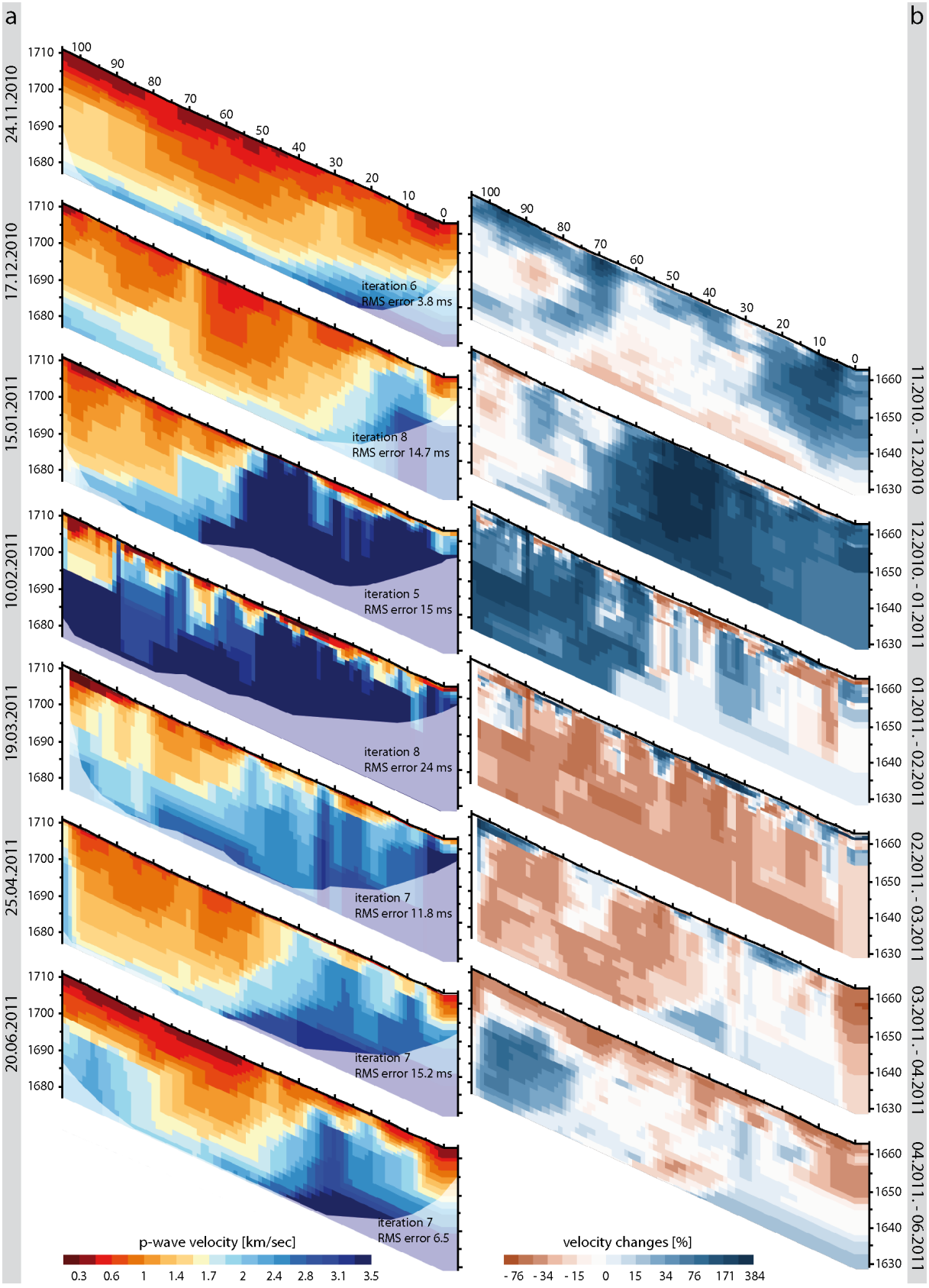

Figure 7.24: SRT-monitoring Val Susauna – November 2010 – June 2011 (a) and corresponding time-lapse tomograms (b). Time-lapse tomograms are calculated for subsequent measurements.

Interpretability of the first SRTM-dataset (24.11.2010; FIGURE 7.24a) is difficult to accomplish. P-wave velocities are below values characteristic for frozen ground. However, between horizontal distances 10-40 m, an area is observable where the vertical velocity gradient is higher than for the central parts of the tomogram, and coincides with the location of the permafrost body shown by ERT-data (FIGURE 7.25). Maximum velocities in this section are between 0.9 and 1.4 m/sec and thereby not representative for frozen ground conditions. However, it must be considered that velocity values might be underestimated due to an inappropriate geophone spacing (4.5 m), which is not capable of detecting the relatively low velocity contrast between frozen and unfrozen ground at this date of the year (cf. CHAPTER 2.1.2). Especially with regard on data presented in FIGURE 6.10, where results of the previous month – using a geophone spacing of 3 m – clearly indicate frozen ground conditions.

Towards December 17th 2010 (FIGURE 7.24), velocity values increase for most parts of the tomogram, with highest magnitude in the near-surface (50-300 %) and at the foot of the slope (60-200 %; horizontal distances 5-25 m, 3-25 m depth). It should be noted that SRT is not capable of detecting the lower boundary of the frozen ground bodies, but assumes an increase of velocity values with depth (cf. CHAPTER 2.1.2).

Between November 24th 2010 and February 10th 2011, the spatial distribution of p-wave velocities representative for frozen ground increases massively. Between November and December, the area of strongest increase is located at the foot of the slope and stepwise shifts upslope (25-55 m between December and January; 55-105 m between January and February). By January 15th 2011, the complete permafrost body is supercooled, as induced by velocity values of more than 4 km/sec. Towards February velocities of the permafrost body show a slight increase (0-60 %). Velocities of 1.8-3 km/sec in February 2011 are indicative for frozen ground in the upper parts of the investigated slope section (horizontal distances 55-90 m). Between February 10th and March 19th 2011 velocity values decrease consistently throughout the tomogram by 30-60 %, except for areas in the shallow subsurface (0-3 m depth), where an increase of values is detected. Towards the measurement in June 2011, dimensions of the high-velocity body decrease. Within the high-velocity body, values show a diverse evolution, with a strong decrease between February and March (30-50 %), little variability between March and April (± 10 %) and a trend to increasing values by up to 20 % towards June

20th. Upslope (horizontal distances 50-105 m), velocities decrease consistently between February 10th and April 25th, by 30-60 % between consecutive measurements. By April 25th, velocities between 0.8 (2 m depth) and 1.25 km/sec (20 m depth) indicate unfrozen conditions in the upper half of the investigated slope section. Towards June 20th, this area is characterised by an on-going decrease of velocities between 0 and 8 m depth (40-50 %) and an increase of values below 10 m depth (40-80 %).

Velocity values within the active layer during the monitoring period vary spatially and temporally. Velocities of 0.3-0.6 km/sec measured in high-winter between 0 and 2 m depth indicate unfrozen conditions within the near-surface layer along the monitoring transect. Velocities above the permafrost body (1.7-2 km/sec) are indicative for a partly frozen active layer during high-winter; measurements from June 20th indicate unfrozen conditions (0.4-1.2 km/sec).

In general, results from ERTM and SRTM (see also FIGURE 7.26) lead to coinciding interpretations regarding the frozen ground distribution and evolution during winter 2010/11, but differ in some individual details. Beside the permafrost body, which is not detected by SRT in November 2010, and underestimated in size in December 2010, results from ERT and SRT differ with regard on the area defined as seasonal frozen ground (horizontal distances 55-105 m; 3-8 m depth) for most parts of the monitoring period. Coinciding results for this area are given solely for the measurement in February, where resistivity- (70-170 kΩm) and velocity- (2.1-3 km/sec) values are indicative for frozen ground. Contradictory results might be ascribed to an inappropriate geophone spacing, as discussed in CHAPTERS 6.2 and 6.3. ERT and SRT data are in good agreement regarding the spatial characterisation of the permafrost body. Both datasets from January 15th indicate a differentiation into two main sections. Areas with maximum values located between horizontal distances 10-20 m (180-210 kΩm; 3.8-4.7 km/sec) and between 35-50 m (8-110 kΩm; 3.5-4.7 km/sec). Between these areas (horizontal distances 20-35 m) distinctly lower values are recorded (40-75 kΩm; 2-3.5 km/sec). It should be noted again, that the spatial heterogeneity of resistivity- and velocity distribution is in parts underrepresented, due to limitations of the colour scales. This problem arises especially for the logarithmic scale of ERT. Resistivity- as well as velocity values show a strong spatial heterogeneity within the permafrost body during winter. For the

measurement of February 10th, values range between 180-900 kΩm and 3-4.8 km/sec, respectively.

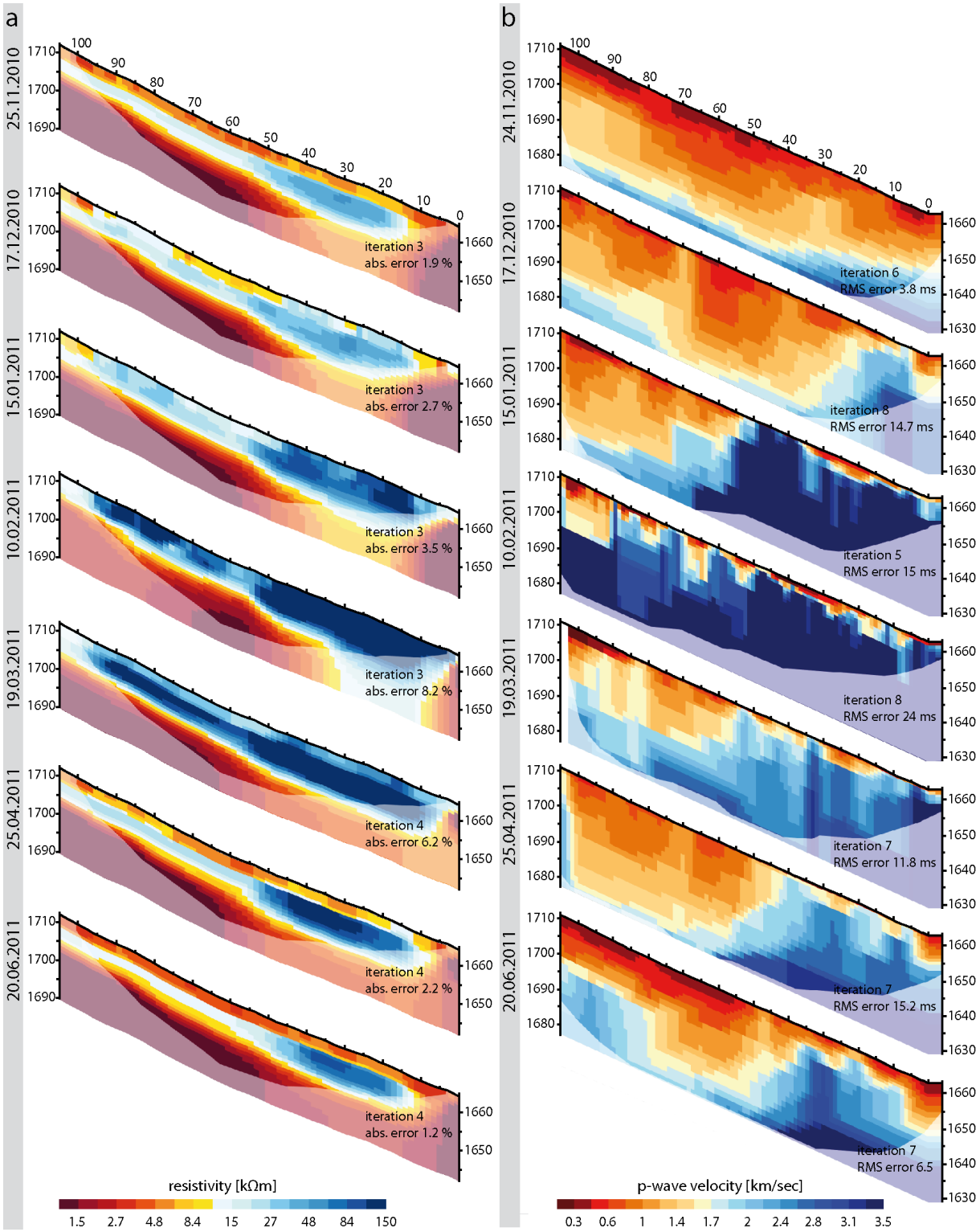

Figure 7.25: Comparison of images from SRT- (b) and ERT-monitoring (a) at the Val Susauna during winter 2010/2011.

Correspondingly, ERT and SRT-data document a gradual downsizing of the permafrost body between March 19th and June 20th. Even though the localization does not precisely coincide, both methods detected an area with highest values within the upper parts of the permafrost body, between horizontal distances 25-40 m (below ~3 m depth). Antipodal results are detected with regard on the active layer. Between January 15th and March 19th, ERT- data indicate frozen conditions for most parts of the investigated slope section, while p-wave velocities are indicative for partly unfrozen conditions and a high spatial variability of active layer thickness.

The temporal variability of the subsurface velocity evolution is illustrated more explicitly in FIGURE 7.26. Velocity values extracted from SRTM-data according to FIGURE 7.6 are displayed in comparison to corresponding ERTM-data, data on temperatures and snow cover. As shown above, winter 2010/11 is characterised by below-average snow-thicknesses and temperatures. Warm-snaps during high-winter with air-temperatures above 0°C effectuate increased temperatures in both vents and within the humus layer at several days.

All curves of velocity data (FIGURE 7.26 d) show an increase of values between November 25th 2010 and February 10th 2011. However, the magnitude of increase is – except for section 2 (permafrost) – in general relatively low. Median velocity values indicate unfrozen conditions for all sections in November and December. At least for section 2 (permafrost) this result must be interpreted as erroneous and a results of an inappropriate geophone spacing (cf. CHAPTER 2.1.2). Between December and the onset of snowmelt in March, p-wave velocities evolve diverse for the four sections. Section 2 (permafrost) shows a strong increase between December 10th and January 15th (from 1.3 to 3.7 km/sec), a complanate increase between January and February 10th (3.9 km/sec), followed by a strong decrease towards March (2.4 km/sec). The velocity curve of section 2 (seasonal frozen ground) has its peak by February 10th, with median velocity values of 2.6 km/sec, indicative for frozen conditions. Velocity values for the remains of the monitoring period are below boundary values for frozen ground (cf. CHAPTER 6.2.1).

The course of the curve of section 1 (active layer) indicates unfrozen conditions for November and December (below 1 km/sec). Maximum values of 2 km/sec – indicating a frozen active layer – are achieved by January 15th. Between February 10th and April 26th, median velocities fluctuate around the boundary value for frozen/unfrozen

conditions of 1.5 km/sec. By June 20th median p-wave velocities of 0.9 km/sec are representative for an unfrozen active layer. Median velocity values of section 4 (near-surface layer) peak by February 15th (1.2 km/sec), but remain below the boundary value defined for frozen ground throughout the monitoring period.

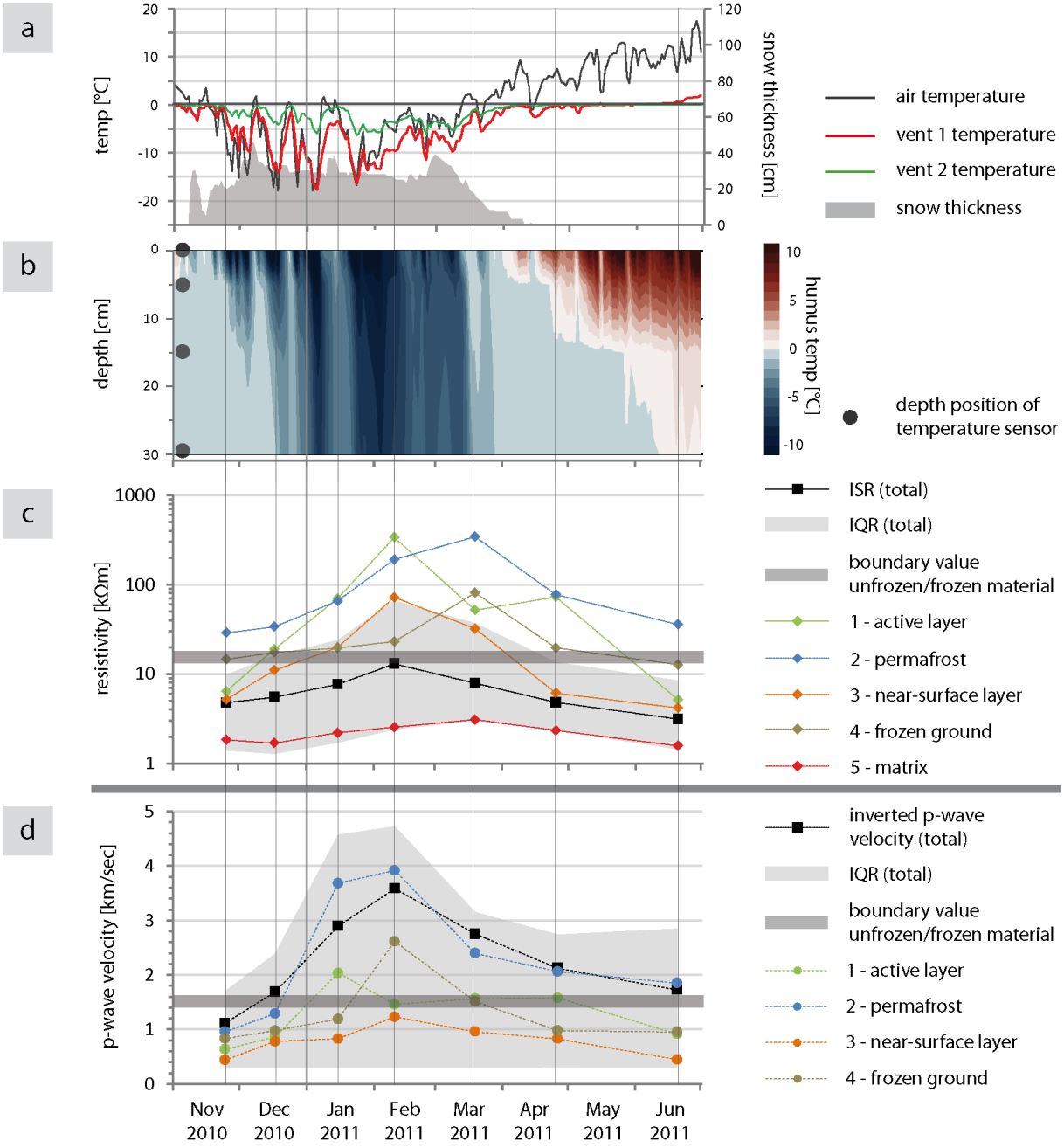

Figure 7.26: Val Susauna – extracted p-wave velocities (d) in comparison to resistivity data (c), humus temperatures (b) as well as data on snow-thickness and air temperature (a) for the SRT-monitoring period in winter 2010/2011.

Focusing on sections 2 (permafrost) and 4 (frozen ground), both curves have their peak by February 10th, followed by a strong decrease of values towards March. Corresponding ERT-data (FIGURE 7.26 c) show a maximum of median resistivity values by March 19th. Comprising the course of the temperature curves, the 15-day temperature mean prior to the measurement in February are distinctly colder (AT: -7.7 °C; vent 1: -11.3 °C; vent 2: -7 °C) compared to the 15 days after (AT: -3.7 °C; vent 1: -7 °C; vent 2: -3.4 °C). The same trend is observable for the humus layer (exemplarily for 30 cm depth) where the temperature mean within the 15 days prior to the date of the monitoring measurement are -7.4 °C and for the 15 day-period after -5.5 °C.

Even though the monitoring measurements in February took place during the coldest period of the winter 2010/11, not all sections have reached their maximum velocity/resistivity value by this date. Resistivity data of the active layer (section 1) and the near-surface layer (section 3) have their maximum – with values indicative for frozen conditions – by February 10th. Velocity data of the active layer (section 1) show a maximum by January 15th, and decrease towards February. Velocity values of the near-surface layer show a maximum by February 10th, but remain below values indicative for frozen ground.

Furthermore, ERT and SRT data do not coincide with regard on the evolution of geophysical parameters within the sections defined as permafrost (2) and frozen ground (4). While SRTM-data indicate maximum values by February 15th, followed by a decrease, resistivity values reach their maximum by March 19th and decrease subsequently. Towards June 2011 resistivity- and velocity values of the active layer and the near-surface layer accordingly decrease below boundary values characteristic for frozen ground, which is in agreement with positive humus temperatures. Median resistivity- and velocity values of the permafrost section are clearly higher than the defined boundary values for frozen/unfrozen ground. By June 20th, p-wave velocities within section 4 (seasonal frozen ground) of 0.96 km/sec and resistivity values of 12.7 kΩm are below boundary values defined for frozen ground.

7.3.4 Synthetic data modelling

Based on results from ERT-monitoring a number of synthetic geocryologic models (FIGURE 7.27) were created and inverted, conducting the back-and-forth interpretation

procedure (CHAPTER 2.1.1.5) to achieve a more sophisticated interpretability of ERTM data.

Four scenarios are presented in FIGURE 7.27, showing the geocryologic model, the inverted model, virtual boreholes as well as extracted data for the sections *permafrost* and *active layer*. All four scenarios are based on a geocryologic model, which assumes consistent matrix resistivity values of 2 kΩm. The characteristic area with finer-grained material at the foot of the slope is represented by a section with 0.5 kΩm (horizontal distances 96-105 m, all depth-levels). The scenarios differ with regard on the modelled sections referred to as the "permafrost body" (horizontal distances 52-94 m; 2-8 m depth), the "frozen ground body" (horizontal distances 6-52 m; 2-6 m depth), the "active layer" above the permafrost body (0-2 m depth) and the "near-surface layer" above the frozen-ground body (0-2 m depth).

Scenario (a) tries to emulate the subsurface resistivity distribution in summer, as it is typically detected at the Val Bever and Val Susauna site. The active layer as well as the near-surface layer is unfrozen, with resistivities equal to values of the matrix. Resistivity values of the permafrost body (170 kΩm) exceed those of the frozen ground body (70 kΩm). Late autumn/early winter conditions are simulated in scenario (b), with a freezing of the active layer and unaltered conditions in the permafrost- and frozen ground bodies. Resistivity values of the permafrost- and frozen-ground bodies were kept constant; values within the active layer and the near-surface layer were increased to 70 kΩm and 30 kΩm, respectively

The two remaining scenarios simulate the subsurface conditions prior to the onset of snowmelt (scenario c) and within an early stage of snowmelt (scenario d). Both scenarios assume supercooled conditions for the permafrost body (500 kΩm) and the frozen ground body (70 kΩm). Solely values within the active layer were modified, with consistently frozen conditions (170 kΩm) in scenario (c) and decreased resistivity values (70 kΩm) – as an effect of snowmelt – in scenario (d).

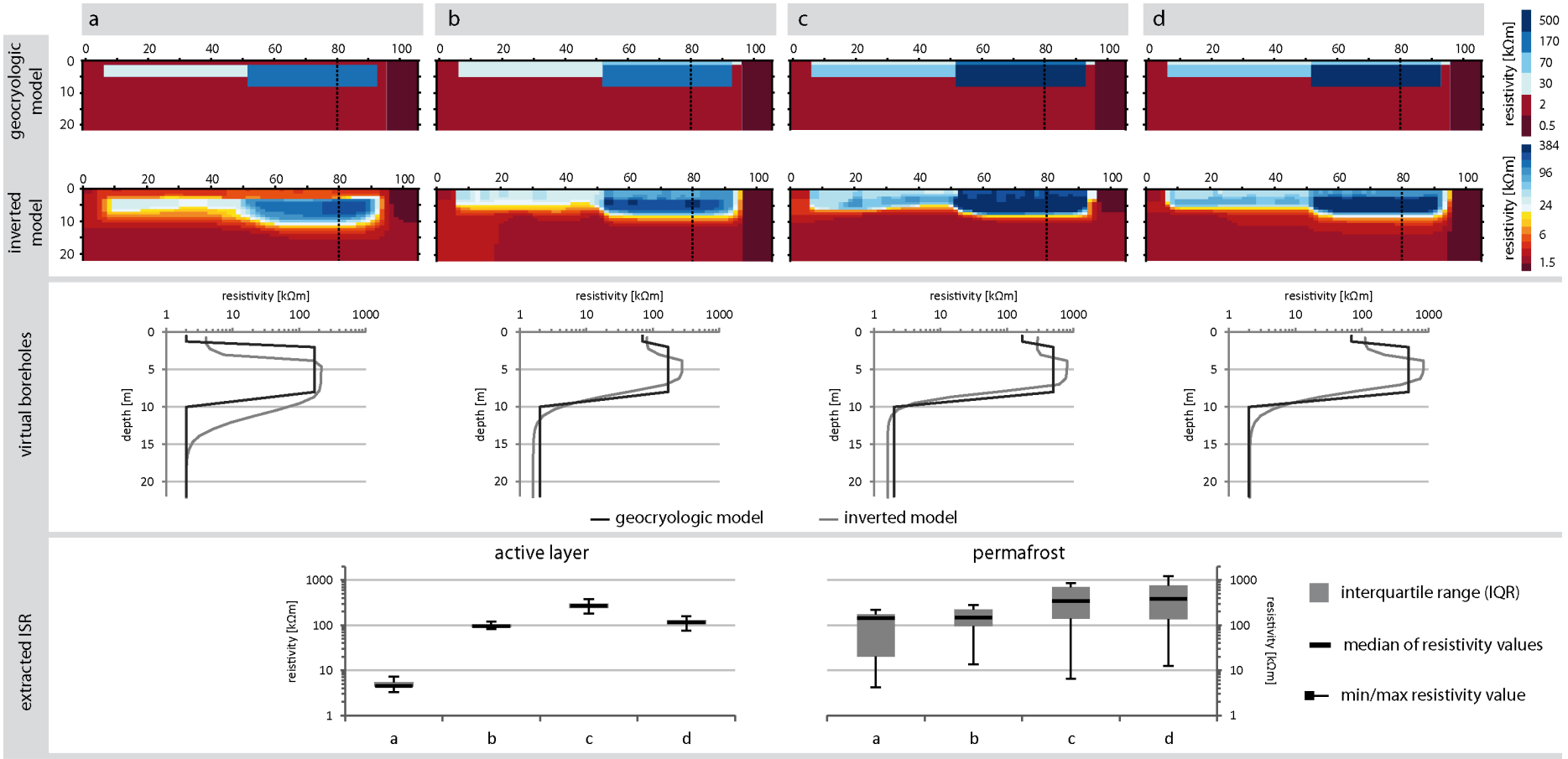

Figure 7.27: Geocryologic models and results from synthetic data modelling with geocryologic model, inverted model and extracted virtual boreholes for four scenarios. (a) summer conditions – unfrozen active layer and matrix, high resistive body towards foot of the slope (permafrost/frozen ground) and a resistive structure (seasonal frozen ground) upslope; (b) increased resistivity within active layer, unaltered conditions in permafrost and frozen ground bodies; (c) resistivity values increased for active layer, permafrost- and frozen ground body; (d) snowmelt conditions – active layer resistivity is reduced compared to (c).

In general a good agreement between inverted and geocryologic model is achieved for all four scenarios. The thickness as well as the resistivity of the active layer is overestimated for all scenarios, with best results for scenario (b), where the gradient of resistivity values between active layer and permafrost body is relatively low. Based on extracted data presented within the virtual boreholes, an active layer thickness of around 3 m would be construed. Accordingly, active layer thickness is overestimated by approximately 1 m for all scenarios. Resistivity values within the active layer are in general overestimated for all four scenarios as shown in the virtual boreholes as well as for the extracted ISR-data. Even minimum values exceed given values of the geocryologic model. The scattering of data is relatively low, with interquartile ranges of 1.14 kΩm (scenario a), 14.16 kΩm (scenario b), 62.84 kΩm (scenario c) and 21.65 kΩm (scenario d).

Conform to active layer thickness, the depth of the permafrost table is overestimate by around 1 m. Inversion results regarding the base of the permafrost body are in good agreement with the corresponding geocryologic models for scenarios (b), (c) and (d). The depth location of the permafrost base is strongly overestimated for scenario (a) where given matrix values are achieved at a depth of 15 m. Horizontal extent of the permafrost body is reproduced well for all scenarios. The spatial resistivity distribution within the permafrost bodies of the inverted models indicates a higher heterogeneity than presumed within the geocryologic models. This is illustrated best by the boxplots of extracted ISR data. A large interquartile range and a high variance illustrate a strong scattering of resistivity values within the permafrost body. The large scattering towards low resistivity values is strongly driven by the overestimation of the active layer thickness. Therefore, these low values (2-3 m depth) are included in the extracted data of the permafrost section (2-8 m depth). A most interesting effect is the influence of the resistivity distribution within the active layer on resistivity values in the permafrost body below. Permafrost resistivity values were kept constant for scenarios (a) and (b) with 170 kΩm, and with 500 kΩm for scenarios (c) and (d), while the resistivity distribution within the active layer is variable. For scenarios (a) and (b) an increase of resistivity values within the active layer – and therefore a decreased resistivity contrast between active layer and permafrost body – is correlated with a slight exaggeration of resistivity values for scenario (b). Differences are relatively low regarding the median values (144 kΩm for scenario a; 147 kΩm for scenario (b). Diversities become more

obvious with regard on maximum values (219 kΩm for scenario a; 281 kΩm for scenario (b) as well as for the interquartile range of extracted ISR-data. For scenarios (c) and (d) the obverse effect occurs. A decrease of resistivity values within the active layer determines an increase of resistivity values within the permafrost body. Median values of scenario d exceed those of scenario (c) by 35 kΩm. Likewise, minimum and maximum resistivity values are higher for scenario (d) by 6 kΩm (min) and by 380 kΩm (max).

7.4 Discussion

The discussion of results within this chapter is subdivided into two main parts. In the first part the general methodological/technical approach, its applicability and the reliability of geophysical monitoring data is discussed. The second part is focused on the analysis and discussion of monitoring results. A model of the ground thermal regime and the permafrost evolution at ventilated talus slopes below the timberline is given in Chapter 9.1.

7.4.1 Discussion of the methodological/technical approach

7.4.1.1 Electrical resistivity tomography monitoring (ERTM)

The fixed ERTM arrays used in this study were based on a self-made, low-cost construction. In general the system has proven at the three presented sites to be robust and long-lasting, but also at other sites, where it has been adopted (Kästl, 2012; Kneisel et al., accepted). Technical failures could mainly be ascribed to a rupture of the cables at the transition to the electrodes, because of stresses and strains. These defects could be minimized by burying the complete array, which might not be possible at all sites. However, the construction allows for rapid reparation. Data gaps occurred at all sites during the summer half-year 2010. These technical failures were due to ingress of water into the plug during snowmelt, which could be eliminated by an anew soldering of the plug and an improved sealing of the system. The most prominent task remains to keep the whole cable-construction waterproof, especially where the cable-cores are extracted as takeouts from the main cables. The thin copper-cables are highly prone to corrosion, which reduces the stability of the cable-cores. Corrosion caused the failure of the cable at the Brüeltobel site by April 2011, which could not be repaired. As the basic construction of the monitoring arrays functioned fine throughout the monitoring period, the most important step for optimising the system would be an improved sealing, to keep the construction waterproof.

The electrode spacing of the ERTM arrays was set to 3 m for the Val Bever and Val Susauna, and 1.8 m for the Brüeltobel study sites. Both setups provided an – in general – good subsurface resolution. However, the resolution in the shallow subsurface is limited

for the arrays using 3 m electrode spacing. As shown by synthetic data modelling (FIGURE 7.27) the depth of the permafrost table is consistently overestimated by about 1 m applying an electrode spacing of 3 m. This is in good agreement with results presented in CHAPTER 6 (borehole data (FIGURE 6.6); joint application of ERT and SRT) as well as by the joint ERT/SRT monitoring approach at the Val Susauna within this Chapter (FIGURE 7.25). ERT-data indicate an in general slightly thicker active layer with a minor spatial heterogeneity, compared to SRT-data. However, all setups were capable of detecting the spatially variable propagation of the freezing front during winter and the thawing of the active layer in spring. It must be considered that the active layer thickness at the investigated sites is very low (< 3 m), which is in agreement with investigations at the Dreveneuse d'en bas and Creux du Van talus slopes by MORARD (2011). For studies focusing mainly on the analysis of active layer processes ERT setups with electrode spacings of 2 m and smaller should be used, as done by e.g. KNEISEL et al. (accepted). At sites above timberline active layer thicknesses of more than 5 m can be expected (HOELZLE et al., 2002; PERMOS, 2001, 2004, 2007, 2009, 2010), requiring for a site-specific adjustment of the applied electrode spacing. Nonetheless, the 3 m ERTM setup remains the optimal choice for the monitoring sites in the Val Bever and Val Susauna. The subsurface resolution, the detection of the permafrost body and permafrost base as well as seasonally frozen areas provided very good results. Here, the application of smaller spacings might have reached its limits, as shown by synthetic data modelling in CHAPTER 5 (FIGURE 5.4). With the minor penetration depth smaller spacings are not capable of detecting the base of high-resistive structures thicker than 10 m; larger spacings would strongly reduce the resolution capacity of the subsurface (see also CHAPTER 5 and, i.e. HILBICH et al. (2009b)).

For this study the array types Wenner and dipole-dipole were chosen, with regard to robustness and high vertical resolution (Wenner) in combination with high lateral and vertical resolution, but a higher error-proneness, of the dipole-dipole array. Especially the robustness is an important precondition for year-round monitoring approaches, as the contact resistances vary distinctly throughout the seasons as a result of variable moisture contents and freezing. As assumed, repeatability tests indicate a superior robustness and repeatability for Wenner data compared to dipole-dipole arrays (cf. FIGURE 7.7 & FIGURE 7.8). R-values (TABLE 7.4) indicate a generally very good correlation between repeated measurements. Solely inverted specific resistivity values

derived from dipole-dipole measurements in winter show a poor correlation. Analogous the relative standard deviation (FIGURE 7.9) shows very narrow interquartile ranges for apparent resistivity values in summer and winter (Wenner and dipole-dipole); inverted specific resistivities show a narrow range in summer, but a broad range in winter. With a median RSD of 33% - compared to 16 % for the Wenner array – a sufficient reliability of inverted dipole-dipole data during winter is not given. These data are in good agreement with results from HILBICH et al. (2011; 2009b), who assigned a higher information value to the interpretation of apparent resistivity data for monitoring near-surface processes, as inverted specific resistivity values are sometimes affected by inversion artefacts, if large temporal changes occur. These data were fundamental for the decision that the results presented in this chapter are based on Wenner data, as the results from dipole-dipole measurements do not provide a robust data-quality throughout the year.

The effect of higher noise levels for the first measurement of the day, as described by PETER-BORIE et al. (2011), could not be verified. It must be considered, that the repeatability tests within this study are not capable of providing clear results on this topic, as measurements were conducted at only two dates, in contrast to 9 dates in the study by PETER-BORIE et al. (2011). However, at both dates values provided by the first measurement were slightly lower compared to the second and third measurement. This effect is clearly observable for both, dipole-dipole and Wenner data, even though measurements were conducted rotationally, beginning with the dipole-dipole array, meaning that the first Wenner array was the second measurement of the day. Whatever might drive this effect, it outlasts at least the first two measurements of the day. Taking into account FIGURE 7.7b, FIGURE 7.8b and TABLE 7.4, the correlation between the second and the third measurement is higher than the correlation between the first and second, as well as the first and third measurement. For a definite explanation of this effect, the amount of data is not sufficient. For the explanation of higher noise levels for the first measurement of the day PETER-BORIE et al. (2011) assumed neither an insufficient injection current, a polarization of the system at the time of the first of the first acquisition, or damages of the buried cables. While damages of the cable can never be completely excluded, it is for sure, that the injected current was kept constant, as the maximum voltage was injected for all measurements. Polarization effects can not be excluded. For a final analysis of this effect, further investigations are required.

7.4.1.2 Seismic refraction tomography monitoring (SRTM)

For the fixed SRT winter-monitoring, a standard cable was used. As the cable was completely buried in the snow during the SRTM period, it was protected against external influences. The biggest problem of the seismic monitoring in winter was to conduct the measurement with 16 source locations. The use of a steel tube (1 m length, Ø 10 cm) that has been stuck through the snow cover for striking has proven to be a practicable method – at least under relatively thin snow-cover conditions. Measurements would be strongly hindered under a thicker snow cover, and would require for longer striking tubes. In contrast to a standard striking plate, a 1 m steel tube has influence on the traveltimes. With view on quantitative geophysics and on the comparability of measurements conducted with- and without steel tube, a correction of the measured traveltimes would be required. This study aimed first of all on a qualitative analysis of the permafrost evolution in winter, complementary to ERT data. As all SRTM measurements were conducted using the steel tube, the comparability of data is granted.

As already addressed above, the main weakness of the SRTM setup in this study is the geophone spacing of 4.5 m. The SRTM approach aimed to achieve a more sophisticated deduction of processes that lead to the high variability of resistivity values during winter. Consequently, the SRTM array was adjusted to cover the same slope section as the ERTM array. As shown in FIGURE 7.25 (see also discussion in CHAPTER 6 as well as FIGURE 6.10 & FIGURE 6.19), ERT and SRT data do not indicate coinciding interpretations for all areas of the tomograms. While the main permafrost body is imaged concordantly by both methods, slope sections uphill, where ERT-data indicate an anomaly with minor thickness compared to the permafrost body and resistivity values slightly higher than boundary values for frozen ground, SRT data indicate unfrozen conditions except for the measurement in high-winter. Furthermore, the permafrost body is not detected by the SRTM dataset measured in late November 2010, while the SRT measurement of October 2010 – using 3 m geophone spacing (FIGURE 6.10b) – clearly detected a high velocity anomaly. Dimension size of the permafrost body in December 2010 is most probably underestimated by the SRTM measurement. Regarding the fact that a general decrease of temperatures is measured between October and November (FIGURE 7.19a), it is most unlikely, that the permafrost body is completely degraded during this period. It is by far more probable that, due to

degradation of the permafrost body and reduced ice-contents, the velocity contrast between active layer and permafrost body in autumn is too small to be detected (hidden layer; c.f. CHAPTER 2.1.2; see also SCHROTT & HOFFMANN (2008), REYNOLDS (2011)) using a geophone spacing of 4.5 m. As discussed in CHAPTER 6, it can not clearly be excluded, that the resistive anomaly upslope of the permafrost body likewise represents perennially frozen ground. Hidden layer effects, due to an insufficient thickness of a given structure, or insufficient velocity contrasts (REYNOLDS, 2011; SCHROTT & HOFFMANN, 2008) could result in a none-detection of the structure, using SRT with inappropriate geophone spacings.

However, during high-winter and the period of snowmelt, SRTM-data provided valuable information on the permafrost evolution. ERTM- and SRTM-data coincide eminently (FIGURE 7.25) regarding the evolution of geophysical parameters within the permafrost body during the period of supercooling (December 2010 towards February 2011 – massive increase of values and of the areal extent), as well as between March and June 2011 (decrease of values and areal extent). Between February and March, SRT and ERT show decreasing values within the active layer, due to increasing air temperatures and the onset of snowmelt. While ERT-data show an increase of values within the permafrost body, velocity values decrease (FIGURE 7.25 & FIGURE 7.26). In general, it must be considered that the reliability of resistivity values in model regions with high resistivities and with strong resistivity contrasts are of critical reliability (HILBICH et al., 2009b). However, synthetic data modelling was used to emulate the resistivity evolution during this period (cf. FIGURE 7.27 scenarios c and d) and to find an explanation for this effect. Results show that an increased resistivity gradient between active layer and permafrost, which is assumed to occur during snowmelt (decreased values within the active layer, constant resistivity conditions within the permafrost body) causes an increased overestimation of values within the high-resistive body during the inversion process. However, this effect is not alienable for scenarios (a) and (b) presented in FIGURE 7.27 (constant resistivity values within the permafrost body, variable values within the active layer). Inverted specific resistivity values within the simulated permafrost body are overestimated for scenario (b), where an initial freezing of the active layer and therefore a reduced resistivity contrast is assumed. In general it must be considered, that a quantitative interpretation of resistivity data, without estimation of data errors (DAY-LEWIS et al., 2005; KRAUTBLATTER et al., 2010;

Oldenburg & Li, 1999) must be handled with care. Likewise, the qualitative interpretability of results is limited using solely one method. Monitoring results presented within this chapter strongly underline the importance of combining methods for the investigation and monitoring of investigations (e.g. Hauck & Kneisel, 2008a; Kneisel et al., 2008; Vonder Mühll et al., 2001) and support the statement by Ikeda (2008), who questioned investigations based on resistivity methods only. However, the SRTM-setup applied in this study should be improved for future investigations; an analysis of data errors and synthetic data modelling should be applied for a more sophisticated analysis of results.

7.4.2 Discussion of monitoring results

Monitoring results of all three study sites show a pronounced annual cycle in the evolution of resistivity values within the detected permafrost bodies and corresponding active layers. A low variability is detected during the summer half-year, followed by a massive increase between October/November and high-winter, and a strong decrease towards pre-winter conditions during snowmelt. Thereby, the seasonal variability exceeds intra-annual variations. This is in good agreement with results from low-altitude talus slopes presented by Morard (2011), but in contrast to the various results from alpine permafrost sites above timberline, where seasonal changes are comparably low (e.g. Kneisel et al., accepted) and mostly restricted to variations in active layer thickness. Thereby, the magnitude of the seasonal permafrost variability is strongly linked to the site-specific thermal regime. Especially the snow-cover distribution distinctly influences the permafrost evolution and the propagation depth of the cold wave at sites above the timberline during winter (Hong et al., 1993; Ishikawa, 2003; Keller & Gubler, 1993; Keller & Tamás, 2003; Luetschg et al., 2003; Rödder & Kneisel, 2012; Zhang, 2005).

The temporal variability of geophysical subsurface parameters was illustrated in comparison to air-, vent- and humus temperatures, as well as in comparison to the snow-cover distribution (Figure 7.15, Figure 7.19, Figure 7.23 & Figure 7.26). For a better visualisation and comparability of results, extracted data for the sections active layer and permafrost are illustrated for all study sites in Figure 7.28. The joint interpretation of climatic- and geophysical data is to remain qualitative. A statistical analysis could

not be conducted, as the data-base of geophysical data is far too low. Furthermore, a quantitative analysis would require for an extensive error estimation of resistivity data, which would exceed the objectives of this study.

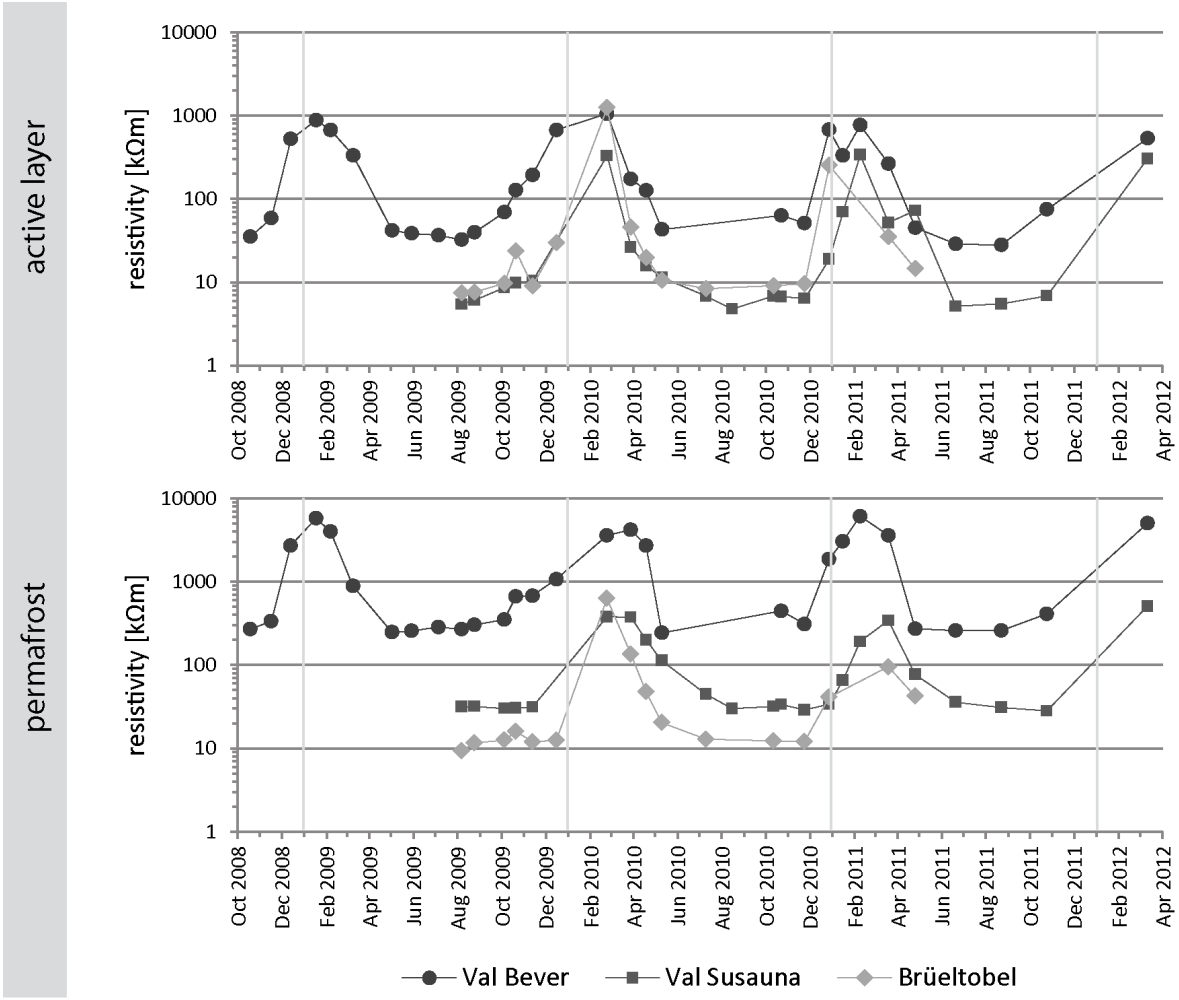

Figure 7.28: Comparisons of resistivity evolution within the active layer and the permafrost bodies during the monitoring period for all sites. Presented data are median resistivity values extracted from sections 1 (active layer) and 2 (permafrost) of ERTM data.

7.4.2.1 Seasonal cycles of the annual permafrost evolution

Based on geophysical monitoring results, the annual cycle of the permafrost evolution at the investigated sites can be differentiated into (1) the period of supercooling, (2) the period of snowmelt and (3) the period of permafrost degradation.

Period of supercooling

The period of supercooling begins with the first cold spells and the onset of the zero-curtain (usually mid-October) and ends in high-winter, when coldest air temperatures and maximum resistivity values are achieved. While the supercooling at the Val Bever and Val Susauna sites involves most parts of the investigated slope sections, at the Brüeltobel areas below the rock-wall remain unfrozen throughout the year. While the monitoring array at the Brüeltobel covers the complete slope section, and therefore both ends of the chimney, the size of the talus slopes at the Vas Bever and Val Susauna exceed the dimensions of the monitoring array by far. It must be assumed that areas at the upper end of the chimney remain unfrozen throughout the year, due to an outflow of relatively warm air during winter (cf. CHAPTER 1.1.1 & CHAPTER 8.2.3.1).

The increase of resistivity values within this period is almost exponential for all three study sites, which is in agreement with results shown by MORARD (2011) for the Dreveneuse d'en bas and Creux du Van talus slopes. Thereby, it is questionable, if this increase constitutes a massive ice growth and a growth of the permafrost body in volume. In fact, it must be assumed, that permafrost in talus slopes can not be regarded as a massive ice body, but rather a porous medium, that allows for ventilation throughout the permafrost body. During the period of supercooling, the inflow of cold air into the vents at the foot of the talus slopes, determines a massive cooling of the permafrost body. Consequently, it must be assumed that the increase of resistivity values represents a massive loss of unfrozen water content within the permafrost body as a first step of supercooling. A growth in ice volume is hard to explain, as the amount of available unfrozen water is very limited. This assumption coincides with results from synthetic data modelling (FIGURE 7.27c). It could be demonstrated that an increase of resistivity values within the permafrost body evokes an equal increase of resistivity values in the inverted model, but no changes in dimensions of the high resistive body. However, monitoring results of all investigated sites show a first period, where resistivity values within the permafrost body increase, followed by a period towards high-winter, where the size of high resistive anomaly strongly increases. This indicates, that a growth of the frozen bodies occurs, after a supercooling of the permafrost "core". The amount of fine grained material in the shallow subsurface is relatively low. It must be assumed, that the amount of fine grained material in the cavities between the talus material increases with depth (KÖRNER, 2003), determining a comparably high water-storage capacity. The inflow of cold air during winter most likely provokes a cooling of the whole

talus slope, beginning at the bottom. As the temperatures within the permafrost body are lowest, and the amounts of unfrozen water are comparably low, this area is supercooled rather rapidly. The unfrozen areas below and upslope of the permafrost body are assumed to contain higher amounts of unfrozen water. During the cooling of these areas, the release of latent heat evokes – corresponding to the zero-curtain within the active layer – a decelerated freezing. This effect is more pronounced at the Val Bever monitoring site, which must be ascribed to differences in the thermal regime, driven by the bouldery talus material at Val Bever that allows for an efficient ventilation of the slope in winter.

The monitoring period was characterised by highly variable winter conditions (snow cover, air temperatures) at all sites. Results show that a clear coupling between snow cover thickness and subsurface resistivity distribution is not given. Presuming a linear relation between permafrost temperatures and resistivity values, a thick snow cover would result in a reduced penetration depth of the cold wave, and therefore warm permafrost temperatures and comparatively low resistivity values. A thin snow cover would allow a pronounced cooling of the subsurface and therefore higher resistivity values. Thereby, the winter temperatures are assumed to have a minor influence, as the depth penetration of the cold wave is driven by the snow cover thickness (Hong et al., 1993; Ishikawa, 2003; Keller & Gubler, 1993; Keller & Tamás, 2003; Luetschg et al., 2003; Rödder & Kneisel, 2012; Zhang, 2005). Maximum resistivity values of the permafrost body and the active layer in high winter are rather stable throughout the monitoring period at the Val Bever (Figure 7.15) and Val Susauna (Figure 7.19), despite of varied snow thicknesses (high-winter resistivity data at the Brüeltobel were only recorded for one winter). It must be concluded that neither the insulation capacity of the snow cover is reduced at the investigated sites, or that the cooling of the talus slope is mainly driven by the ventilation process of the chimney effect. Most probably, it is a combination of both. It could be observed, that the snow cover – and therefore its insulation capacity – is highly disturbed at the investigated sites, due to dwarf-grown trees, large boulders and funnels within the snow cover (cf. Figure 8.10). This allows for a deep propagation of the cold wave, independent from snow cover distribution, based on conductive heat flow. In addition, talus material and permafrost body are supercooled due to convective heat transport of the chimney effect.

A definite correlation between absolute winter temperatures (air and vents) and magnitude of supercooling is hard to construe from resistivity data, as the intra-annual variability of resistivity values is marginal, with no clear trend. Nonetheless, a strong coupling between the course of the temperature curves (early cold spells, onset and duration of zero curtain periods) and evolution of geophysical parameters could be observed. However, this correlation differs between the study sites, indicating divergent modes of function of the ground thermal regimes.

Regarding the permanently and seasonally frozen subsurface areas, the date of massive increase of geophysical parameters coincides with the end of the zero-curtain period (FIGURE 7.15, Figure 7.19, Figure 7.23 & Figure 7.26). During the zero-curtain period, variability of geophysical parameters is relatively low, with a slight increase of resistivity values in the shallow subsurface, reflecting temperatures around 0 °C. However, increased resistivity values – involving all extracted sections – that can be correlated with relatively short cold-snaps were detected for some dates within the zero-curtain period at the Val Bever. At the Val Susauna and Brüeltobel, this effect could not be detected by ERTM data. Again, this effect must be ascribed to the higher efficiency of the ventilation process at the Val Bever, where larger voids are present in the bouldery talus material. At the Val Susauna and Brüeltobel, the ventilation process is restricted to single vents, while most parts of the slope are covered with a consistent humus cover. At the Val Bever, a fragmentary humus cover allows cold air to enter into the talus slope through numerous vents at the foot of the slope, enabling a more effective ventilation process and a more rapid cooling of the subsurface. This effect is detected most pronounced at the Val Bever in winter 2009/10, where subsurface resistivity values show a stepwise increase between measurements, as the dates of measurement coincide with short cold-snaps. In October 2010, an increase of resistivity values – caused by a short cold spell – is followed by a drop of values towards November, after a period of relatively warm air temperatures. This emphasizes the differences in the ground thermal regime between the study sites as well as the strong coupling of air temperatures and temperatures within the talus slope. However, for a more detailed analysis of processes, the temporal resolution of monitoring measurements should be distinctly increased in future investigations.

Period of snowmelt

The period of snowmelt begins with the end of high-winter (late February/mid-March), when a trend to decreasing air temperatures is determinable, and lasts until the end of the zero curtain period between May and late July (the time span of this period generally exceeds the duration of snowmelt).

A strong decrease of resistivity values is detected at all sites, with differences in the development between the three sites. The onset of snowmelt is associated with decreasing resistivity values in the active- and near-surface layer. Resistivity values within the subsurface partly show an increase, which could most likely be ascribed to an inversion problem (see discussion above). However, this is only verified by SRTM for one winter at the Val Susauna. For this subject further investigations would be of importance. The most pronounced decrease of resistivity values occurs during the zero-curtain periods. Minimum resistivity values (pre-winter values) are achieved by the end of the zero-curtain period. The duration of the zero-curtain period at Val Bever is distinctly shorter than at the other sites, and, consequently the drop of resistivity values proceeds more rapid. At Val Susauna and Brüeltobel, active layer resistivity values decrease rapidly with the onset of the zero-curtain period, as a consequence of the high amounts of unfrozen water, while permafrost values decrease slowly.

The rapid reaction at the Val Bever can be ascribed to the fragmentary humus cover and the bouldery substrate. Meltwater can percolate unhindered through the bouldery material into the subsurface. The organic layer at the Val Susauna and Brüeltobel usually remains frozen until early summer, which limits the percolation of water derived from snowmelt. Percolating meltwater refreezes on the supercooled talus. During the phase change of the meltwater from unfrozen to frozen state, latent heat is released (WAKONIGG, 1996). Consequently, the freezing results in a growth of the volumetric ice content, but an increase of temperatures. Warmer ice temperatures determine higher contents of unfrozen water and therefore a decrease of resistivities.

Period of Permafrost Degradation

The summer period is characterised by a constant outflow of air at the foot of the slope, causing warm air to enter through vents in the upper parts of the slopes (cf. CHAPTER 1.1.1 and WAKONIGG (1996)). The summer circulation is connected with a constant

degradation of the permafrost body, as the warm air is cooled on its way down as results of the loss of energy during the melting of ground ice (WAKONIGG, 1996).

Surprisingly, variability of the resistivity distribution is markedly low for all sites throughout this period. A complete disappearance of frozen ground can be excluded, as resistivity values remain higher than the site-specific boundary values for frozen/unfrozen ground. Results from SRT measurements (CHAPTER 6; joint monitoring in this chapter) show strong differences in seismic velocities within the permafrost bodies between measurements in spring and autumn, confirming the assumption of permafrost degradation during summer, but proving the persistence of frozen ground throughout the year. The problems of the SRTM measurement in November 2010 have been discussed above. It must be considered, that ERT measurements are not completely capable of detecting the permafrost degradation during summer. Even though further investigations would be of interest to solve this problem, it is assumable, that the resistivity decrease, which is expected as result of permafrost degradation (increased amount of conductive unfrozen water), is compensated by the resistivity increase, caused by the increasing size of air-filled voids. However, a clear interpretation of this phenomenon is to be found.

Resistivity values within the near-surface are rather low. This can be ascribed to the high water storage capacity of the organic material. More complex is the situation at the Brüeltobel. While the variability of resistivity values is low within the active layer, values vary on a wide range within the uncovered talus material in the upper parts of the investigated slope and exceed resistivity values of the permafrost body. This can be regarded as a reaction of dry spells that provoke a strong decrease of conductivity within the talus material, where only low amounts of fine grained material can be found, provoking a low water storage capability. It might be questioned, if frozen conditions last throughout the summer, if resistivity values of the permafrost body are lower than the uncovered talus, which is demonstrably unfrozen during summer. However, it must be assumed that the amount of fine-grained material increases with depth (KÖRNER, 2003). Higher amounts of fine-grained material strongly influence the water-storage capacity and therefore the conductivity of the talus material. Within the section defined as the permafrost body, resistivity values almost double the values of the surrounding matrix throughout the summer period, indicating persistently frozen conditions. Further

investigations would be of interest to solve this problem. Especially, as discussed in CHAPTER 6, further SRT measurements would provide valuable information. However, due to the sensitive eco-system at the Brüeltobel, the number of measurements was kept to a minimum.

7.5 Conclusions

Results from geophysical monitoring presented in this chapter provided valuable information on the permafrost evolution in talus slopes below the timberline. A high seasonal subsurface variability has been detected that exceeds the intra-annual variability. Differences in the ground thermal regime between the study sites were detected, leading to the following conclusions:

- Bouldery talus substrate with fragmentary humus cover allows for a rapid and massive cooling of the slope in winter, but also for an early warming of the talus material as a consequence of percolating meltwater in spring; insulation capacity of the organic layer is reduced.
- Sites with pebbly talus material and a thick humus layer show a delayed onset of supercooling, but a prolonged preservation of supercooled subsurface temperatures, due to the high insulation capacity of the humus layer and an accompanied prolonged zero-curtain period.
- The ground thermal regime is not solely driven by the convective heat transport of the chimney effect, but also by the conductive heat flow within the active layer and, emphasized, within the humus layer.
- The influence of the snow cover on the ground thermal regime appears to be of minor importance, as the insulation capability is strongly reduced.

Methodologically, the application of seismic refraction tomography monitoring in addition to electrical resistivity tomography monitoring represents an outstanding improvement to the investigation of the temporal permafrost variability. Additional information derived from SRTM measurements helped to achieve a more sophisticated interpretability of processes during the monitoring period. Furthermore, a clarification of data from ERTM was enabled, which illustrated ambiguous results on the permafrost evolution during summer and high-winter. In this context, synthetic data modelling again has proven to be a valuable tool for the verification and profound interpretation of ERTM data. The application of repeatability tests helps to appraise the reliability and interpretability of ERTM data. A regular application of repeatability tests can be recommended. Especially with view on the fact that resistivity values of the first

measurement of the day were lower compared to the following measurements further investigations would be of interest.

Measurements indicate high temporal permafrost- and frozen ground variability and a rapid reaction of geophysical subsurface parameters to short cold spells, especially in late autumn/early winter. For a more detailed analysis of processes, a higher temporal resolution, ideally with daily measurements would be a of interest for future investigations

8 The ground thermal regime

It has been shown that permafrost, which occurs in talus slopes below the timberline, is characterised by a distinct temporal variability (CHAPTER 7) and a high spatial heterogeneity. These permafrost bodies show sharp boundaries to areas with no frozen ground (CHAPTER 6). As discussed in CHAPTER 1.1.1, the most important factors that control the thermal regime at sites with permafrost below the timberline are assumed to be a low income of solar radiation, a thick organic layer with high insulation capacities, the snow cover thickness and duration, as well as the activity of the thermally induced chimney effect (DELALOYE & LAMBIEL, 2005; DELALOYE et al., 2003; GUDE et al., 2003; KNEISEL et al., 2000b; KNEISEL & SCHWINDT, 2008; MORARD, 2011; SAWADA et al., 2003; WAKONIGG, 1996; ZACHARDA et al., 2007).

The influences of most of the given factors have been analysed in various publications: the importance of the chimney effect for the ground thermal regime of supercooled talus slopes (see also citations above, and MORARD et al., 2008; PHILLIPS et al., 2009), the influence of substrate characteristics on the thermal regime of permafrost sites above the timberline (GRUBER & HOELZLE, 2008; JULIUSSEN & HUMLUM, 2008; RÖDDER & KNEISEL, 2012; SCHNEIDER et al., 2012) and the interactions of organic surface material and vegetation composition with permafrost in high latitudes (DINGMAN & KOUTZ, 1974; FUKUI et al., 2008; GAVRILIEV, 2003; GUGLIELMIN, 2003; GUGLIELMIN et al., 2008; IKARD et al., 2009; MINKE et al., 2009; MOSKALENKO, 2003; PAVLOV & MOSKALENKO, 2002; RISEBOROUGH, 2002; WALKER et al., 2008; WALKER et al., 2003; WANG et al., 2010). However, their influence for permafrost sites below the timberline is less well recognized. Results presented in CHAPTER 7 indicate that in addition to the convective heat transport of the chimney effect, the conductive heat transport through the organic surface material might be an important and regulative factor for the ground thermal regime. Furthermore, differences in the seasonal patterns of frozen ground evolution between the three investigated study sites were revealed. These might be closely linked to differences in the nature of the talus substrate and characteristics of the organic material. While the snow cover is assumed to have a major influence on ground temperatures at alpine permafrost sites above the timberline (cf. CHAPTER 1.1.1 and e.g. ZHANG (2005)) the results presented in CHAPTER 7 showed that no distinct

relationship between geophysical subsurface properties and snow-cover distribution was detectable during the monitoring period of this study.

A deeper understanding of the factors determining the site-specific thermal regime, as well as the spatially limited and temporally highly variable permafrost occurrences in vegetated talus slopes is the main aim of the approach presented in this chapter. Hereby the focus is not solely on why permafrost exists at these sites, but also why permafrost does not exist in the immediate surroundings. Special focus is on the:

- interaction between permafrost, humus cover and vegetation characteristics,
- influence of the snow cover on the ground thermal regime,
- analysis of the mode of functioning of the thermal regime and the connection of parameters, as well as their spatial and temporal variability,
- differences in the thermal regime between the three study sites as a result of the site-specific surface and subsurface factors as well as climatic conditions.

8.1 Methodological approach

The investigation of the ground thermal regime is based on the analysis of temperature logger data in combination with repeated BTS-measurements. The temperature loggers used for data collection were distributed in various slope positions. To test the interdependency between permafrost and humus distribution, as well as the thermal characteristics of the organic layer an extensive mapping of humus -thickness, -temperature and -moisture has been conducted at the Val Susauna study site. Further details on methods applied within this study are given in CHAPTER 2.2.

8.1.1 Miniature temperature data logger

Details on logger positions for the three monitored sites are given in FIGURE 8.1, TABLE 8.1 & TABLE 8.2 (see also TABLE 4.2). The logger positions were selected for optimal measurement of air- and ground-surface temperatures, the temperature inside vents and within the humus layer. At the same time, a central criterion for the selection of logger positions was the proximity to the geophysical monitoring arrays. This approach could not be realised completely at the Val Bever site. While the humus temperature logger is located close to the ERTM-array, and therefore in the central parts of the permafrost occurrence, the majority of data loggers, as well as the borehole, are unfortunately distributed in the area of the forest aisle, in the margins of the permafrost occurrence. Here, the data loggers were distributed along the vertical transect of the forest aisle, measuring the air temperature (approximately 2 m height, attached to branches) as well as the ground surface temperature at the base of the trunk of trees and within a distance of 2-3 m from the tree trunk.

Aim of the logger distribution at the Val Susauna was a comparison of temperatures in different slope positions by measuring the air- and ground surface temperatures. In addition to the logger positions in the central parts of the dwarf-growth area, temperatures were recorded in the upper margins of the permafrost occurrence, in a small area with unvegetated talus at the foot of the slope (cf. FIGURE 3.4) and in the neighbouring forest, where no permafrost was detected. To monitor temperatures in vents, two vents were selected: vent 1 close to the foot of the slope and vent 2 in the upper margins of the dwarf-growth zone. Humus temperatures were recorded in central

parts of the *Hexenwäldli* as well as in the neighbouring forest to allow a comparison of thermal characteristics of the organic layers in permafrost-affected areas with a site without permafrost.

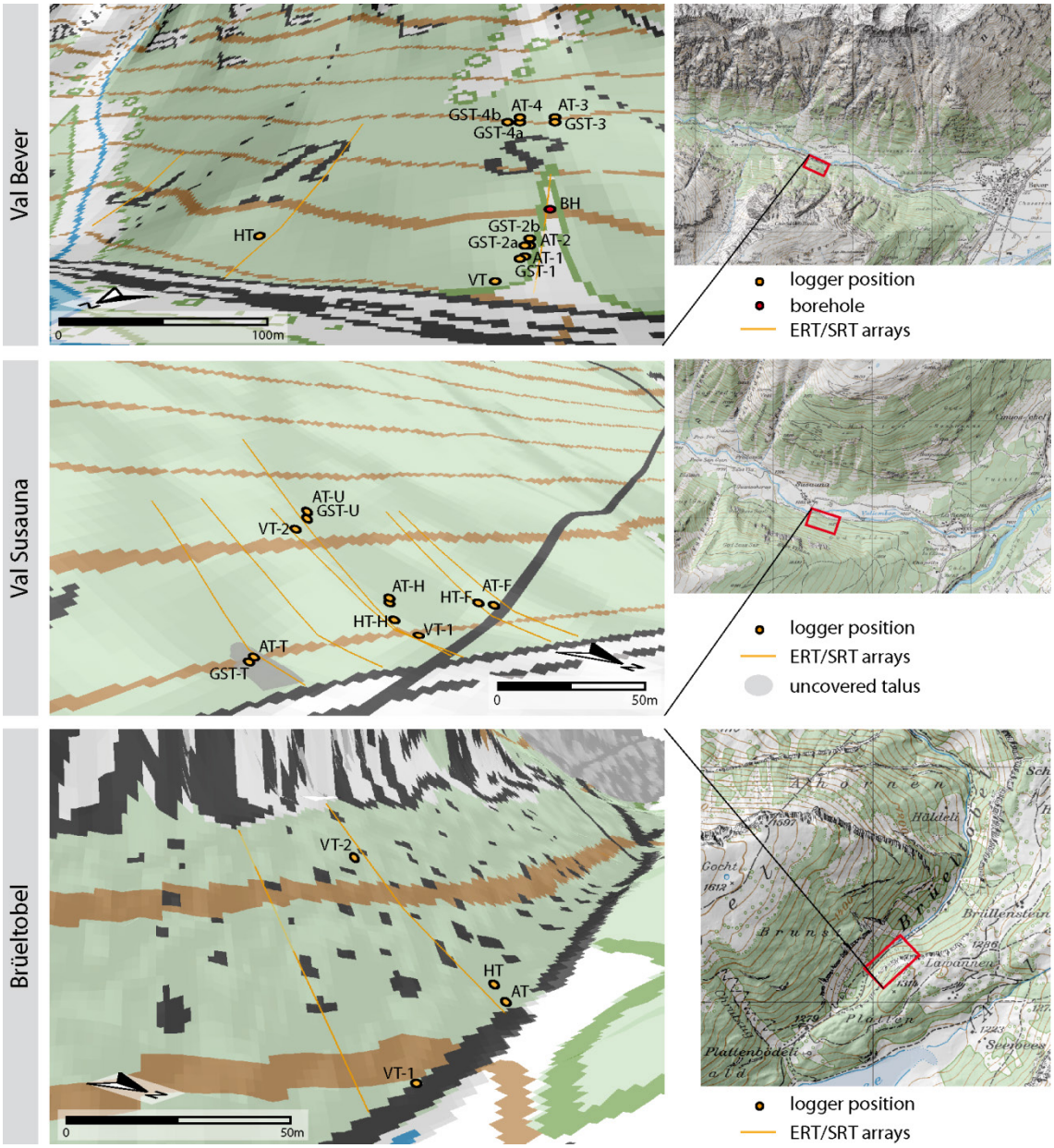

Figure 8.1: Location of temperature data loggers at the talus slopes of the Val Bever, Val Susauna and Brüeltobel (© swisstopo). Abbreviations according to TABLE *4.2*

Due to the limited number of temperature data loggers, it was not possible to record ground surface temperatures at the Brüeltobel as well. Instead, the focus was set on monitoring vent temperatures at the foot of the slope and below the rock wall at the top of the talus slope. The humus temperature logger is located in the central part of the *Hexenwäldli*. The data logger or measuring air-temperatures has been attached in

tow meters height to a tree at the lower margins of the dwarf-growth area, as trees in the *Hexenwäldli* are barely reach a height of around 1 meter.

Table 8.1: Details on locations of temperature data loggers at the Val Bever.

	logger name	data logger	elevation [m a.s.l.]	location	slope position	surface characteristics
Val Bever	BH	thermistor string (Geoprecision)	1801	borehole	forest aisle	thin humus layer, grass covered
	HT	thermistor string (Geoprecision)	1790	humus layer, 3 depth-levels	forest	thick, fragmented humus layer; mosses and lichens
	VT	wireless logger (Geoprecision)	1783	inside vent	edge of forest	thick humus layer, moss covered
	AT-1	wireless logger (Geoprecision)	1790	branch, 2m height	edge of forest	thick humus layer, moss covered
	GST-1	UTL-1	1790	stem-base	edge of forest	thick humus layer, moss covered
	AT-2	UTL-2	1793	branch, 2m height	edge of forest	thick humus layer, moss covered
	GST-2a	UTL-3	1793	stem-base	edge of forest	thick humus layer, moss covered
	GST-2b	UTL-4	1795	3m from stem-base	edge of forest	thick humus layer, moss covered
	AT-3	UTL-5	1840	branch, 2m height	forest aisle	thin humus layer, grass covered
	GST-3	UTL-6	1840	stem-base	forest aisle	thin humus layer, grass covered
	AT-4	UTL-7	1840	branch, 2m height	edge of forest	thin humus layer, grass covered
	GST-4a	UTL-8	1840	stem-base	edge of forest	thin humus layer, grass covered
	GST-4b	UTL-9	1840	3m from stem-base	edge of forest	thin humus layer, grass covered

Humus temperatures were recorded in three depth levels of the organic layer at each site: in 5 cm depth, close to the interface between humus and talus material (30 cm depth for Val Bever and Val Susauna, 35 cm depth for the Brüeltobel) and in-between those two layers (15-20 cm depth). To keep the disturbance of the humus layer at a minimal level, the humus was cut open with a shovel unto the interface between organic layer and talus material was reached. The vents were instrumented with wireless miniature data loggers (Geoprecision) to guarantee the accessibility of data throughout the year. The loggers were placed circa 30-40 cm inside the vents, to ensure that only those temperatures, which were representative for the thermal circulation of the chimney effect, were measured. Logger VT2 at the Brüeltobel has been placed between the loose

talus material in the upper margins of the unvegetated area (FIGURE 3.6), assumably representative for the upper vent.

Table 8.2: Details on locations of temperature data loggers at the Val Susauna and Brüeltobel.

	logger name	data logger	elevation [m a.s.l.]	location	slope position	surface characteristics
Val Susauna	HT-H	thermistor string (Geoprecision)	1682	humus layer, 3 depth-levels	central dwarf-growth zone	thick humus layer, moss covered
	HT-F	thermistor string (Geoprecision)	1684	humus layer, 3 depth-levels	forest	thin humus layer, covered with litter
	VT-1	wireless logger (Geoprecision)	1678	inside vent, foot of slope	lower margins of dwarf-growth zone	thick humus layer, moss covered
	VT-2	wireless logger (Geoprecision)	1704	inside vent, upslope	upper margins of dwarf-growth zone	thick humus layer, moss covered
	AT-H	MLog (Geoprecision)	1688	branch, 2m height	central dwarf-growth zone	thick humus layer, moss covered
	GST-H	wireless logger (Geoprecision)	1688	stem-base	central dwarf-growth zone	thick humus layer, moss covered
	AT-U	UTL-1	1710	branch, 2m height	upper margins of dwarf-growth zone	thick humus layer, moss covered
	GST-U	wireless logger (Geoprecision)	1710	stem-base	upper margins of dwarf-growth zone	thick humus layer, moss covered
	AT-T	UTL-1	1680	branch, 2m height	uncovered talus, foot of slope	unvegetated dolomitic talus
	GST-T	wireless logger (Geoprecision)	1680	stem-base	uncovered talus, foot of slope	unvegetated dolomitic talus
	AT-F	MLog (Geoprecision)	1684	branch, 2m height	forest	thin humus layer, covered with litter
Brüeltobel	HT	thermistor string (Geoprecision)	1208	humus layer, 3 depth-levels	central dwarf-growth zone	thick humus layer, moss covered
	VT-1	wireless logger (Geoprecision)	1198	inside vent, foot of slope	ditch of the hiking path	limestone boulders
	VT-2	wireless logger (Geoprecision)	1230	stem-base	below the rock-wall	transition between uncovered talus and grass covered area
	AT	wireless logger (Geoprecision)	1205	branch, 2m height	lower margins of dwarf-growth zone	thick humus layer, covered with mosses and grass

In addition to classical interpretation of temperature curves, temperature logger data were analysed using degree-day factors. To detect dependencies between logger positions, data sets of air-, vent- and humus temperatures were correlated. Data analyses were performed for the hydrological year (October 1st – September 30th) and seasons (winter half-year October 24th – March 21st and summer half-year March 22nd – October 23rd). Correlations are calculated for periods in high-winter and high-summer.

During the last years it became common to apply the TTOP-model (Temperature at Top Of Permafrost) to model regional permafrost distributions (Juliussen & Humlum, 2008; Rödder & Kneisel, 2012; Smith & Riseborough, 1996, 2002). Within this model, an important factor for the calculation is the thermal conductivity of the thawed/frozen ground, assuming solely a vertical, conductive heat flow. As on the sites monitored in this study the thermal ventilation of the chimney effect demonstrably influences the thermal characteristics of the whole permafrost body it must be expected that the TTOP-model is not capable to correctly depict the temperature at the top of the permafrost table. Therefore, the TTOP-model was not applied within this study.

Degree days used in this study represent the sum of positive (DDT – thawing degree days) and negative (DDF – freezing degree days) mean day temperatures. Degree day factors are calculated for all temperature data loggers, to allow for a broad analysis of temperature data in different slope positions. Correspondingly, n-factors were calculated for all datasets as the ratio between the degree day factor at the specific logger position and the degree day factor of the corresponding air temperature. Correlations were calculated to test the dependency between two temperature datasets using the Pearson product-moment correlation coefficient (e.g. Bahrenberg et al., 2010; Schönwiese, 2006). Calculated were the correlation coefficient (r) as the measure of the direction of the correlation as well as the determination coefficient (r^2) as a measure for the strength of correlation.

8.1.2 Bottom temperature of the winter snow cover (BTS)

BTS-measurements were conducted at all three study sites in each winter of the monitoring period, with an additional measurement at Val Bever in high-winter 2008. Information on BTS measurements are given in Table 8.3. Details on the methodology are given in Chapter 2.2.2. As discussed in Chapter 2.2.1, a fundamental precondition for BTS-measurements is a sufficiently thick snow cover of more than 80 cm (Haeberli, 1973; Hoelzle et al., 1993). Especially in winter 2010/11 the snow thickness was distinctly below the boundary value of 80 cm. Furthermore, the snow thicknesses are, in general, very heterogeneous at the study sites. . In particular, this can be ascribed to the numerous trees, and at the Val Bever site, to large granitic boulders that influence the local snow thickness. However, as a fundamental aim of this study was to investigate

the ground thermal regime in winter, driven by interactions between permafrost, snow cover and winter temperature evolution, all BTS-measurements were used for analysis (cf. TABLE 8.3). Due to the variable snow cover conditions, and the avalanche activity, the spatial dimensions of the BTS-grids as well as the number of measurement points are variable each winter. Locations of survey points are indicated in the corresponding figures. At the steep slope of the Brüeltobel, measurements were hard to accomplish in general, with very low snow thicknesses especially in the upper, unvegetated slope.

Table 8.3: Details on BTS-surveys.

	date	# of survey points	Ø winter temp [°C]	Ø snow depth	BTS corr. max/min [°C]	Ø BTS corr. [°C]
Val Bever	25.03.2008	55	-	86,4	0.7/-8.5	-2,5
	12.03.2009	63	-	177,9	-1.4/-9.1	-4,2
	23.02.2010	41	-4,3	101,2	-0.4/-10.6	-5,0
	08.02.2011	63	-3,0	59,8	1.3/-6.3	-2,4
Val Susauna	11.03.2009	48	-	150,5	-0.9/-9.2	-4,1
	23.02.2010	47	-5,3	80,7	-1.7/-11.3	-5,0
	10.02.2011	85	-4,5	57,3	-0.4/-10.5	-4,3
Brüeltobel	25.02.2009	36	-	174,7	-0.6/-8.1	-4,4
	22.02.2010	46	-1,1	175,5	0.8/-8.3	-4,3
	07.02.2011	19	-0,5	88,4	1.6/-4.5	-1,9

BTS-data were processed using the geostatistical analyst within ESRI ArcGIS 10. For spatial interpolation between survey points, the IDW-method (Inverse Distance Weighting) has been used. Usually, for illustrating results from BTS-measurements, temperatures are classified according to HAEBERLI (1973) into the classes *permafrost probable* (BTS < -3 °C), *permafrost possible* (BTS -3 °C - -2 °C) and *no permafrost probable* (BTS > -2 °C). In this study, the measured BTS-data are used for imaging, with no classification of temperatures. This is first of all due to the large range of temperatures measured at the study sites, but also to achieve a better comparison of the temperature evolution during the period of measurements. Supplemental data on snow cover, as well as on air temperatures (period October 2008-September 2009) are derived from the meteorological station Samedan (provided by MeteoSwiss). Details are given in CHAPTER 7.2.5.

8.1.3 Humus temperature and moisture

To test the interdependency between permafrost and humus distribution, as well as on the thermal properties of the organic layer and vegetation characteristics, the Val Susauna site was chosen for an extensive mapping approach. Focus was set on humus thickness, -temperature and -moisture as well as on the vegetation composition and tree height. Further details on the methodology are given in CHAPTER 2.2.3.

In total 31 profiles were dug at the study site in permafrost-affected areas, but also in non-permafrost areas in the neighbouring forest. Survey points are illustrated in the corresponding figures. Distance between neighbouring humus profiles was around 10-15 m. To keep the disturbance of the sensitive ecosystem to a minimum, the profiles were kept as small as possible. Depth of the profiles was determined by the humus thickness, varying between 15 and more than 50 cm. Temperature and water content have been measured in 5 cm depth-steps – beginning at surface level down to the interface between humus and talus material – for each profile. As far as possible, three measurements were conducted for each depth level; results were averaged.

Soil identification involved recording humus thickness as well as a simple morphological identification of the humus layers according to GREEN et al. (1993), ARBEITSKREIS STANDORTSKARTIERUNG (2003) and AG BODEN (2005). For recording the vegetation composition, the relative percentage of mosses, lichen, shrubs and bare ground has been estimated in the immediate surroundings of each humus profile. Furthermore, the tree height in the surroundings of the survey points has been estimated and differentiated into four classes (0-2 m, 2-5 m, 5-10 m and $>$ 15 m). Tree- and shrub species were recorded, but will not be considered in the following.

All recorded data were processed using the geostatistical analyst within ESRI ArcGIS 10. For the spatial interpolation between survey points, the IDW-method (Inverse Distance Weighting) has been used.

8.2 Results and interpretation

8.2.1 Results from BTS measurements

Results from BTS-measurements at the three study sites are presented in FIGURE 8.2, FIGURE 8.3 & FIGURE 8.4 (see also TABLE 8.3). At all three study sites large areas with BTS values distinctly below -3 °C – indicating the probability of the existence of permafrost – are detected. A narrow transition zone between these areas and areas with temperatures above -2 °C, where permafrost is not likely, is shown for all study sites. The permafrost distribution indicated by BTS-values is in good agreement with results from geophysical mapping and quasi-3D imaging. While snow thicknesses as well as the thermal characteristics are highly variable throughout the period of measurements, the general patterns of areas that indicate probable permafrost occurrences remain constant. At all three sites, coldest BTS were measured where snow cover is thickest, or, especially at the Val Bever, no clear relationship between snow thickness and BTS is visible.

8.2.1.1 Val Bever

BTS-data measured at the Val Bever (FIGURE 8.2) cover a period of four winters between 2008 and 2011. Atmospheric winter temperatures as well as snow cover conditions are highly variable throughout the period of measurements. The snow thickness in March 2009 is distinctly above, in February 2011 far below average (cf. TABLE 8.3). Air temperatures are only available for the winters 2009/10 and 2010/11, with lowest temperatures measured in the latter. The variance of minimum and average BTS values (TABLE 8.3) is rather high, with no clear interrelation to measured snow thicknesses. Here, a correlation between BTS and air temperatures appears stronger. However, it must be kept in mind that the measurement in 2011 as been conducted considerably earlier (February 8th) compared to the other measurements.

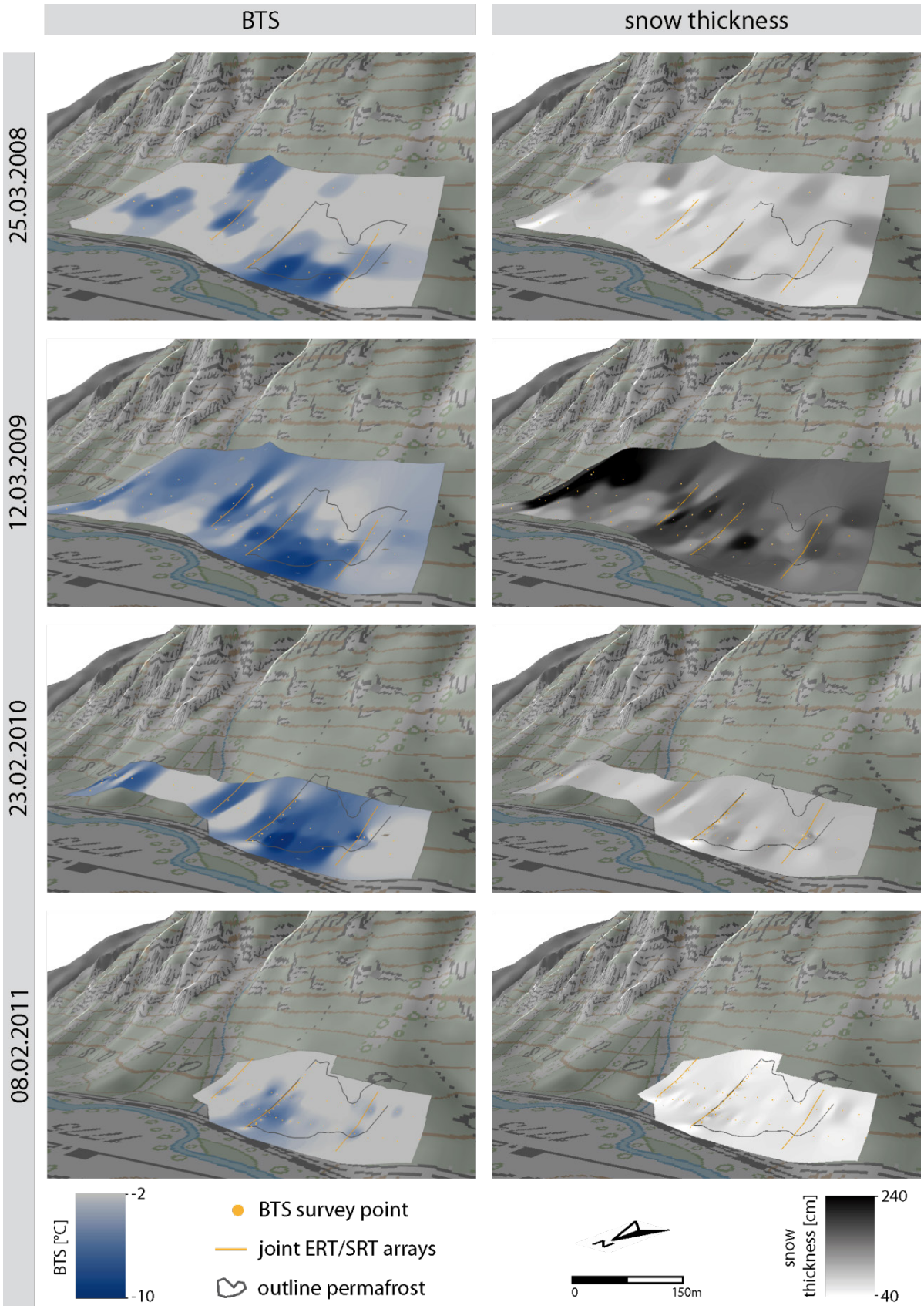

Figure 8.2: BTS-data recorded at the Val Bever in four consecutive winters (2008-2011) (basemap © swisstopo).

The areal distribution of BTS values indicating probable permafrost occurrences is in good agreement with results from geophysical mapping and quasi-3D resistivity imaging (cf. CHAPTER 6). Lowest temperatures are detected towards the foot of the slope in the section outlined as permafrost by quasi-3D ERT, between the geophysical arrays VB-mon and VB-S1 (cf. FIGURE 6.2). Temperatures decrease upslope and towards both sides of this supercooled section. Results from geophysical mapping and BTS-measurements show, that forest aisle and the borehole, accordingly (geophysical array VB-S1 in the western parts of the study site), are located in the western margins of the supercooled slope area.

A second, isolated area with temperatures down to -10 °C is detected towards the east, in the central parts of the BTS grids. Geophysical arrays VB-L7 were measured in this slope section, where a thick humus- and moss cover can be found and trees show a distinct dwarfing (cf. FIGURE 6.8, FIGURE 6.2 & CHAPTER 6.1.1). A further area with permafrost-indicative BTS values is detected in the eastern margins of the study site. Geophysical test-measurements (not shown) were likewise indicative for at least seasonal frozen ground in this area. The general shapes of these supercooled areas are illustrated by BTS-data for all four dates of measurements. Transition between supercooled areas and areas with temperatures warmer -2 °C is more pronounced for the measurement in 2008 compared to the following years. This effect might be ascribed to the spatial alignment of survey points and the spatial interpolation.

8.2.1.2 Val Susauna

Three years of BTS measurements at the Val Susauna are presented in FIGURE 8.3. While in 2009 a large area of the talus slope was investigated, measurements in the following years were concentrated on the area of the *Hexenwäldli* and the immediate surroundings.

Coldest temperatures, down to -11 °C (cf. TABLE 8.3) were detected in the area of the *Hexenwäldli*, where permafrost has been proven by geophysical measurements (cf. CHAPTERS 6.2.1.2, 6.2.2, 7.3.2.2 & 7.3.3). BTS-values of more than -2 °C indicate that permafrost is not likely in the surrounding forest to the west as well as to the east (BTS dataset from March 2009). The temperature distribution in the central parts of the study site, where permafrost has been detected, shows a strong heterogeneity, ranging

between temperatures higher than -3 °C and extremely cold temperature of less than -10 °C. In general, temperatures get lower towards the western half of the *Hexenwäldli*. Likewise, quasi-3D ERT (FIGURE 6.18) shows higher resistivity values in the western half of the permafrost body.

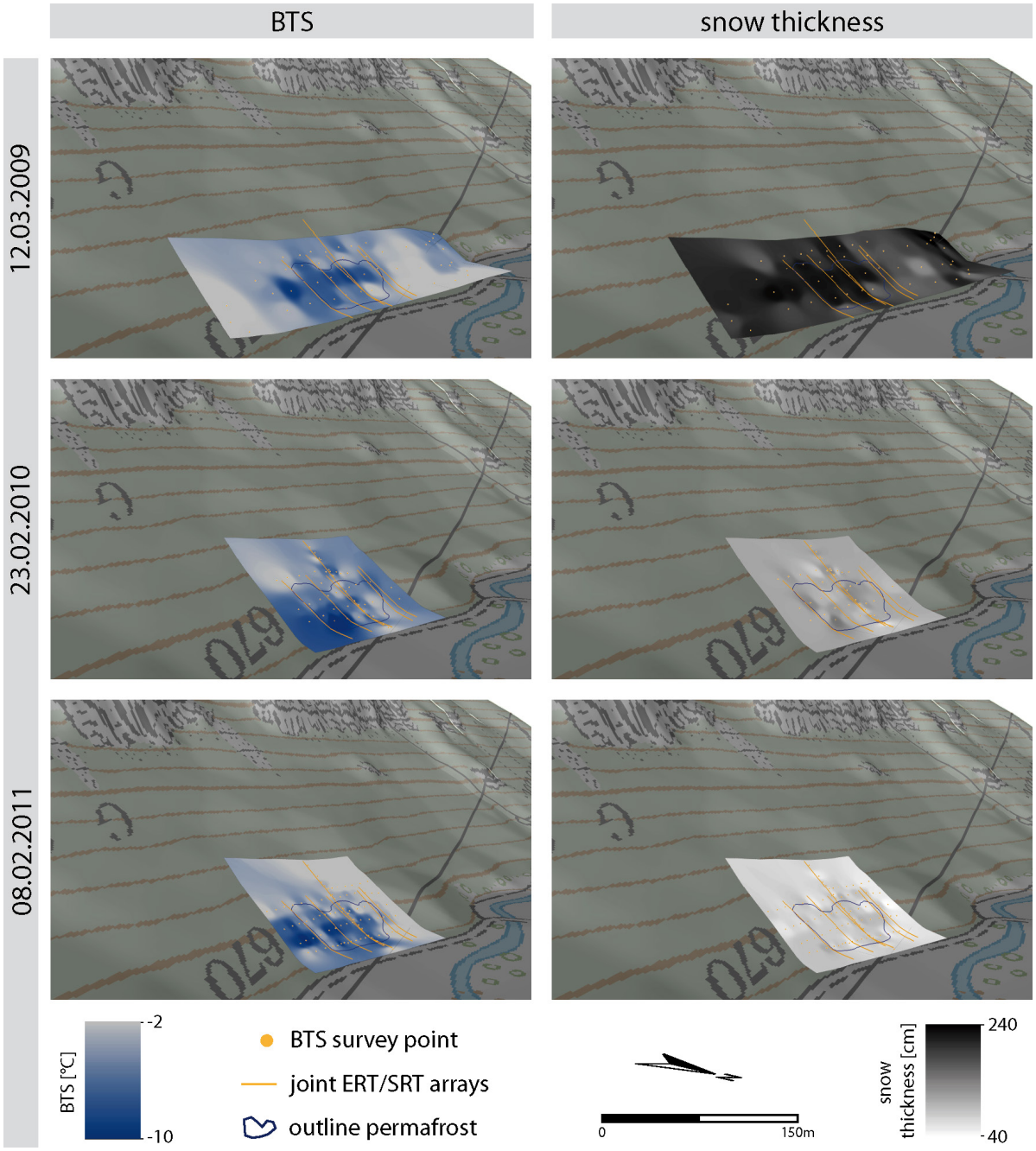

Figure 8.3: BTS-data recorded at the Val Susauna in three consecutive winters (2009-2011) (basemap © swisstopo).

In general, BTS values are lowest in areas where snow thickness is highest. This is especially obvious for the BTS dataset from 2009, where many survey points were located in the forest surrounding the *Hexenwäldli*. Naturally, the snow thicknesses are lower in the tall-grown forest, and higher in the area of the dwarf-forest. Congruent to results from the Val Bever, snow thickness was highest in 2009 and lowest in 2011 (cf. TABLE 8.3). Coldest BTS values were detected in 2010, where snow-thickness was intermediate. Therefore, a clear temporal relationship between BTS and snow thickness is not observable; a spatial relationship is observable, with cold BTS correlating to high snow thicknesses, which is inverse to the usual assumption.

8.2.1.3 Brüeltobel

Figure 8.4 presents results from BTS-measurements at the Brüeltobel in late February of 2009 and a picture of the investigated slope section. Additionally, values on BTS campaigns of the following years are given in TABLE 8.3. Clearly recognizable are the tops of the dwarf grown trees in FIGURE 8.4 in the *Hexenwäldli* of the Brüeltobel, which emerge through the thick snow cover.

The BTS-values are distributed in three sections: A belt of cold temperatures indicative for a probable permafrost occurrence (down to -8 °C) pervades through the central parts of the talus slope, covering the area of the *Hexenwäldli* with a thick humus/moss cover and dwarf-grown trees. At the foot of the slope (tall conifers) and below the rock wall (uncovered talus, i.e. deciduous trees; cf. FIGURE 3.6a) temperatures are higher than -2 °C. Temperatures of around -2 and -4 °C are detected in the area of the rock promontory (cf. CHAPTER 3.2) located between the two geophysical arrays. This section is characterised by a comparably thin humus cover and mainly grasses and shrubs in the undergrowth. Based on site knowledge, it is unlikely, that frozen ground persists in this area of the slope.

Congruent to results of the Val Susauna, snow thickness is highest in the area of the *Hexenwäldli*, where BTS is lowest. Due to redistribution effects, the snow cover in the upper parts of the talus slope is relatively thin. Lowest BTS are measured at the foot of the slope. A clear relationship between BTS and snow thickness could not be detected at the Brüeltobel (TABLE 8.3). Average BTS, as well as minimum and maximum values are lowest in winter 2010/11. In that winter, snow thickness and winter temperatures

were exceptionally low. Snow thicknesses were assimilable for the two previous winters; only minor differences in BTS- values were detected.

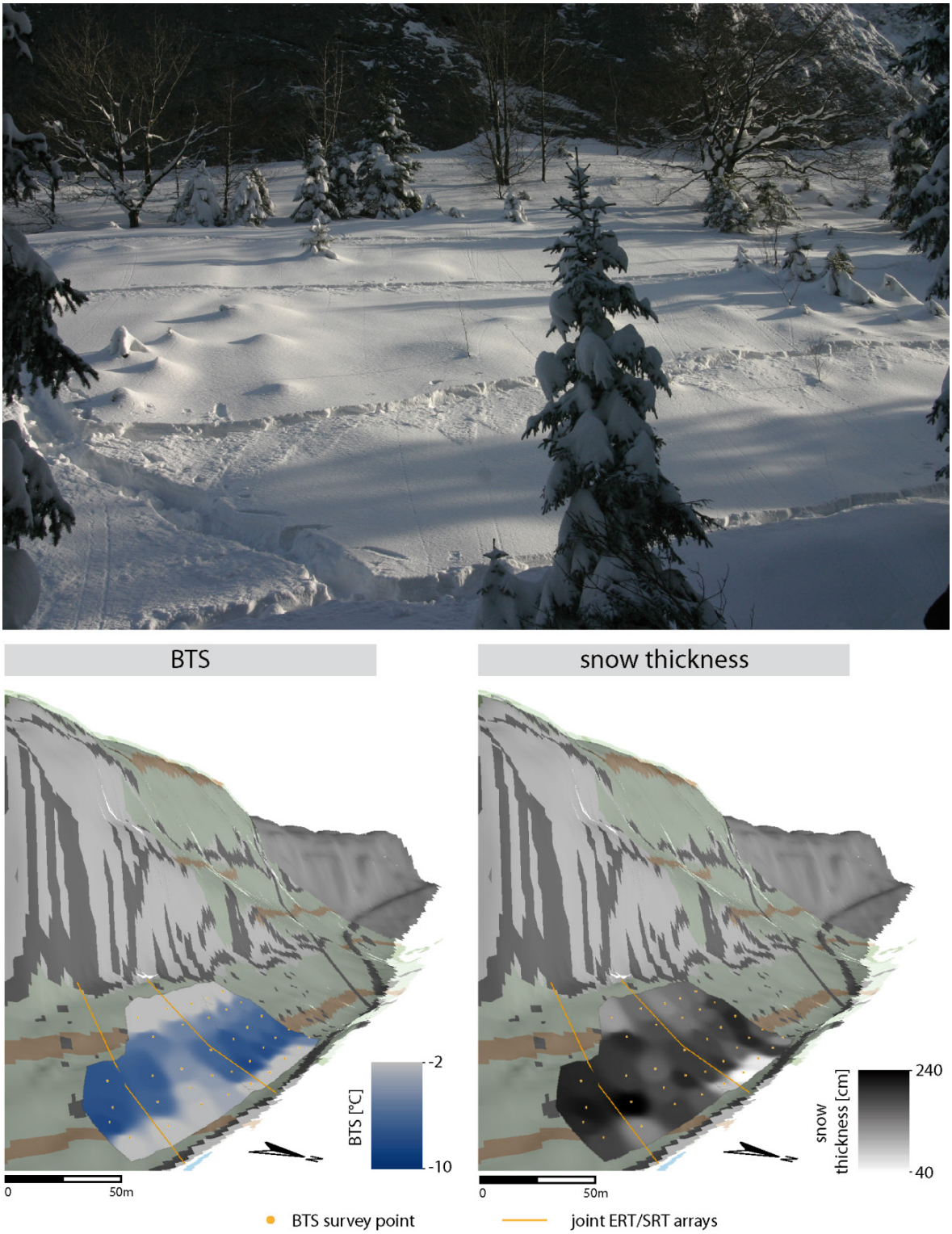

Figure 8.4: BTS-data recorded at the Brüeltobel in February 2009. At the top, a photo of the study site with tracks of the BTS-surveying in the snow. Attention should be paid to treetops of the dwarf-grown spruces that are traceable through the snow cover. (basemap © swisstopo)

8.2.2 Humus and vegetation mapping at Val Susauna

Results from humus- and vegetation mapping in comparison to the permafrost distribution (cf. CHAPTER 6.2.2.) at the Val Susauna are presented in FIGURE 8.5. A list of plant and tree species is given in TABLE 8.4. FIGURE 8.6 shows humus temperature and moisture values for the different depth levels.

The estimated tree height allows for a differentiation of the study site into two main areas. The *Hexenwäldli* is characterised by predominantly pine (*Pinus mugo*) and spruce (*Picea abies*) trees (< 5 m, mostly between 2 and 3 m); the tall grown forest mostly by spruce trees (> 15 m). Especially the spruce trees in the *Hexenwäldli* show a distinct dwarfing. Comparing results from tree height estimation with the resistivity depth slide (cf. FIGURE 6.18) the extent of the permafrost body coincides very well with the areal distribution of the *Hexenwäldli*. Likewise, to the transition between frozen and unfrozen ground, the transition between *Hexenwäldli* and areas with tall grown trees is narrow. In the centre of the investigated site, the area of the *Hexenwäldli* is divided into two main parts by a spur of tall trees. This is mirrored in the quasi-3D ERT depth slice, where the permafrost body is likewise differentiated.

Comparing the proportion of mosses, bare ground (unvegetated humus, mostly covered with organic litter material) and humus thicknesses, it is observable, that highest amounts of mosses as well as thickest humus layers (>30 cm) are detected in the area of the Hexenwäldli. Humus thickness in the neighbouring forest is distinctly lower (<20 cm), bare ground and scattered shrubs are dominant. Besides the tall-grown forest, most parts of the investigated slope section are covered with mosses by up to 100%. Partly, the moss cover is interspersed with small shrubs (<5-10 cm; for species see Table 8.4). In four spots, the proportion of mosses is strongly reduced to values below 40-50 %. Within three of these spots (eastern part of the investigated slope section, around 1700 m a.s.l.) an increased amount of lichens (up to 70 %) has been detected. A fourth spot, located in the central parts of the study site towards the foot of the slope, contains a spur of tall trees, which divides the Hexenwäldli. Here, an increased proportion of bare ground is detected.

Humus temperature and moisture at the base of humus layer or at the transition to the talus material respectively, are included in FIGURE 8.5 to illustrate the relation to the surface composition. Temperature and moisture data for all the recorded depth

levels are presented in detail in FIGURE 8.6. In general, base temperatures of the humus layer are lowest in areas with permafrost below (<4 °C) and highest in the forest as well as in the eastern parts of the grid towards the foot of the slope (>8 °C). Humus moisture is highest in areas where permafrost has been detected below, and roughly mirrors the permafrost distribution in the subsurface, with two areas of high moisture contents (40-60 %) divided by a less moist section (20-30 %). Humus temperatures were relatively high in the forest, where thicknesses are mainly below 15-20 cm. High temperatures are also found in the eastern parts of the grid, towards the foot of the slope, where humus thickness exceeds 40 cm. Highest thickness of the organic layer of up to 70 cm has been recorded in the transition zone between *Hexenwäldli* and forest in the western part of the grid. While humus moisture in this area is rather high, temperatures do not differ distinctly from central parts of the *Hexenwäldli*, where humus thicknesses are between 30 and 50 cm.

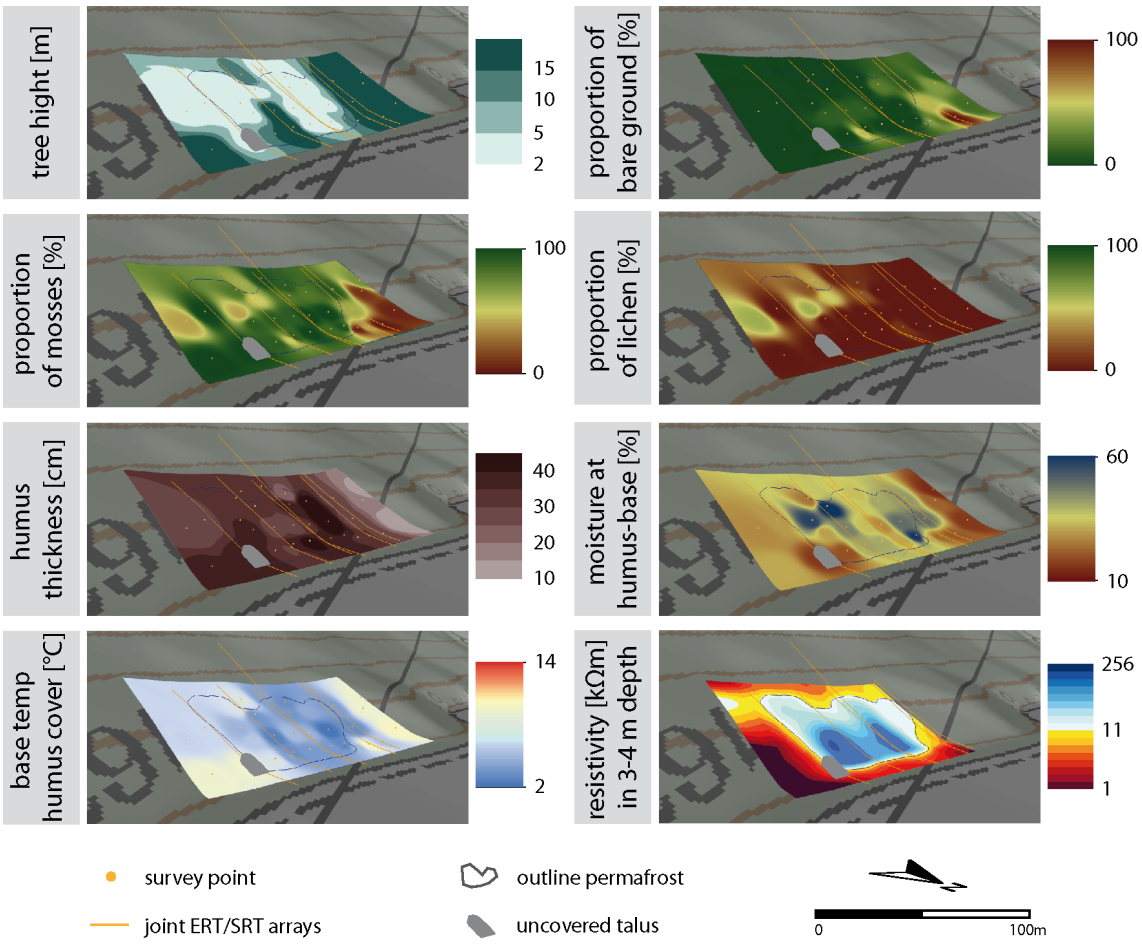

Figure 8.5: Results from humus and vegetation mapping at Val Susauna in comparison to permafrost distribution derived from quasi-3D imaging, conducted in late August 2010 (22./23 and 28.08.2010) (basemap © swisstopo).

Table 8.4: Selection of dominant plant species identified at the Val Susauna.

conifers	shrubs	mosses	lichens
Picea abies	*Vaccinium myrtillus*	*Sphagnum spec.*	*Cladonia rangiferina*
Larix decidua	*Vaccinium vitis-idaea*	*Hylocomium splendens*	*Cladonia arbuscula*
Pinus mugo	*Vaccinium uliginosum*		
Pinus cembra	*Empetrum nigrum*		
	Dryas octopetala		

As illustrated in FIGURE 8.6 humus temperatures clearly decrease with depth; moisture contents in general increase with depth. Temperature values within the upper four depth-slices divide the study sites into three main areas. High temperatures (10-14 °C) were measured in the tall grown forest and in a belt along the foot of the slope. Lower temperatures (<8 °C) are detected in the remains of the investigated area, which are predominantly characterised by dwarf-grown trees. Below a depth of 15 cm, the variability of temperatures with depth is minor. Within the range of the influence of the permafrost body, humus temperatures are rather homogeneous, ranging between 2.5 and 4.5 °C. Temperatures between 8 and 10 °C (below 15 cm depth) were detected in the forest to the west of the *Hexenwäldli* as well as in areas towards the foot of the slope, in the eastern parts of the study site.

Especially prominent in the first three depth slices is a small section with relatively cold temperatures (5-6 °C) located in the central parts of the grid, close to the foot of the slope, where mostly rather high temperatures of up to 14 °C are measured. This section is congruent to the area discussed above, where the widespread moss cover is reduced in favour of an increased proportion of bare ground. Humus cover in this section is slightly thinner compared to the immediate surroundings and is characterised by high amounts of talus. While digging the humus profile a strong and cold draught has been perceptible, driven by the ventilation system of the chimney effect. Located in the central parts of the ventilation system it must be assumed that digging the profile disturbed the thermal ventilation to some point. It can not be determined unequivocally, if the relatively low humus temperatures in this profile are due to the disturbance that allowed for a cooling of the humus material by the focused outflow of cool air.

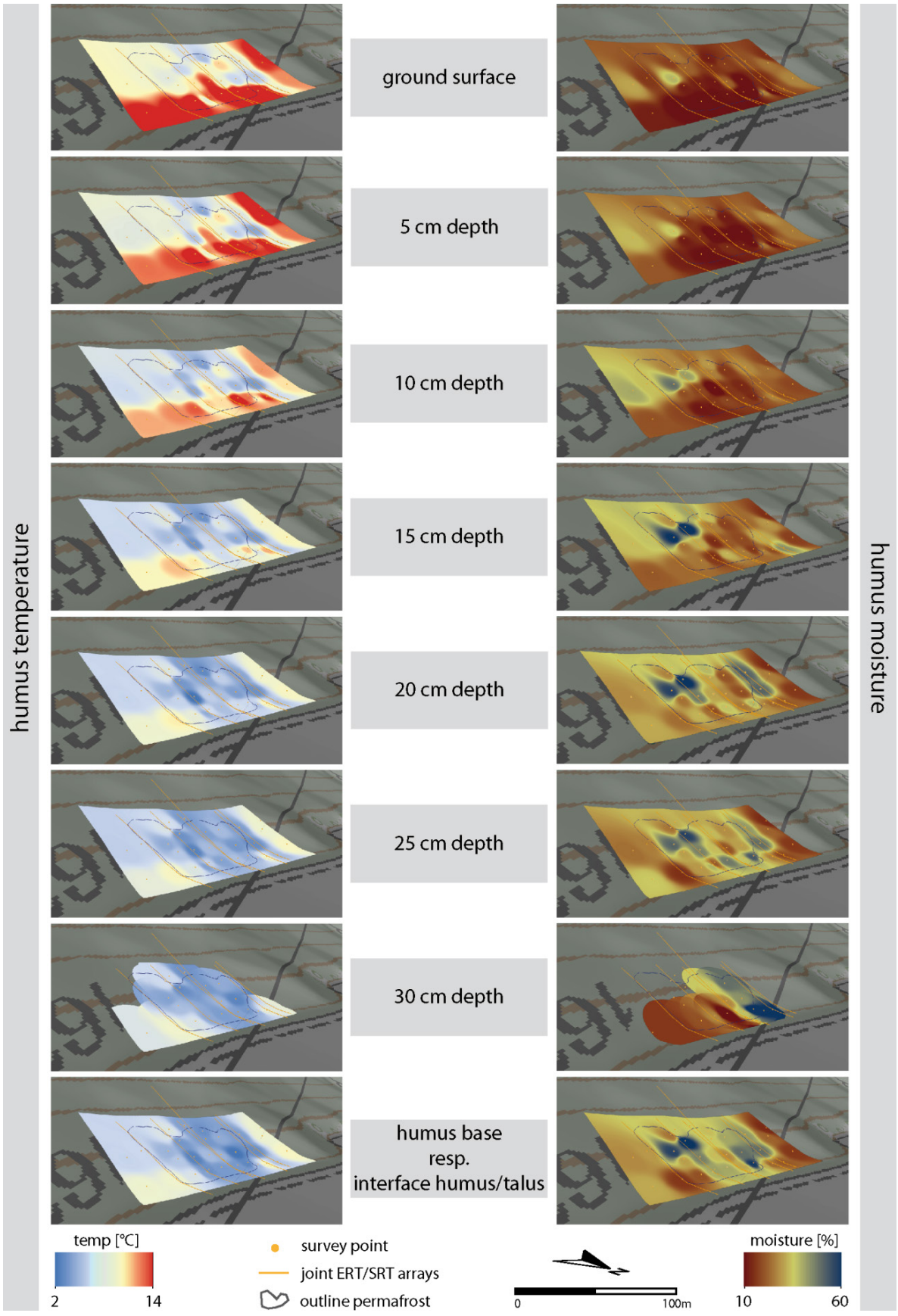

Figure 8.6: Results from humus temperature and-moisture mapping at the Val Susauna conducted in late August 2010 (22./23 and 28.08.2010) (basemap © swisstopo).

Regarding results on humus moisture, the first three depth slices show rather homogeneous results, with moisture contents mostly between 10-20 %. Small sections with higher moisture contents are detected in spots in the eastern parts of the slope. As shown in FIGURE 8.5, especially high contents of lichens are present within reach of these survey points. The moisture contents in the *Hexenwäldli* with permafrost below are rather heterogeneous.

A general increase of moisture with depth can be observed. Highest values were detected in the slope section where high amounts of lichens were recorded at the surface (maximum between 15 and 20 cm depth) and in the transition between *Hexenwäldli* and forest, where humus thickness is highest (maximum in 30 cm depth). In the forested area, moisture variability with depth is comparably low. A general increase of humus moisture is recorded with depth; humus temperatures decrease towards a depth of around 15 cm and remain almost constant below. Therefore, with regard to interactions between permafrost and surface composition, the information value of moisture contents as well as of temperatures is highest at the humus base. As presented above (FIGURE 8.5) a connection between permafrost distribution and humus moisture is observable. Especially the vertical differentiation into two central parts is apparent, with highest resistivities in the subsurface (cf. FIGURE 8.5) and highest moisture contents at the interface between humus layer and talus material.

8.2.3 Analysis of temperature logger data

An overview of temperature records for the hydrological years 2010 and 2011 is given in FIGURE 8.7. Further details are presented in TABLE 8.4 and TABLE 8.5. Due to various drop-outs, especially of UTL-data loggers, temperature time-series are partly incomplete and could not be involved into the analysis of the hydrological years.

Mean temperatures at the Val Bever (FIGURE 8.7) are positive for all data loggers in the hydrological years of 2010 and 2011 – except for vent temperatures. In general, temperatures in 2011 where higher than in 2010. The variance of temperature data is distinctly higher for air- than for ground-surface and humus temperatures, as expected. Except for humus temperatures, data loggers were distributed along the forest aisle (cf. FIGURE 8.1 & TABLE 8.1) in the western parts of the study site. Temperature characteristics along the forest aisle show a distinct spatial heterogeneity and variability

between the two years of data records. Mean air temperatures are highest at logger position AT1 (see also FIGURE 8.1). However, comparing air temperatures of winter- and summer-half year, minor differences between logger positions are observable in the winter half-year (TABLE 8.5); differences between freezing degree days (DDFs) are smaller compared to thawing degree days (DDTs) (TABLE 8.5). Regarding the relatively small distance between logger positions AT1 and AT2 of around 10 m (cf. FIGURE 8.1) differences in mean temperatures of around 1 °C are quite high. In contrast, the differences in mean temperatures between AT2 and AT3/AT4 are comparably low, regarding a difference in elevation of 47 m. Comparing AT3 (forest) and AT4 (forest aisle) located at a comparable elevation level, temperatures in the forest aisle are consistently and considerably lower. Especially the number of DDTs are distinctly lower for AT3 than at AT4.

As expected, ground-surface temperatures are lower for all logger positions compared to air temperatures, with high variability of temperature variance and IQRs (FIGURE 8.7). The different characteristics of ground-surface temperatures mirror the location of temperature data loggers at the stem-base of trees (GST1-4a) and at a distance to the tree (GST1-4b), within the moss and exceed differences in elevation a.s.l. While variations in mean temperatures within the hydrological years are comparably low, temperatures at the stem-base are characterised by a higher variance, colder winter-, but higher summer temperatures. This effect mirrors the influence of the snow cover, which is usually thinnest in the immediate surroundings of the tree trunks, providing no insulation against atmospheric temperatures. The moss cover provides a slight insulation and buffers higher summer temperatures. Accordingly, the number of thawing degree-days as well as freezing degree-days are higher at the stem-base.

Regarding ground-surface, humus and vent temperatures of all sites, it is noticeable, that median- and mean temperatures diverge. Thereby the median temperature is shifted towards 0 °C compared to the mean value. Most likely, the influence of the zero-curtain period causes a relative increase of 0 °C-temperature values and consequently a shift of the distribution curve towards 0 °C. In this context, the explanatory power of mean annual temperature values recorded at sites where zero-curtain periods are observable is rather low, as data are not normally distributed.

Median temperatures in the humus layer are slightly lower than temperature means; the divergence decreases with depth. The variance of temperature values is highest in 5 cm depth. Differences between the second and third depth level are comparably low. With slightly lower minimum- and higher maximum temperatures, the variance is higher in 2010 than in 2011. While thawing degree-days decrease with depth, freezing degree-days show an increase with depth, reflecting the insulating properties of the humus layer.

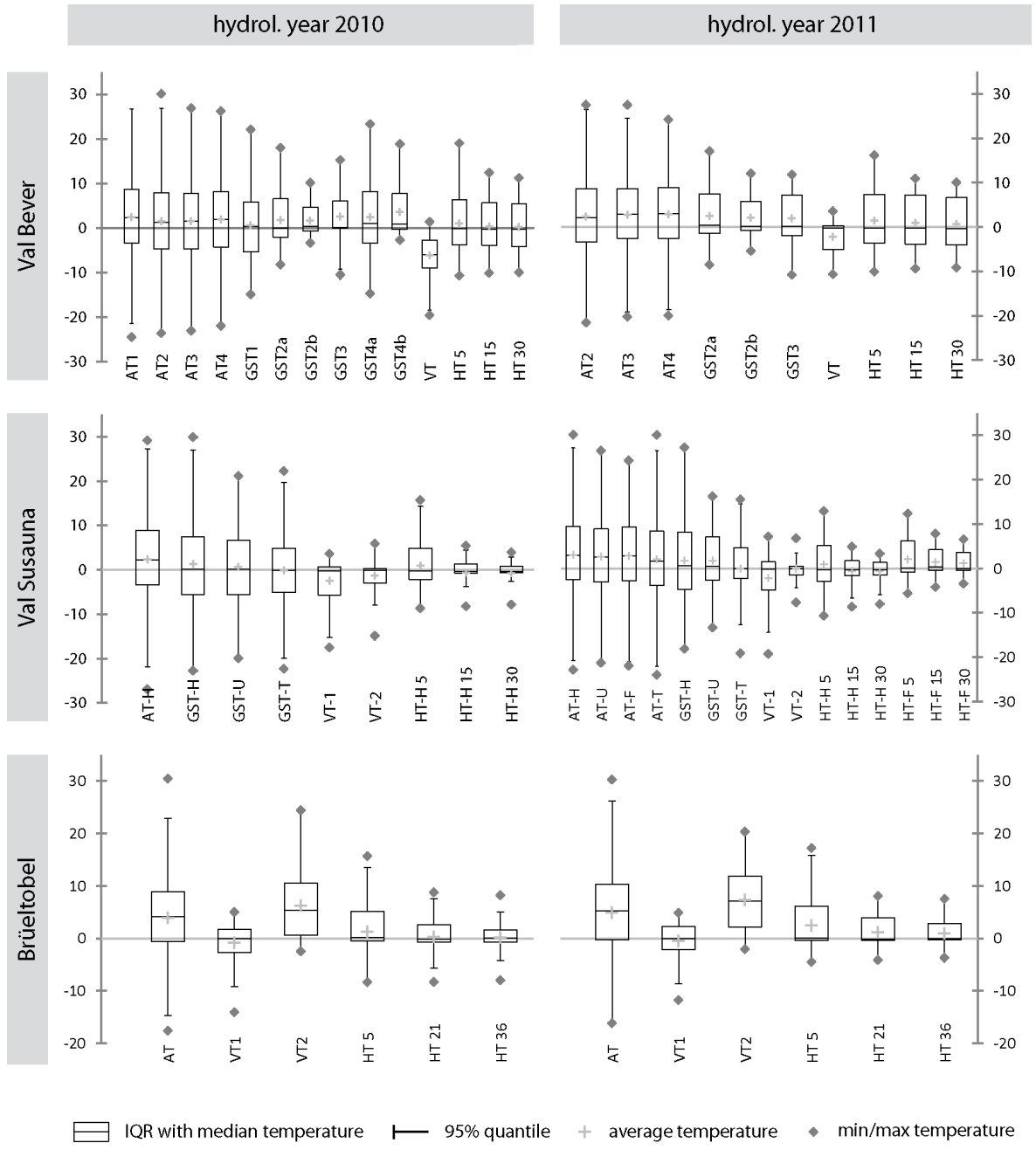

Figure 8.7: Boxplots of temperature logger data for the hydrological years 2010 and 2011 recorded at the study sites Val Bever, Val Susauna and Brüeltobel.

Median and mean vent temperatures of both years are clearly negative, with distinctly lower values in 2010. Only 44 thawing degree days but 1241 freezing degree days were recorded in the hydrological year of 2010 within the vent. Especially the scattering of temperature data to negative values is distinctly higher in 2010, reflecting colder winter temperatures. Thereby, it has to be taken into account that the dataset of 2011 does not cover the complete hydrological year, as temperature data from September 2011 are not included. However, it is not likely that temperature data from September would induce lower median values.

Correspondingly to the Val Bever, the hydrological year in the Val Susauna of 2011 was in general warmer than 2010 (FIGURE 8.7, TABLE 8.5 & TABLE 8.6). Due to numerous failures of UTL-data loggers, especially in 2010 (cf. TABLE 4.2), a complete comparability between the two years is not possible. With a distinctly higher variance and higher mean values, air temperature characteristics strongly diverge from the remaining temperature data sets at the Val Susauna. While air temperatures show a normal distribution of temperature data, median- and mean temperatures diverge for GST, humus and vent temperatures.

Despite of an altitudinal difference of more than 100 m between the Val Bever and Val Susauna, only minor differences in mean air temperatures are detected between the two sites (TABLE 8.5 & TABLE 8.6). Air temperature recordings in the Val Susauna indicate strong differences between the four logger positions (cf. FIGURE 8.1, TABLE 8.2). Mean air temperatures are highest in the central parts of the *Hexenwäldli* (AT-H) and lowest at logger position AT-T (cf. TABLE 8.2). Mean air temperatures in the forest (AT-F) are slightly lower compared to the *Hexenwäldli*. Thereby, the differences are higher in the winter half-year (1 °C) than during summer (0.3 °C). Differences in the variance of air temperatures are generally rather low. Regarding the degree days in air temperatures, only small differences can be noted (TABLE 8.6). One exception is logger position AT-T, with a distinctly lower number of DDTs and a higher number of DDFs compared to the other loggers. This is an indicator for a pronounced micro-climate.

Table 8.5: Overview on temperature logger data recorded at the Val Bever.

	logger name	mean/median temp [°C]				Ø winter-temp [°C]		Ø summer-temp [°C]		DDT		DDF		n_T		n_F	
		2010		2011													
		mean	median	mean	median	2009/10	2010/11	2010	2011	2010	2011	2010	2011	2010	2011	2010	2011
Val Bever	AT-1	2,44	2,35			-4,26	-3,04	8,70		1802		913					
	AT-2	1,52	1,25	2,38	2,15	-4,89	-4,14	7,86	8,41	1606	1719	1051	851	0,89		1,15	
	AT-3	1,53	1,47	2,78	2,83	-4,53	-3,24	7,23	8,31	1556	1016	997	736	0,86		1,09	
	AT-4	1,91	1,92	2,88	3,06	-4,16	-3,07	7,65	8,33	1638	1768	940	717	0,91		1,03	
	GST-1	0,52	0,36		-0,31	-4,56	-3,40	5,22		1155		968		0,64		1,06	
	GST-2a	1,74	-0,08	2,41	0,36	-2,39	-1,54	5,58	6,09	1159	1272	524	399	0,64		0,57	
	GST-2b	1,59	0,36	2,11	0,13	-0,22	-0,83	3,29	4,84	780	1021	200	253	0,43		0,22	
	GST-3	2,54	0,13	1,98	0,13	0,27	-1,90	4,93	5,59	1035	1173	109	452	0,57		0,12	
	GST-4a	2,37	1,02			-3,34		7,71		1599		736		0,89		0,81	
	GST-4b	3,54	0,80			0,27		6,63		1403		111		0,78		0,12	
	VT	-6,15	-5,97			-6,31		-4,56		44		1241		0,02		1,36	
	HT 5	0,90	-0,18	1,43	-0,25	-3,64	-3,33	5,38	5,92	1131	1232	789	703	0,63		0,86	
	HT 15	0,37	-0,25	0,95	-0,25	-3,55	-3,27	4,22	4,96	955	1076	801	710	0,53		0,88	
	HT 30	0,12	-0,37	0,70	-0,37	-3,61	-3,32	3,79	4,53	905	985	825	725	0,50		0,90	

The higher mean ground-surface temperatures of 2011 are mirrored first of all in distinctly warmer winter-temperatures (TABLE 8.6). Differences in summer temperatures are less pronounced. In analogy with air temperature data, coldest ground surface temperatures with slightly negative median temperatures in both hydrological years are recorded in the section with uncovered talus at the foot of the slope (GST-T). Comparing GST-H and GST-U (upper margins of the *Hexenwäldli*), mean temperatures of GST-H almost double values of GST-U in 2010; minor differences are detected in 2011. Regarding median temperatures, values of GST-H and GST-U are relatively similar for both years. Similar median values are most probably due to the eminent influence of the zero-curtain period at both logger positions. Higher mean values in the *Hexenwäldli* reflect the higher temperature variance, especially towards high temperatures. Mean winter temperatures in the *Hexenwäldli* are lower in the winter half-year and higher in the summer half-year compared to the remaining GST-logger positions. This mirrors the rapid response to varying atmospheric temperatures in the *Hexenwäldli*. In contrast to the forest with tall-grown trees, the dwarf-grown trees in the *Hexenwäldli* are not capable of buffering the heat exchange with the atmosphere, resulting in a higher temperature variance.

Differences in the median humus temperatures in the *Hexenwäldli* between 2010 and 2011 are remarkably low (FIGURE 8.7; TABLE 8.6). Mean winter temperatures are lower for all three depth levels in 2011 compared to 2010, which is contrary to the trends observed at all remaining logger positions. Summer temperatures are slightly higher in 2011. Likewise, IQR as well as the variance are higher in 2011. This effect is most pronounced in 15 and 30 cm depth and negligible in 5 cm depth. Comparisons between humus temperatures in the *Hexenwäldli* (HT-H) and the neighbouring forest (HT-F) show distinct divergences. Median temperatures of the hydrological year 2011 are slightly negative in the *Hexenwäldli* and slightly positive in the forest (TABLE 8.6). Thereby, mean winter- as well as mean summer temperatures are distinctly lower for HT-H compared to HT-F. Comparing the three depth levels between the *Hexenwäldli* and the forest location, IQR and variance in 5 cm depth are higher for HT-H than for HT-F; IQR of the depth levels 15 and 30 cm is distinctly smaller for HT-H than for HT-F. While the variance for HT-F 15 and 30 is almost symmetrical, HT-H 15 and 30 show a pronounced scattering towards negative temperature values. A decrease of DDTs and

DDFs with depth is detected at both logger positions; DDTs are distinctly higher at the forest site, DDFs at the *Hexenwäldli* exceed those measured at the forest.

Mean annual temperatures are clearly negative at both vents and are distinctly lower than median values, which are slightly below 0 °C. Temperatures are consistently lower at vent 1 compared to vent 2. The variance as well as IQR is higher for vent 1, with a strong trend to negative temperature values. Lowest DDTs at the Val Susauna were recorded in the two vents. Thereby, DDTs are lower for vent 1 in both years. The differences in DDTs between the two vents were more pronounced in 2011 (Table 8.6). Freezing degree days between the two vents diverge distinctly, with DDTs of vent 1 being two to three times higher than DDTs of vent 2. In general, both vents show a comparable temperature characteristic, with a clear trend to negative temperatures.

Mean and median temperatures at the Brüeltobel (Figure 8.7; Table 8.6) are slightly higher in 2011 compared to 2010 for all logger positions. This is observable for the winter- as well as summer half-years. As expected, mean air temperatures at the Brüeltobel are higher, the IQR and variance were smaller compared to the Val Bever and Val Susauna. In accordance to the other study sites, humus- as well as vent-temperature data of the hydrological years are not normally distributed, with divergences between mean and median temperatures. Humus temperature characteristics are comparable to data from the Val Susauna; mean and median temperatures, IQR and temperature variance decrease with depth. Median temperatures are close to 0 °C in all depth levels; minor differences were detected between 2010 and 2011, even though air temperatures are higher in 2011 by 1 °C.

Table 8.6: Overview on temperature logger data recorded at the Val Susauna & Brüeltobel.

	logger name		mean/median temp [°C]				Ø winter-temp [°C]		Ø summer-temp [°C]		DDT		DDF		n_T		n_F	
			2010		2011		2009/10	2010/11	2010	2011	2010	2011	2010	2011	2010	2011	2010	2011
			mean	median	mean	median												
Val Susauna	AT-H		2,31	2,31	3,02	2,90	-5,25	-3,48	8,84	9,02	1785	1893	978	792				
	AT-U				2,66	2,61	-5,30	-3,54	7,53	8,34	1516	1752	1014	785	0,85	0,93	1,04	0,99
	AT-T				2,04	2,78		-4,54		8,17		1288		1113		0,68		1,41
	AT-F				2,84	1,70		-4,36		8,72		1769		780		0,93		0,99
	GST-H		1,36	0,16	1,73	0,55	-5,62	-4,63	7,37	7,71	1479	1580	1015	940	0,83	0,83	1,04	1,19
	GST-U		0,68	0,16	1,72	0,43	-5,42	-2,84	5,86	5,98	1198	1249	971	619	0,67	0,66	0,99	0,78
	GST-T		-0,15	-0,08	-0,11	-0,05	-5,70	-4,50	4,55	4,10	925	855	995	887	0,52	0,45	1,02	1,12
	VT-1		-2,50	-0,26	-2,20	-0,17	-6,12	-5,38	0,49	0,82	166	242	1085	1042	0,09	0,13	1,11	1,32
	VT-2		-1,26	-0,05	-0,02	0,00	-3,71	-1,64	0,68	1,45	210	361	684	370	0,12	0,19	0,70	0,47
	HT-H	5	0,91	-0,20	0,86	-0,25	-2,72	-3,08	4,37	4,65	882	565	952	625	0,49	0,30	0,97	0,79
		15	-0,62	-0,37	-0,61	-0,31	-2,47	-2,64	1,14	1,35	279	510	324	542	0,16	0,27	0,33	0,68
		30	-0,76	-0,31	-0,71	-0,29	-2,30	-2,41	0,70	0,92	201	481	245	503	0,11	0,25	0,25	0,64
	HT-F	5			2,06	0,06		-1,69		5,05		1022		309		1,05		0,39
		15			1,39	0,32		-0,81		3,07		692		215		0,71		0,27
		30			1,12	0,00		-0,59		2,38		565		199		0,58		0,25
Brüeltobel	AT		3,87	4,16	4,87	5,26	-1,12	-0,53	8,46	9,82	1941	2199	513	421				
	VT-1		-0,86	-0,01	-0,50	0,00	-3,11	-2,52	1,08	1,46	312	353	626	534	0,16	0,16	1,22	1,27
	VT-2		6,16	5,39	7,30	7,12	2,84	3,29	9,68	10,92	2268	2670	20	4	1,17	1,21	0,04	0,01
	HT	5	1,29	0,20	2,44	0,07	-1,55	-0,51	4,09	5,20	938	1125	467	234	0,48	0,51	0,91	0,56
		21	0,28	-0,18	1,15	-0,12	-1,64	-0,49	2,19	2,66	584	643	482	225	0,30	0,29	0,94	0,53
		36	0,12	0,02	0,92	0,00	-1,49	-0,29	1,73	2,04	499	524	453	187	0,26	0,24	0,88	0,44

Distinctly divergent temperature characteristics are detected between vent 1 (foot of slope) and vent 2 (below rock wall). With median temperatures around 0 °C, small IQR and an asymmetrical variance that is shifted towards negative values, vent 1 data exhibit characteristics comparable to vent temperatures at the Val Bever and Val Susauna. Vent 2 shows antipodal characteristics with clearly positive mean and median temperatures that exceed air temperatures. Variance and IQR are distinctly larger for vent 2. Temperature data show a strong scattering towards positive temperatures. Antipodal temperature characteristics are especially pronounced with regard on temperature degree days (TABLE 8.6). Lowest DDTs are detected for vent 1. DDTs at vent 2 are seven times higher. Highest number of freezing degree days at the Brüeltobel are detected at the lower vent. Temperatures at the upper vent only sporadically drop below 0 °C, as indicated by the extremely low number of 4 DDFs in 2011 and 20 in 2010.

8.2.3.1 Influence of snow- and humus cover on the ground thermal regime

Snow cover distribution in parts has been discussed in CHAPTER 7, presenting geophysical monitoring results. Here (FIGURE 8.8), data are presented in comparison to air- and humus temperatures at the three study sites and to borehole temperatures measured at the Val Bever for the period from October 2008 to October 2011.

As presented above, winter temperatures are lowest in 2010/11; minor differences were recorded for the two previous years. Little differences were recorded between mean summer temperatures of the measure period. Comparing the three test sites (FIGURE 8.8), the courses of temperature curves in summer are almost congruent, but diverge distinctly in winter. Here, maxima in daily temperatures were recorded at the Brüeltobel, minima in daily temperatures at the Val Susauna.

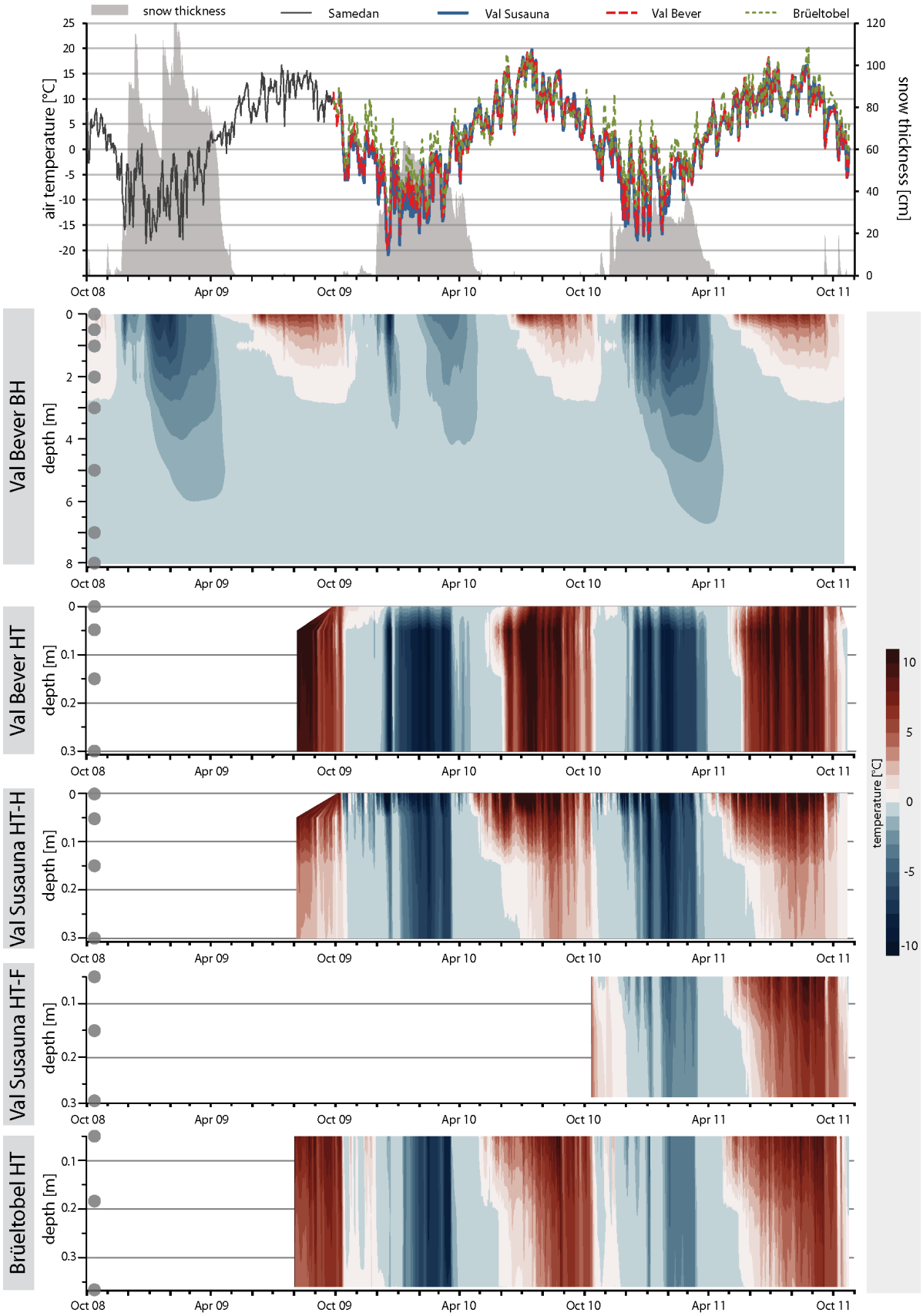

Figure 8.8: Comparison of air temperature data and snow cover distribution with borehole- and humus temperatures of the study sites Val Bever, Val Susauna and Brüeltobel.

Recorded at the meteorological station Samedan, the assignability of snow-cover data to the study sites has to be handled with care. While the general trend of snow cover distribution (e.g. above average/below average snow thickness) can be regarded as assignable, the assignability of factors like onset of a consistent snow cover and onset/end of snowmelt are not incontestable. It has been observed that in spring the snow cover lasts distinctly longer at the study sites than in the main valley of the Engadin, where the meteorological station is located. In autumn, a consistent snow cover is usually developed earlier at the study sites. Due to the generally distinctly higher precipitation rates in the Appenzell region (cf. CHAPTER 3.2), snow cover thickness is higher in the Appenzell than in the alpine dry valley of the Engadin. However, qualitatively the snow cover thickness in winter 2008/09 is far above average; in winter 2010/11 distinctly below average, for all sites. Snow cover distribution in winter 2009/10 can be regarded as average.

8.2.3.2 Snow

A strong connection between snow cover thickness, humus- and borehole temperatures is not recognizable (FIGURE 8.8). Borehole temperatures of the Val Bever show a comparable penetration depth of the cold-wave in winter 2008/09 and 2010/11 between 6-7 m depth, despite of the distinctly divergent snow cover and winter temperature characteristics. Especially within the uppermost 3 m, borehole temperatures in 2010/11 are distinctly lower than in 2008/09, with a high temporal variability. Cold-wave penetration in winter 2009/10 turns out to be distinctly more shallow and divided into two periods of supercooling. The first period (December 2009), where temperatures within the uppermost 3 m are distinctly cooled down to less than -7 °C, is followed by a period, where temperatures are only slightly below 0 °C, until in early February a second period of supercooling begins. Borehole temperatures in this period do not reach values of the first period of supercooling in December. They also show no signs of being influenced by short-term variations of air temperatures, as observed for winter 2010/11. In contrast to this, the first period of supercooling can be connected to a drop of air temperatures, clearly. Air temperatures in January 2010 are not explanative for increased borehole temperatures. Furthermore, this effect is not observable in the humus temperatures recorded at the Val Bever (for logger position see FIGURE 8.1). Here, a

rapid, continued supercooling was detected to temperatures below -10 °C with slight temporal variations. Thereby humus temperatures in winter 2009/10 are even lower than in winter 2010/11, which is contrary to borehole data. Consequently the evolution of borehole temperatures in winter 2009/10 must be regarded as a small-scale phenomenon, confined to areas of the forest aisle. Most likely, this effect can be explained by the avalanche activity within the forest aisle.

As shown in FIGURE 8.9, the main accumulation of the avalanche of the snow-rich winter of 2008/09 was at the valley bottom, partly behind the railway embankment. Main accumulation of the distinctly smaller avalanche in winter 2009/10 was in the area of the borehole (FIGURE 8.9). Consequently it must be assumed, that the avalanche of 2009/10 caused a small-scale disturbance of the thermal regime that resulted in a decreased supercooling of the subsurface in the area of the accumulation zone. Based on these results it must be assumed that the insulation capability of the snow cover is of minor importance for the supercooling of the subsurface, which is most likely due to the numerous snow-funnels (FIGURE 8.10), that allow a heat-exchange between atmosphere and subsurface throughout winter.

Data from the Val Susauna and Brüeltobel (FIGURE 8.8) provide different results. Even though atmospheric temperatures at the Val Susauna are distinctly lower in winter 2009/10, humus temperatures are slightly lower in winter 2010/11 (TABLE 8.6) and show a higher temporal variability and a rapid response to variations in atmospheric temperatures. Thereby, the thermal disparity between humus temperatures in 5 cm depth and atmospheric temperatures is around 2.5 °C in winter 2009/10 and only 0.4 °C in winter 2010/11. The temperature gradient in winter 2010/11 between air- (AT-F) and humus temperatures measured in the forest (HT-F) is distinctly higher (2 °C) than in the Hexenwäldli (0.4 °C). Likewise, the freezing degree days (cf. TABLE 8.6) in 5 cm humus depth of the Hexenwäldli almost double those measured in the forest. This indicates higher insulation capabilities of the snow cover in the forest compared to the Hexenwäldli.

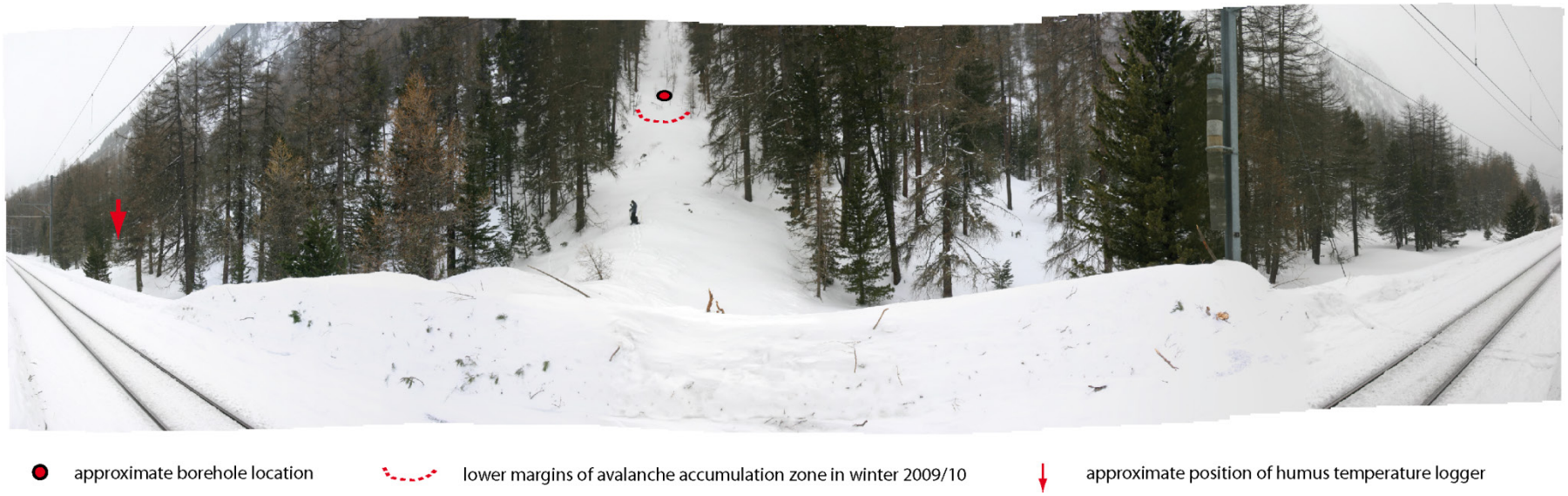

Figure 8.9: Panorama photo of the Val Bever (29.01.2013) with forest aisle in the centre. In the foreground, profile of the avalanche deposits on the railroad embankment.

Figure 8.10: Snow funnels at the Val Bever. Photos a, b and c show the lower vent. (a) a consistent snow cover is precluded by a small pine tree and thermal ventilation. (b, c and d) icicles and large snow crystals indicate temporal melting and refreezing. (e) snow funnel in the front of boulder.

At the Brüeltobel, humus temperatures mirror atmospheric temperatures rather accurate, independent from snow thickness. In winter 2009/10 humus temperatures in 5 cm depth are slightly lower than air temperatures (by 0.4 °C); in winter 2010/11 humus- and air temperatures are almost equal, despite of the strong differences in snow-thickness. A minimal supercooling of the humus layer and a very long zero-curtain period reflects the extremely warm air temperatures at the Brüeltobel.

8.2.3.3 Humus

Besides the period of supercooling the annual humus temperature evolution is characterised by prolonged zero-curtain periods and a summer period where humus temperatures are positive. Thereby, a zero-curtain period is detected in spring and in autumn (cf. FIGURE 8.8; see also FIGURE 8.11). The onset of the zero-curtains in autumn occurs very rapidly at all three sites, when air temperatures drop below 0 °C. Onset of the zero-curtains occurs almost simultaneously at all three depth levels, indicating a high thermal conductivity of the moist organic material in autumn. The occurrence of a zero-curtain period in autumn is due to the high moisture contents in the humus layer, and the release of latent heat during the phase change during freezing that keeps humus temperatures at 0 °C until all water is frozen.

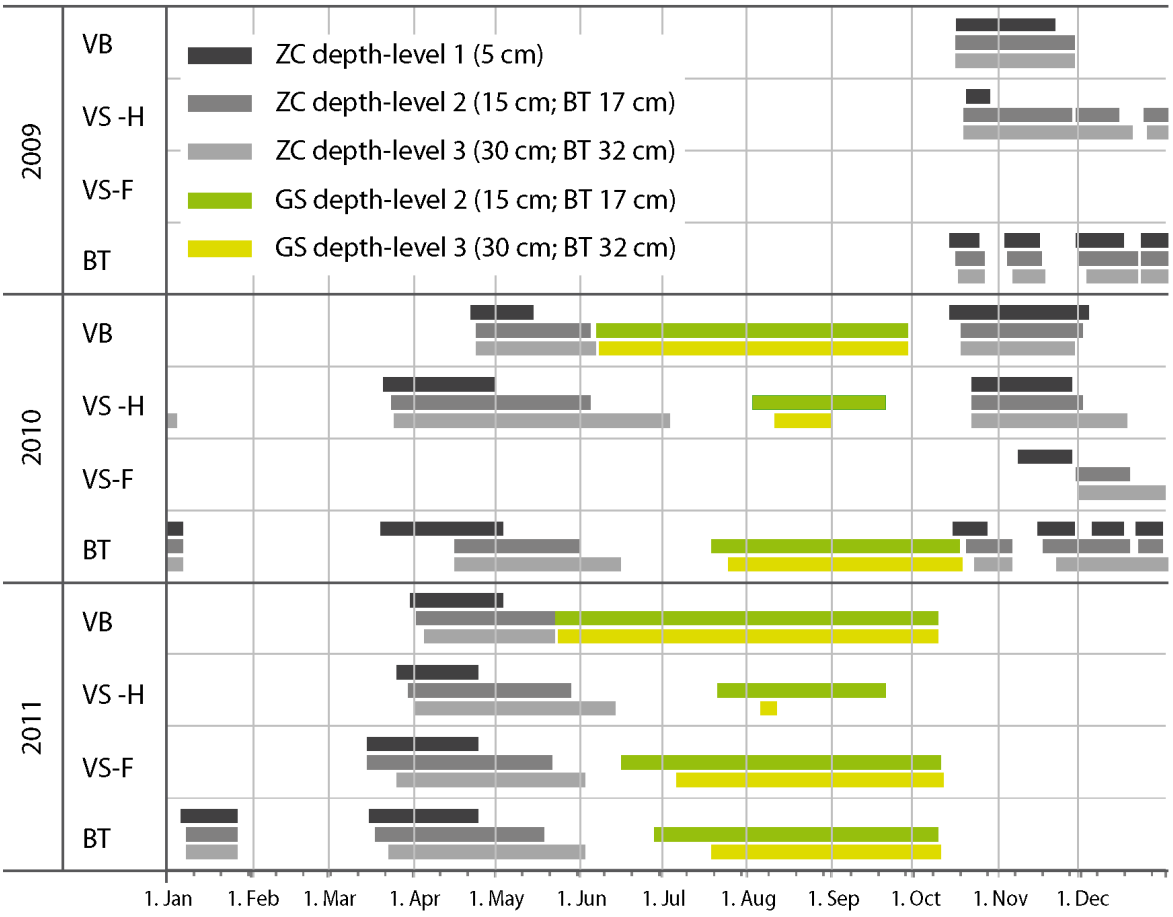

Figure 8.11: Duration of the zero-curtain and growing season derived from humus temperature loggers for the periods of measurement at the Val Bever, Val Susauna and Brüeltobel. (according to KÖRNER *&* PAULSEN *(2004), the growing season is defined as the period with temperatures above 3.2 °C).*

Characteristics of the zero-curtain period in autumn diverge between the three study sites. Consistent temperature conditions were recorded at the Val Bever. At Val Susauna, the zero-curtain period in the upper 15 cm was intercepted by various temperature variations to negative as well as to positive temperatures (FIGURE 8.11). At the Brüeltobel, temperature increases and short temperature drops comprise all depth layers. Duration of the autumn zero-curtain period is longest at the Brüeltobel, lasting until January and is shortest at the Val Bever (FIGURE 8.11). Humus temperatures recorded at the forest in the Val Susauna state an exception, with a distinctly delayed onset and a strong vertical differentiation. The transition between zero-curtain period and period of supercooling is sharp, with an increase of temperatures and a rather strong coupling to variations in air temperatures.

Likewise, a narrow transition zone between the period of supercooling and the onset of the zero curtain period can be observed in spring (cf. FIGURE 8.8; FIGURE 8.11). Humus temperatures remain at 0 °C due to the absorption of latent heat during the phase change from frozen to unfrozen state. Thereby the influence of snowmelt and the thawing of the high ice contents in the organic layer collude and result in a zero-curtain period that lasts until June/July at the humus base. Duration and characteristics of the zero-curtain period diverges between the three study sites. Within the uppermost 5 cm the zero-curtain ends with the end of snowmelt, which occurs earlier in the *Hexenwäldlis* of the Val Susauna and Brüeltobel compared to the forest of the Val Bever. At the Val Bever, humus temperatures below 15 cm depth show a rapid increase of temperatures. Little vertical differentiations were detected between the different depth levels, indicating a low insulation capability of the organic material. At the Brüeltobel and the Val Susauna, a strong vertical differentiation of humus temperatures point to a distinctly higher insulation capability of the humus layer. Especially pronounced are the differences between the logger positions *Hexenwäldli* and forest at the Val Susauna. Temperature profiles differ with regard to vertical temperature differentiation as well as maximum temperatures at the humus base (*Hexenwäldli*, 30 cm humus depth 3.7 °C; forest, 30 cm humus depth 6.5 °C). However, maximum temperatures at the humus base are still higher at the Brüeltobel (8.2 °C) and Val Bever (10 °C).

Table 8.7: Details on growing seasons, temperature means and extremes for humus temperatures at the three study sites.

			duration of growing season [days]	seasonal mean [°C]	absolute maximum [°C]	absolute minimum [°C]
2010	VB	HT 2	132	7.8	12.4	-10.2
		HT 3	131	7.3	11.2	-10.1
	VS	HT-H 2	25	4.0	5.5	-8.3
		HT-H 3	13	3.5	3.9	-7.9
		HT-F 2	-	-	-	-
		HT-F 3	-	-	-	-
	BT	HT 2	84	5.5	8.8	-8.3
		HT 3	79	5.2	8.2	-8.0
2011	VB	HT 2	110	7.7	10.9	-9.4
		HT 3	109	7.2	10.1	-9.2
	VS	HT-H 2	34	3.6	4.9	-8.6
		HT-H 3	2	3.3	3.4	-8.1
		HT-F 2	111	5.5	7.9	-4.2
		HT-F 3	95	5.0	6.5	-3.4
	BT	HT 2	95	5.3	8.1	-4.1
		HT 3	77	5.0	7.5	-3.7

According to Körner & Paulsen (2004) the growing season (Figure 8.11 & Table 8.7) is defined as the period with temperatures in the rooting zone warmer than 3.2 °C. While Körner & Paulsen (2004) used the temperature in a depth of 10 cm, growing duration of growing seasons in Figure 8.11 & Table 8.7 refer to 15 cm depth (Brüeltobel 21 cm depth) and the interface between humus and talus material (30 cm depth; Brüeltobel 36 cm depth).

The growing season differs distinctly with regard to the tow depth levels and between the study sites. While the transition between zero-curtain and growing season at the Val Bever is almost seamless, the transitional period at Val Susauna (*Hexenwäldli*) and Brüeltobel covers a period of up to 2 month. The onset as well as the ending of the growing seasons at Val Bever shows only marginal differentiations between the two depth levels. At Brüeltobel, the onset of the growing season is delayed in the deeper depth level by around 10-15 days; the ending of the growing season occurs almost simultaneously for both depth levels. At the *Hexenwäldli* of the Val Susauna, conditions strongly diverge. The growing season in 30 cm depth is significantly shorter for both years, with only 2 growing days in 2011 (Table 8.7). The duration of the growing

seasons shows the strongest differentiation with depth in the Val Susauna *Hexenwäldli*, and the lowest at Val Bever. Likewise, the differentiation of maximum humus temperatures with depth is strongest at Val Susauna, where maximum temperatures are around 3.4-3.9 °C in 30 cm depth. While the differences in the characteristics of the growing season differ strongly between the two measurement sites at Val Susauna, the divergences between the Val Susauna forest, Brüeltobel and Val Bever are less pronounced. Here, maximum temperatures as well as the seasonal mean are slightly lower in the forest of the Val Susauna, where no permafrost is present, compared to the Val Bever and Brüeltobel.

8.2.3.1 Analysis of the thermal ventilation

To analyse the influence of the thermal ventilation on the ground thermal regime FIGURE 8.12, FIGURE 8.13 & FIGURE 8.14 illustrate the temperature curves for atmospheric temperatures in comparison to vent temperatures and humus temperatures in 5cm depth and at the humus base for the three study sites.

The activity of the chimney effect is deducible from temperature data at all three study sites and allows for a differentiation of temperature records into the period of supercooling during winter and the high-summer period. Autumn and spring are characterised by regular reversions of the direction of circulation (transitional period), which is, in the near-surface, interfered by the zero-curtain period.

Brüeltobel

At the Brüeltobel, the seasonal differences between the courses of the temperature curves are illustrated ideally (FIGURE 8.11). As indicated in FIGURE 8.7, the temperature characteristics between vent 1 and 2 are opposing at the Brüeltobel. For most parts of the summer half-year the temperature curve of vent 2, located upslope below the rock-wall runs parallel to the air temperature curve, mostly with a slight offset towards warmer temperature values. For vent 1, at the foot of the slope this period is characterised by relatively steady temperatures, ranging around 0°C for most parts of the zero-curtain period, followed by a gradual increase of temperatures towards October. Temperatures of vent 1 show almost no daily variability and appear completely decoupled from atmospheric temperature variations. This period corresponds with the

summer-circulation of the chimney effect, with an inflow of relatively warm air into the talus slope through vents at the top of the slope. The air is cooled on its way down through the slope, warming the interior of the talus slope, and flows out through vents at the foot of the slope (cf. HARRIS & PEDERSEN, 1998; WAKONIGG, 1996).

In high-winter, the situation is antipodal. While temperatures in the lower vent follow the atmospheric temperatures, fluctuations of temperatures in the upslope vent are strongly reduced and remain – except for scattered days – positive throughout winter. This period represents the winter circulation of the chimney effect, with an inflow of cold air through vents at the foot of the slope, which is warmed while it is cooling down the interior of the talus slope, and exits through vents at the top of the slope (cf. HARRIS & PEDERSEN, 1998; WAKONIGG, 1996).

FIGURE 8.12a shows exemplarily the period of transition between summer- and winter circulation at a measurement interval of 20 minutes. Taking a closer look at the period of summer circulation (FIGURE 8.12a), the temperature profile shows an increase to maximum values (~4 °C) at three consecutive nights around 3 AM., while air temperatures decrease to a minimum at the same time. This represents a short collapse of the circulation system, as the gradient between inside and outside temperatures is minimal. With a drop of atmospheric temperatures around October 12th, the circulation is reversed until October 21st, where a strong increase of air temperatures forces a further reversion of the circulation, as the gradient between temperatures outside and inside the talus slope is inverted.

The transition between winter- and summer circulation is illustrated in FIGURE 8.12b. As expected, the temperature curve of the upper vent is slightly above 0 °C, with little variability during the period of winter circulation and follows the atmospheric temperature after May 19th. In contrast to the winter circulation in October (FIGURE 8.12a), the course of the temperature curve in the lower vent shows little correlation to atmospheric temperatures in February. However, even though daily variability of temperatures in vent 1 is low, a period of positive air temperatures (February 17th – March 4th) causes a gradual increase of vent temperatures; with the consecutive drop of air temperatures, temperatures in vent 1 likewise decrease strongly. The inert reaction of vent temperatures in spring at the Brüeltobel might be explained by the influence of the snow cover. Vent 1 is located in the ditch of a hiking path. In early winter, with a

shallow snow cover, the reversible thermal circulation is capable of keeping funnels through the snow cover open, enabling for a convective air exchange and a strong coupling between air- and vent temperatures. During winter, the snow is usually accumulated in the ditch by vehicles clearing snow from the hiking path, plugging snow funnels and preventing a direct convective circulation. Therefore, the response of vent temperatures occurs with a delay and dampened, due to the isolation capability of the snow accumulation.

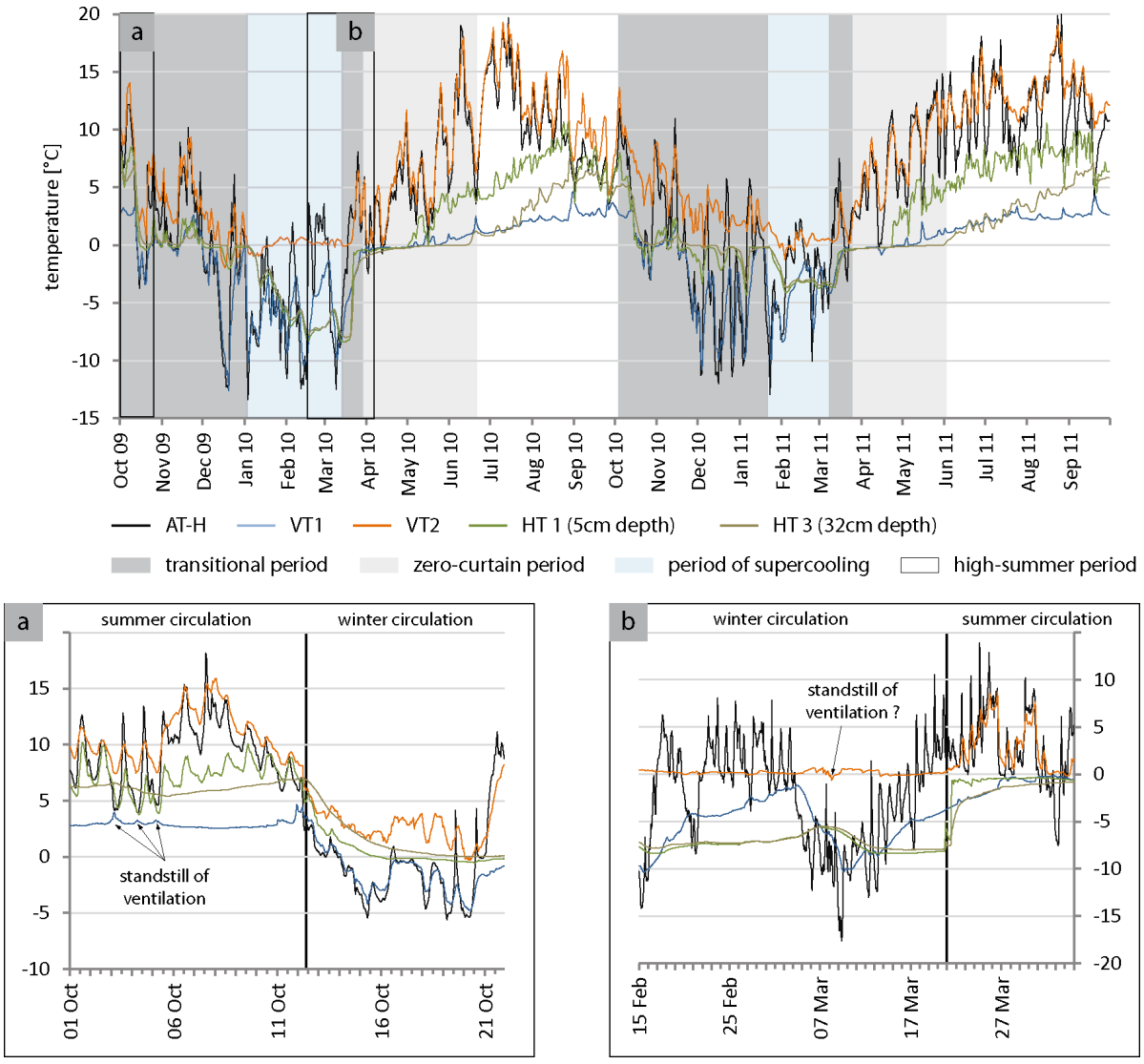

Figure 8.12: Temperature data from the Brüeltobel, comparing air-, vent- and humus temperatures for the complete period of measurements (daily mean temperatures) and selected periods (a and b; hourly interval).

Humus temperatures in depth level 1 (5 cm depth) and 3 (32 cm depth) show a strong coupling to atmospheric temperatures in winter. The response to variations in air

temperatures in 32 cm depth is slightly dampened and delayed compared to the first depth level. Especially in winter 2010/11 the cooling of the humus layer occurs not earlier than mid-February, with a rather short duration of supercooling. Here, it is interesting to see, that the continuous decrease of humus temperatures to negative values occurs when the temperatures of the upper vent level out around 0°C, even though atmospheric temperatures as well as temperatures in the lower vent have dropped distinctly between November and February.

With the end of the zero-curtain period (cf. FIGURE 8.11) humus temperatures constantly increase until air temperatures decrease in the autumn transition phase. Due to the high insulation capacity of the organic material, daily temperature variations in the humus layer are rather low. The course of the temperature curve HT 3 appears to correlate to temperatures of the lower vent during summer. This is especially visible for temperature data in mid-June 2010 (end of zero-curtain period). Here, a drop of atmospheric temperatures (and correspondingly temperatures in the upper vent) can be correlated with a rapid increase of temperatures in the lower vent. While humus temperatures in 5 cm depth decrease with decreasing air temperatures, an increase of temperature values was detected at the base of the humus layer, parallel to the curve of VT 1. During summer 2010 and 2011 further temperature peaks in vent 1 and HT-3 are in accordance, but not developed as distinct.

Val Susauna

Temperature curves recorded at the Val Susauna (FIGURE 8.13) show the same characteristics as detected at the Brüeltobel. A clear differentiation between zero-curtain period and transitional period in autumn is hard to achieve, as the zero-curtain period is driven by humus conditions, the transitional period by the ventilation. As shown above, the two investigated vents both represent lower vents, despite of the considerable difference in altitude.

During winter, as well as during the autumn ZCP, both vents show a strong correlation to air temperatures. However, temperatures in vent 2 appear buffered, with much warmer minimum values compared to vent 1. For long periods of the summer half-year, vent temperatures remain consistently around 0 °C. Increases of temperatures occur first at the vent 1 and, with a delay, at vent 2. Temperature decreases during the

transitional periods in autumn occur first and with a stronger magnitude at vent 1. Higher temperature variability in high-summer is recorded for both vents in 2010, compared to 2011, while no conspicuous differences in atmospheric temperature characteristics are observable. Regarding the temperature curves in August 2011, a distinct drop of air temperatures is observable (11th and 28th of August 2011). The air temperature decrease of August 11th can be correlated with a short-term temperature drop in both vents as well as in HT 1. Contrary to this, the decrease of temperatures in vent 2 and HT 1 on August 28th can be correlated with a temperature increase within vent 1.

Humus temperatures at the Val Susauna show comparable characteristics to the Brüeltobel. Differences between the two depth levels are minor compared to the Brüeltobel during winter, but are more pronounced in summer. Especially the duration of the ZCP differs distinctly between the two sites. It is striking, that the coupling between HT-H 1 and AT appears higher between May and June compared to June/July. Unfortunately, soil moisture contents could not be monitored. However, it can be assumed that the moisture in the organic material is higher in May/June compared to June/July, influencing the insulation capacity, which is distinctly higher under dry conditions (French, 2007; Williams & Smith, 1991). Temperatures at the humus-base show a course similar to the temperature curve of vent 1. Especially during high-summer a slight delay between vent- and humus temperatures is observable.

The transitional periods as shown in Figure 8.13a, b (resolution 20 minutes) are characterised by a long ZCP within the humus layer and air temperatures varying strongly between days with positive and negative temperature means. Consequently, the direction of the thermal circulation is inverted regularly. Figure 8.13c shows a period of three weeks where the reversion of the circulation is well imaged by temperature data.

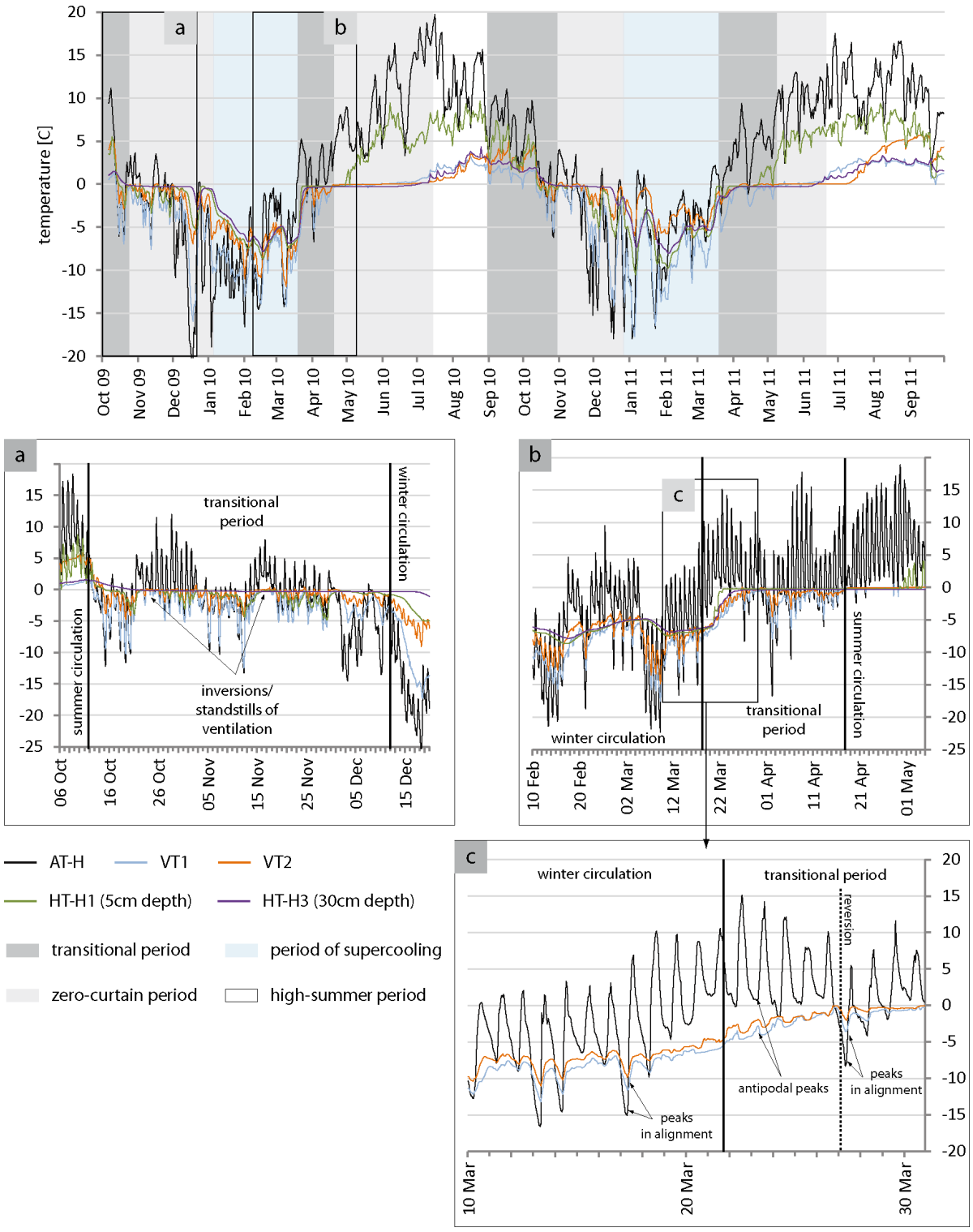

Figure 8.13: Temperature data from the Val Susauna, comparing air-, vent- and humus temperatures for the complete period of measurements (daily mean temperatures) and selected periods (a, b and c; hourly interval).

The winter circulation is characterised by an inflow of cold air through the lower vents. While air temperatures in high-winter mostly remain below the freezing point,

temperatures in spring and autumn typically increase to positive values by day. Between March 10th and March 20th, decreases of air temperatures at night are connected to a decrease of vent temperatures – at a minor magnitude and with a slight delay. Negative peaks of air- and vent temperatures are in alignment. Between March 21st and March 27th, air temperatures are mostly positive, but in all cases warmer than vent temperatures. A drop of atmospheric temperatures at night causes an increase of vent temperatures, as the gradient between temperatures outside and inside the talus slope becomes minimal. Negative and positive peaks of air and vent temperatures are antipodal during this period. The drop of air temperatures by March 27th and March 28th causes a short reversion of the direction of ventilation, followed by a level out of vent temperatures around 0°C, indicating a constant outflow of cold air at the foot of the slope.

Val Bever

The temperature pattern at the Val Bever (FIGURE 8.14) shows the same characteristics as data from the Brüeltobel and Val Susauna sites. A strong coupling between vent- and air temperatures is observable in winter, representing an inflow of cold air into the talus slope, while they appear completely decoupled during summer, indicating an outflow of cold air. Correspondingly to the Val Susauna and Brüeltobel, the transitional periods in autumn (FIGURE 8.14b) and spring (FIGURE 8.14a) are characterised by regular inversions and/or standstills of the direction of ventilation, driven by the gradient between atmospheric temperature and temperature in the interior of the talus slope. Humus temperatures sow a slightly different characteristic compared to the other two study sites. Temperature values from both depth levels indicate – except for the zero-curtain periods – a strong coupling to air temperatures throughout the year. Temperatures in the humus layer are slightly buffered with a slight delay to variations in atmospheric temperatures. Especially the rapid increase of temperatures at the humus base with the end of the zero-curtain period is conspicuously different to the other two sites and indicates a rather low insulation capability of the humus layer in the Val Bever. Furthermore, in contrast to the Brüeltobel and Val Susauna no indications for a coupling between temperatures in the vent and at the humus-base are observable.

Taking a closer look at the vent temperatures in winter, distinct differences are observable between winter 2009/10 and 2010/11. While vent temperatures in winter

2009/10 rapidly response to variations in air temperatures, characteristics of the vent-temperature curve in winter 2010/11 appear buffered and show a course similar to humus temperatures (cf. FIGURE 8.14c). This effect is not developed in early winter 2010/11, where vent temperatures show the typical, rapid response to drops in air temperatures below the freezing point (FIGURE 8.14c). This effect is comparable to the characteristics of the course of lower vent temperatures at the Brüeltobel, where the convective ventilation was prevented by snow accumulations.

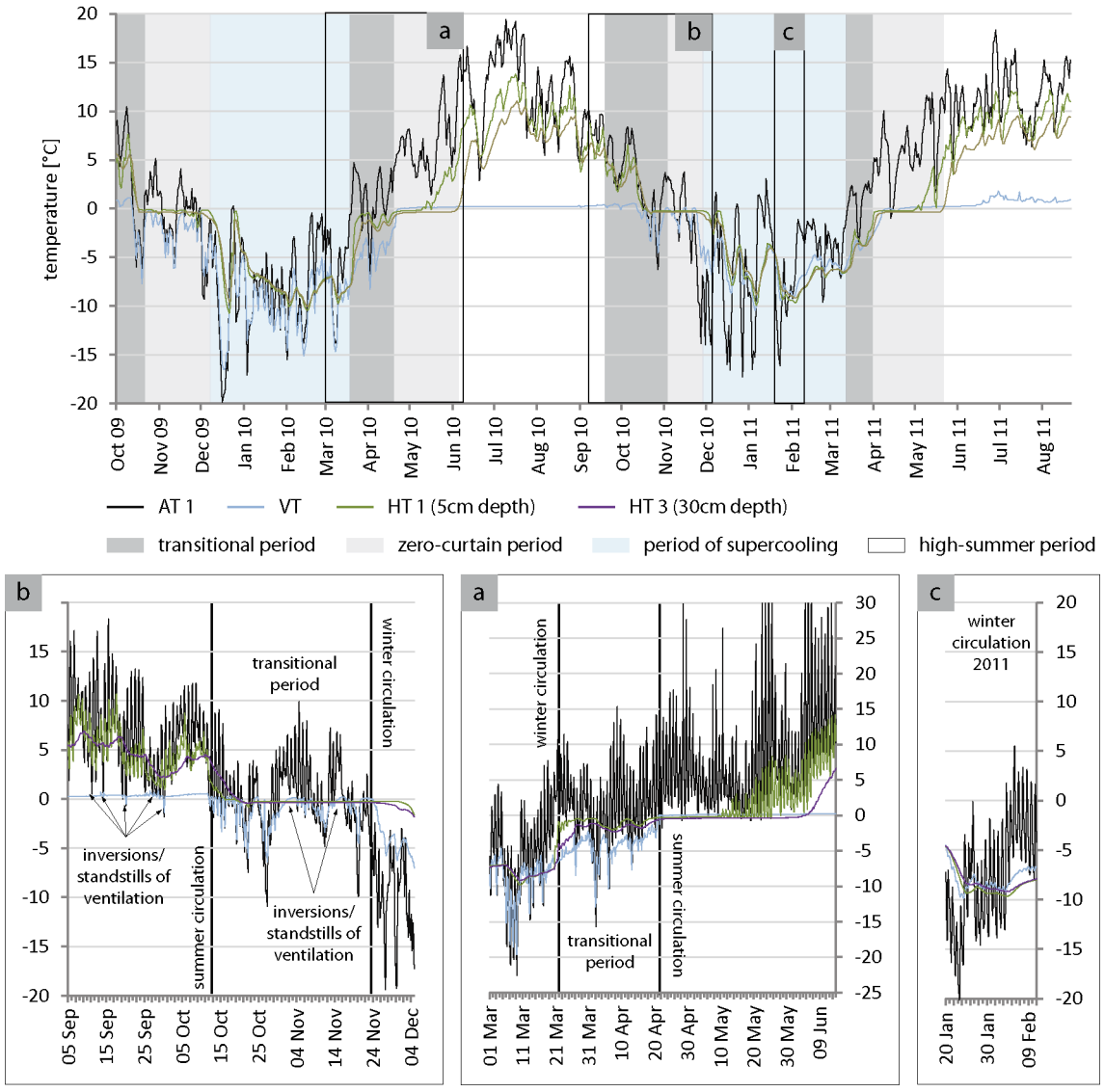

Figure 8.14: Temperature data from the Val Bever, comparing air-, vent- and humus temperatures for the complete period of measurements (daily mean temperatures) and selected periods (a, b and c; hourly interval).

The close relation between the course of humus- and vent temperatures implies that the ventilation in winter 2010/11 was – at least in the area of the investigated vent –

disturbed and the cooling in the area of the vent was restricted to conductive heat transport. As only a very shallow snow cover was developed in winter 2010/11 (cf. FIGURE 8.2; TABLE 8.3) it is very unlikely, that the vent has been plugged by snow, solely. Instead, it is more likely, that the regular temperature increases in winter 2010/11 have caused short-term snowmelt, with an accumulation and refreezing of meltwater inside the vent. This effect is typically observable in spring, when ice-curtains are developed within the vents due to refreezing of meltwater (cf. FIGURE 8.15, see also FIGURE 8.10).

Figure 8.15: Photographs of a vent at the foot of the talus slope in the Val Bever during spring. (a, b and c) ice and icicles formed due to the refreezing of meltwater, with a complete plugging of the vent by a typical icicle curtain (a) in early spring. (d) leftovers of ice in mid-June.

The reduced supercooling during winter 2010/11 is mirrored in the course of the vent temperatures in summer 2011. In contrast to summer 2010, where maximum vent temperatures were around 0.5 °C (maximum values in late September), maximum vent temperatures in summer 2011 of 1.5 °C were achieved by July. However, summer temperatures for all logger positions were higher in 2011 in comparison to 2010 (cf.

TABLE 8.5). Therefore, it can not be determined definitely, if higher vent temperatures in 2011 are due to reduced supercooling in winter, or driven by higher summer temperatures.

8.2.3.2 Relationships and dependencies of temperature data

Results presented above indicate dependencies and correlations between air-, vent- and humus temperatures. Thereby the characteristics of dependencies appear to differ between summer and winter, driven by the direction of ventilation. To test these dependencies, datasets of air-, vent- and humus temperatures from high-winter and high-summer where correlated, presenting the correlation coefficient (r) and the determination coefficient (r^2) for the three study sites (FIGURE 8.16, FIGURE 8.17 & FIGURE 8.18).

For all sites different correlations characteristics can be observed between high-summer and high-winter, which supports assumptions drawn from temperature data analysis presented above. Correlation and determination coefficients are in general rather low. This is most probably due to the fact that the heat transfer is for all cases slightly buffered by an isolating snow cover or organic material. As a consequence, temperature variations are in general slightly delayed compared to atmospheric temperatures, which results in rather low r and r^2 values.

Brüeltobel

Regarding the determination coefficient (r^2) for the Brüeltobel datasets (FIGURE 8.16), distinct differences are observable between high-summer and high-winter. In high-winter r^2-values are in general quite low, meaning that a rather low percentage of the variance of one temperature data set can be explained by the variance of the correlated dataset. Highest r^2 is detected for the correlation between AT and the temperature in both vents. However, the correlation coefficient (r) is positive for the relation between air temperature and the lower vent temperatures, but negative for AT and VT2. Thereby an r-value of -1 would indicate that the temperature evolution is opposed. Likewise, the correlation coefficient between the lower and the upper vent is negative.

The correlation between air- and humus temperatures indicates very low causal relationships (r^2 ~0.05; r ~0.25), with no differences between the three depth levels. A

correlation coefficient of ~0.4 between VT1 and humus temperatures still indicates a low correlation. The correlation between the upper vent and humus temperatures in all depth levels are negative, with $r \sim$ -0.6, indicating an opposed relation between the variables. In summer, the relationships are more complex. While around 70% of temperature values within the upper vent can be explained by air temperatures (r^2=0.7), with a rather high correlation between datasets (r=0.83), the correlation between AT and VT1 is negative (r=-0.79). In contrast to high-winter data, the humus temperatures in depth levels 2 and 3 show distinctly different dependencies compared to the first depth level. Correlation coefficients between HT5, AT, VT1 and VT2 are very low, ranging between -0.06 and 0.3.

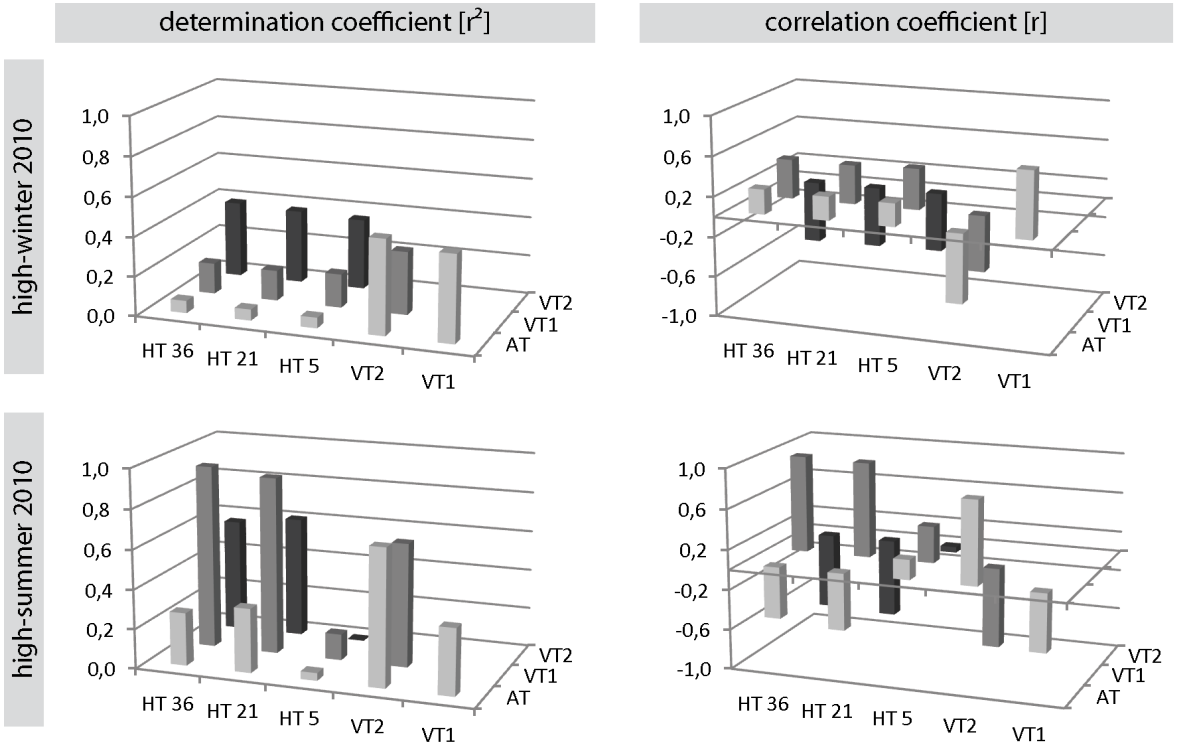

Figure 8.16: Results from correlations between air-, vent- and humus temperatures at the Brüeltobel, presenting bar charts of the determination (r^2) and correlation coefficients (r).

Depth levels HT21 and HT36 show comparable correlation characteristics. Thereby, highest correlation coefficients are detected between HT36 and temperatures of the lower vent (r=0.965) with 93% of humus temperatures being explained by vent temperatures. Correlation between HT21 and VT1 is slightly lower. Correlation

coefficients between humus temperatures HT21/HT36 and atmospheric as well as vent 2 temperatures are negative.

Val Susauna

At the Val Susauna (FIGURE 8.17), correlation and determination coefficients are generally rather high in winter. Correlations between vent- and humus temperatures are distinctly higher in comparison to correlations between atmospheric- and humus temperatures. With an r of 0.9, temperatures in vent 1 and vent 2 highly correlate, emphasising the assumption that both investigated vents represent lower vents. The fact that correlation coefficients are highest between vent temperatures and humus temperatures in 5 cm depth implies the assumption that this might be a spurious correlation, as no logic explanation for dependencies between the two variables is available. Furthermore, it is most likely, that both, vent and humus temperatures are first of all driven by atmospheric temperatures, but the temperature signal is buffered/delayed due to the snow cover. However, the correlation between air- and vent temperatures (r=0.65-0.75) is distinctly higher than the correlation between air- and humus temperatures (r=0.2-0.5). This effect might be explained by the direct – convective – heat transport between atmosphere and vents through funnels in the snow cover, causing a rapid response of vent temperatures to variations in atmospheric temperatures. The snow cover buffers the influence of variable air temperatures on humus temperatures, but is not capable of providing a complete decoupling.

Summer-data provide a picture comparable to the Brüeltobel. A high correlation can be observed between atmospheric temperatures humus temperatures in the *Hexenwäldli* in 5 cm depth (r=0.82). Correlation coefficients to humus temperatures in 15 and 30 cm depth are slightly negative, with r^2 values around 0. R-values around 0.53 indicate a causal relationship between temperatures in vent 1 and humus temperatures (*Hexenwäldli*) in 15 and 30 cm depth. High correlation coefficients between temperatures in vent 2 and HT-F 15/HT-F 30 must be interpreted as a spurious correlation, as no heat exchange between the two locations is logically explainable.

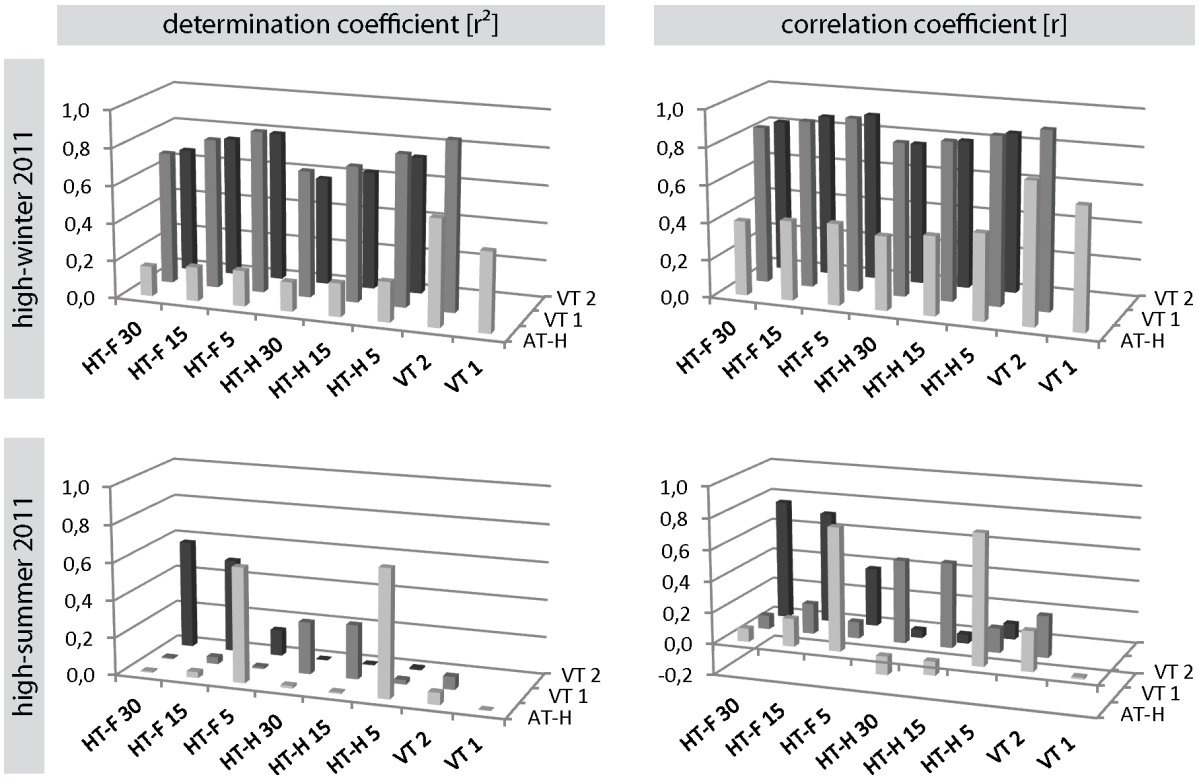

Figure 8.17: Results from correlations between air-, vent- and humus temperatures at the Val Susauna, presenting bar charts of the determination (r^2) and correlation coefficients (r).

Val Bever

The correlation between air- and vent temperatures at the Val Bever (FIGURE 8.18) shows results comparable to data from the Val Susauna and Brüeltobel. In high-winter a causal relationship between air- and vent temperatures is indicated by r-values of 0.77 (r^2=0.58), while no relationships are observable between temperature data in summer (r=-0.2; r^2=0.04).

Humus temperatures in high-winter show no correlation to air-temperatures and a low correlation to vent temperatures (r=0.3-0.34), with minor differences between the three depth levels. In summer, humus temperatures in 5 cm depth correlate to air temperatures with an r of 0.8 (r^2=0.65); no correlation, respectively a slightly negative correlation, is detected to vent temperatures (r=-0.26; r^2=0.07), which is in accordance to results from Val Susauna and Brüeltobel.

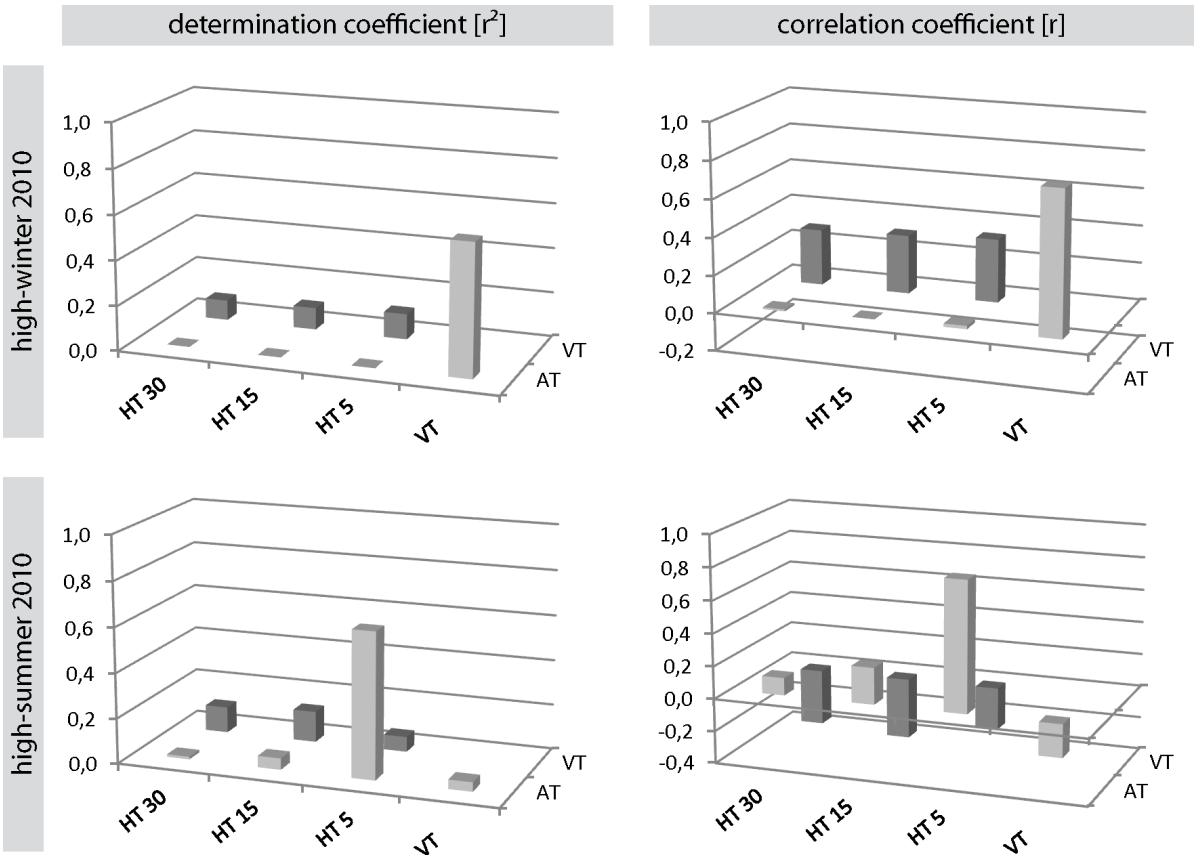

Figure 8.18: Results from correlations between air-, vent- and humus temperatures at the Val Bever, presenting bar charts of the determination (r^2) and correlation coefficients (r).

Correlating humus temperatures in 15 and 30 cm depth with air- and vent temperatures in high-summer, resulting correlation coefficients are very low, with r^2 below 0.14, indicating that no causal relationship exists between the locations. However, in contrast to both other study sites, humus temperatures in 15 and 30 cm depth at the Val Bever show a generally low but negative correlation to vent temperatures (r=-0.37/-0.34), while the correlation to air temperatures is slightly positive, with higher values for the 15 cm depth level (r=0.23) than for 30 cm depth (r=0.18).

8.3 Discussion

Investigations on the ground thermal regime indicate a high complexity of processes that deduce a strong spatial heterogeneity of the ground thermal regime and distinct differences between the study sites.

Conclusions on the influence of the snow cover on the ground thermal regime at the investigated study sites are drawn based on the analysis of BTS-data as well as borehole- and temperature logger data. Generally, the presented data indicate that a connection between snow thickness and a related decoupling between atmospheric- and ground surface temperatures, as typically assumed for lowland permafrost in high latitudes (Williams & Smith, 1991; Zhang, 2005) and alpine permafrost sites above the timberline (Haeberli, 1973; Keller & Gubler, 1993; Luetschg et al., 2008; Luetschg et al., 2004) is not ascertainable for the investigated talus slopes. Here, results coincide with data presented by Morard (2011), who likewise detected a limited insulation capability of the snow cover at talus slopes below the timberline.

Results from the three study sites (Figure 8.2, Figure 8.3 & Figure 8.4) indicate, that BTS were linked more pronounced to winter temperatures than to snow thicknesses. Borehole data (Figure 8.8) support this assumption, at least for the Val Bever. Furthermore, coldest BTS were measured in areas, where the snow cover was thickest. Thereby, the snow thickness was strongly linked to the vegetation composition. At Val Susauna and Brüeltobel, snow was thickest in the *Hexenwäldli*; at Val Bever in areas where the tree density as well as crown density, especially of the larch tress is reduced (cf. Figure 3.3b).

The reduced insulation capability can be ascribed to a strong disturbance of the snow cover, due to vegetation (e.g. Woo & Marsh, 2005) and due to snow funnels (Bernhard et al., 1998; Gruber & Hoelzle, 2008) that allow for a constant convective heat exchange between atmosphere and talus slope. Furthermore, Morard (2011) showed that a convective heat exchange through an undisturbed snow cover is possible, as a consequence of the pressure gradient between atmosphere and the interior of the talus slope. Phillips et al. (2009) showed that metamorphism of the snow cover leads to an increased interstitial pore space, allowing for ventilation through the snow cover. The comparison of temperatures in 5 cm depth at Val Susauna indicates that the

insulation capability of the snow cover is higher in the forest than in the *Hexenwäldli*, which is reflected in the gradient between air- and humus temperatures as well as in the number of freezing degree days (cf. TABLE 8.6).

The comparison of air- and humus temperatures with snow thickness revealed distinct differences between the three study sites. While at the Val Bever the comparably cold and snow-rich winter of 2009/10 could be associated with warmer humus temperatures than in winter of 2010/11 (warm, minor snow thickness), the conditions at the Val Susauna and Brüeltobel were vice-versa; humus temperatures in 2009/10 were colder than in 2010/11 (cf. FIGURE 8.8, TABLE 8.5 & TABLE 8.6). Causative, this must be ascribe either to differences in the effectiveness of the insulation capability of the snow cover or to the thermal ventilation, while a definitive interpretation is hard to accomplish.

Even though it has been shown that in winter the influence of atmospheric temperatures on the ground thermal regime exceed snow-cover effects, results emphasise a conditional importance of the snow cover. Ground surface temperatures from the Val Bever, measured at the base of tree trunks and in a certain distance, expose distinct differences. Thereby, the snow thickness in close distance to tall trees has been distinctly lower than in the surroundings (for a summary of the research on the influence of vegetation on snow accumulation and snowmelt processes see WOO & MARSH (2005)). Freezing n-factors at the stem base (cf. TABLE 8.5) were distinctly higher compared to values in the surroundings, indicating a stronger coupling to atmospheric temperatures under thin snow cover. However, n_F-values recorded at Val Bever were in the same order of magnitude as values from borehole locations in two glacier forefields in the upper Engadin presented by RÖDDER & KNEISEL (2012), where a high insulation capability of the snow cover and a significant influence on the ground thermal regime has been proven. This effect points to a strong spatial heterogeneity of the insulation capability of the snow cover. Even though a complete decoupling between ground-surface and air temperatures did not occur, it must be assumed that the snow cover strongly buffers variations in atmospheric temperatures.

Comparing air-, humus- and borehole temperatures with snow cover distribution at the Val Bever (FIGURE 8.8), areal limited effects of the snow cover and avalanche

deposits could be detected that determine a small-scale heterogeneity in the ground thermal regime.

A comparable penetration depth of the cold wave could be detected for winters 2008/09 and 2010/11 for the borehole at Val Bever (FIGURE 8.8). With an above-average snow thickness, winter temperatures were distinctly colder in 2008/09 compared to the warm winter of 2010/11 with little snow. Thereby, temperatures within the uppermost 2 m depth showed a higher variability and colder minimum temperatures in 2010/11. This underlines the buffer effect of a thick snow cover under generally reduced insulation capabilities and, in the reverse, the efficiency of cooling under low snow thicknesses.

A further interesting effect in winter borehole temperatures has been detected in 2009/10 (FIGURE 8.8). Here, an avalanche, with its main accumulation in the area of the borehole (cf. FIGURE 8.9) has locally disturbed the ground thermal regime. A distinctly reduced penetration depth of the cold wave and an interruption of the supercooling for almost one month could be detected in the borehole, while humus temperatures, recorded in a distance of approximately 120 m (cf. FIGURE 8.1), indicated a consistent and efficient cooling. On the one hand, this underlines the heterogeneity of the ground thermal regime, on the other hand, the significance of snow-characteristics are emphasised. The formation of snow-funnels, as a result of ventilation mechanisms, as well as convective and conductive heat exchange through the snow cover is strongly influenced by the snow cover evolution. PHILIPS et al. (2009) showed that ventilation-induced cooling events were correlated with snow depth below 50 cm and a strongly metamorphosed snowpack. They also emphasised local effects of wind, solar radiation and surface roughness on the characteristics of the snow cover as well as the importance of more impermeable layers such as wind/rain crusts on convection. Furthermore, they point out that avalanche deposits at the base of talus slopes may hinder the ventilation process. Accordingly, the avalanche deposits of the Val Bever locally prevented convection and therefore lead to a local reduction of the supercooling. A cooling of the subsurface – with a comparably low magnitude and minor penetration depth – was initiated in high-winter 2010 and might either be ascribed to conductive heat transport through the avalanche deposits or to convective heat transport "from below" by the chimney effect.

This points out to a strong influence of the "vertical" component of heat exchange and supercooling, at least for the Val Bever site. For the Flüela Pass site, PHILIPS et al. (2009) showed that avalanche deposits at the foot of the slope, where lower vents were detected, hinder the ventilation effects. Avalanche deposits at the Val Bever were accumulated at an elevation of approximately 1800 m a.s.l., while the lower vents are located at around 1785 m a.s.l., meaning that the lower vents were not disturbed by the avalanche. Therefore, the supercooling must have been strongly affected by an area-wide vertical heat exchange between subsurface and atmosphere through the snow cover in all slope positions. A supercooling solely due to the chimney effect, initiated at single vents at the foot of the slope appears rather implausible, at least for the Val Bever. An alienation of results to the other study sites has to be handled with care; further borehole temperature data could provide considerable results.

Further effects of the snow cover on the ventilation mechanism of the chimney effect were detected at the Val Bever and Brüeltobel. Temperatures in the lower vent of the Brüeltobel (FIGURE 8.12) showed a high temporal variability and a strong coupling to atmospheric temperature variations in early winter, when the snow cover was thin, but a strongly buffered course of temperatures in high- and late-winter. This effect could be ascribed to the location of the lower vent in the ditch of the hiking path through the Brüeltobel. During winter, the snow has been artificially accumulated (snow-clearing) and compacted in the ditch of the hiking path as a consequence of snow-clearing, plugging the lower vents and preventing an efficient heat exchange by convection. As a supercooling could be observed by ERTM (cf. CHAPTER 7.3.2.3), it must be concluded that – confirm to results from the Val Bever – the vertical heat exchange through the snow cover in areas with permafrost in the subsurface is of major importance for the supercooling of the slope.

A comparable effect has been observed in Winter 2010/11 in the instrumented lower vent of the Val Bever (cf. FIGURE 8.14). A strong buffering of vent temperatures could be observed, beginning in early winter, while temperature curves of the previous winter indicated a strong coupling between air- and vent temperatures. Here, the effect could be ascribed to the comparably warm air temperatures in connection with an early snowfall (FIGURE 8.8). As presented by WAKONIGG (1996), and affirmed in this study, the high temperature variability provokes regular reversions of the ventilation direction

between day and night in autumn and early winter. According to the period of snowmelt, a thawing of the snow cover and an ensuing refreezing of the melt water could be observed in autumn. The magnitude of ice growth is assumed to be distinctly lower compared to the period of snowmelt in spring (WAKONIGG, 1996). However, it can be assumed that the warm autumn temperatures provoked regular snowmelt and a refreezing of the melt water especially in the vents, where temperatures are generally lowest. The emerging icicle-curtains could result in a partial plugging of the ventilation system, a reduction of the convective heat flow through the vents and, consequently, to a reduced supercooling of the talus slope. However, as the data basis is rather low and the distinct spatial heterogeneity of the ground thermal regime has been emphasised, it might be possible that the discussed effects are only locally developed.

Returning to BTS-measurements, it has to be pointed out, that the interpretation of datasets must be treated with caution. For realizing reliable BTS-measurements, a snow-thickness of at least 60-80 cm must be exceeded, to provide a sufficient insulation capability and a decoupling of ground-surface and atmospheric temperatures in high-winter (HAEBERLI, 1973; HOELZLE et al., 1993; KELLER, 1994; KELLER & TAMÁS, 2003; LUETSCHG et al., 2003). It has been shown that, independent from thickness, the insulation capability of the snow cover is constricted, due to ventilation processes (snow funnels) and disturbances by vegetation. Nonetheless, BTS-data from all three study sites are in good agreement with the results from geophysical permafrost mapping (CHAPTER 6) and a pronounced differentiation between supercooled areas and areas with comparably warm BTS. It might be reasonably assumed that BTS are not controlled by the heat flow between subsurface and base of the snow cover, but rather denote areas that are affected by local disturbances of the snow cover, resulting in a supercooling due to a rapid heat exchange with the atmosphere. Accordingly, it has to be assumed that – in supercooled talus slopes – cold BTS are not necessarily representative for the probability of permafrost, but rather for slope areas where an efficient supercooling might enable the formation of permafrost, or at least perennial ground ice. If the ground ice outlasts depends on the magnitude of supercooling in winter and the magnitude of degradation during summer.

The influence of the organic surface layer on the ground thermal regime is firstly characterised by its seasonally variable thermal conductivity, in dependence of moisture

and temperature (WILLIAMS & SMITH, 1991). Here, an enhanced cooling of the subsurface is favoured during the cold season, as a consequence of a high thermal conductivity of the moist or frozen organic material. During the summer season, moisture contents in the organic material are usually reduced, as an effect of evapotranspiration, providing an effective insulation of the subsurface from warm air temperatures (WILLIAMS & SMITH, 1991). Vegetation characteristics and composition are in turn influenced by cold ground temperatures, which influence root growth (ALVAREZ-URIA & KÖRNER, 2007) and lead to reduced decomposition rates and an accumulation of organic material.

A detailed mapping of humus characteristics and vegetation composition has only been conducted in the Val Susauna (FIGURE 8.5). As described in CHAPTER 3, surface and vegetation characteristics distinctly diverged between the three study sites. A consistent and thick organic surface layer and a distinct dwarf growth could be observed in the *Hexenwäldlis* of Val Susauna and Brüeltobel. The humus layer in the Val Bever was strongly fragmented due to the bouldery granitic material; the tree stock, dominated by larch and pine trees, did not show dwarfing, but – especially in areas influenced by permafrost – a distinctly reduced crown density compared to remaining slope sections (cf. FIGURE 3.3a & b). Differences in the adaption of tree species can be derived to their divergent requirements regarding ecological and hydrothermal soil conditions (NIKOLAEV, 2003). For a site in Yakutia, NIKOLAEV (2003) showed that, due to a minor rooting depth (~50 cm), larch trees (dominant at Val Bever) are more tolerant to cryogen processes than spruce (Val Susauna and Brüeltobel) and pine trees (Val Susauna and Val Bever), which show reduced growth rates under cold ground temperatures (see also ALVAREZ-URIA & KÖRNER (2007), KÖRNER & PAULSEN (2004)).

The mapping approach conducted at the Val Susauna (FIGURE 8.5 & FIGURE 8.6) revealed a clear connection between humus characteristics, vegetation composition and permafrost distribution as revealed by geophysical investigations (CHAPTER 6.2.2).

Results showed that humus temperature and moisture were almost constant below a depth of 20 cm (FIGURE 8.6). Thereby, coldest temperatures were measured in the area of the *Hexenwäldli* (2-5 °C), where permafrost has been detected in the subsurface and where the organic surface layer was thickest. With up to 10 °C, humus temperatures in the neighbouring forest (below 20 cm depth) were distinctly higher. The humus moisture

showed a more pronounced spatial heterogeneity compared to humus temperatures, but generally higher moisture contents in the area of the *Hexenwäldli*, and highest moisture values in areas where high amounts of lichens were detected (FIGURE 8.5). Within the uppermost 15 cm, moisture contents were comparably homogeneous, with slightly higher values in the forest compared to the *Hexenwäldli*. Likewise, a divergent humus temperature pattern was detected in the uppermost 15 cm, with warmest temperatures in the lower parts of the *Hexenwäldli* and in the forest (10-17 °C). Unfortunately, humus moisture could not be monitored in this study. However, the income of solar radiation in the lower parts of the *Hexenwäldli* is – despite of the northern exposure of the slope – comparably high in high summer. Consequently, the evaporation rates within the uppermost centimetres of the organic layer can be very high on sunny days, causing presumably high moisture variability in the course of the day. Moisture conditions in the dense forest can be assumed to be rather constant, with little temporal variability. A parallel monitoring of humus temperatures and humus moisture would be especially interesting to quantify the influence of latent heat effects during summer. Even though WAKONIGG (1996) presumed that latent heat effects are of minor importance for the cooling of block fields under humid climates (see also HARRIS & PEDERSEN (1998)), it must be assumed that evaporation and sublimation strongly affect the insulation capability of the organic layer. Especially with regard on the fact that the areas with permafrost are often located in the sunniest parts of the talus slopes (see also DELALOYE & LAMBIEL (2003)). Data from Northern Alaska show that 30-60% of the net solar energy in summer is expended on evapotranspiration at the surface boundary (KANE et al., 1990; KANE et al., 2001). Thereby, differences in the importance of evapotranspiration must be expected between the *Hexenwäldlis* of Val Susauna and Brüeltobel and the more dense forest at the Val Bever, where shading effects reduce the income of solar radiation at the surface.

As the time slot for conducting the mapping approach was rather short, due to a predicted change in weather, measurements had to be restricted to recording humus temperature and moisture. A broad analysis of the humus characteristics could have allowed for further conclusions.

Strongest connection has been detected at the Val Susauna between permafrost distribution and tree height. Likewise, humus thickness and proportion of mosses in the

undergrowth was highest in the area with permafrost in the subsurface. This can be directly ascribed to cold temperatures in the root zone and in the organic layer. Thereby, cold ground temperatures affect decomposition rates and lead to an increased accumulation of organic material. ALVAREZ-URIA & KÖRNER (2007) show that even under favourable air temperatures a reduced plant growth can be determined by cold soil temperatures, and give a value of ~6 °C as the critical temperature for significant root growth. KÖRNER & PAULSEN (2004) give a seasonal mean ground temperature of 6.7 °C (±0.8 SD and 2.2 K amplitude for different climatic zones) for high altitude climatic treelines. Humus temperatures in the *Hexenwäldli* were area-wide below the boundary value given by ALVAREZ-URIA & KÖRNER (2007) (between 2-4 °C below 20 cm depth) by the date of measurement in late August and above the boundary value in the neighbouring forest (up to 10 °C below 20 cm depth). Regarding the long-term results from temperature logger data (FIGURE 8.11 & TABLE 8.7), the duration of the growing season (period with ground temperatures above 3.2 °C (KÖRNER & PAULSEN, 2004)) differs strongly between the *Hexenwäldli* and the forest. Furthermore, differences in the duration of the growing season between 15 and 30 cm depth are peculiar in the *Hexenwäldli*, but minor in the forest. However, the seasonal temperature mean in the forest is – even though distinctly warmer than in the *Hexenwäldli* – slightly below 6 °C (TABLE 8.7). Thereby, the growing season in the forest of the Val Susauna shows comparable thermal characteristics to the Brüeltobel, where a distinct dwarf growth is observable. For the Brüeltobel *Hexenwäldli*, SCHUDEL (2002) showed an increased growth of the dwarfed and normally grown spruce trees during recent years, conform to climatic warming using dendroecology. Here, dendroecological investigations at the Val Susauna would be of interest, to compare growth characteristics between Brüeltobel and Val Susauna, especially with view on the climatic evolution and the differences between forest and *Hexenwäldli*. However, as the period of measurements in the forest of the Val Susauna covers solely one year, further interpretation on the growing parameters will be avoided, as this would exceed the scope of this study.

The analysis of humus temperature data revealed distinct divergences between the three study sites. Thereby, humus characteristics differ with regard on insulation capability, duration of the zero-curtains and, as already discussed above, with regard on the duration of the growing seasons.

Humus temperature patterns at the Val Bever diverged strongly from data measured at Val Susauna and Brüeltobel, indicating divergences in the insulation capability of the organic surface layer (cf. FIGURE 8.7, see also FIGURE 8.8). At Val Susauna and Brüeltobel, a distinctly smaller variance as well as lower maximum temperatures below 15 cm depth compared to the 5 cm depth-level indicated a high insulation capability of the organic layer and a decoupling from short-term variations in atmospheric temperatures below a depth of 10-15 cm. Temperature differences with depth were by far less developed within the humus layer at Val Bever, indicated by almost similar IQRs for the three depth levels.

Differences between the study sites can be ascribed to mainly two factors. On the one hand, characteristics of the organic layer are assumed to play a major role. The consistent and thick humus layer at Val Susauna and Brüeltobel opposes an organic surface layer at the Val Bever, which is strongly fragmented by granitic boulders. This is assumed to strongly affect the heat exchange processes. However, providing a consistent humus layer, heat exchange with the atmosphere is assumed to be mainly influenced by conductive (WILLIAMS & SMITH, 1991) and convective (KANE et al., 2001) processes with a vertical gradient. A fragmentation of the organic layer and the presence of voids at the interfaces between organic layer and boulders strongly affect the heat exchange processes, especially with view on convection, but also with regard to percolating rain- and melt water.

On the other hand, the temporal variability of humus moisture and the associated effects on thermal conductivity affect the ground thermal regime. The comparably high income of solar radiation in the *Hexenwäldlis* of Val Susauna and Brüeltobel evoke high evapotranspiration rates (KANE et al., 1990; KANE et al., 2001). Consequently, the insulation capability of the uppermost layers of the organic material is highest, on sunny and warm days and lowest on cool and humid days. The dense forest at the Val Bever reduces the income of solar radiation at the ground surface and therefore reduces evaporation rates on warm days. The thermal conductivity during summer is more constant, as fluctuations in humus moisture are reduced. Consequently, the heat exchange between atmosphere and deep humus layers is temporally delayed, but in general more effective compared to the Val Susauna and Brüeltobel.

A further difference in thermal characteristics of the organic layer could be observed in the Val Susauna, between *Hexenwäldli* and forest site (cf. FIGURE 8.7). At both logger positions a buffering of temperatures with depth (variance, IQR, mean, median and maximum values) has been detected. However, the magnitude of difference is distinctly higher in the *Hexenwäldli*. An interesting effect could be observed comparing minimum temperatures. In the *Hexenwäldli* – and likewise at the permafrost sites in Val Bever and Val Susauna – differences in minimum temperatures with depth are rather small; the small variance reflects the long zero-curtain period (see also TABLE 8.7). In the forest, a strong gradient between minimum temperatures in 5 and 30 cm depth can be observed, with warmest minima at the humus base. This is assumed to be an effect of differences in the characteristics of the organic layer. The water storage capability of the peat-like organic material at the permafrost sites is distinctly higher compared to the forest site (cf. results from humus moisture mapping in FIGURE 8.6). Consequently, it must be assumed that the thermal conductivity during winter is distinctly higher in the *Hexenwäldli*. Air temperatures as a driving factor can be precluded, as differences between *Hexenwäldli* and forest during winter were rather low (FIGURE 8.7 &, TABLE 8.6).

Correlations between air-and humus temperatures must be interpreted with care. Correlations were calculated only for high-summer and high-winter, to avoid ambiguities caused by zero-curtain periods. However, as discussed above, the snow- and humus cover buffer and delay heat exchange processes. As a consequence, correlation and determination coefficients were in general comparably low.

Correlation coefficients in high-winter indicated no or solely slight relations between air- and humus temperatures, with negligible differences between the depth levels at all study sites (FIGURE 8.16, FIGURE 8.17 & FIGURE 8.18). In contrast, divergences of correlations were significant between the depth levels in high-summer. Thereby, air temperatures showed a good correlation with humus temperatures in 5 cm depth, but no correlation to humus temperatures in deeper layers. This underlines the high insulation capability of the humus cover as discussed above. However, it has been shown, that the insulation capability of the organic surface layer at the Val Bever is distinctly lower compared to the other two sites. The fact that no correlation could be detected between air- and humus temperatures (below 15 cm depth) at the Val Bever again points

to a strong buffering of heat exchange by the humus cover. Correlations were calculated using hourly measurements. A daily basis would have produced higher correlation coefficients, as time-delay effects would be slightly compensated, but could have also increased the likeliness of spurious correlations. Furthermore, to test the correlation between temperatures at the humus-base and within the vents, a higher temporal resolution was of interest.

It has been shown, that temperatures in the lower vents correlate with air temperatures in winter, but do not correlate in summer. The situation is reversed for the upper vent at the Brüeltobel (FIGURE 8.16) that shows a very low correlation to atmospheric temperatures during winter, and distinctly higher correlation coefficients in summer. Determination coefficients between the two vents at the Brüeltobel are comparably high in summer and winter, with negative r-values indicating an antipodal relationship. These correlation effects are clearly assignable to the reversible ventilation activity of the chimney effect. In winter the inflow of cold air at the lower vents, and the outflow of warmed air through upper vents determines a high correlation between atmospheric and lower vent temperatures, but no correlation to the upper vent. In summer the situation is reversed; air and vent temperatures correlate in the upper parts of the slopes, where warm air enters, is cooled on its way down and flows out through lower vents, where no correlation to atmospheric temperatures is detected (see also WAKONIGG (1996), HARRIS & PEDERSEN (1998)).

Even more interesting are the correlations between temperatures in the vents and at the base of the humus layer. Relationships between these parameters are observable in the temperature curves of FIGURE 8.12, FIGURE 8.13 & FIGURE 8.14, and were additionally quantified in FIGURE 8.16, FIGURE 8.17 & FIGURE 8.18. Thereby, once again, thermal characteristics diverge between the study sites. It has been shown that the influence of the chimney effect on the ground thermal regime is best illustrated for the Brüeltobel study site, where temperatures could be recorded in the upper and the lower vent (FIGURE 8.16). In high-winter, no correlations were detected between temperatures in the lower vent and in the humus cover; correlations between organic layer temperatures and the upper vent were negative, with low determination coefficients. In high summer, a very high correlation between temperatures in the organic layer (21 cm depth and at the humus base) and in the lower vent has been detected, while correlation

to the upper vent were negative again. In high summer, the same effect – with a minor magnitude – could be observed at the Val Susauna. In contrast to the Brüeltobel, high correlations were detected between vent- and humus temperatures in high winter. Thereby r and r^2 decreased with depth. At the Val Bever, significant correlations could not be detected, neither in summer nor in winter.

Two mechanisms are conceivable to explain the observed correlation effects. On the one hand, the detected correlations could indicate true relationships between vent- and humus temperatures. On the other hand, high determination and correlation coefficients could be spurious. Eventually, vent and humus temperatures are both controlled by air temperatures; an equal time-delay in the thermal conductivity affects the spurious correlations.

Here, a true relationship between vent- and humus temperatures (21 cm depth and humus base) can be expected. The fact that correlations at the humus base are higher than in 21cm depth can be regarded as a determining factor, indicating a heat flow from the interior of the talus slope towards the organic layer. Little differences between the depth levels in 36 and 21 cm underline the high thermal conductivity of the peat-like and moist organic material below ~15 cm depth. Likewise, a temporarily antipodal course of temperatures curves, with temperatures in 5 cm depth running parallel to air temperatures and, respectively, in 36 cm depth parallel to vent temperatures, underline divergent dependencies (cf. Chapter 8.2.3.1; and FIGURE 8.12).

Determination and correlation coefficients at the Val Susauna between vent- and humus temperatures (15 and 30 cm depth) during high-summer are assumed to represent true relationships, even though r- and r^2 are rather small. This effect can be attributed to the long distances the air has to cover on its way through the talus slopes (WAKONIGG, 1996), resulting in temporal delays.

High correlations between vent- and humus temperatures at the Val Susauna (*Hexenwäldli* and forest) in high-winter must be regarded as spurious. As r and r^2 decrease with depth, it can be precluded that the heat flow from the subsurface controls humus temperatures. Here, it is more probable that both, vent and humus temperatures are controlled by atmospheric temperatures. A buffering of the heat flow by the snow cover and an associated temporal delay at a comparable order of magnitude determines

high correlation between vent- and humus temperatures, but low correlation to air temperatures.

Dependencies between temperatures in the lower vent and at the humus base in summer must thereby be regarded as "passive". Both are controlled by the temperature in the interior of the talus slope and therefor by the magnitude of cooling of the air in summer on its way from the upper vents through the slope. The fact that humus temperatures – constituting parts of the active layer – as well as vent temperatures show corresponding characteristics during summer point out, that the ventilation covers probably the whole talus slope, and likewise flows through the permafrost body. This emphasises the concept of the frozen ground body being a porous medium with various corresponding voids. This interpretation is in contrast to results by PHILLIPS et al. (2009), who investigated a ventilated talus slope above the timberline at the Flüela Pass (Swiss Alps). Their results indicate that the ventilation mechanism is restricted to a layer of coarse blocky material below the permafrost body, where large voids are present. Results from geophysical monitoring (CHAPTER 7) indicate that supercooling- as well as degradation processes comprise the whole permafrost bodies. The fact that the ventilation as well as percolation mechanisms are oriented along voids that run through the permafrost bodies state a plausible explanation for these effects. As ice-growth is assumed to occur during snowmelt due to a refreezing of percolating melt water on the supercooled talus (WAKONIGG, 1996), the ground ice might be envisioned as coatings around the talus material. This could be observed in spring at the Val Susauna, in the small slope area with uncovered talus at the foot of the slope (cf. FIGURE 8.19, for location see also FIGURE 3.5).

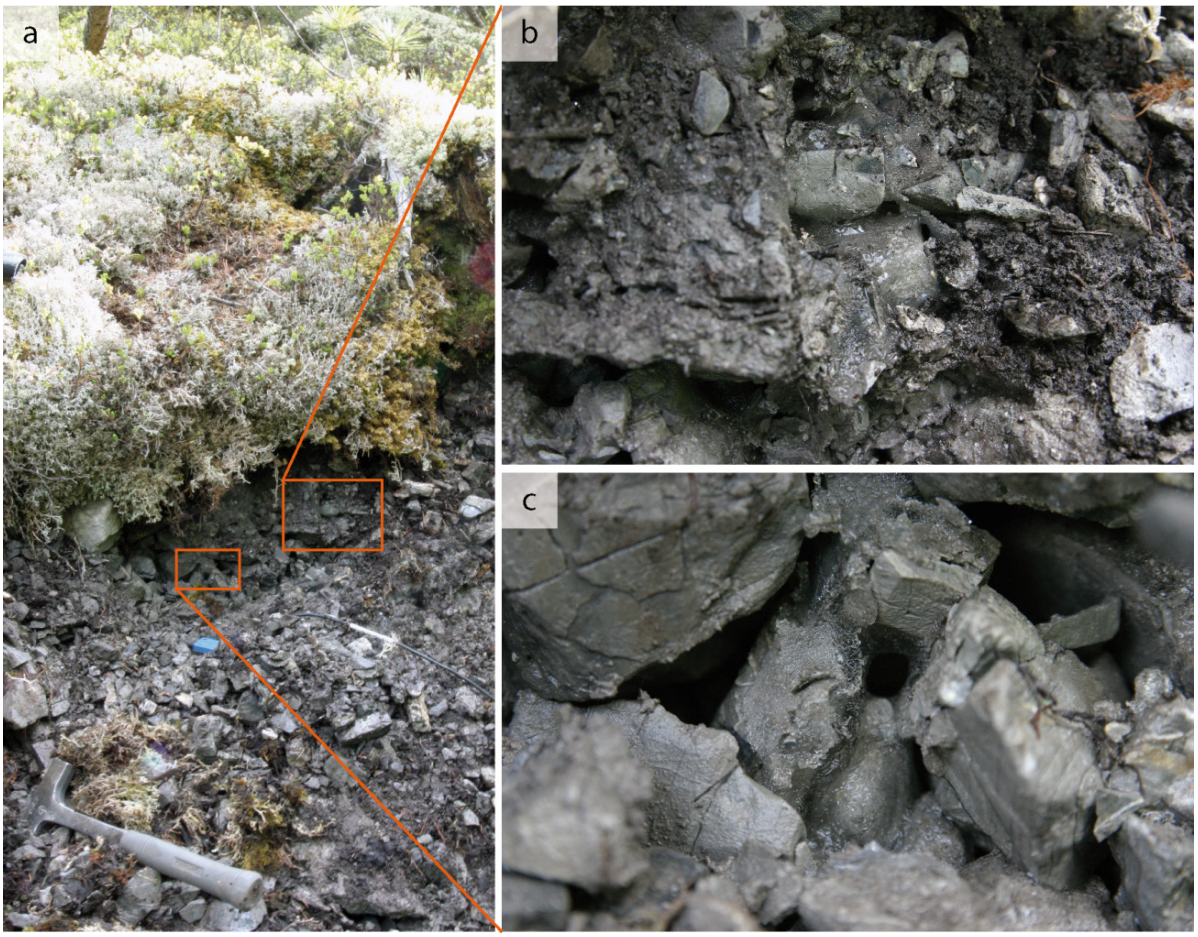

Figure 8.19: Photographs of ice-coatings around the dolomitic talus at the Val Susauna. (a) upper parts of the slope area with uncovered talus; squares indicate the location of macro shots. (b) Ice-coatings and frozen fine grained and organic material. (c) Ice coatings and various voids.

8.4 Conclusions

Aiming at analysing the ground thermal regime in ventilated talus slopes below the timberline, various approaches were combined, including BTS-measurements, mapping of the organic surface layer and the vegetation composition as well as temperature data logging. Results indicate strong differences in the ground thermal regime between the three study sites and especially to classical permafrost sites above the timberline.

The following central conclusions can be drawn:

- The fact that convective heat transport of the chimney effect, driven by the temperature/density gradient between air inside and outside the talus slope is of major importance for the ground thermal regime of supercooled talus slopes below the timberline has been confirmed in this study.
- In summer, the outflow of cold air is strongly focused on the lower vents; the consistent humus cover is constantly cooled from below and prevents – due to its high insulation capability – an area-wide air exchange.
- In winter, the cooling comprises large areas at the foot of the slope, where disturbances of the snow cover due to snow funnels and dwarfed trees allow for an efficient – mostly convective – heat exchange with a vertical gradient between atmosphere and subsurface.
- Data indicate that the whole permafrost bodies might be characterised as a porous medium, allowing for a rapid heat exchange with the air flowing through voids within the permafrost.
- The insulation capability of the snow cover is generally reduced, due to disturbances by snow funnels and vegetation; likewise, the influence of the snow cover on the ground thermal regime is of minor importance, compared to permafrost sites above the timberline. However, even though a decoupling between air and ground-surface temperatures is not achieved, a buffering of short-term atmospheric temperature variations has been detected; the efficiency of supercooling is higher under thin snow. At least for the Val Susauna a higher insulation capability of the snow cover has been detected in the permafrost-free forest than in the *Hexenwäldli*.

- The relation between snow thickness and ground surface temperatures is partly inverted, which is mostly due to the vegetation composition and the presence of dwarf-grown trees. Coldest temperatures can be detected where snow cover is thickest.
- Snow cover effects such as artificial/natural accumulation and/or compaction as well as avalanche deposits can hinder the convective heat exchange and locally affect a reduced supercooling.
- Warm air temperatures in autumn might lead to temporal snowmelt and refreezing of melt water. The associated formation of icicle curtains in lower vents can likewise hinder the convection.
- Even though a decoupling between atmosphere and ground surface, independent from snow thickness, is not achievable, supercooled slope areas are well detected by BTS-measurements. Thereby, cold BTS do not necessarily depict the probability of the permafrost presence, but rather indicate where an efficient supercooling might enable for a significant and potentially perennial ice formation during snowmelt.
- The organic surface layer does not solely affect the ground thermal regime in summer, due to high insulation capabilities, but also enables an increased supercooling in winter due its high water storage capacity and the corresponding high thermal conductivity under frozen conditions.
- The insulation capability strongly diverges between study sites as a function of the distribution of the organic surface layer and vegetation composition. Thereby, the nature of the talus material is of major importance. Finer-grained talus (dolomitic or limestone) enables for the development of a consistent and thick humus layer; organic layers at sites with bouldery talus is strongly fragmented.
- At sites with a consistent and thick humus layer and dwarf-grown trees,
    - the insulation capability enables almost constant humus temperatures and moisture below 10-15 cm depth. Variations in atmospheric temperatures are buffered within the uppermost 5-10 cm;
    - the income of solar radiation is often highest, where subsurface temperatures are coolest. Here, high amounts of incoming solar energy are expended on

evapotranspiration. Rapid drying of the organic material increases the insulation capability;

  - a constant cooling from below by convective heat transport of the thermal ventilation furthermore enables cold and consistent temperatures at the humus base.

- At sites with a fragmented organic surface layer and a dense forest,
  - the insulation capability of the humus/moss cover in summer is strongly reduced, with a minor vertical temperature differentiation;
  - shading effects of the dense forest lead to more constant moisture conditions and therefore higher thermal conductivity in summer;
  - voids and interfaces between organic material and bouldery talus enable a more efficient heat transport by convection and percolation of rain-/melt water.
- At all sites, the organic material determines a stronger buffering of warm than of cold temperatures, supporting an efficient supercooling.

PART III - SYNTHESIS

9 Synthesis

The superordinate aim of this thesis was the determination of the temporal variability and spatial heterogeneity of permafrost in talus slopes in relation to the site-specific ground thermal regime. A broad methodological approach has been applied to cope with the central aims of the thesis and allowed to expand the knowledge of the mechanisms that permit the persistence of frozen ground in talus slopes below the timberline. The results of investigations have been discussed in detail and central conclusions have been drawn in the corresponding chapters in Part II of this thesis.

In this chapter, results will be brought together, to conceptualize a model of the ground thermal regime, differences between the study sites and the influence on frozen ground distribution. Furthermore, an approach will be presented to map the permafrost distribution based on the temperature at the interface between talus and organic surface layer, followed by a discussion of potential future evolution of permafrost in vegetated talus slopes in the course of climatic change.

At first, with regard to the central objectives presented in CHAPTER 1.2, the main findings of this thesis will be summarized.

- Frozen ground has been detected at all three study sites based on the joint application of electrical resistivity and seismic refraction tomography. The existence of permafrost has been proven at all three sites by ERTM and, at Val Bever by borehole temperature data. The spatial permafrost distribution could be estimated at Val Bever and Val Susauna study sites using quasi-3D resistivity imaging and geophysical mapping.
- The temporal permafrost variability, assessed by electrical resistivity monitoring, has proven to be extremely high at all study sites. Thereby, the seasonal variability, with supercooling in winter, growth in volumetric ice content during snowmelt and frozen ground degradation during summer distinctly exceeds the long-term variability.
- Conductive heat exchange of the chimney effect has confirmed to be of major importance on the temporal variability and spatial distribution of permafrost. Thereby, it became apparent that the distribution of the organic layer and characteristics of the talus substrate modifies the mechanism of the thermal

circulation and determines divergences between the study sites (see discussion in CHAPTER 9.1.1).

- The assumption that surface properties and especially the characteristics of the organic surface layer modify the ground thermal regime in a more complex way than assumed for ventilated talus slopes has proven true. Besides insulating the subsurface during summer, increased thermal conductivity of the frozen organic layer in winter allows an efficient conductive cooling of the subsurface (see discussion in CHAPTER 9.1.1).
- Spatial permafrost distribution has proven to be closely linked to surface properties, in specific, humus thickness, -temperature and -moisture as well as vegetation distribution, in specific, percentage of mosses and tree height.
- Independent from thickness, the snow cover has proven to be incapable of prohibiting an efficient supercooling of the talus slope in winter. However, the snow-cover buffers rapid variations in atmospheric temperatures; accumulations of dense snow, e.g. due to avalanches, are capable of locally modifying the ground thermal regime and limiting a supercooling. Insulation capability of the snow cover at Val Susauna has proven to be higher in the permafrost-free forest than in the *Hexenwäldli* with permafrost in the subsurface, even under minor snow thickness.

With regard to objectives aiming at the methodological approaches the following findings can be summarised.

- The development of a robust, low-cost electrical resistivity monitoring system could be achieved and installed at all three study sites. Year-round monitoring measurements allowed for a sophisticated analysis of the seasonal permafrost variability. Thereby, especially the consideration of temperature data recorded in the near-surface, allowed a broad analysis of data.
- The so-far first seismic refraction tomography monitoring for recording the evolution of permafrost during the winter half-year could be accomplished at the Val Susauna. Thereby, the information of the evolution of acoustic- in combination with electrical properties of the subsurface has proven to substantially increase the information value of monitoring the permafrost evolution.

- Based on a broad synthetic data modelling approach, suggestions could be proposed to increase the efficiency of quasi-3D resistivity imaging at the difficult terrain of mountain permafrost sites. Furthermore, quasi-3D measurements were conducted at the Val Bever and Val Susauna study sites and allowed an estimation of the spatial permafrost distribution and a comparison of permafrost distribution with surface properties.

9.1 Permafrost evolution, distribution and the ground thermal regime

Within recent years the understanding of processes in supercooled talus slopes has been increasingly improved (e.g. DELALOYE & LAMBIEL, 2005; DELALOYE & LAMBIEL, 2007; DELALOYE et al., 2003; KNEISEL & SCHWINDT, 2008; LAMBIEL & PIERACCI, 2008; MORARD, 2011; PHILLIPS et al., 2009; RASKA et al., 2011; ROSSEL et al., 2004; SAWADA, 2008; SAWADA et al., 2003; ZACHARDA et al., 2007), but some questions remain unanswered. The main issues of the thermal ventilation, the ground thermal regime and recent scientific findings have been summarised in CHAPTER 1.1.1. The results of this study are in agreement with general concepts of the supercooling in ventilated talus slopes, but also revealed some important amendments for a further improvement of the process understanding. Especially the comparison of three substantially divergent study sites allowed more sophisticated statements on the ground thermal regime and its influence on the seasonal evolution and the spatial distribution of permafrost in vegetated talus slopes below the timberline. Thereby it could be shown that the mechanism of the chimney effect slightly differs between the bouldery talus slope of the Val Bever and the pebbly slopes of the Val Susauna and Brüeltobel. Likewise, the influence of the surface distribution causes substantial divergences with the Val Susauna and the Brüeltobel on the one hand and the Val Bever on the other hand.

9.1.1 Divergences in the seasonal mechanism of the ground thermal regime between the three study sites

The mechanism of the chimney effect is illustrated in FIGURE 9.1, presenting the summer- and winter circulation for the talus slopes of the Val Bever and Brüeltobel. The mechanism of ventilation of the Brüeltobel is assumed to be assimilable to the Val Susauna site. An approach to summarize and illustrate the small-scale influence of substrate and distribution of the organic surface layer on the ground thermal regime and the associated permafrost and active-layer evolution is presented in FIGURE 9.2, comparing the Val Bever on the one hand with Val Susauna and Brüeltobel on the other hand.

It has been shown that a fundamental difference in the ground thermal regime between the three study sites is based on the distribution of the organic surface layer

and the vegetation composition in the lower parts of the talus slopes. Thereby, a consistent and thick moss-covered humus layer at Val Susauna and Brüeltobel opposes an organic layer at the Val Bever, which is strongly fragmented and pervaded with voids due to large granitic boulders. This determines differences in the convective heat exchange, and affects the percolation of melt water.

Driven by the density gradient between relatively high atmospheric temperatures and low temperatures in the interior of the talus slopes in summer, the ventilation is characterised by an outflow of cold air at the foot of the slope (FIGURE 9.1). This necessarily causes an aspiration of relatively warm air at the top of the talus slopes, which is cooled on its way down through the slope. This affects a warming of the interior of the slopes and, as a consequence, a degradation of frozen ground. The outflow of cold air at Brüeltobel and Val Susauna is focused on sporadic vents, located in the lowest parts of the slopes. The fragmented organic layer at the Val Bever allows a spacious outflow of cold air through numerous voids. However, the spatial heterogeneity of surface characteristics is rather high at the Val Bever, indicating very complex mechanisms of the ventilation system, which requires for an areal analysis of vent-temperature evolution.

Furthermore, it must be assumed that the railroad embankment (cf. FIGURE 3.2) prohibits an efficient convective airflow, and causes pools of cold air. Consequently, the temperature gradient between air inside- and outside the slope is decreased, affecting the velocity of the ventilation.

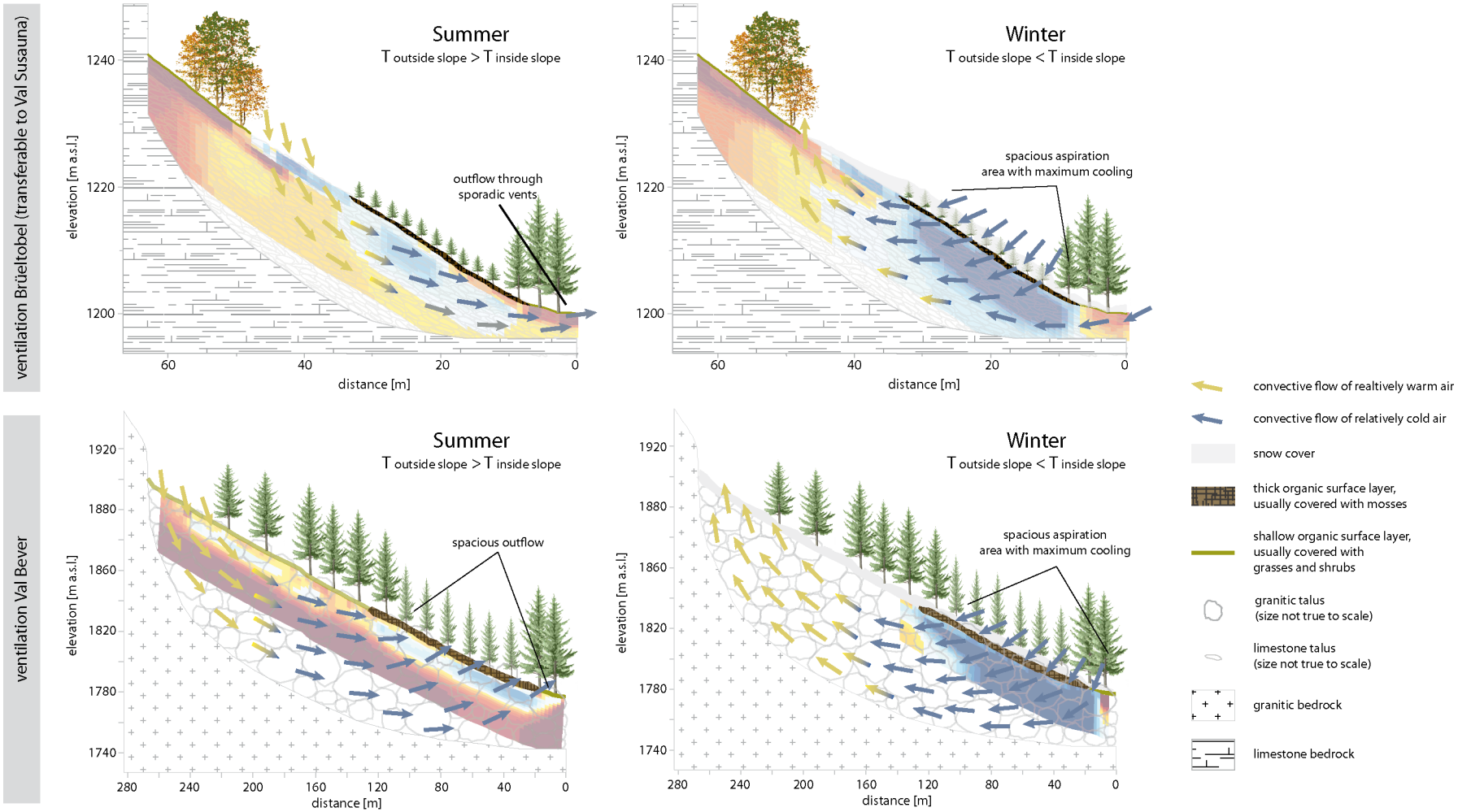

Figure 9.1: Illustration of the mechanism of the chimney effect in summer and winter, exemplarily for the study sites Brüeltobel and Val Bever.

On a small scale, divergences between the sites in summer become more obvious (cf. FIGURE 9.2). The insulation capability of the organic layer in the *Hexenwäldlis* of the Brüeltobel and Val Susauna has proven to be very high, with almost isothermal conditions below 15 cm depth, which can be ascribed to two central factors. (I) the insulation capability is highest, when outside temperatures are highest. This proceeds in conformity with a rapid drying of the organic material; evaporation expends high amounts of the incoming solar energy (KANE et al., 2001). (II) below 15 cm depth the humus is consistently moist, determining a high thermal conductivity. The flow of cold air in the interior of the slope constantly cools the moist organic material from below, determining stable temperature conditions. Insulation capability of the organic layer at Val Bever is distinctly lower. This can be ascribed to more consistent moisture conditions (low income of solar radiation in the forest and low evaporation rates), to a distinct fragmentation and a large number of voids of the humus layer. Here, the amount of heat transport into the subsurface by convective heat flow and percolating water is assumed to be distinctly higher than at Val Susauna and Brüeltobel.

The drop of atmospheric temperatures in autumn affects the reversion of the chimney effect (FIGURE 9.1) and the onset of the zero-curtain in the organic surface layer (FIGURE 9.2). The winter circulation is characterised by the ascent of the relatively warm air in the interior of the slope. This causes an aspiration of cold air at the foot of the slope and an efficient supercooling of the talus material, with highest magnitudes of cooling in the lowest parts of the slope. Thereby, the influence of the snow cover on the supercooling is of minor importance.

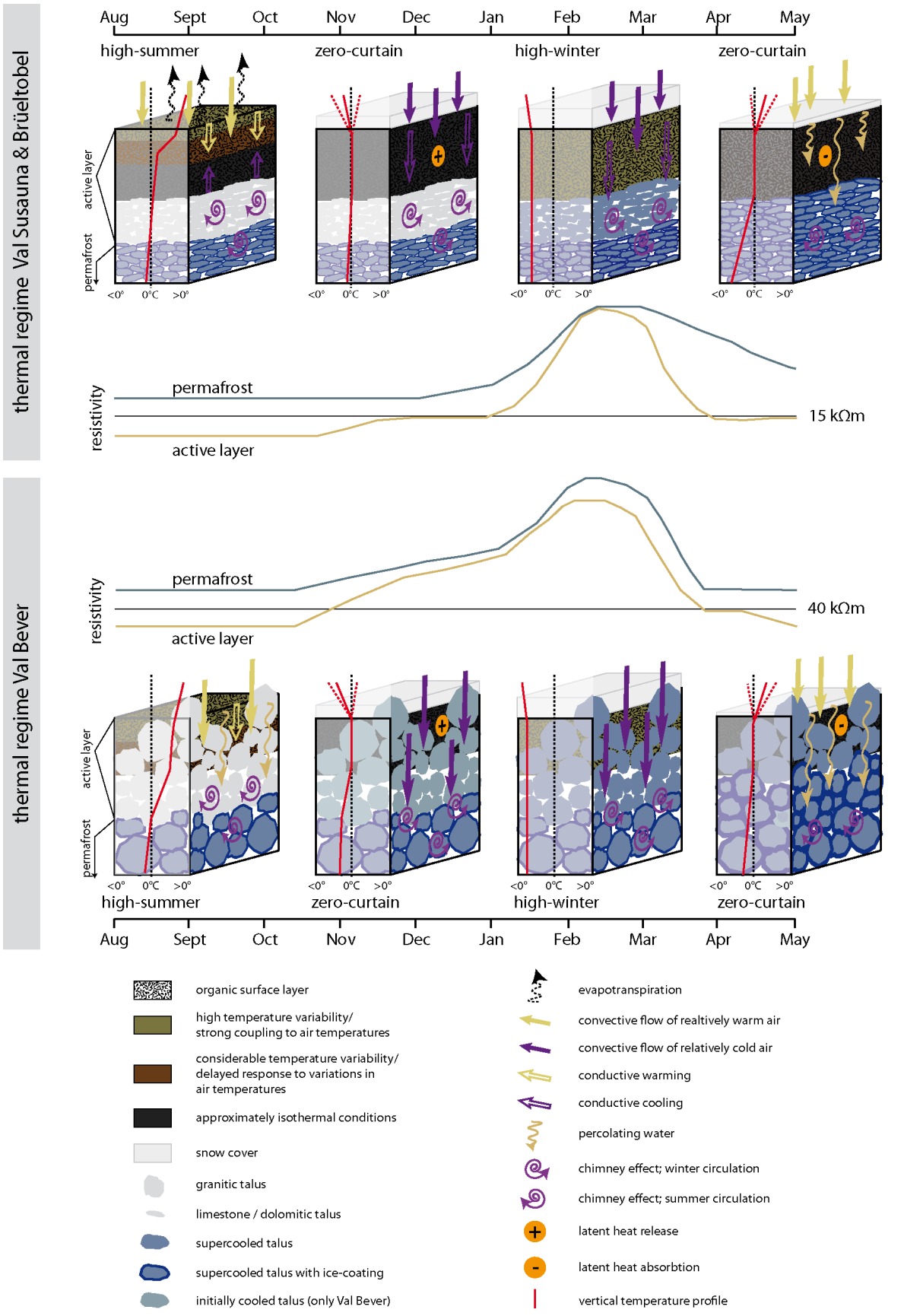

Figure 9.2: Conceptualised model of seasonal mechanisms of the ground thermal regime, its effect on the active-layer and frozen ground evolution and the resistivity distribution in the active layer and the permafrost body.

During the autumn zero-curtain and the high-winter period, differences in the mechanisms of cooling between the study sites could be highlighted (FIGURE 9.2). With the onset of the zero-curtain, resistivity values of the active layer increase at all study sites, as a response to decreased temperatures and partial freezing. Thereby, the fragmented organic layer at Val Bever enables a spacious convective cooling of the talus material in the active layer, which affects a more distinct increase of electrical resistivity values than at Val Susauna and Brüeltobel. At these sites, the heat transport into the subsurface through the organic layer is mostly conductive and therefore strongly buffered due to latent heat release during the cooling of the humus material. Likewise, the increase of resistivity values in the permafrost body of the Val Bever is initiated with the first reversions of the chimney effect in autumn, as a response to the convective cooling. Permafrost resistivities at Val Susauna and Brüeltobel increase not until the end of the zero-curtain period, when the efficiency of conductive heat flow through the organic material is strongly increased, due to high ice-contents. During winter, it is hard to distinguish between the cooling by convective and conductive heat flow. It is assured, that the snow cover does not prevent a convective heat flow. Below the snow cover, a convective air-exchange is most likely at Val Bever, through the numerous voids, but is ambiguous for Val Susauna and Brüeltobel, where the humus layer is massively frozen. However, the cooling occurs with a strong vertical component and is not solely driven by the inflow of cold air through lower vents.

Temperature increase in spring causes the onset of snowmelt, associated with the onset of the zero-curtains (FIGURE 9.2) and a reversion of the chimney effect to summer circulation (FIGURE 9.1). This affects a massive decrease of resistivity values in the active layer of all sites, as a result of the rapid increase of unfrozen water contents and the efficient heat transport by percolating melt water. As the percolation of melt water and therefore the heat transport is by far more efficient through the inconsistent organic layer at the Val Bever, the drop of resistivity values in the permafrost body occurs with a distinctly higher magnitude at the Val Bever than at Val Susauna and Brüeltobel. Thereby, decreasing resistivity values of the permafrost body can be ascribed to a growth in volumetric ice content, as the percolating melt water refreezes on the supercooled talus material. Ground ice is assumed to form coatings around the talus material as well as icicle curtains, where the refreezing is initiated by cold airflow, especially in the areas of lower vents. The absorption of latent heat during the process of freezing affects an

increase of ice temperatures and therefore an increased amount of unfrozen water content, which decreases the electrical resistivity. This modification of a zero-curtain in the permafrost body is assumed to be the reason for the rather low variability of resistivity values during summer. As illustrated in FIGURE 9.2, resistivity variability is marginal (cf. CHAPTER 7), while the comparison of seismic velocities (cf. CHAPTER 6) showed a strong decrease between early and late summer. The general warming of the interior of the talus slopes in summer is reflected in a slight but consistent increase of temperatures in the lower vents and at the base of the humus layer. The constant degradation of ground ice in summer results in a persistent absorption of latent heat. Therefore, relatively high amounts of unfrozen water can be expected within the permafrost bodies, which provoke a relatively high and constant electrical conductivity. The decrease in volumetric ice-content is of minor importance for the electrical resistivity, but strongly affects seismic velocities.

9.1.2 Thoughts on the initiation of supercooling

The temperature of the air flowing out of the lower vents in summer is a function of the temperature/density difference between air outside and inside the slope (especially at the foot of the slope), controlling the velocity of air flow and the magnitude of cooling. Furthermore, an important factor is the length of the slope, respectively the distance between upper and lower vent. As the interior of the whole slope is assumed to be colder than the outside air in the summer half-year, the air flowing through the slope is already cooled down to a point in its upper parts. This minimizes the temperature difference between supercooled talus and air in the lower parts of the slope, and, therefore, the magnitude of frozen ground degradation. An – in my view – still open question is why permafrost persists only sporadically in some slope positions. The factors that enable for a supercooling and a persistence of frozen ground have been discussed; also to a point, why permafrost does not exist in the surroundings. As the chimney effect is generally active in all talus slopes, providing permeable talus, the vegetation and humus composition is assumed to play a crucial role. Meaning, that a supercooling might occur in almost all slope positions, but the degradation is minimized only in locations, where insulating organic layers are present. Consequently, explanations for the recent and sporadic permafrost distribution – or at least perennial frozen ground – are plausible.

However, it remains an open question what initiates the whole process, and why the vegetation and organic material develops completely divergent. So, what came first – supercooled subsurface or insulating organic layers? The assumption that cold ground conditions determine a reduced growth and an accumulation of organic material is most obvious. Consequently, the thermal subsurface conditions must have been primarily present. This again indicates that differences in the ground thermal characteristics must have been present along the slope that determined divergent growth-conditions.

Two factors are thinkable for the divergent evolution and the solely sporadic presence of permafrost. The fundamental precondition for the activity of the chimney effect is the presence of a temperature/density gradient between the air outside and in the interior of the slope. One scenario could be that a density gradient in summer was only possible with the general climatic warming after the little ice-age. Small-scale differences in the vegetation patterns, that influence the efficiency of the chimney effect, might be predetermined by the alpine morphodynamic (e.g. avalanches), or even might be anthropogenically caused (e.g. forest clearance). The second plausible scenario would be that differences in the vegetation composition are due to small-scale differences in the efficiency of the chimney effect. As discussed, the most important factor for the initiation of the chimney effect is the presence of a gradient of air density. Thereby, the density gradient between air and talus material must first of all be present in the lower parts of the slope. Here, a positive factor is that the solar radiation at the foot of the slope is generally rather high. Thereby, the lateral differences along the slope appear to be negligible during high-summer and winter, meaning that the assumption that differences in the efficiency of the chimney effect are controlled by the incoming solar radiation at the foot of the slope is rather implausible. The picture is different with regard on temperature differences in the area of the upper vents, at the top of the talus slopes, below the rock walls. Assuming that steep rock-walls determine local shading effects, the energy balance in summer could be locally negative in sporadic slope areas. Consequently, the air aspirated into the slope through the upper vents in summer is slightly colder and probably slightly less moist, where the rock-wall determines shading compared to neighbouring areas. This might strongly influence the magnitude of heat exchange between the air flowing down through the slope and the talus material, meaning that less energy flows from the relatively warm air to the talus material. This could results in a locally reduced degradation of the frozen ground in the subsurface

below shading rock-walls compared to neighbouring areas and a local negative heat balance. This effect might be self-energising when the negative heat balance at the foot of the slope provokes an increased accumulation of organic material, determining an increased temperature gradient at the foot of the slope. Subsequently, as shown in CHAPTER 9.1.1, the organic layer and vegetation composition enables for a more efficient supercooling in winter.

However, this theory still has to be affirmed. Two approaches could provide promising results. Ground surface temperatures should be recorded below the rock wall, in areas upslope from permafrost occurrences as well as in the surroundings, where no permafrost is detected below, to provide information on temperature differences. An extensive modelling of the incoming solar radiation, based on digital elevation models, to analyse if significant differences in the energy balance are detectable, should support these results. The combination of these approaches could deliver valuable information on the distribution of permafrost in talus slopes below the timberline. Furthermore, if the permafrost distribution could be ascribed to local shading effects, these results could be implemented into statistical models to predict the permafrost distribution.

9.2 The bottom temperature of the high-summer humus cover for determining the areal permafrost distribution?

It has been shown that – providing a consistent humus cover – a correlation between temperatures in deeper layers of the humus layer and the lower vents exists in high summer (cf. CHAPTER 8.2.3). WAKONIGG (1996) discussed that air flowing out through lower vents in summer with a temperature of 0 °C indicates the presence of ground ice; warmer temperatures point to ice-free conditions. He also emphasised that a mixture of air from frozen and unfrozen areas of the slope could result in warmer vent temperatures, even though ice is present. Results from geophysical measurements (CHAPTERS 6 & 7) and temperature data logging (CHAPTER 8) confirm these assumptions and show that despite of positive temperatures in the lower vents and at the base of the humus cover, permafrost was present.

Based on the fact that the summer temperatures in lower vents and at the humus base (transition between organic material and talus) are a function of the temperature within the slope, the temperature of the air aspired into the slope and the distance between upper and lower vents, it must be assumed that a boundary value is available for lower vent- and humus-base temperatures that indicates the presence of permafrost. As the magnitude of the mixtures of air is hard to predict, it is questionable, if a precise boundary value will be ascertainable. However, results from humus temperature mapping indicate a close relationship between permafrost distribution and bottom temperature of the high-summer humus cover (BTH). Thereby, the temperature at the humus base is controlled by heat flow from the subsurface and is efficiently decoupled from variations in air temperatures during summer, due to the high insulation capability of the humus cover and high evapotranspiration rates that expend high amounts of the incoming solar energy within the uppermost 5-10 cm of the humus cover.

Consequently, analogous to the BTS-method developed by HAEBERLI (1973), the BTH could be a promising tool for determining the spatial permafrost distribution in talus slopes below the timberline. The application of this approach should move parallel to the recording of the thermal gradient between temperatures at the near-surface and at the humus-base, to determine the insulation capability of the humus cover. Most probably, this approach is only practicable if a sufficiently thick and particularly

consistent humus cover is present. As shown for the Val Bever, the disturbance of the organic layer by boulders reduces the insulation capability of the humus cover, determining low information value of the BTH on permafrost distribution.

Boundary values of BTS indicating the probability of permafrost have been calibrated by HAEBERLI (1973) by extensive measurements and were confirmed in the past by numerous investigations (e.g. HOELZLE et al., 1993; ISAKSEN et al., 2002; KNEISEL et al., 2000a; LAMBIEL & PIERACCI, 2008; SAWADA et al., 2003). An extensive calibration of the BTH-approach at further sites with permafrost below the timberline would be of great importance to determine reliable boundary values and to cross-check the explanatory power of the approach. According to the BTS-method boundary values of the BTH for predicting the probability of permafrost will be subdivided into the categories permafrost probable, permafrost possible and no permafrost probable (TABLE 9.1).

Table 9.1: Concept of boundary temperatures for the evaluation of permafrost distribution based on the bottom temperature of the high-summer humus cover.

probability of permafrost	BTH
permafrost probable	≤ 3 °C
permafrost possible	3-7 °C
no permafrost probable	> 7°C

The following recommendations are suggested for the conduction of BTH-measurements

Period of measurements

- BTH-measurements should be conducted when the degradation of the ground ice is potentially highest. Meaning, the date of measurement should be in high-summer, when temperatures at the humus base are potentially highest. Measurements beyond the rather short time-frame could be misleading and only indicative for seasonal frozen ground or short temperature drops as they are sensitive to the zero-curtain duration in spring/early summer and the often early temperature drops in late August.

Conduction of measurements

- It is recommendable to measure humus temperatures in different depth levels, to achieve a vertical temperature profile between surface and humus base. This allows for a deduction of the thermal conductivity of the organic layer.

Furthermore, a "zero-amplitude depth" might be identified, below which daily variations of air-temperatures are completely buffered.

- As the humus moisture is a crucial factor for the thermal conductivity, it is advisable, but not necessary to record this parameter.
- The ecosystem of supercooled talus slopes is usually rather sensitive to disturbances. While digging of humus profiles would allow for a sophisticated analysis, simple temperature measurements are sufficient for determining the potential permafrost distribution. Here, the development of temperature probes analogous to BTS-probes would be of interest, to provide minimal-invasive measurements.

Consideration of further parameters

- The humus thickness should always be recorded, as it allows a further potential differentiation between areas with and without permafrost.
- The vegetation composition has shown to be closely linked to the permafrost distribution. It would be a promising approach to combine humus temperature- and vegetation mapping. Thereby, the factors *tree height* and *percentage of mosses in the undergrowth* appear to the most fundamental factors.

9.3 Thoughts on the effects of climate change on permafrost in supercooled talus slopes

To enable a reliable statement on the future development of permafrost in talus slopes below the timberline under a warming climate, a substantially longer time-series of data would be required. However, the strong variability of winter characteristics, with view on winter temperatures and snow cover distribution, allowed broad conclusions on the influence of climatic conditions on the ground thermal regime and the permafrost evolution in winter. In this context, the comparison of the three study sites with Val Bever and Val Susauna on the one hand, both located in the Upper Engadin, with comparable climatic conditions, and the Brüeltobel on the other hand, located in the northern Alps at lower altitude, with higher mean annual air temperatures and precipitation rates, provided exciting results.

While mean annual air temperatures are assumed to generally increase in the future, with magnitude of increase depending on the applied scenario (IPCC, 2007), the influence of climatic changes on the snow cover distribution appears to be more complex. Im et al. (2010) found that precipitation in the winter season will consistently increase, with a significant dependence on topographical elevation. Keller et al. (2005) assume a large decrease of snow depth and a decrease of snow cover duration by up to two month under a seasonal increase in the mean temperature of 3 to 5 K. Uhlmann et al. (2009) highlight the fact that in addition to the altitude of a domaine its exposure, localization inland and the slope gradients strongly affect the snow cover distribution.

It has been shown that the influence of the snow cover on the ground thermal regime is of minor importance. Although a thick snow cover is capable of buffering variations in air temperatures, it is not capable of preventing an efficient supercooling. As a consequence, the existence of permafrost in ventilated talus slopes below the timberline appears to be unaffected from the future development of the snow cover distribution with regard on thickness and duration. However, it has been shown that avalanche deposits locally have a strong effect on the ground thermal regime, by preventing an efficient convective heat exchange. According to this, an increase of periods with snow-conditions prone to avalanches could indeed affect the future permafrost distribution below the timberline. Furthermore, it could be shown that in autumn an early snowfall

in connection with relatively warm temperatures could hinder the ventilation, when icicle curtains form within vents and voids as a result of snow melt and refreezing of meltwater.

Conclusions on the influence of summer temperatures on the permafrost distribution are not possible based on results of this study, as summer conditions were relatively constant throughout the period of measurements. In contrast, winter temperatures were highly variable. Thereby, geophysical monitoring data indicate that the magnitude of supercooling has been rather constant, with minor variations of maximum resistivity values throughout the measurement period. However, it must be considered that a quantitative analysis of geophysical data has not been conducted in this study. Here, a longer timer series of geophysical monitoring measurements as well as further borehole temperature data would enable a more sophisticated interpretation.

Nonetheless, with regard on the comparison between the three study sites, it can be concluded that permafrost can persist under mean annual air temperatures of up to 5 °C (Brüeltobel). Based on dendroecological studies at the Brüeltobel, SCHUDEL (2002) reported an increased growth and predicted a disappearance of the dwarfed trees, as soil temperatures would further increase in the course of climatic warming. As geophysical data still point to the existence of permafrost, further studies on the development of the dwarfed trees in the Brüeltobel would be of interest. Especially with view on the fact that microclimatic conditions in the Brüeltobel and in permafrost-free areas of the Val Susauna show comparable characteristics with view on air- and humus temperatures.

However, the persistence of frozen ground in talus slopes below the timberline is a function of the magnitude of supercooling in winter and the magnitude of degradation in summer. Even though mean annual air temperatures at Val Bever and Val Susauna are with less than 3 °C distinctly below values recorded at the Brüeltobel, it must be assumed that years with above average degradation and below average supercooling might affect a complete disappearance of frozen ground. However, with regard on the high seasonal variability a subsequent aggradation of frozen ground must be expected.

10 Outlook

This study allowed expanding the process comprehension on the ground thermal regime that permits the aggradation and persistence of ground ice in ventilated talus slopes below the timberline, the temporal variability and spatial heterogeneity of permafrost as well as the coupling between permafrost and surface properties. However, supercooled talus slopes below the timberline, but also methodological developments still offer a broad research potential.

While the mechanisms that allow the presence of permafrost are in general understood, with regard on the initiation of supercooling and the reasons for the sporadic occurrence of permafrost and the close proximity of areas with and without permafrost some questions remain open. With view on the initiation of supercooling, it would be of interest to profoundly investigate the organic surface layer concerning age and development to allow conclusions on the stages of succession of the vegetation development. In this context further dendrochronological and dendroecological investigations would provide a comprehensive picture of the evolution of the system. An approach to attribute the spatial permafrost distribution at the foot of the slope to a potentially negative energy balance in upslope areas has been discussed above (CHAPTER 9.1.2). A broad modelling of the incoming solar radiation could provide considerable information.

Conclusions on the thermal processes in the humus cover of the *Hexenwäldlis* were first of all based on temperature recordings, in combination with humus temperature and -moisture mapping conducted at only one date. To quantify the seasonal evolution of the thermal conductivity of the organic layer further investigations would be of interest. Especially the humus moisture should be recorded. Furthermore, a quantification of evaporation rates and of latent heat processes within the shallow subsurface would be of interest, to achieve a deeper understanding of energy-exchange.

An approach to estimate the spatial distribution of permafrost in talus slopes below the timberline based on the bottom temperature of the high-summer humus cover (BTH) has been suggested in CHAPTER 9.2. To establish this method and especially to test its applicability to other supercooled talus slopes further investigations would be of

importance, especially in view of calibrating boundary temperatures for the probability of permafrost.

The monitoring approach using electrical resistivity and seismic refraction tomography conducted at Val Susauna represents a great step forward in the reliable monitoring of the permafrost evolution. A quantitative interpretation of geophysical results could not be accomplished within this study, but would allow an even more sophisticated characterization of permafrost properties and the temporal permafrost evolution, especially with regard to the high spatial heterogeneity and temporal variability of permafrost in supercooled talus slopes.

Even though a major part of the puzzle could be pieced together within this study, supercooled talus slopes with their exceptional microclimate and quaint vegetation composition of dwarfed trees and azonal plants, like the beautiful *Dryas octopetala,* remain fascinating sites and retain many outlines for future research.

References

AG Boden (2005), *Bodenkundliche Kartieranleitung [Manual of Soil Mapping]*, 5 ed., 438 pp., Bundesanstalt für Geowissenschaften und Rohstoffe in Zusammenarbeit mit den Staatlichen Geologischen Diensten, Hannover.

Alumbaugh, D. L., & G. A. Newman (2000), Image appraisal for 2-D and 3-D electromagnetic inversion, *Geophysics*, *65*(5), 1455-1467.

Alvarez-Uria, P., & C. Körner (2007), Low temperature limits of root growth in deciduous and evergreen temperate tree species, *Functional Ecology*, *21*, 211-218.

Arbeitskreis Standortskartierung (2003), *Forstliche Standortaufnahme - Begriffe, Definitionen, Einteilungen, Kennzeichnungen, Erläuterungen*, 6 ed., 352 pp., IHW-Verlag, Eching.

Bächler, E. (1930), Der verwünschte oder verhexte Wald im Brüeltobel, *Appenzeller Kalender*, *209*.

Bahrenberg, G., E. Giese, N. Mevenkamp, & J. Nipper (2010), *Statistische Methoden in der Geographie 1: Univariate und bivariate Statistik*, 5 ed., Borntraeger, Stuttgart.

Barker, R. D. (1989), Depth of investigation of collinar symmetrical four-electrode arrays, *Geophysics*, *54*(8), 1031-1037.

Barsch, D. (1973), Refraktionsseismische Bestimmung der Obergrenze des gefrorenen Schuttkörpers in verschiedenen Blockgletschern Graubündens, Schweizer Alpen, *Zeitschift für Gletscherkunde und Glazialgeologie*, *IX*(1-2), 143-167.

Bast, A., H. Gärtner, I. Roer, & C. Kneisel (2007), Tree-ring analysis at a sporadic permafrost site below timberline, Bever Valley, Switzerland, paper presented at TRACE (Tree Rings in Archaeology, Climatology and Ecology), Riga.

Beniston, M. (2004), *Climate Change and its impacts. An overview focusing on Switzerland.*, Kluwer Academic Publishers, Dordrecht.

Bentley, L., R., & M. Gharibi (2004), Two- and three-dimensional electrical resistivity imaging at a heterogeneous remediation site, *Geophysics*, *69*(3), 674-680.

Bernhard, L., F. Sutter, W. Haeberli, & F. Keller (1998), Processes of snow/permafrost-interactions at a high-mountain site, Murtèl/Corvatsch, Eastern Swiss Alps, paper presented at PERMAFROST - Seventh International Conference, Collection Nordicana, Yellowknife (Canada).

Bichler, A., P. Bobrowsky, M. Best, M. Douma, J. Hunter, T. Calvert, & R. Burns (2004), Three-dimensional mapping of a landslide using a multi-geophysical approach: the Quesnel Forks landslide, *Landslides*, *1*(1), 29-40.

Boeckli, L., A. Brenning, S. Gruber, & J. Noetzli (2012), Permafrost distribution in the European Alps: calculation and evaluation of an index map and summary statistics, *The Cryosphere*, *6*(4), 13.

Brown, J., & V. E. Romanovsky (2008), Report from the International Permafrost Association: State of permafrost in the first decade of the 21(st) century, *Permafrost and Periglacial Processes*, *19*(2), 255-260.

Burger, H. R., A. F. Sheehan, & C. H. Jones (2006), *Introduction to Applied Geophysics - Exploring the shallow subsurface*, 552 pp., W.W. Norton & Company, New York, London.

Cassagne, N., T. Spiegelberger, L. Cecillon, B. Juvy, & J. J. Brun (2008), The impact of soil temperature increase on organic matter and faunal properties in a frozen calcareous scree in the French Alps, *Geoderma*, *146*(1-2), 239-247.

Chambers, J. E., P. B. Wilkinson, A. L. Weller, P. I. Meldrum, R. D. Ogilvy, & S. Caunt (2007), Mineshaft imaging using surface and crosshole 3D electrical resistivity tomography: A case history from the East Pennine Coalfield, UK, *Journal of Applied Geophysics*, *62*(4), 324-337.

Dahlin, T., C. Bernstone, & M. H. Loke (2002), A 3-D resistivity investigation of a contaminated site at Lernacken, Sweden, *Geophysics*, *67*(6), 1692-1700.

Dahlin, T., & M. H. Loke (1997), Quasi-3D resistivity imaging - mapping of three dimensional structures using two dimensional DC resistivity techniques, paper presented at 3rd Meeting Environmental and Engineering Geophysics, Aarhaus, Denmark.

Davis, N. (2001), *Permafrost: A Guide to Frozen Ground*, University of Alaska Press, Fairbanks, Alaska.

Day-Lewis, F. D., K. Singha, & A. M. Binley (2005), Applying petrophysical models to radar travel time and electrical resistivity tomograms: Resolution-dependent limitations, *Journal of Geophysical Research-Solid Earth*, *110*(B8).

De Pascale, G. P., W. H. Pollard, & K. K. Williams (2008), Geophysical mapping of ground ice using a combination of capacitive coupled resistivity and ground-penetrating radar, Northwest Territories, Canada, *Journal of Geophysical Research-Earth Surface*, *113*(F2).

Delaloye, R. (2004), *Contribution à l'étude du pergélisol de montagne en zone marginale*, 240 pp., Département de Géosciences, Université de Fribourg, Fribourg.

Delaloye, R., & C. Lambiel (2005), Evidence of winter ascending air circulation throughout talus slopes and rock glaciers situated in the lower belt of alpine discontinuous permafrost (Swiss Alps), *Norsk Geografisk Tidsskrift - Norwegian Journal of Geography*, *59*, 194-203.

Delaloye, R., & C. Lambiel (2007), Drilling in a low elevation cold talus slope (Dreveneuse, Swiss Prealps), *Geophysical Research Abstracts*, *9*.

Delaloye, R., & C. Lambiel (2008), Typology of vertical electrical soundings for permafrost/ground ice investigation in the forefields of small alpine glaciers, in *Applied Geophysics in Periglacial Environments*, edited by C. Hauck and C. Kneisel, p. 8, Cambridge University Press, Cambridge.

Delaloye, R., E. Reynard, C. Lambiel, L. Marescot, & R. Monnet (2003), Thermal anomaly in a cold scree slope (Creux du Van, Switzerland), paper presented at 8th International Conference on Permafrost, Zürich, Switzerland.

Dey, A., & H. F. Morrison (1979), Resistivity modelling for arbitrarily shaped two-dimensional structures *Geophysical Prospecting*, *27*(1), 106-136.

Dingman, L. S., & F. R. Koutz (1974), Relations among vegetation permafrost and potential insulation in central Alaska, *Arctic and Alpine Research*, *6*(1), 37-42.

Ellis, R. G., & D. W. Oldenburg (1994), Applied geophysical inversion, *Geophysical Journal International*, *116*(1), 5-11.

Etzelmüller, B., I. Berthling, & R. S. Odegard (2003), One-dimensional DC-resistivity depth soundings as a tool in permafrost investigations in high mountain areas of Southern Norway, *Zeitschrift Fur Geomorphologie*, *132*, 19-36.

Etzelmüller, B., M. Hoelzle, E. S. F. Heggem, K. Isaksen, C. Mittaz, D. Vonder Mühll, R. S. Odegard, W. Haeberli, & J. L. Sollid (2001), Mapping and modelling the occurrence and distribution of mountain permafrost, *Norsk Geografisk Tidsskrift - Norwegian Journal of Geography*, *55*(4), 186 - 194.

Everdingen, R. O. v. (1993), A multi-lingual index f permafrost terms, paper presented at 6th International Conference on Permafrost.

Farquharson, C. G. (2008), Constructing piecewise-constant models in multidimensional minimum-structure inversions, *Geophysics*, *73*(1), 1-9.

Felber, T. (1884), Ein Zwergwald im Kanton Appenzell, *Jahrbuch des Schweizerischen Alpenclubs*, *19*, 4.

Fischanger, F., G. Morelli, D. J. LaBrecque, & M. Occhi (2007), Monitoring resins injection with 3D electrical resistivity tomography (ERT) using surface and multi-borehole electrode arrays, paper presented at SAGEEP 20th Annual meeting, Denver.

Fortier, R., A.-M. LeBlanc, M. Allard, S. Buteau, & F. Calmels (2008), Internal structure and conditions of permafrost mounds at Umiujaq in Nunavik, Canada, inferred from field investigation and electrical resistivity tomography, *Canadian Journal of Earth Sciences*, *45*, 367-387.

French, H. (2007), *The Periglacial Environment*, third ed., 458 pp., John Wiley & Sons,Ltd, Chichester.

Friedel, S. (2003), Resolution, stability and efficiency of resistivity tomography estimated from a generalized inverse approach, *Geophysical Journal International*, *153*(2), 305-316.

Friedel, S., A. Thielen, & S. M. Springman (2006), Investigation of a slope endangered by rainfall-induced landslides using 3D resistivity tomography and geotechnical testing, *Journal of Applied Geophysics*, *60*(2), 100-114.

Fukui, K., T. Sone, K. Yamagata, Y. Otsuki, Y. Sawada, V. Vetrova, & M. Vyatkina (2008), Relationships between permafrost distribution and surface organic layers near Esso, Central Kamchatka, Russian Far East, *Permafrost and Periglacial Processes*, *19*, 85-92.

Furrer, E. (1966), Kümmerfichtenbestände und Kaltluftströme in den Alpen der Ost- und Innerschweiz, *Schweizerische Zeitschrift für Forstwesen*, *10*, 13.

Garré, S., M. Javaux, J. Vanderborght, L. Pages, & H. Vereecken (2011), Three-dimensional electrical resistivity tomography to monitor root zone water dynamics, *Vadose Zone Journal*, *10*(1), 412-424.

Gavriliev, R. L. (2003), Quantitative estimation of the thermal conductivity of saturated frozen soils, paper presented at 8th International Conference on Permafrost, Zürich, Switzerland.

Geometrics (2009), SeisImager/2D Manual, *Version 3.3*.

Gharibi, M., & L. R. Bentley (2005), Resolution of 3-D electrical resistivity images from inversions of 2-D orthogonal lines, *Journal of Environmental and Engineering Geophysics*, *10*(4), 339-349.

Green, R. N., R. L. Trowbridge, & K. Klinka (1993), Towards a taxonomic classification of humus forms, *Forest Science*, *39*.

Gruber, S., & W. Haeberli (2007), Permafrost in steep bedrock slopes and its temperature-related destabilization following climate change, *Journal of Geophysical Research: Earth Surface*, *112*(F2), n/a-n/a.

Gruber, S., & M. Hoelzle (2008), The cooling effect of coarse blocks revisited: a modeling study of a purely conductive mechanism, paper presented at 9th International Conference on Permafrost, Fairbanks, Alaska, 29 June 2008 - 03 July 2008.

Gude, M., S. Dietrich, R. Mäusbacher, C. Hauck, R. Molenda, V. Ruzicka, & M. Zacharda (2003), Probable occurence of sporadic permafrost in non-alpine scree slopes in Central Europe, paper presented at 8th International Conference on Permafrost, Zürich, Switzerland.

Guglielmin, M. (2003), Observations on permafrost ground thermal regimes from Antarctica and the Italian Alps, and their relevance to global climate change, *Global and Planetary Change*, *42*, 159-167.

Guglielmin, M., C. J. E. Evans, & N. Cannone (2008), Active Layer thermal regime under different vegetation conditions in permafrost areas. A case study at Signy Island (Maritime Antarctica), *Geoderma*, *144*, 73-85.

Gwinner, M. P. (1971), *Geologie der Alpen - Stratigraphie, Paläogegographie, Tektonik*, 477 pp., E. Schweizerbart'sche Verlagsbuchhandlug, Stuttgart.

Haeberli, W. (1973), Die Basis-Temperatur der winterlichen Schneedecke als möglicher Indikator für die Verbeitung von Permafrost in den Alpen, *Zeitschrift für Gletscherkunde und Glaziologie*, *9*(1-2), 221-227.

Haeberli, W. (1975), *Untersuchungen zur Verbreitung von Permafrost zwischen Flüelapass und Piz Grialetsch (Graubünden)*.

Haeberli, W. (1990), *Permafrost*, Mitteilungen der Versuchsanstalt für Wasserbau, Hydrologie und Glaziologie der ETH, Zürich, Switzerland.

Haeberli, W. (1992), Construction, environmental problems and natural hazards in periglacial mountain belts, *Permafrost and Periglacial Processes*, *3*(2), 111-124.

Haeberli, W., & M. Beniston (1998), Climate Change and Its Impacts on Glaciers and Permafrost in the Alps, *Ambio*, *27*(4).

Haeberli, W., J. Noetzli, L. Arenson, R. Delaloye, I. Gärtner-Roer, S. Gruber, K. Isaksen, C. Kneisel, M. Krautblatter, & M. Philipps (2010), Mountain permafrost: development and challenges of a young research field, *Journal of Glaciology*, *56*(200), 1043-1058.

Haeberli, W., & D. Vonder Mühll (1996), On the characteristics and possible origin of ice in rock glacier permafrost, *Zeitschrift Fur Geomorphologie*, *104*, 43-57.

Hantke, R. (1991), *Landschaftsgeschichte der Schweiz und ihrer Nachbargebiete: Erd-, Klima- und Vegetationsgeschichte der letzten 30 Millionen Jahre*, Ott Verlag, Zürich.

Harris, C. (2005), Climate Change, Mountain Permafrost Degradation and Geotechnical Hazard, in *Global Change and Mountain Regions*, edited, pp. 215-224.

Harris, C., et al. (2009), Permafrost and climate in Europe: Monitoring and modelling thermal, geomorphological and geotechnical responses, *Earth-Science Reviews*, *92*(3-4), 117-171.

Harris, C., M. C. R. Davies, & B. Etzelmüller (2001), The assessment of potential geotechnical Hazards associated with mountain permafrost in a warming global climate, *Permafrost and Periglacial Processes*, *12*, 145-156.

Harris, C., M. Luetschg, M. C. R. Davies, F. Smith, H. H. Christiansen, & K. Isaksen (2007), Field instrumentation for real-time monitoring of periglacial solifluction, *Permafrost and Periglacial Processes*, *18*(1), 105-114.

Harris, C., & D. Vonder Mühll (2003), Permafrost and Climate in Europe. Climate Change, Mountain Permafrost Degradation and Geotechnical Hazard, in *Global Change and Protected Areas*, edited, pp. 71-82.

Harris, S. A., & D. E. Pedersen (1998), Thermal regimes beneath coarse blocky materials, *Permafrost and Periglacial Processes*, *9*(2), 107-120.

Hauck, C. (2001), *Geophysical methods for detecting permafrost in high mountains*, 204 pp., Mitteilungen der Versuchsanstalt für Wasserbau, Hydrologie und Glaziologie der ETH Zürich, Zürich.

Hauck, C. (2002), Frozen ground monitoring using DC resistivity tomography, *Geophysical Research Letters*, *29*(21).

Hauck, C., M. Bach, & C. Hilbich (2008), A 4-phase model to quantify subsurface ice and water content in permafrost regions based on geophysical data sets, paper presented at Ninth International Conference on Permafrost, Institute of Northern Engineering, Fairbanks, Alaska.

Hauck, C., M. Boettcher, & H. Maurer (2010), A new model for quantifying subsurface ice contend based on geophysical data sets, *The Cryosphere Discussions*, *4*(2), 787-821.

Hauck, C., & C. Kneisel (2006), Application of capacitively-coupled and DC electrical resistivity imaging for mountain permafrost studies, *Permafrost and Periglacial Processes*, *17*, 169-177.

Hauck, C., & C. Kneisel (Eds.) (2008a), *Applied Geophysics in Periglacial Environments*, Cambridge University Press, Cambridge.

Hauck, C., & C. Kneisel (2008b), Quntifying ice content in low-altitude scree slopes, in *Applied Geophysics in Periglacial Environments*, edited by C. Hauck and C. Kneisel, p. 12, Cambridge University Press, Cambridge.

Hauck, C., & D. Vonder Mühll (2003a), Evaluation of geophyical techniques for aplication in mountain permafrost studies, *Zeitschrift Für Geomorphologie*, *132*, 161-190.

Hauck, C., & D. Vonder Mühll (2003b), Inversion and interpretation of two-dimensional geoelectrical measurements for detecting permafrost in mountain regions, *Permafrost and Periglacial Processes*, *14*, 305-318.

Hauck, C., & D. Vonder Mühll (2003c), Permafrost monitoring using time-lapse tomography, paper presented at 8th International Conference on Permafrost, Zürich, Switzerland.

Hauck, C., D. Vonder Mühll, & M. Hoelzle (2005), Permafrost monitoring in high mountain areas using a coupled geophysical and meteorological approach, in *Climate and Hydrology of Mountain Areas*, edited by C. d. Jong, D. Collins and R. Ranzi, pp. 59-71, Wiley.

Heierli, H. (1984), *Die Ostschweizer Alpen und ihr Vorland*, 209 pp., Gebr. Norntraeger, Berlin. Stuttgart.

Herz, T., L. King, & H. Gubler (2003), Microclimate within coarse debris of talus slopes in the alpine periglacial belt and its effect on permafrost, paper presented at 8th International Conference on Permafrost, Zürich, Switzerland.

Hilbich, C. (2009), Geophysical monitroing systems to assess and quaintfy ground ice evolution in mountain permafrost, 169 pp, Friedrich-Schiller-Universität, Jena.

Hilbich, C. (2010), Time-lapse refraction seismic tomography for the detection of ground ice degradation, *The Cryosphere*, *4*(3), 243-259.

Hilbich, C., & R. Delaloye (2007), Interactions between air circulation within talus slope and permafrost evolution - results from temperature monitoring and time-lapse electrical resistivity tomography, *Geophysical Research Abstracts*, *9*.

Hilbich, C., C. Fuss, & C. Hauck (2011), Automated Time-lapse ERT for Improved Process Analysis and Monitoring of Frozen Ground, *Permafrost and Periglacial Processes*, *22*(4), 306-319.

Hilbich, C., C. Hauck, R. Delaloye, & M. Hoelzle (2009a), A geoelectric monitoring network and resistivity-temperature relationships of different mountain permafrost sites in the Swiss Alps, paper presented at Proceedings of the 9th International Conference on Permafrost, Fairbanks, Alaska.

Hilbich, C., C. Hauck, M. Hoelzle, M. Scherler, L. Schudel, I. Völksch, D. Vonder Mühll, & R. Mäuschbacher (2008), Monitoring mountain permafrost evolution using electrical resistivity tomography: A 7-year study of seasonal, annual, and long-term variations at Schilthorn, Swiss Alps, *Journal of Geophysical Research*, *113*.

Hilbich, C., L. Marescot, C. Hauck, M. H. Loke, & R. Mausbacher (2009b), Applicability of electrical resistivity tomography monitoring to coarse blocky and ice-rich permafrost landforms, *Permafrost and Periglacial Processes*, *20*(3), 269-284.

Hiller, B. (2001), *Humusformen im Waldgrenzökoton (Oberengadin, Schweiz)*, Westfälische Wilhelms-Universität, Münster.

Hiller, B., & A. Müterthies (2005), Humus Forms and Reforestation of an Abandoned Pasture at the Alpine Timberline (Upper Engadine, Central Alps, Switzerland), in *Mountain Ecosystems, Studies in Treeline Ecology*, edited by G. Broll and B. Keplin, pp. 203 - 218, Springer, Berlin Heidelberg.

Hoch, G. (2008), The carbon supply of Picea abies trees at a Swiss montane permafrost site, *Plant Ecology & Diversity*, *1*(1), 13-20.

Hoelzle, M., W. Haeberli, & F. Keller (1993), Application of BTS-Measurements for modelling mountain permafrost distribution, paper presented at Proceedings Sixth International Conference on Permafrost, Peking.

Hoelzle, M., D. Vonder Mühll, & W. Haeberli (2002), Thirty years of permafrost research in the Corvatsch-Furtschellas area, Eastern Swiss Alps: a review, *Norsk Geografisk Tidsskrift - Norwegian Journal of Geography*, *56*(2), 137-145.

Holtmeier, F.-K. (2000), *Die Höhengrenzen der Gebirgswälder*, Westfälische Wilhelms-Universität, Münster.

Hong, M., L. Zongchao, & L. Yifeng (1993), Effects of snow cover on thermal regime of frozen soils, paper presented at Proceedings Sixth International Conference on Permafrost, Peking.

Hsü, K. J. (1995), *The Geology of Switzerland - An introduction to tectonic facies*, 250 pp., Princeton University Press, Princeton.

Ikard, S. J., M. N. Gooseff, J. E. Barrett, & C. Takacs-Vesbach (2009), Thermal characterisation of active layer across a soil moisture gradient in the McMurdo Dry Valleys, Antarctica, *Permafrost and Periglacial Processes*, *20*(1), 27-39.

Ikeda, A. (2006), Combination of conventional geophysical methods for sounding the composition of rock glaciers in the Swiss Alps, *Permafrost and Periglacial Processes*, *17*(1), 35-48.

Ikeda, A. (2008), Reassessments of DC resistivity in rock glaciers by comparing with P-wave velocity: a case study in the Swiss Alps, in *Applied Geophysics in Periglacial Environments*, edited by C. Hauck and C. Kneisel, p. 16, Cambridge University Press, Cambridge.

Im, E. S., E. Coppola, F. Giorgi, & X. Bi (2010), Local effects of climate change over the Alpine region: A study with a high resolution regional climate model with a surrogate climate change scenario, *Geophysical Research Letters*, *37*(5), L05704.

IPCC (Ed.) (2007), *Summary for Policymakers*, Cambridge University Pres, Cambridge, United Kingdom and New York, USA.

Isaksen, K., C. Hauck, E. Gudevang, R. S. Odegard, & J. L. Sollid (2002), Mountain permafrost distribution in Dovrefjell and Jotunheimen, southern Norway, based on BTS and DC resistivity tomography data, *Norsk Geografisk Tidsskrift - Norwegian Journal of Geography*, *56*(2), 122-136.

Ishikawa, M. (2003), Thermal regimes at the snow-ground interface and their implications for permafrost investigation, *Geomorphology*, *52*(1-2), 105-120.

Juliussen, H., & O. Humlum (2008), Thermal regime of openwork block fields on the mountains Elgåhogna and Sølen, central-eastern Norway, *Permafrost and Periglacial Processes*, *19*(1), 1-18.

Kääb, A., J. Reynolds, & W. Haeberli (2005), Glacier and Permafrost Hazards in High Mountains, in *Global Change and Mountain Regions*, edited, pp. 225-234.

Kane, D. L., R. E. Gleck, & L. D. Hinzman (1990), Evapotranspiration from a small Alaskan Arctic watershed, *Journal Name: Nordic Hydrology; (Denmark); Journal Volume: 21*, Medium: X; Size: Pages: 253-272.

Kane, D. L., K. M. Hinkel, D. J. Goering, L. D. Hinzman, & S. I. Outcalt (2001), Non-conductive heat transfer associated with frozen soils, *Global and Planetary Change*, *29*(3–4), 275-292.

Kästl, J. (2012), Räumliche Heterogenität und zeitliche Variabilität der Permafrostverbreitung im Gletschervorfeld des Val Muragl, Unpublished Dipolam Thesis thesis, University of Würzburg, Würzburg.

Keller, F. (1992), Automated mapping of mountain permafrost using the program PERMAKART within the geographical information system ARC/INFO, *Permafrost and Periglacial Processes*, *3*(2), 133-138.

Keller, F. (1994), *Interaktionen zwischen Schnee und Permafrost*, 145 pp., Vischer, D., Zürich, Switzerland.

Keller, F., S. Goyette, & M. Beniston (2005), Sensitivity Analysis of Snow Cover to Climate Change Scenarios and Their Impact on Plant Habitats in Alpine Terrain, *Climatic Change*, *72*(3), 299-319.

Keller, F., & H. Gubler (1993), Interaction between snow cover and high mountain permafrost, Murtèl/Corvatsch, Swiss Alps, paper presented at Proceedings Sixth International Conference on Permafrost, Peking.

Keller, F., & M. Tamás (2003), Enhanced ground cooling in periods with thin snow cover in the Swiss National Park, paper presented at 8th International Conference on Permafrost, Zürich, Switzerland.

Kneisel, C. (1998), *Permafrost in Gletschervorfeldern: Eine vergleichende Untersuchung in den Ostschweizer Alpen und Nordschweden*, 156 pp., Trier.

Kneisel, C. (1999), *Permafrost in Gletschervorfeldern - Eine vergleichende Untersuchung in den Ostschweizer Alpen und Nordschweden*, Trierer Geographische Studien, Trier.

Kneisel, C. (2003a), Electrical resistivity tomography as a tool for geomorphological investigations - some case studies, *Zeitschrift Fur Geomorphologie*, *132*, 37-49.

Kneisel, C. (2003b), *Sporadic and discontinous mountain permafrost occurrence in the Upper Engadine, eastern Swiss Alps*, 561-566 pp.

Kneisel, C. (2004), New insights into mountain permafrost occurrence and characteristics in glacier forefields at high altitude through the application of 2D resistivity imaging, *Permafrost and Periglacial Processes*, *15*(3), 221-227.

Kneisel, C. (2006), Assessment of subsurface lithology in mountain environments using 2D resistivity imaging, *Geomorphology*, *80*(1-2), 32-44.

Kneisel, C. (2007), The nature and dynamics of frozen ground in alpine and subarctic periglacial environments, Unpublished professorial dissertation thesis, University of Würzburg, Würzburg.

Kneisel, C. (2010), The nature and dynamics of frozen ground in alpine and subarctic periglacial environments, *The Holocene*, *20*(3), 423-445.

Kneisel, C., W. Haeberli, & R. Baumhauer (2000a), Comparison of spatial modelling and field evidence of glacier/permafrost relations in an Alpine permafrost environment, *Annals of Glaciology, Vol 31, 2000*, *31*, 269-274.

Kneisel, C., & C. Hauck (2003), Multi-method geophysical investigation of a sporadic permafrost occurence, *Zeitschrift für Geomorphologie Supplementbände - Geophysical applications in geomorphology*, *132*.

Kneisel, C., C. Hauck, R. Fortier, & B. Moorman (2008), Advances in geophysical methods for permafrost investigations, *Permafrost and Periglacial Processes*, *19*(2), 157-178.

Kneisel, C., C. Hauck, & D. Vonder Mühll (2000b), Permafrost below the timberline confirmed and characterised by geoelectrical resistivity measurements, Bever Valley, eastern Swiss Alps, *Permafrost and Periglacial Processes*, *11*(4), 295-304.

Kneisel, C., & A. Kääb (2007), Mountain permafrost dynamics within a recently exposed glacier forefield inferred by a combined geomorphological, geophysical and photogrammetrical approach, *Earth Surface Processes and Landforms*, *32*, 1797-1810.

Kneisel, C., T. Rödder, & D. Schwindt (accepted), Frozen ground dynamics resolved by multi-year and year-around electrical resistivity monitoring at three alpine site in the Swiss Alps, *Near Surface Geophysics*.

Kneisel, C., C. Rothenbuhler, F. Keller, & W. Haeberli (2007), Hazard assessment of potential periglacial debris flows based on GIS-based spatial modelling and geophysical field surveys: A case study in the Swiss Alps, *Permafrost and Periglacial Processes*, *18*, 259-268.

Kneisel, C., & D. Schwindt (2008), Geophysical mapping of isolated permafrost lenses at a sporadic permafrost site at low altitude in the Swiss Alps, paper presented at 9th International Conference on Permafrost, Fairbanks, Alaska.

Knödel, K., H. Krummel, & G. Lange (2005), Handbuch zur Erkundung des Untergrundes von Deponien und Altlasten, in *Geophysik*, edited.

Körner, C. (2003), *Alpine plant life: Functional plant ecology of high mountain ecosystems. Second edition*, i-344 pp., Springer-Verlag New York Inc.; Springer-Verlag GmbH & Co. KG.

Körner, C., & G. Hoch (2006), A Test of Treeline Theory on a Montane Permafrost Island, *Arctic, Antarctic, and Alpine Research*, *38*(1), 113-119.

Körner, C., & J. Paulsen (2004), A world-wide study of high altitude treeline temperatures, *Journal of Biogeography*, *31*(5), 713-732.

Krautblatter, M. (2008), Rock permafrost geophysics and its explanatory power for permafrost-induced rockfalls and rock creep: a perspective, paper presented at 9th International Conference on Permafrost, Fairbanks, Alaska.

Krautblatter, M., & C. Hauck (2007), Electrical resistivity tomography monitoring of permafrost in solid rock walls, *Journal of Geophysical Research-Earth Surface*, *112*(F2).

Krautblatter, M., & M. Moser (2009), A nonlinear model coupling rockfall and rainfall intensity based on a four year measurement in a high Alpine rock wall (Reintal, German Alps), *Natural Hazards and Earth System Sciences*, *9*(4), 1425-1432.

Krautblatter, M., & S. Verleysdonk (2008), Rock wall permafrost monitoring with high-resolution 2D-ERT: lessons learnt from error estimates and a comparison of Wenner, Schlumberger, Gradient and Dipole-type arrays, *Geophysical Research Abstracts*, *10*.

Krautblatter, M. T., S. Verleysdonk, A. Flores-Orozco, & A. Kemna (2010), Temperature-calibrated imaging of seasonal changes in permafrost rock walls by

quantitative electrical resistivity tomography (Zugspitze, German/Austrian Alps), *Journal of Geophysical Research*.

Labhart, T. P. (2005), *Geologie der Schweiz*, 7 ed., 210 pp., Ott Verlag, Bern.

Lambiel, C., & K. Pieracci (2008), Permafrost distribution in talus slopes located within the alpine periglacial belt, Swiss Alps, *Permafrost and Periglacial Processes*, *19*(3), 293-304.

Lambiel, C., & E. Reynard (2001), Regional modelling of present, past and future potential distribution of discontinuous permafrost based on a rock glacier inventory in the Bagnes-Hérémence area (Western Swiss Alps), *Norsk Geografisk Tidsskrift - Norwegian Journal of Geography*, *55*(4), 219 - 223.

Landolt, E. (2003), *Unsere Alpenflora*, 7 ed., Schweizer Alpen-Club SAC.

Lanz, E., H. Maurer, & A. G. Green (1998), Refraction tomography over a buried waste disposal site, *Geophysics*, *63*(4), 1414-1433.

Loke, M. H. (1994), The inversion of two-dimensional apparent resistivity data, unpubished Ph.D. thesis thesis, University of Birmingham, Birmingham (U.K.).

Loke, M. H. (2002), RES2DMOD ver. 3.01 - Rapid 2D resistivity forward modelling using the finite-difference and finite-element methods.

Loke, M. H. (2010), Tutorial: 2-D and 3-D electrical imaging surveys.

Loke, M. H., I. Acworth, & T. Dahlin (2003), A comparison of smooth and blocky inversion methods in 2D electrical imaging surveys, *Exploration Geophysics*, *34*, 182-187.

Loke, M. H., & R. D. Barker (1995), Least-squares deconvolution of apparent resistivity pseudosections, *Geophysics*, *60*(6), 1682-1690.

Loke, M. H., & R. D. Barker (1996a), Practical techniques for 3D resistivity surveys and data inversion, *Geophysical Prospecting*, *44*(3), 499-523.

Loke, M. H., & R. D. Barker (1996b), Rapid least-squares inversion of apparent resistivity pseudosections by a quasi-Newton method, *Geophysical Prospecting*, *44*, 131-152.

Loke, M. H., & T. Dahlin (2002), A comparison of the Gauss-Newton and quasi-Newton methods in resistivity imaging inversion, *Journal of Applied Geophysics*, *49*(3), 149-162.

Luetscher, M., & P.-Y. Jeannin (2004), The role of winter air circulations for the presence of subsurface ice accumulations: an example from Monlési ice cave (Switzerland), *Theoretical and Applied Karstology*, *17*, 6.

Luetschg, M., P. Bartelt, M. Lehning, V. Stoeckli, & W. Haeberli (2003), Numerical simulation of the interaction processes between snow cover and alpine permafrost, paper presented at 8th International Conference on Permafrost, Zürich, Switzerland.

Luetschg, M., & W. Haeberli (2005), Permafrost evolution in the Swiss Alps in a changing climate and the role of the snow cover, *Norsk Geografisk Tidsskrift - Norwegian Journal of Geography*, *59*, 78-83.

Luetschg, M., M. Lehning, & W. Haeberli (2008), A sensitivity study of factors influencing warm/thin permafrost in the Swiss Alps, *Journal of Glaciology*, *54*(187), 696-704.

Luetschg, M., V. Stoeckli, M. Lehning, W. Haeberli, & W. Ammann (2004), Temperatures in two boreholes at Flüela Pass, Eastern Swiss Alps: the effect of snow redistribution on permafrost distribution patterns in high mountain areas, *Permafrost and Periglacial Processes*, *15*(3), 283-297.

Lugon, R., & R. Delaloye (2001), Modelling alpine permafrost distribution, Val de Rechy, Valais Alps (Switzerland), *Norsk Geografisk Tidsskrift - Norwegian Journal of Geography*, *55*(4), 224 - 229.

Marescot, L., M. H. Loke, D. Chapellier, R. Delaloye, C. Lambiel, & E. Reynard (2003), Assessing reliability of 2D resistivity imaging in mountain permafrost studies using the depth of investigation index method, *Near Surface Geophysics*, *1*(2), 57-67.

Marty, C., M. Phillips, M. Lehning, C. Wilhelm, & A. Bauder (2009), Klimaänderung und Naturgefahren in Graubünden (climate change and natural hazards in the Grisons), *Schweizerische Zeitschrift fur Forstwesen*, *160*(7), 201-209.

Maurer, H., & C. Hauck (2007), Instruments and methods - Geophysical imaging of alpine rock glaciers, *Journal of Glaciology*, *53*(180), 110-120.

Minke, M., N. Donner, N. Karpov, P. d. Klerk, & H. Joosten (2009), Patterns in vegetation composition, surface height and thaw depth in polygon mires in the Yakutian Arctic (NE Siberia): a microtopographical characterisation of the active layer, *Permafrost and Periglacial Processes*, *20*(4), 357-368.

Möbus, G. (1997), *Geologie der Alpen: eine Einführung in die regional-geologischen Einheiten zwischen Genf und Wien*, Sven von Loga, Köln.

Molenda, R. (1996), Zoogeographische Bedeutung Kaltluft erzeugender Blockhalden im außeralpinen Mitteleuropa: Untersuchungen an Arthropoda, insbesondere Coleoptera., *Verhandlungen des naturwissenschaftlichen Vereins Hamburg*, *35*.

Morard, S. (2011), *Effets de la circulation d'air par effet de cheminée dans l'évolution du régime thermique des éboulis froids de basse et moyenne altitude*, 223 pp., Département de Géosciences, Université de Fribourg, Fribourg.

Morard, S., & R. Delaloye (2010), Time-Lapse Electrical Resistivity Tomography (ERT) to Estimate Temperature Changes at Depth and Isolated Permafrost Patches in Two Low Elevation Ventilated Cold Talus Slopes – Western Switzerland, paper presented at 3rd European Conference on Permafrost (EUCOP III), Svalbard, Norway, June 13-17, 2010.

Morard, S., R. Delaloye, & J. Dorthe (2008), Seasonal Thermal Regime of a Mid-Latitude Ventilated Debris Accumulation, paper presented at 9th International Conference on Permafrost, Fairbanks, Alaska, July 2008.

Morelli, A., G. Morelli, P. Chiara, A. Pacchini, & F. Fischanger (2004), Characterization of complex archaeological sites using 3D Electrical Resistivity Tomography, paper presented at SAGEEP 17th Annual meeting, Colorado Springs.

Moskalenko, N. G. (2003), Interactions between vegetation and permafrost on some CALM grids in Russia, paper presented at 8th International Conference on Permafrost, Zürich, Switzerland.

Müller, M. (1987), Bodenbildung auf silikatunterlage in der alpinen stufe des Oberengadins (Zentralalpen, Schweiz), *CATENA*, *14*(5), 419-437.

Nikolaev, A. N. (2003), The Influence of soil temperature on radial increments of larch pine stems in central Yakutia, paper presented at 8th International Conference on Permafrost, Zürich, Switzerland.

Oldenburg, D. W., & Y. Li (1999), Estimating depth of investigation in dc resistivity and IP surveys, *Geophysics*, *64*(2), 403-416.

Oldenburg, D. W., P. R. McGillivray, & R. g. Ellis (1993), Generalized subspace methods for large-scale inverse problems, *Geohysical Journal International*, *114*.

Papadopoulos, N. G., P. Tsourlos, G. N. Tsokas, & A. Sarris (2006), Two-dimensional and three-dimensional resistivity imaging in archaeological site investigation, *Archaeological Prospection*, *13*(3), 163-181.

Papadopoulos, N. G., P. Tsourlos, G. N. Tsokas, & A. Sarris (2007), Efficient ERT measuring and inversion strategies for 3D imaging of buried antiquities, *Near Surface Geophysics*, *5*(6), 349-361.

Park, S. (1998), Fluid migration in the vadose zone from 3-D inversion of resistivity monitoring data, *Geophysics*, *63*(1), 41-51.

Park, S. K., & P. G. Van (1991), Inversion of pole-pole data for 3-D resistivity structure beneath arrays of electrodes, *Geophysics*, *56*(7), 951-960.

Pavlov, A. V., & N. G. Moskalenko (2002), The thermal regime of soils in the north of Western Siberia, *Permafrost and Periglacial Processes*, *13*(1), 43-51.

PERMOS (2001), Permafrost in Switzerland 1999/2000*Rep.*, 32 pp, Cryospheric Commission of the Swiss Academy of Sciences.

PERMOS (2004), Permafrost in Switzerland 2000/2001 and 2001/2002*Rep.*, 86 pp, Cryospheric Commission of the Swiss Academy of Sciences.

PERMOS (2007), Permafrost in Switzerland 2002/2003 and 2003/2004*Rep.*, 106 pp, Cryospheric Commission of the Swiss Academy of Sciences.

PERMOS (2009), Permafrost in Switzerland 2004/2005 and 2005/2006*Rep.*, 100 pp, Cryospheric Commission of the Swiss Academy of Sciences.

PERMOS (2010), Permafrost in Switzerland 2006/2007 and 2007/2008*Rep.*, 68 pp, Cryospheric Commission of the Swiss Academy of Sciences.

Peter-Borie, M., C. Sirieix, V. Naudet, & J. Riss (2011), Electrical resistivity monitoring with buried electrodes and cables: noise estimation with repeatability tests, *Near Surface Geophysics*, *9*(4), 369-380.

Phillips, M., E. Z. Mutter, M. Kern-Luetschg, & M. Lehning (2009), Rapid degradation of ground ice in a ventilated talus slope: Flüela Pass, Swiss Alps, *Permafrost and Periglacial Processes*, *20*(1), 1-14.

Raska, P., K. Kirchner, & M. Raska (2011), Winter microclimatic regime of low-altitude scree slopes and ist relation to topography: case study from the Ceske Stredohori Mts. (N Czech Republic), *Geografia Fisica e Dinamica Quaternaria*, *34*(2).

Reisigl, H., & R. Keller (1989), *Lebensraum Bergwald: Alpenpflanzen in Bergwald, Baumgrenze und Zwergstrauchheide*, 144 pp., Gustav Fischer, Stuttgart.

Reynolds, J. M. (2011), *An Introduction to Applied and Environmental Geophysics*, 2 ed., John Wiley & Sons.

Riedlinger, T. (1999), Untersuchung potentieller Permafrostvorkommen unterschiedlicher Höhenlage im Oberengadin (Schweiz), Unpublished diploma thesis thesis, 131 pp, University of Trier, Trier.

Riseborough, D. W. (2002), The mean annual temperature at the top of permafrost, the TTOP model, and the effect of unfrozen water, *Permafrost and Periglacial Processes*, *13*(2), 137-143.

Rist, A. (2002), Unterkühlte Blockschutthalden mit Hexenwäldli - Abiotische Faktoren zur Charakterisierung des Phänomens, Unpublished Diploma Thesis thesis, 65 pp, TU München-Weihenstephan, SLF Davos, München, Davos.

Rödder, T., & C. Kneisel (2011), Permafrost mapping using quasi-3D resistivity imaging, Murtèl, Swiss Alps, *Near Surface Geophysics*, *9*.

Rödder, T., & C. Kneisel (2012), Influence of snow cover and grain size on the ground thermal regime in the discontinuous permafrost zone, Swiss Alps, *Geomorphology*, *175–176*(0), 176-189.

Rossel, V., G. Weber, & J.-M. Gobat (2004), Humus forms on permafrost in a cold scree slope (Creux-du-Van, Neuchâtel, Switzerland), paper presented at Eurosoil, Freiburg, Germany, 4-12 September 2004.

Rucker, D. F., M. T. Levitt, & W. J. Greenwood (2009), Three-dimensional electrical resistivity model of a nuclear waste disposal site, *Journal of Applied Geophysics*, *69*(3-4), 150-164.

Růžička, V., & J. Hajer (1996), Spider (Araneae) of stoney debris in North Bohemia, *Arachnologische Mitteilungen*, *12*, 10.

Sannel, A. B. K., & P. Kuhry (2008), Long-term stability of permafrost in subarctic peat plateaus, west-central Canada, *Holocene*, *18*(4), 589-601.

Sasaki, Y. (1994), 3-D resistivity inversion using the finite-element method, *Geophysics*, *59*(12), 1839-1848.

Sawada, Y. (2008), Origin an age of the perennial ice within the block slope in Shikaribestu Mountains, Hokkaido, Japan: possible archive of paleoclimate, paper presented at 9th International Conference on Permafrost, Fairbanks, Alaska.

Sawada, Y., M. Ishikawa, & Y. Ono (2003), Thermal regime of sporadic permafrost in a block slope on Mt. Nishi-Nupukaushinupuri, Hokkaido Island, Northern Japan, *Geomorphology*, *52*(1-2), 121-130.

Scales, J. A., & R. Snieder (2000), The anatomy of inverse problems, *Geophysics*, *65*(6), 3.

Schneider, S., M. Hoelzle, & C. Hauck (2012), Influence of surface and subsurface heterogeneity on observed borehole temperatures at a mountain permafrost site in the Upper Engadine, Swiss Alps, *The Cryosphere*, *6*(2).

Schönwiese, C. D. (2006), *Praktische Statistik für Meteorologen und Geowissenschaftler*, 4 ed., 302 pp., Borntraeger, Stuttgart.

Schrott, L., & T. Hoffmann (2008), Refraction Seismics, in *Applied Geophysics in Periglacial Environments*, edited by C. Hauck and C. Kneisel, p. 24, Cambridge University Press, Cambridge.

Schudel, K. (2002), Hexenwäldli – Dendroökologie von Kümmerfichtenbeständen auf unterkühlten Schutthalden, Unpublished Diploma Thesis thesis, 64 pp, ETH Zürich, Zürich.

Schwindt, D. (2007), Geophysikalische Kartierung und bodenkundliche Charakterisierung eines subalpinen Standorts mit Permafrost, edited, p. 140, University of Trier, Trier.

Schwindt, D., & C. Kneisel (2009), Quasi-3D resistivity imaging – results from geophysical mapping and forward modeling, *Geophysical Research Abstracts*, *11*.

Schwindt, D., & C. Kneisel (2010), Temporal permafrost variability at three subalpine talus slopes in the Swiss Alps, by geoelectrical monitoring and supplemental methods paper presented at 3rd European Conference on Permafrost (EUCOP III), Svalbard, Norway, June 13-17, 2010.

Schwindt, D., & C. Kneisel (2011), Optimisation of quasi-3D electrical resistivity imaging â€“ application and inversion for investigating heterogeneous mountain permafrost, *The Cryosphere Discuss*, *5*(6).

Scott, W. J., P. V. Sellmann, & J. A. Hunter (1990), Geophysics in the study of permafrost, in *Geotechnical and Environmental Geophysics*, edited by S. H. Ward, pp. 355-384, Society of Exploration.

Sheehan, J. R., W. E. Doll, & W. A. Mandell (2005), An evaluation of methods and available software for seismic refraction tomography analysis, *Journal of Environmental and Engineering Geophysics*, *10*(1), 21-34.

Silvester, P. P., & R. L. Ferrari (1996), *Finite elements for electrical engineers*, 3 ed., 516 pp., Cambridge University Press, Cambridge.

Smith, M. W., & D. W. Riseborough (1996), Permafrost monitoring and detection of climate change, *Permafrost and Periglacial Processes*, *7*(4), 301-309.

Smith, M. W., & D. W. Riseborough (2002), Climate and the limits of permafrost: A zonal analysis, *Permafrost and Periglacial Processes*, *13*(1), 1-15.

Soupios, P., I. Papadopoulos, M. Kouli, I. Georgaki, F. Vallianatos, & E. Kokkinou (2007), Investigation of waste disposal areas using electrical methods: a case study from Chania, Crete, Greece, *Environmental Geology*, *51*, 1249-1261.

Telford, W. M., L. P. Geldart, & R. E. Sheriff (1990), *Applied Geophysics*, Second Edition ed., 792 pp., Cambridge University Press.

Timur, A. (1968), Velocity of compressional waves in porous media at permafrost temperatures, *Geophysics*, *33*(4), 584-595.

Trümpy, R. (1980), *Geology of Switzerland - a guide-book. Part A: An Outline of the Geology of Switzerland*, 104 pp., Wepf & Co., Basel, New York.

Uhlmann, B., S. Goyette, & M. Beniston (2009), Sensitivity analysis of snow patterns in Swiss ski resorts to shifts in temperature, precipitation and humidity under conditions of climate change, *International Journal of Climatology*, *29*(8), 1048-1055.

Vonder Mühll, D. (1993), *Geophysikalische Untersuchungen im Permafrost des Oberengadins*, 222 pp., Zürich, Switzerland.

Vonder Mühll, D., C. Hauck, & H. Gubler (2002), Mapping of mountain permafrost using geophysical methods, *Progress in Physical Geography*, *26*(4), 643-660.

Vonder Mühll, D., C. Hauck, H. Gubler, R. McDonald, & N. Russill (2001), New geophysical methods of investigating the nature and distribution of mountain permafrost with special reference to radiometry techniques, *Permafrost and Periglacial Processes*, *12*(1), 27-38.

Wakonigg, H. (1996), Unterkühlte Schutthalden, in *Beiträge zur Permafrostforschung in Österreich*, edited, pp. 209-223, Arbeiten aus dem Institut für Geographie der Karl-Franzens-Universität Graz.

Walker, D. A., et al. (2008), Arctic patterned-ground ecosystems: A synthesis of field studies and models along a North American Arctic Transect, *Journal of Geophysical Research-Biogeosciences*, *113*(G3).

Walker, D. A., et al. (2003), Vegetation-soil-thaw-depth relationships along a low-arctic bioclimate gradient, Alaska: synthesis of information from the ATLAS studies, *Permafrost and Periglacial Processes*, *14*(2), 103-123.

Wang, G., L. a. Liu, G. Liu, H. Hu, & T. Li (2010), Impacts of grassland vegetation cover on the active-layer thermal regime, northeast Qinghai-Tibet Plateau, China, *Permafrost and Periglacial Processes*, *21*(4), 335-344.

Wegmann, G. (1995), Permafrostvorkommen auf geringer Meereshöhe - Eine Fallstudie im Brüeltobel (AI), edited, p. 80, ETH Zürich, Zürich.

Williams, P. J., & M. W. Smith (1991), *The Frozen Earth - Fundamentals of Geocryology*, Cambridge University Press, Cambridge.

Woo, M. K., & P. Marsh (2005), Snow, frozen soils and permafrost hydrology in Canada, 1999-2002, *Hydrological Processes*, *19*(1), 215-229.

Yi, S. H., M. K. Woo, & M. A. Arain (2007), Impacts of peat and vegetation on permafrost degradation under climate warming, *Geophysical Research Letters*, *34*(16).

Zacharda, M., M. Gude, S. Kraus, C. Hauck, R. Molenda, & V. Ruzicka (2005), The relict mite Rhagidia gelida (Acari, Rhagidiidae) as a biological cryoindicator of periglacial microclimate in European highland screes, *Arctic Antarctic and Alpine Research*, *37*(3), 402-408.

Zacharda, M., M. Gude, & V. R (2007), Thermal regime of three low elevation scree slopes in central Europe, *Permafrost and Periglacial Processes*, *18*(3), 301-308.

Zhang, T. (2005), Influence of the seasonal snow cover on the ground thermal regime: an overview, *Reviews of Geophysics*, *43*(4), RG4002.

Zimmerman, R. W., & M. S. King (1986), The effect of the extend of freezing in seismic velocities in unconsolidatad permafrost, *Geophysics*, *51*(6), 1285-1290.

"A little love and affection

in everything you do,

will make the world a better place,

with or without you"

Neil Young (2003), Falling From Above